Feasibility of Applying Controllable Lubrication Techniques to Reciprocating Machines

Pulido, Edgar Estupinan; Santos, Ilmar

Publication date:
2009

Document Version
Publisher's PDF, also known as Version of record

Feasibility of Applying Controllable Lubrication Techniques to Reciprocating Machines

PhD Thesis

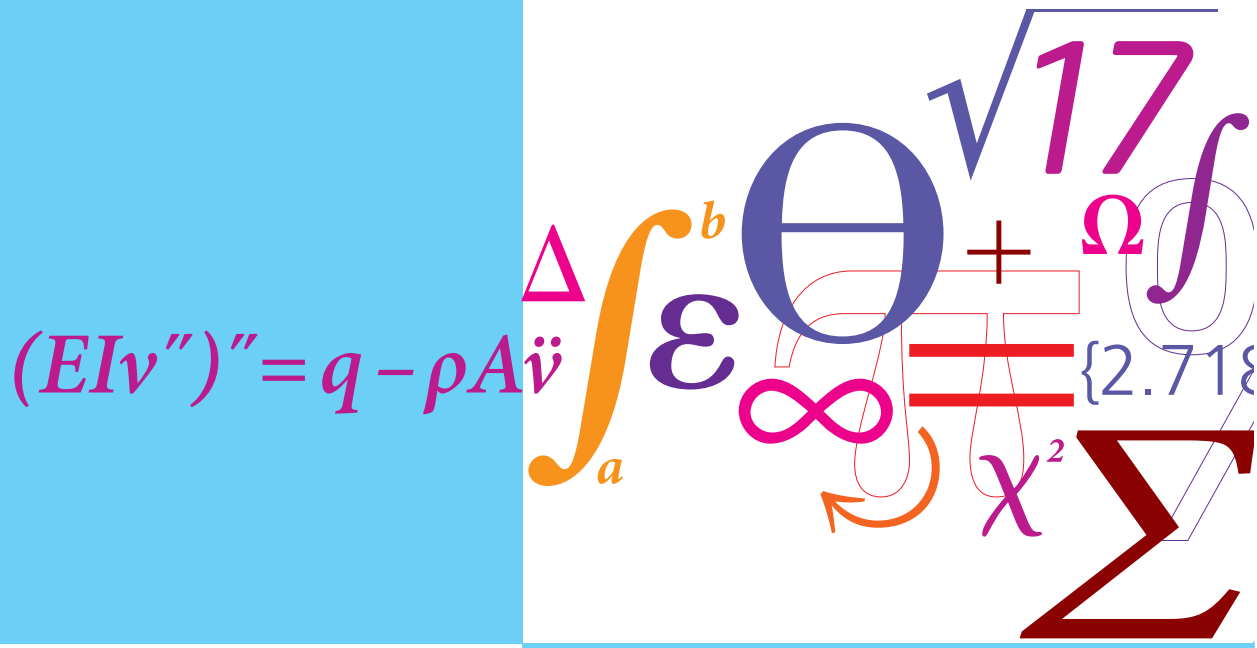

Edgar Estupiñan Pulido
DCAMM Special Repport No. S111
December 2009

DTU Mechanical Engineering
Department of Mechanical Engineering

Feasibility of Applying Controllable Lubrication Techniques to Reciprocating Machines

Edgar Estupiñan Pulido

Department of Mechanical Engineering
Technical University of Denmark

Title of the thesis:
Feasibility of Applying Controllable Lubrication Techniques
to Reciprocating Machines

Ph.D. student:
Edgar Estupiñan Pulido
E-mail: eep@mek.dtu.dk

Supervisor:
Ilmar Ferreira Santos
E-mail: ifs@mek.dtu.dk

Address:
Nils Koppels Allé, Building 404, DK-2800.
Kgs. Lyngby, Denmark
Department of Mechanical Engineering
Technical University of Denmark

ISBN 978-87-89502-95-3

Preface

This thesis is submitted as partial fulfilment of the requirements for awarding the Danish Ph.D. degree. The work was carried out from September 2006 to December 2009 at the Department of Mechanical Engineering (*MEK*), Solid Mechanics (*FAM*), Technical University of Denmark (*DTU*). The project was supervised by Associate Professor Dr.-Ing. Ilmar Ferreira Santos.

First of all, I would like to thank my supervisor for his permanent support and guidance, and for inspiring me not only technically, but in many other aspects. I want to thank my closest colleagues from DTU, Stefano Morosi, Martin Haugaard, Said Lahiri and the newcomer Alejandro Cerda, for the pleasure of working together, for all the stimulating talks, and pleasure moments during these years. I also want to thank my former colleagues from DTU, Klaus Kjølhede and Niels Heinrichson, and to Professor Peder Klit, for making me feel welcome when I just arrived, and for introducing me to the Danish culture.

I specially want to thank my dear wife Yury, for making my life more enjoyable during all these years together, for her permanent support and encouragement, and for always being on my side.

I want to gratefully acknowledge the support given by the Programme Alβan, the European Union Programme of High Level Scholarships for Latin America, scholarship No. E06D101992CO. Last but not least, I wish to thank the support given by the University of Tarapacá, Chile.

I dedicate this work to my mother for making me always feel that geographical distances does not count in a mother's love, and to my son Simon for bringing so much joy to my life.

Technical University of Denmark
Kgs. Lyngby, December 2009

Edgar Estupiñan

Abstract

The use of active lubrication in journal bearings helps to enhance the thin fluid films by increasing the fluid film thickness and consequently reducing viscous friction losses and vibrations. One refers to active lubrication when conventional hydrodynamic lubrication is combined with dynamically modified hydrostatic lubrication. In this case, the hydrostatic lubrication is modified by injecting oil at controllable pressures, through orifices circumferentially located around the bearing surface.

In order to study the performance of journal bearings of reciprocating machines, operating under conventional lubrication conditions, a mathematical model of a reciprocating mechanism connected to a rigid / flexible rotor via thin fluid films was developed. The mathematical model involves the use of multibody dynamics theory for the modelling of the reciprocating mechanism (rigid bodies), finite elements method for the modelling of the flexible rotor (crankshaft) and hydrodynamic fluid film theory for describing the dynamics of the thin fluid films. When active lubrication is introduced to modify conventional hydrodynamic lubrication, by means of aplying radial oil injection at controllable oil pressures, the Reynolds equation is modified to accomodate the terms related to the controllable oil injection pressures and orifice distribution on the bearing surface. The active bearing forces and the dynamics of the oil injection system are coupled to the set of nonlinear equations that describes the dynamics of the reciprocating engine, obtained with the help of multibody dynamics (rigid components) and finite elements method (flexible components), and the global system of equations is numerically solved. The analysis of the results was carried out with focus on the behaviour of the journal orbits, maximum fluid film pressure minimum fluid film thickness. The reduction in the cyclic averaged power consumption due to viscous friction forces is also studied.

The modelling of two oil injection systems is presented in the work. The main governing equations of the dynamics of a piezo-actuated oil injection system and a mechanical-actuated unit injector are developed. It is shown how the dynamics of the oil injection system is coupled to the dynamics of the bearing fluid film through equations. Applying controllable radial oil injection to dynamically loaded journal bearings helps: a) to reduce friction losses by increasing the fluid film thickness; b) to reduce vibrations (i.e., smaller journal centre orbits); and c) to increase the effective carrying load area by modifying the pressure distribution profile, which can make it possible to use bearings of smaller dimensions with similar load-carrying capacity.

Resumé (in Danish)

Anvendligheden af aktiv smøring i reciprokerende maskiner

Brugen af aktiv smøring i glidelejer forøger tykkelsen af smørefilmen, hvorved tab fra viskos friktion og vibrationer mindskes. Konventionel hydrodynamisk smøring kombineret med dynamisk modificeret hydrostatisk smøring, kaldes aktiv smøring. Her modificeres den hydrostatiske smøring ved at injicere olie igennem dyser i lejets overflade.

For at studere egenskaberne af glidelejer i stempel maskiner under konventionelle smøringsbetingelser er en matematisk model af en krumtapmekanisme forbundet til en stiv / fleksibel rotor via en væskefilm udarbejdet. Den matematiske model involverer brugen af "multi-body-dynamic" teori til modelleringen af en krunmtapmekanisme, "Finite Element" metoden bruges til modellering af den fleksible rotor (krumtappen) og hydrodynamisk smørefilmteori bruges til at beskrive dynamikken af væskefilmen. Når aktiv smøring introduceres for at modificere den konventionelle hydrodynamiske smøring, ved hjælp af radial indsprøjtning af olie, modificeres Reynolds ligning med led der beskriver indsprøjtningen. De aktive lejekræfter og dynamikken af olieindsprøjtningssystemet kobles til systemet af ikke lineære ligninger der beskriver dynamikken af den stempelmaskinen, som er udledt ved hjælp af "Finite Element" metoden. Efterfølgende løses systemet numerisk. Analysen af resultaterne baserer sig påundersøgelse af lejesølernes bevægelse i lejerne, maksimalt smørefilmtryk og minimum smørefilmtykkelse. Reduktionen af det gennemsnitlige energiforbrug fra viskose kræfter studeres ligeledes.

Modelleringen af to olieindsprøjtningssystemer præsenteres i dette arbejde. De vigtigste beskrivende ligninger for et dynamisk piezo-aktueret olieindsprøjtningssystem og en mekanisk aktueret injektor udledes. Det vises hvordan dynamikken af et olieindsprøjtningssystem kobles matematisk til lejet. Ved anvendelse af radial olieindsprøjtning i dynamisk belastede glidelejer opnås det at: a) friktionstabet reduceres, da filmtykkelsen øges; b) vibrationer mindskes (dvs. lejesølens bevægelsesamplitude mindskes); og c) at den effektivt bærende flade øges ved modifikation af trykprofilen, hvilket gør det mulig at bruge mindre lejer med uændret bæreevne.

List of Pubications

The following articles in journals and conference proceedings complement the work presented in this thesis. For the completeness of this thesis, copies of the journal articles are included at the end of the manuscript in appendix B.

Journal Articles

[J1] E.A. Estupiñan and I.F. Santos. Dynamic modeling of hermetic reciprocating compressors, combining multibody dynamics, finite elements method and fluid film lubrication. *International Journal of Mechanics*, Vol.1 (4), 2007, pp. 36-43.

[J2] E.A. Estupiñan and I.F. Santos. Modelling hermetic compressors using different constraint equations to accommodate multibody dynamics and hydrodynamic lubrication. *Journal of the Brazilian Society of Mechanical Sciences and Engineering*, Vol.31 (1), 2009, pp. 35-46.

[J3] E.A. Estupiñan and I.F. Santos. Linking rigid multibody systems via controllable thin fluid films. *Tribology International*, Vol. 42 (10), 2009, pp. 1478-86.

Conference Articles

[C1] I.F. Santos and E.A. Estupinan*. Combining multibody dynamics, finite elements method and fluid film lubrication to describe hermetic compressor dynamics. In proceedings of the *6th WSEAS International Conference on System Science and Simulation in Engineering (ICOSSSE'07)*, ISBN 978-960-6766-14-5, pp. 237-242, November 21-23,2007, Venice, Italy.

[C2] E.A. Estupiñan* and I.F. Santos. Linking rigid multibody systems via controllable thin fluid films. In proceedings of *NORDTRIB 2008, 13th Nordic Symposium on Tribology*, ISBN 978-952-15-1959-8, paper: NT2008-42-30, June 13-16, Tampere, Finland.

[C3] E.A. Estupinan* and I.F. Santos. Feasibility of applying controllable lubrication to the main bearings of reciprocating engines. In proceedings of *23rd International Conference on Noise and Vibration Engineering - ISMA 2008*, ISBN 978-90-7380-286-5, pp. 2015-27, September 15-17, 2008. Katholieke Universiteit Leuven, Belgium.

*Oral presenter.

[C4] E.A. Estupinan* and I.F. Santos. Linking rigid and flexible multibody systems via thin fluid films actively controlled. In proceedings of *STLE/ASME International Joint Tribology Conference - IJTC 2008*, ISBN 978-0-7918-3837-2, October 20-22, 2008, Miami (FL), USA.

[C5] E.A. Estupinan and I.F. Santos*. Feasibility of applying controllable lubrication to dynamically loaded journal bearings. In proceedings of *XIII International Symposium on Dynamic Problems of Mechanics - DINAME 2009*, Almeida, C. A. (Editor), ABCM, March 2-6, 2009, Angra dos Reis, RJ, Brazil.

[C6] E.A. Estupinan* and I.F. Santos. Feasibility of applying active lubrication to dynamically loaded fluid film bearings. In proceedings of *64th STLE Annual Meeting and Exhibition - STLE 2009*, May 17-21, 2009, Orlando (FL), USA.

[C7] E.A. Estupinan* and I.F. Santos. Active lubrication applied to internal combustion engines - evaluation of control strategies. In proceedings of *The Sixtheenth International Congress on Sound and Vibration - ICSV16*, ISBN: 978-83-60716-71-7, July 5-9, 2009, Krakow, Poland.

[C8] E.A. Estupinan and I.F. Santos*. Active lubrication strategies applied to dynamically loaded fluid film bearings. In proceedings of *World Tribology Conference 2009 - WTC IV*, ISBN: 978-4-9900139-9-8, Sept. 6-11, 2009, Kyoto, Japan.

[C9] E.A. Estupinan* and I.F. Santos. Schemes for applying active lubrication to main engine bearings. In proceedings of *11th Pan-American Congress of Applied Mechanics - PACAM XI*, Jan. 4-8, 2010, Foz do Iguaçu, Brazil.

All the above articles were written under the supervision of Prof. Ilmar Santos. Additional oral presentations related to the work carried out during this project were given during the following events:

Symposiums

- E.A. Estupinan. Presentation of PhD project: Feasibility of applying active lubrication to internal combustion engines. *2nd Alβan Conference - Grenoble 2007*, May 11-12,2007, Grenoble, France. (Oral presentation).

- E.A. Estupinan. Active lubrication applied to reciprocating engines - control strategies. *12th Internal Sumposium - DCAMM*, March 23-25, 2009, Sørup Herregård, Ringsted, Denmark. (Oral presentation).

- E.A. Estupinan. Active lubrication applied to main bearings of internal combustion engines. *3rd Alβan Conference - Porto 2009*, June 19-20, 2009, Porto, Portugal. (Oral presentation and written manuscript).

*Oral presenter.

Contents

List of Figures

List of Tables

Symbols and Nomenclature

Latin Symbols

A	:	transversal area [m^2]
a_b ; $\bar{a}_b$	:	axial land width [m] ; axial land width ratio (a_b/l_b)
B_i	:	notation for the moving reference i, $x_i y_i z_i$
c_b	:	clearance of bearing [m]
C_d	:	discharge coefficient
d_o	:	diameter of orifices [m]
D_p	:	piston diameter [m]
e_b	:	bearing eccentricity [m]
e_c	:	mass eccentricity of crank [m]
f_{vf}	:	viscous friction force [N]
$\mathbf{f_A}$	:	vector of reaction forces in pin crank-connecting rod
$\mathbf{f_B}$	:	vector of reaction forces in pin piston-connecting rod
$\mathbf{f_b}$	:	vector of journal bearing forces
F_b	:	bearing load capacity [N]
$h(\varphi,t)$	:	oil film thickness [m]
h_p	:	length of crank pin, [m]
I	:	notation for the inertial reference system XYZ
l	:	length of connecting rod [m]
l_b	:	width of bearing [m]
l_o	:	length of orifices [m]
m	:	mass [kg]
$p(\varphi,z,t)$	:	fluid film pressure profile [Pa]
p_{max}	:	maximum fluid film pressure [Pa]
P	:	pressure [Pa]
P_g	:	combustion gas pressure [Pa]
Q	:	flow [m^3/s]
r_b	:	bearing radius [m]
r_c	:	radius crank-pin centre [m]
S	:	Sommerfeld number: $\frac{\mu\dot{\theta}r_b l_b}{\pi F_b}\left(\frac{r_b}{c_b}\right)^2$

t	:	time [s]
$\mathbf{T_i}$	:	transformation matrix in the coordinate i
v_{rms}	:	vibration of journal (root mean square value) [mm/s]
V	:	instantaneous volume [m^3]
$(W_f)_{avg}$	:	cyclic averaged power dissipation [W]
x	:	displacement [m]
x_C,y_C	:	displacements in X and Y directions of crank centre [m]
x_B	:	displacement of piston in X-direction [m]

Greek Symbols

α	:	rotation angle of the connecting rod [rad]
β	:	rotation angle around X-X axis [rad] ; Bulk modulus [Pa]
Γ	:	rotation angle around Y-Y axis [rad]
Δt	:	time step [s]
ε	:	eccentricity ratio (e_b/c_b)
η,ξ	:	radial axis of moving reference frame attached to journal bearing
θ_c	:	rotational angle of the crank [rad]
Θ	:	angle measure from X axis in the clockwise direction
λ	:	bearing aspect ratio ($l_b/2r_b$)
μ	:	oil film viscosity [Pa.s]
ρ	:	oil density [kg/m^3]
τ_z	:	motor shaft torque [N.m]
ϕ	:	attitude angle [rad]
φ	:	angle measured from maximum OFT
Ω, $\dot{\theta}$	:	angular velocity of the rotor, [rpm] and [rad/s] respectively
$F(\varphi, z)$	:	function that describes position of orifices along the bearing surface [m^2]

Subscripts

A	:	relative to the centre of conrod bearing
b	:	relative to the bearings
B	:	relative to the centre of mass of piston
B_i	:	relative to the $i-th$ mobile reference frame
c	:	relative to the crank
cc	:	relative to the control chamber
cr	:	relative to the connecting rod
cv	:	relative to the control valve
cp	:	relative to the cylinder pump
C	:	relative to the centre of the crank/journal
dv	:	relative to the delivery valve
inj	:	relative to the injection

I	:	relative to the inertial reference frame
jb	:	relative to the journal bearing
nv	:	relative to the needle valve
ns	:	relative to the needle seat
o	:	relative to the orifices
p	:	relative to the piston
pz	:	relative to the piezostack
r,t	:	relative to radial and transversal directions respectively
vf	:	relative to the viscous friction
X,Y	:	relative to X and Y directions, respectively

Abbreviations

ALJB	Active lubricated journal bearing
BDC	Bottom dead centre
CHL	Conventional hydrodynamic lubrication
DOF	Degree of freedom
DLJB	Dynamically loaded journal bearing
EHD	Elasto-Hydrodynamics
FD	Finite differences
FEM	Finite element method
FJB	Finite-width journal bearing
HRC	Hermetic reciprocating compressor
ICE	Internal combustion engine
LJB	Infinitely long-width journal bearing
MBD	Multibody dynamics
OFT	Oil film thickness
SJB	Short-width journal bearing
TDC	Top dead centre
THD	Thermo-hydrodynamics
TEHD	Thermo-elasto-hydrodynamics

Chapter 1

Introduction

1.1 Motivation

Internal combustion engines (*ICE*s) are widely used as a power source, being the most important component in a vast variety of ground and sea transportation vehicles, as in many other engineering applications. Compared to alternative systems, *ICE*s keep a high popularity due to its performance, reliability and versatility, having still a huge potential to deal with the challenges of the future (Schulte and Wirth, 2004; Tung and McMillan, 2004). As the demands placed upon engines have increased, tribology plays an increasingly important role in the development of new generations of engines (Priest and Taylor, 2000). The creative combination of engine dynamics and tribology, information science, control techniques, artificial intelligence and numerical algorithms is a modern trend, which leads to new methodologies and technologies for tribological engine design (Santos, 2009). It not only presents an effective approach to engine design but also explores a new direction for research and design methodology.

In order to increase comfort, safety, and reliability together with the improvement in driving performance, fuel consumption, emissions and manufacturing, significant developments were achieved during the last decades, which can be partially reflected by the number of mechatronic systems implemented in today's cars (Schöner, 2004; Isermann, 2006). In fact, in vehicles, a large number of pure mechanical systems have been changed to mechatronical systems. Some examples of typical automotive mechatronic systems are: antiblocking system (*ABS*), electronic stability program (*ESP*), electronic fuel injection system (*EFI*), electronic exhaust gas recirculation system (*EGR*), and climate comfort systems, among others. However and despite all the significant technological developments in automotive industry and particularly in the development of powertrain systems, the energy losses produced by friction and heat are still kept in a significant percent. Recent studies showed that the frictional losses in the engine of a light duty vehicle, could amount to as much as 48% of the total energy consumption, being the major contributor the friction in piston skirts and piston rings (Tung and McMillan, 2004). Frictional losses associated with the bearings and crankshaft alone could amount to 30% of the total engine losses, as illustrated in Fig. 1.1. It explains why, particularly in recent years, much attention has been paid to the reduction of friction, noise and vibrations in powertrain systems, with focus on the use of new lubricants, new composite materials and new geometric bearing designs, but still using conventional lubrication methods.

Several friction models of different degree of complexity, have been developed to evaluate friction losses in *ICE*s, among them, the studies by Rezeka and Henein (1984); Ciulli (1992); Taraza et al. (2000); Richardson (2000). Considering that in a modern *ICE* a significant part of the total power loss is due to bearings, the implementation of innovative technological solutions are of great importance.

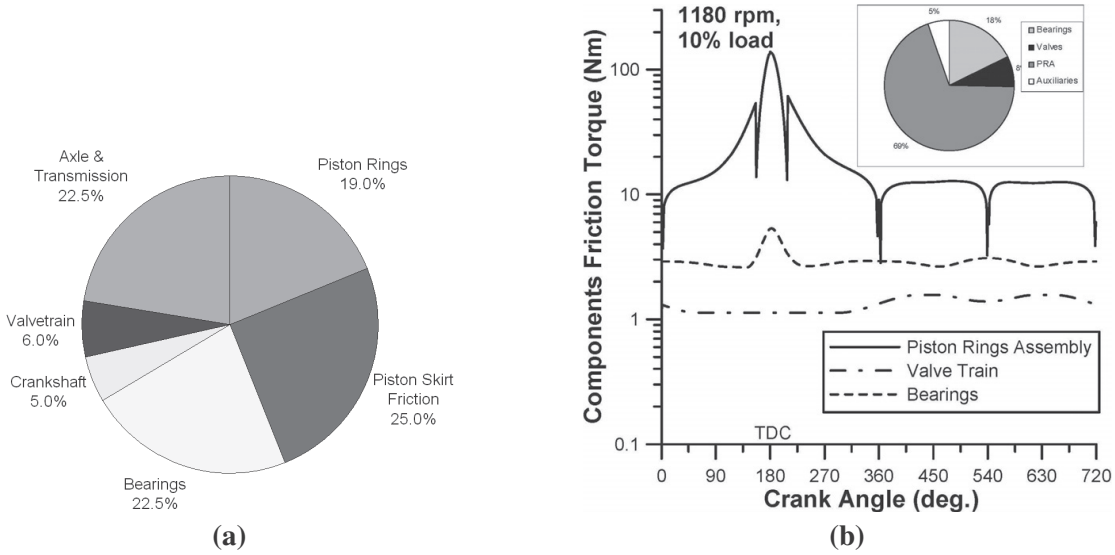

Figure 1.1: *(a) Distribution of friction losses in an engine of a light duty vehicle (Spearot, 2000); (b) Components friction torque variation during an engine cycle (Rakopoulos and Giakoumis, 2007).*

When the hydrostatic and the hydrodynamic lubrication are simultaneously combined in a journal bearing, with the aim of reducing wear between rotating and stationary parts, one refers to the hybrid lubrication, which offers the advantages of both lubrication mechanisms. When part of the hydrostatic pressure is also dynamically modified by means of hydraulic control systems, one refers to active lubrication. In previous studies using tilting pad journal bearings, it was shown that by the combination of fluid power, electronics and control theory, active lubrication makes feasible the reduction of wear and the attenuation of vibration (Santos, 1994).

In this framework, the main aim of this PhD project is to investigate the feasibility of applying active lubrication to combustion engines main bearings with the aim of reducing wear and vibrations simultaneously. It is important to keep in perspective the fact that engines are primarily mechanical products with mechanical functionality. Electrical assemblies and embedded software are only enabling technologies, and not the critical engine functions themselves. However, sophisticated functions such as engine management, traction control, and active vehicle dynamics can only be implemented today by the judicious combination of mechatronic technologies. Most of the research towards vibration control in combustion engines uses conventional techniques based on compensation for unbalance or machine elements flexibility, optimization of components based on refined finite element models, among other techniques (Lugner and Plochl, 2004). Active lubrication appears as an innovative mechatronic tool towards active control of vibration in engines.

1.2 Problem definition

1.2.1 Aims and Objectives of the Project

The main scientific aim of this project is to investigate the feasibility of reducing friction losses, wear and vibrations in dynamically loaded journal bearings (*DLJB*) by modifying the hydrodynamic fluid film through active/controllable lubrication techniques. By using actively lubricated bearings, it is expected that mechanical vibrations and friction losses could be greatly reduced so that machines life can be prolonged and bearing size can be reduced. The investigations carried out in this work are primarily devoted to engine main journal bearings or the so called crankshaft journal bearings. An important part of this project is aimed at investigating feasible schemes for applying controllable radial oil injection, evaluating different strategies for controlling oil injection pressures.

1.2.2 Methodology and main stages of the project

During the first stage of this project, the focus was put on the modelling of *DLJB*s operating under hydrodynamic lubrication conditions, evaluating analytical and numerical solutions of the Reynolds equation and using a hermetic reciprocating compressor (*HRC*) as a case study. The equations of motion of the main reciprocating mechanism were obtained using multibody dynamics (*MBD*), where the dynamics of the fluid films were incorporated. Additionally, the flexibility of the crankshaft was included by means of a finite elements formulation *FEM*. For the solution of the global system, a numerical method was computationally implemented, which is explained in chapter 5. Comparisons between a complete rigid model and a flexible model were carried out giving some insights into the behaviour of the minimum oil film thickness (*OFT*), maximum film pressures and vibration levels. The main results obtained during this first stage of the project are included in papers: [J1]*, [J2]*, and in (Santos and Estupinan, 2007).

The next step of this project was focused upon the modelling of *DLJB*s operating with hybrid lubrication conditions, which involves the modification of Reynolds equation to account for the active oil injection. A numerical scheme for the solution of the modified Reynolds equation was implemented, and the active fluid film forces computed and coupled to the set of nonlinear equations obtained from the *MBD* model of the reciprocating mechanism. The numerical results were obtained for different control rules of pressure injection and the results compared to the conventional lubrication case. The main results obtained in this part of the work are included in paper [J3]*, in (Estupinan and Santos, 2008c,b), and in section 6.1 of this thesis. Additional insights into the behaviour of the journal orbits using different hybrid bearing configurations and injection pressure rules were given in (Estupinan and Santos, 2009d).

In the following studies, the main bearing of a single cylinder *ICE* was the centre of the analysis and the numerical simulations. The main results obtained during this stage of the project are included in section 6.2. The first numerical results were obtained, when the conventional and hybrid lubrication performances of the main bearing were compared focusing on the behaviour of minimum *OFT* and maximum oil film pressures. An estimation of the cyclic averaged power consumption was also included. The main findings are included in (Estupinan and Santos, 2008a, 2009c). Additional

*Included in appendix B

numerical results were obtained when bearing performance was analyzed considering two different operational speeds, giving some insigths on the vibrations reduction of the journal. The main results are included in (Estupinan and Santos, 2009a,b). In the studies mentioned above, different control rules for modifying the oil injection pressures were analyzed, however, the modelling of the dynamics of the oil injection system was avoided. Thus, a more holistic approach was addresed in the study of Estupinan and Santos (2010), where the equations that describe the dynamics of the oil injection system (i.e., oil injector and their subsystems) were coupled to the dynamics of the controllable fluid films, and consequently to the dynamics of the mechanical parts. Such an approach is described in more detail in this thesis, in section 4.2, including the fundamental equations for a piezo-actuated oil injector and for a mechanical unit injector. Nevertheless, the main emphasis has been put on the piezoelectric actuated system, considering that compactness and faster response can be expected using such type of system.

In summary, two main case studies were considered during this work: a) main bearing of a hermetic reciprocating compressor; b) crankshaft main bearing of a single cylinder combustion engine. In order to be able to evaluate the performance of main bearings operating under controlled lubrication conditions, the following main steps were involved during the mathematical modelling and numerical simulations: I) the equations of motion were obtained using *MBD* for the rigid components and *FEM* for the flexible parts; II) the modified Reynolds equations for *DLJB* operating with conventional and active lubrication (by means of controllable radial oil injection) were presented; III) the motion equations were coupled to the modified Reynolds equation; IV) a numerical solution combining a finite difference formulation (for discretizing Reynolds equation) and using the implicit Newmark method (for integrating the global system in time) was implemented; V) several alternatives for the orifices distribution and the injection control rules were evaluated; VI) the dynamics of the oil injection and the dynamics of the fluid films were coupled through equations, and the results were obtained considering different alternatives for the oil injection system.

1.2.3 Previous work

Although the development of active lubricated bearings has a short history of a little more than one and a half decades, several attempts have already shown, theoretically and experimentally, the potential of using them to control the static and dynamic properties of rotor-bearing systems. The achievements of using active lubricated journal bearings (*ALJB*), in rotor-bearing systems, have been reported since 1993 when a first generation of an *ALJB* operating with active control hydraulic chambers was presented by Santos (1994). After that, active research has been continued on this field. Special emphasis has been put on active lubrication applied by means of servohydraulic systems, using tilting pad journal bearings with multiple orifices, and multi-recessed journal bearings, as reported by several studies published (Santos, 1994; Santos and Russo, 1998; Santos et al., 2001, 2004; Santos and Watanabe, 2006). A recent and complete review of works related to developments and applications of active lubrication is included in the work of Santos (2009).

1.2.4 Contribution of the work

The main contributions of this work are presented in the articles listed at the beginning of this manuscript. The major contributions can be summarized as:

- A theoretical investigation on active lubrication applied to dynamically loaded journal bearings, through controllable radial oil injection, is carried out. Significant improvements in bearing performance are obtained.
- Linking of flexible and rigid multibody systems via thin fluid films: developing of the mathematical model and implementation of the numerical solution.
- Formulation of simple oil injection rules, synchronized with the instantaneous crankshaft angle, which are suitable to improve the global performance of bearings working under dynamic load conditions.
- Different approaches for applying controllable radial oil injection have been proposed and their correspondent mathematical models presented.

1.2.5 Organization of Thesis

This thesis is divided in seven chapters.

Chapter 2: This chapter includes a review of the state of the art of multibody dynamics studies with focus on the modelling of reciprocating machines; particularly combustion engines. The equations that describe the dynamics of a piston-connecting rod-crank mechanism are also presented.

Chapter 3: This chapter covers a review of relevant studies related to the modelling of dynamically loaded journal bearings. Based on the hydrodynamic fluid film theory, the formulation of Reynolds equation for *DLJB* is described. Considering the well known short and long bearing assumptions, analytical solutions of Reynolds equation are presented. At the end of this chapter, a numerical solution of Reynolds equation based on the finite difference method is detailed.

Chapter 4: This chapter presents the basics of active lubrication and presents the modified Reynolds equation for active lubrication and for *DLJB*. Different approaches for applying active lubrication through radial oil injection are also explored.

Chapter 5: This chapter describes how the system of equations coming from the different submodels of the system are coupled together, giving some insights into the numerical method of solution.

Chapter 6: This chapter focuses on the study of two cases: a) main bearing of a hermetic reciprocating compressor; b) main crankshaft bearing of an internal combustion engine. In both cases, the numerical results are obtained and analyzed when the bearings operate with conventional lubrication and when the bearings operate with controllable hybrid lubrication conditions by means of radial oil injection.

Chapter 7: This chapter summarises the main results and conclusions of the thesis. Some aspects for future research are addressed.

Chapter 2

A Review of Multibody Dynamics with Focus on Combustion Engines

A Multi-body System (*MBS*) consists of a finite number of bodies having mass and/or inertia and which are connected by weightless joints and force elements (Kortüm and Vaculín, 2004). The bodies of a *MBS* can be rigid or flexible and the force elements can be passive (reaction forces) or active (from control systems).

2.1 A short review

Multi-body dynamics (*MBD*) has come a long way since the gyrodynamic analysis reported by Euler (1776), which was later refined by Gammel (1920). The pioneer contributions made 300 years ago with the inception of Newton-Euler equations and more than 200 years ago with Lagrange equations for constrained systems, are nowadays fundamental to the design and analysis of complex vehicles, machines and mechanisms, as recently cited by Rahnejat (2000). The attempts to use *MBD* in different engineering applications began late in 1800 and the beginning of 1900, as reported by Roberson and Schwertassek (1988). For instance, during the second and third decades of the 1900s the use of rational dynamical analysis was important in the power technology industry, in order to study dynamical problems in steam turbines and reciprocating steam engines. However, it was not until the 1960s and onward when the work in the field of *MBD* was importantly motivated by the needs in the aerospace industry (e.g., detailed engineering analysis in the design of spacecrafts and high speed mechanisms), simultaneously with the advances of electronic digital computers (Bremer, 1999). This resulted in a growing interest for the development of general purpose *MBD* programs. The first programs developed in the late 60's were only for a limited class of rigid *MBS*, mainly problems which could be analyzed with 2-D models. Later, during the 70's, the ability to treat kinematic chains and three dimensional motion was added. During the 80's, the possibility of allowing elasticity subject to certain restrictions in individual bodies was added. Nowadays, two main approaches (i.e., dynamical formalisms) are well known in *MBD*: Lagrangian and Eulerian (Roberson and Schwertassek, 1988).

In the last thirty years, the largest growth area of application of *MBD* focused on vehicle dynamics. Particularly, the modelling and analysis of powertrain systems has been one of the areas of higher interest due to the potential industry applications. The growing interest in vehicle dynamics has been also driven by the strict requirements in terms of safety, reduction of noise and vibrations, light weight and fuel efficiency in vehicles, which bring new challenges to the automotive engineers. In recent years, the research in *MBD* applied to vehicle dynamic analysis has been mainly related to the inclusion of flexibility, impact dynamics and tribology in the *MBD* models, as cited by Rahnejat (2000). A list of relevant papers related to the application of *MBD* applied to the modelling of *ICE* is presented in table 2.1.

In order to cope with all the new design requirements, advanced modelling techniques and sophisticated real-time numerical solvers have been successfully used during the last 15 years (Arnold et al., 2004, 2007). Although a real-time solution is not necessarily required in all cases, more complexity is added to the problem when such algorithms have to deal with highly non-linear systems of equations and challenging constraints. For instance, it can be desired that a *MBD* model includes the dynamic response across a range of frequencies going from low-frequency rigid body motions (e.g., displacement dynamics of the piston and connecting rod motions) to high-frequency noise and vibrations generated by structural deformation and transient impacts (e.g., elastic response of the crankshaft and support bearings) Rahnejat (2000). A work that started in the 70's with the introduction of the first practical approach for large rigid multibody dynamic systems, based upon Lagrangian dynamics, culminated years later in the development of *ADAMS* (Automatic Dynamic Analysis of Mechanical Systems). The earlier programs such as: *DISCOS*, *DADS* and *MEDYNA*, included bodies with distribute elasticity. After a period of time, where the *MBS* codes were mainly used in space projects, *MBS* became of interest for vehicle technology applications with programs such as: *MAGLEV* (magnetically levitated vehicles), *ADAMS* (derived from DADS), *MEDYNA* (with special focus on wheel/rail interaction), and *SIMPACK* (which includes flexible bodies modelling), as reported by Kortüm and Vaculín (2004). The program *EVAS*, which enables to analyze structural and kinematic coupled vibrations in engines is also presented in the study of Kawamoto et al. (2000). Current developments are focused on combining *FEA* and *MBS* codes in order to have one global application for modelling of mechanical systems. Nowadays, most of the commercial *MBD* simulation systems work as stand-alone programs. However, some efforts are also addressed towards developing web-based dynamic simulation systems, such as the *O-DYN* program (Han, 2004).

Multibody system simulation tools provide a powerful basis for the simulation of multidisciplinary problems in the field of vehicle system dynamics (Arnold et al., 2004). Recent extensions of *MBD* simulation tools are modal reduction techniques, advanced contact models, special solvers for the time-integration of mixed continuous/discrete systems and the coupling of *MBD* with various specialised Computer Aided Engineering tools (*CAE*), such as, finite elements modelling (*FEM*), computational fluid dynamics (*CFD*) and computer aided design (*CAD*), as outlined by Vaculín et al. (2004).

Table 2.1: *Review of literature - Multibody dynamics with focus on the modelling of internal combustion engines (ICEs).*

Year	Author	Overview
1977	Orlandea et al.	First practical solution methodology for large rigid multi-body dynamic systems.
1982	Knoll and Peeken	Study of the slapping of the piston skirt against the cylinder bore.
1987	Lacy	Torsional vibration analysis of a four-cylinder gasoline engine, using a multi-body model. The crankshaft nodes were connected to the main bearing housing by an oil-film module having a linear and rotary stiffness and damping. Eccentricity is assumed to remain constant.
1991	Katano et al.	Prediction of dynamic forces generated in an engine under actual operating conditions.
1994	Zeischka et al.	Prediction of a four-stroke, four-cylinder, in-line internal combustion engine, through a multibody elasto-dynamic model of the crankshaft and the engine block, making use of FE models to represent the elastic behaviour of some components. Hydrodynamic forces computed by impedance charts, providing the journal reactions in function of the Sommerfeld number.
1995	Okamura et al.	This study shows that dynamic stiffness and damping matrices can be concatenated into an overall matrix within the dynamic stiffness matrix method as a multi-body approach. Method that enables the representation of the crankshaft as a three-dimensional structure.
1997	Boysal and Rahnejat	Multibody dynamic model for a single cylinder, four stroke engine. It includes the study of the non-linear jump phenomenon through multibody dynamic analysis using complex crankshaft orbits.
1998	Rahnejat	Publishing of a book covering theory and practical examples o multibody dynamics applied to vehicle dynamics.
2000	Rahnejat	Brief outline of the historical evolution of engineering dynamics and particularly practical applications of multi-body dynamics are discussed. It is shown in this paper that the most potential areas for research in this field are related with the inclusion of component flexibility, impact dynamics and tribology in multi-body models.
2001	Offner et al.	Based on multibody dynamics, a simulation tool for the mathematical modelling of the body structures and the calculation of the nonlinear connecting forces is developed. The model considers deformations caused by the body dynamics and by contact elasticity.
2002	Kushwaha et al.	Multibody model of a four-cylinder diesel engine. This model incorporates component flexibility and combined torsion-deflection modes of the flexible crankshaft system are studied. Numerical predictions agree with experimental findings.
2003	Ma and Perkins	A *MBD* model for an internal combustion engine is developed, including main components such as the engine block, pistons, connecting rods, modelled as rigid bodies and crankshaft, balance shafts, main bearings, and engine mount, modelled as flexible bodies.
2007	Perera et al.	Multi-physics approach to engine analysis. The *MBD* model includes rigid and flexible parts combining with the fluid film theory. Good agreement between the theoretical and experimental spectrum of the engine.
2009	Drab et al.	A *MBD* model for crankshaft dynamics simulation is developed and efficiently solved using a BDF-based time integration algorithm. Comparisons to commercial softwares show that the algorithm developed speed up the simulation more than 50%.

2.2 *MBD* modelling of combustion engines

Vehicle dynamics has became one of the major areas of applications of *MBD* (Eberhard and Schiehlen, 2006; Schiehlen, 2007). In the analysis of mechanical components of *ICE*s, dynamic simulation based on the principles of multibody dynamics plays a main role, being nowadays a standard tool in design and developing process of new engines (Drab et al., 2009). In the field of vehicle dynamics powerful computer-based applications have been developed in order to speed up the modelling and to obtain faster results.

In principle, the main mechanical parts of *ICE*s (crankshaft, camshaft, connecting rods, pistons) are elastic components subjected to fluctuating acting forces, inertial forces, and variable torques. Therefore, in order to account for their flexural and torsional deflection responses, an elasto-dynamic analysis is required. From the point of view of elasto-dynamic analysis, the model of an engine could be formulated and represented either by a transfer matrix or an overall dynamic stiffness matrix. The later is a more generalized approach which may include three dimensional elastic behaviour. The crankshaft-block sub-system is one of the most studied components in *ICE*s, due to its strong influence on the operational behaviour of the engine (Katano et al., 1991; Okamura et al., 1995; Morita and Okamura, 1995). One of the methodologies developed to analyze an *ICE*'s crankshaft-block interaction, and to solve the journal bearing lubrication problem using finite elements, is described in (Mourelatos, 2001b,a). This methodology (called *CRANKSYM*) enables the coupling of crankshaft structural dynamics, main bearing hydrodynamics and engine block stiffness using a system-based approach.

In contrast to elasto-dynamic analysis of *ICE*s, the use of simplified models can frequently be a good initial approach to predict the dynamic behaviour of the engine components, as shown by Rahnejat (1998). Usually in simplified models, piston and connecting rod are considered rigid. A non-linear multibody dynamic model of a single-cylinder, four strokes *ICE*, is outlined in the study by Boysal and Rahnejat (1997). Such a model comprises all body inertial components and assembly constraints, and assumes hydrodynamic finite-width journal bearings, where the main loads are coming from the combustion process.

Generally, *MBD* models yield to a set of equations which is a combination of differential equations and non-linear algebraic functions. Because each one of the components of the system may respond in different frequency ranges, these type of systems are usually referred to as "stiff" problems, which may require for their solution efficient numerical algorithms. In an *ICE*, sources of non-linearity comprise the constraint functions that connect the inertial elements of the system, force/reaction elements that include the cylinder combustion force history and lubricated contact forces (piston compression ring to cylinder liner and journal bearing forces). In this thesis, a simplified approach for the modelling of main mechanical components of reciprocating machinery (i.e., piston, connecting rod and crank) was adopted, which is explained in the next section.

2.3 Mathematical modelling of reciprocating machines

Based on multibody dynamics theory, the formulation of representative motion equations that describe the dynamics of a slider crank mechanism in a typical reciprocating machine is presented in this section. These equations will be further coupled to the dynamics of the fluid film bearings, which will be described in chapter 5. In the model, connecting rod and crank are considered as rigid bodies, and piston motion is modelled as a particle. Three different approaches were considered in order to account for the reaction forces at the crank-rotor connection. The three cases differ in the definition of the restrictive conditions of motion of the centre of the crank:

- Case (I). Considering a rigid crank bearing model. This is the most simple case, in which crank is only allowed to rotate, neglecting lateral displacements and tilting oscillations of the crank.
- Case (II). Considering a rigid crankshaft model. In this case, the crank is allowed to have lateral displacements but not tilting oscillations. In other words, the crankshaft is considered rigid and supported by fluid film bearings.
- Case (III). Considering a flexible crankshaft model. In this case, the crank is allowed to have lateral displacements and tilting oscillations. Similarly to case (II), reaction forces at the crank-rotor connection are given by the dynamics of the bearing fluid film, but in this case the rotor (crankshaft) is considered flexible and will be modelled using finite elements.

For each one of the three cases, the motion equations for the piston-connecting rod-crank system are formulated with the help of *MBD* theory, using the Newton-Euler's method and using a frame notation of common use in multibody dynamics (Bremer, 1988; Ulbrich, 1996; Santos, 2001). Figure 2.1 is a sketch representing the main geometric characteristics of the system, indicating reference frames and main angles of rotation (β, Γ, θ and α).

2.3.1 Inertial and moving reference frames

In order to be able to describe all the representative vectors, one inertial reference frame (I_{XYZ}) and four moving reference frames (B_i) were defined. The inertial reference frame is attached to the center of the bearing (point **O**), the moving reference frames $B_1(X_1Y_1Z_1)$, $B_2(X_2Y_2Z_2)$ and $B_3(X_3Y_3Z_3)$ are attached to the crank and the moving reference frame $B_4(X_4Y_4Z_4)$ is attached to the connecting rod. Thus, B_1 $(X_1Y_1Z_1)$ is obtained by rotating I the angle β, around the X axis; B_2 $(X_2Y_2Z_2)$ is obtained by rotating B_1 the angle Γ, around the Y_1 axis; B_3 $(X_3Y_3Z_3)$ is obtained by rotating B_2 the angle θ, around the Z_2 axis; B_4 $(X_4Y_4Z_4)$ is obtained by rotating I the angle α, around the Z axis. With the help of the geometric transformation matrices $\mathbf{T}_\beta$, $\mathbf{T}_\Gamma$, $\mathbf{T}_\theta$ and $\mathbf{T}_\alpha$ any vector can be easily transformed from one reference frame to another. The transformation matrices are given by:

$\mathbf{T}_\beta$: transformation from the inertial frame I to the moving frame B_1.

$$\mathbf{T}_\beta = \begin{bmatrix} 1 & 0 & 0 \\ 0 & \cos\beta & \sin\beta \\ 0 & -\sin\beta & \cos\beta \end{bmatrix} \tag{2.1}$$

$\mathbf{T}_\Gamma$: transformation from the inertial frame B_1 to the moving frame B_2.

$$\mathbf{T}_\Gamma = \begin{bmatrix} \cos\Gamma & 0 & -\sin\Gamma \\ 0 & 1 & 0 \\ \sin\Gamma & 0 & \cos\Gamma \end{bmatrix} \tag{2.2}$$

$\mathbf{T}_\theta$: transformation from the inertial frame B_2 to the moving frame B_3.

$$\mathbf{T}_\theta = \begin{bmatrix} \cos\theta & \sin\theta & 0 \\ -\sin\theta & \cos\theta & 0 \\ 0 & 0 & 1 \end{bmatrix} \tag{2.3}$$

$\mathbf{T}_\alpha$: transformation from the inertial frame I to the moving frame B_4.

$$\mathbf{T}_\alpha = \begin{bmatrix} \cos\alpha & -\sin\alpha & 0 \\ \sin\alpha & \cos\alpha & 0 \\ 0 & 0 & 1 \end{bmatrix} \tag{2.4}$$

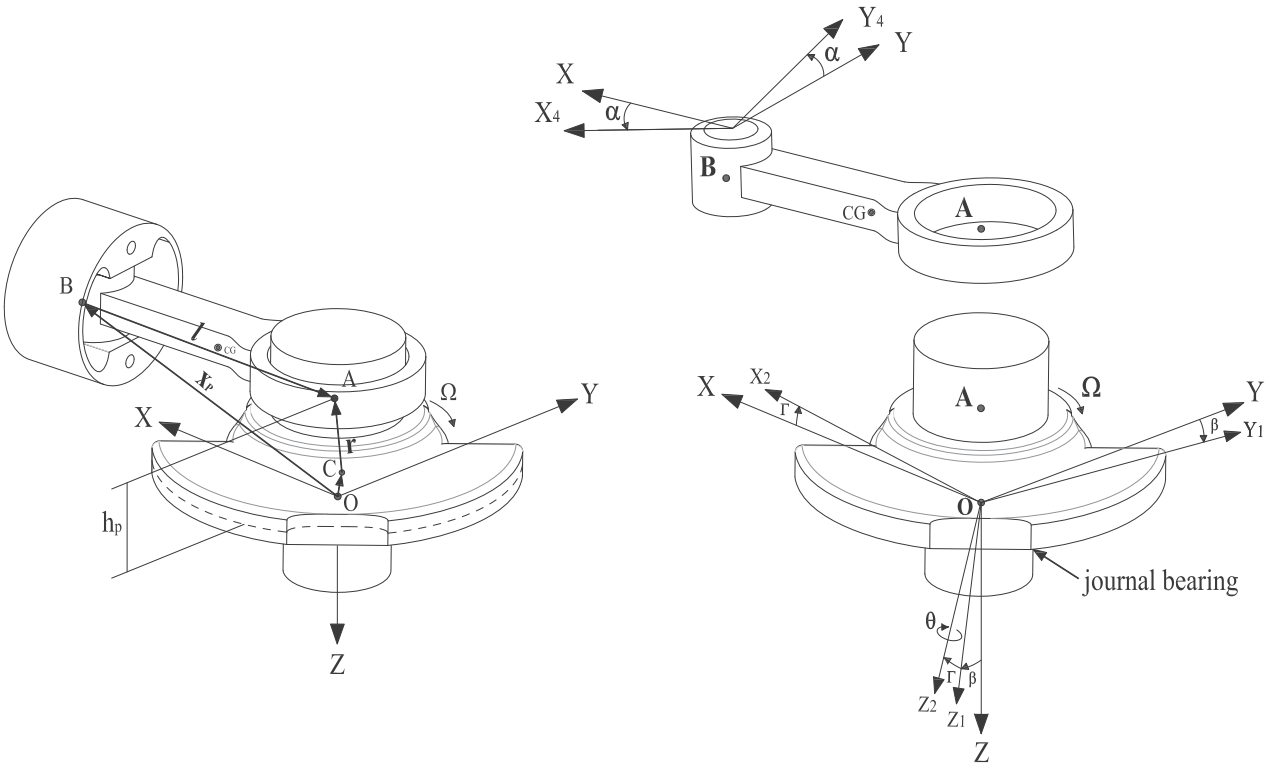

Figure 2.1: *Geometry and reference systems. left: illustration of the main constraint equation; right: reference frames and rotation angles.*

The angular velocities for each one of the moving reference frames can be written as:

$$_I\dot{\boldsymbol{\beta}} = \begin{Bmatrix} \dot\beta \\ 0 \\ 0 \end{Bmatrix};\ _{B_1}\dot{\boldsymbol{\Gamma}} = \begin{Bmatrix} 0 \\ \dot\Gamma \\ 0 \end{Bmatrix};\ _{B_2}\dot{\boldsymbol{\theta}} = \begin{Bmatrix} 0 \\ 0 \\ \dot\theta \end{Bmatrix};\ _I\dot{\boldsymbol{\alpha}} = \begin{Bmatrix} 0 \\ 0 \\ -\dot\alpha \end{Bmatrix}$$

2.3.2 Constraint equations and kinematic equations

A different constraint equation will be established for each one of the three cases considered. The expressions to calculate velocities and accelerations of the piston ($\dot{x}_B$, $\ddot{x}_B$) and the connecting rod ($\dot{\alpha}$, $\ddot{\alpha}$), are obtained by differentiating once and twice the constraint equation given for each case.

The absolute angular velocity of the crank ($\boldsymbol{\omega}$), written with help of the moving reference frame B_3, is given by:

$$ {}_{B_3}\boldsymbol{\omega} = {}_{B_3}\dot{\boldsymbol{\beta}} + {}_{B_3}\dot{\boldsymbol{\Gamma}} + {}_{B_3}\dot{\boldsymbol{\theta}} \tag{2.5} $$

where:

$$ {}_{B_3}\dot{\boldsymbol{\beta}} = \mathbf{T}_\theta \mathbf{T}_\Gamma \mathbf{T}_\beta \, {}_I\dot{\boldsymbol{\beta}} $$

$$ {}_{B_3}\dot{\boldsymbol{\Gamma}} = \mathbf{T}_\theta \mathbf{T}_\Gamma \, {}_{B_1}\dot{\boldsymbol{\Gamma}} $$

$$ {}_{B_3}\dot{\boldsymbol{\theta}} = \mathbf{T}_\theta \, {}_{B_2}\dot{\boldsymbol{\theta}} $$

Since in cases (I) and (II), the tilting oscillations of the crank are not considered (i.e., $\dot{\beta}$ and $\dot{\Gamma}$ are equal to zero), the transformation matrices B_1 and B_2 are not required, and the moving reference frame B_3 will be simply obtained by rotating I the angle θ, around the Z axis. Thus, in these two cases the absolute angular velocity of the crank is simplified to: ${}_{B_3}\boldsymbol{\omega} = \{0 \;\; 0 \;\; \dot{\theta}\}^T$, where $\dot{\theta}$ is also equal to Ω.

Case (I)

• Main constraint equation:

$$ {}_I\mathbf{x_p} + {}_I\mathbf{l} = {}_I\mathbf{r} \tag{2.6} $$

where,

$$ {}_I\mathbf{r} = \mathbf{T}_\theta^{\mathrm{T}} \cdot {}_{B_3}\mathbf{r} $$

$$ {}_{B_3}\mathbf{r} = \left\{ \begin{array}{ccc} r_c & 0 & -h_p \end{array} \right\}^T $$

$$ {}_I\mathbf{l} = \left\{ \begin{array}{ccc} -l\cos\alpha & l\sin\alpha & 0 \end{array} \right\}^T $$

$$ {}_I\mathbf{x_p} = \left\{ \begin{array}{ccc} x_B & 0 & -h_p \end{array} \right\}^T $$

• Velocities:

$$ \left[\begin{array}{cc} 1 & l\sin\alpha \\ 0 & l\cos\alpha \end{array} \right] \left\{ \begin{array}{c} \dot{x}_B \\ \dot{\alpha} \end{array} \right\} = \left\{ \begin{array}{c} -r_c\dot{\theta}\sin\theta \\ r_c\dot{\theta}\cos\theta \end{array} \right\} \tag{2.7} $$

• Accelerations:

$$ \left[\begin{array}{cc} 1 & l\sin\alpha \\ 0 & l\cos\alpha \end{array} \right] \left\{ \begin{array}{c} \ddot{x}_B \\ \ddot{\alpha} \end{array} \right\} = \left\{ \begin{array}{c} -r_c(\ddot{\theta}\sin\theta - \dot{\theta}^2\cos\theta) - l\dot{\alpha}^2\cos\alpha \\ r_c(\ddot{\theta}\cos\theta - \dot{\theta}^2\sin\theta) + l\dot{\alpha}^2\sin\alpha \end{array} \right\} \tag{2.8} $$

Case (II)

• Main constraint equation:

$$ {}_I\mathbf{x_p} + {}_I\mathbf{l} = {}_I\mathbf{r} + {}_I\mathbf{c} \tag{2.9} $$

where, ${}_I\mathbf{c} = \left\{ \begin{array}{ccc} x_C & y_C & 0 \end{array} \right\}^T$.

• Velocities:

$$ \left[\begin{array}{cc} 1 & l\sin\alpha \\ 0 & l\cos\alpha \end{array} \right] \left\{ \begin{array}{c} \dot{x}_B \\ \dot{\alpha} \end{array} \right\} = \left\{ \begin{array}{c} -r_c\dot{\theta}\sin\theta + \dot{x}_C \\ r_c\dot{\theta}\cos\theta + \dot{y}_C \end{array} \right\} \tag{2.10} $$

• Accelerations:

$$ \left[\begin{array}{cc} 1 & l\sin\alpha \\ 0 & l\cos\alpha \end{array} \right] \left\{ \begin{array}{c} \ddot{x}_B \\ \ddot{\alpha} \end{array} \right\} = \left\{ \begin{array}{c} -r_c(\ddot{\theta}\sin\theta - \dot{\theta}^2\cos\theta) - l\dot{\alpha}^2\cos\alpha + \ddot{x}_C \\ r_c(\ddot{\theta}\cos\theta - \dot{\theta}^2\sin\theta) + l\dot{\alpha}^2\sin\alpha + \ddot{y}_C \end{array} \right\} \tag{2.11} $$

Case (III)

• Main constraint equation.
In this case the main constraint equation is also given by Eq. (2.9), but due to the rotations in β and Γ, vector ${}_I\mathbf{r}$ is obtained by:

$$ {}_I\mathbf{r} = \mathbf{T}^{\mathbf{T}}_{\beta} \cdot \mathbf{T}^{T}_{\Gamma} \cdot \mathbf{T}^{\mathbf{T}}_{\theta} \cdot {}_{B_3}\mathbf{r} $$

• Velocities:

$$ \left[\begin{array}{cc} 1 & l\sin\alpha \\ 0 & l\cos\alpha \end{array} \right] \left\{ \begin{array}{c} \dot{x}_B \\ \dot{\alpha} \end{array} \right\} = \left\{ \begin{array}{c} k_1 \\ k_2 \end{array} \right\} \tag{2.12} $$

• Accelerations:

$$ \left[\begin{array}{cc} 1 & l\sin\alpha \\ 0 & l\cos\alpha \end{array} \right] \left\{ \begin{array}{c} \ddot{x}_B \\ \ddot{\alpha} \end{array} \right\} = \left\{ \begin{array}{c} k_3 \\ k_4 \end{array} \right\} \tag{2.13} $$

where:

$$ \begin{aligned} k_1 &= -r_c(\dot{\Gamma}s\Gamma c\theta + \dot{\theta}c\Gamma s\theta) - h_p\dot{\Gamma}c\Gamma + \dot{x}_C \\ k_2 &= r_c\dot{\beta}(c\beta s\Gamma c\theta - s\beta s\theta) + r_c\dot{\theta}(c\beta c\theta - s\beta s\Gamma s\theta) \\ &\quad + \dot{\Gamma}(r_c s\beta c\Gamma c\theta - h_p s\beta s\Gamma) + \dot{\beta}h_p c\beta c\Gamma + \dot{y}_C \\ k_3 &= -r_c\ddot{\Gamma}s\Gamma c\theta + \dot{\Gamma}^2(h_p s\Gamma - r_c c\Gamma c\theta) + 2r_c\dot{\theta}\dot{\Gamma}s\Gamma s\theta \\ &\quad - r_c\dot{\theta}^2 c\Gamma c\theta - h_p\ddot{\Gamma}c\Gamma - r_c\ddot{\theta}c\Gamma s\theta - l\dot{\alpha}^2 c\alpha + \ddot{x}_C \\ k_4 &= -r_c\dot{\theta}^2(c\beta s\theta + s\beta s\Gamma c\theta) - \dot{\beta}^2(r_c c\beta s\theta + r_c s\beta s\Gamma c\theta + h_p s\beta c\Gamma) \\ &\quad - \dot{\Gamma}^2(r_c s\beta s\Gamma c\theta + h_p s\beta c\Gamma) + \ddot{\beta}(h_p c\beta c\Gamma - r_c s\beta s\theta + r_c c\beta s\Gamma c\theta) \\ &\quad + \ddot{\Gamma}(r_c s\beta c\Gamma c\theta - h_p s\beta s\Gamma) - 2r_c\dot{\theta}\dot{\beta}(s\beta c\theta + c\beta s\Gamma s\theta) \\ &\quad + 2\dot{\beta}\dot{\Gamma}(r_c c\beta c\Gamma c\theta - h_p c\beta s\Gamma) - 2r_c\dot{\theta}\dot{\Gamma}s\beta c\Gamma s\theta \\ &\quad + r_c\ddot{\theta}(c\beta c\theta - s\beta s\Gamma s\theta) + l\dot{\alpha}^2 s\alpha + \ddot{y}_C \end{aligned} $$

using in these equations:

$$s\theta = \sin\theta;\ c\theta = \cos\theta;\ s\alpha = \sin\alpha;\ c\alpha = \cos\alpha;\ s\beta = \sin\beta;\ c\beta = \cos\beta;\ s\Gamma = \sin\Gamma;\ c\Gamma = \cos\Gamma.$$

2.3.3 Equations of motion

The equations of motion are formulated using Newton-Euler's method, following the methodology described by Santos (2001). The formulation of the equations of motion are presented in this section only for case (III). However, the equations of motion written in a matrix form and for all cases are included in appendix A.

The equations of motion for each body are given by equations (2.14-2.18). The force equations are described in the inertial reference frame and the moment equations of the crank and the connecting rod are described in the moving reference frames B_3 and B_4 respectively.

- *Force equation - crank*

$$\sum {}_I\mathbf{f} = m_c \cdot {}_I\bar{\mathbf{a}}_c \Rightarrow {}_I\mathbf{f_A} + {}_I\mathbf{f_{ub}} + {}_I\mathbf{f_b} = m_c\{\ \ddot{x}_C,\quad \ddot{y}_C,\quad 0\ \}^T \tag{2.14}$$

where, ${}_I\mathbf{f_{ub}}$ is the vector of the crank unbalance force and ${}_I\mathbf{f_b}$ is the vector of the dynamic journal bearing forces.

- *Moment equation - crank*

$$\sum {}_{B_3}\mathbf{M_C} = {}_{B_3}\mathbf{r} \times {}_{B_3}\mathbf{f_A} + {}_{B_3}\boldsymbol{\tau} = {}_{B_3}\mathbf{I_c}\frac{d}{dt}\left({}_{B_3}\boldsymbol{\omega}\right) + {}_{B_3}\boldsymbol{\omega} \times \left({}_{B_3}\mathbf{I}_c \cdot {}_{B_3}\boldsymbol{\omega}\right) + m_c \cdot {}_{B_3}\bar{\mathbf{r}}_{C-cm} \times {}_{B_3}\mathbf{a_C} \tag{2.15}$$

where: ${}_{B_3}\mathbf{f_A} = \mathbf{T}_\theta \cdot \mathbf{T}_\Gamma \cdot \mathbf{T}_\beta \cdot {}_I\mathbf{f_A}$; ${}_{B_3}\boldsymbol{\tau} = \{\ 0,\quad 0,\quad \tau_z\ \}^T$ and
${}_{B_3}\bar{\mathbf{r}}_{C-cm} = \{\ e_c,\quad 0,\quad 0\ \}^T$.

- *Force equation - connecting rod*

$$\sum {}_I\mathbf{f} = m_{cr} \cdot {}_I\bar{\mathbf{a}}_{cr} = {}_I\mathbf{f_A} + {}_I\mathbf{f_B} \tag{2.16}$$

where:

$$\begin{aligned} {}_I\bar{\mathbf{a}}_{\mathbf{cr}} &= {}_I\mathbf{a}_B + {}_I\dot{\boldsymbol{\alpha}} \times {}_I\dot{\boldsymbol{\alpha}} \times {}_I\bar{\mathbf{r}}_{\mathbf{cr}} + {}_I\ddot{\boldsymbol{\alpha}} \times {}_I\bar{\mathbf{r}}_{\mathbf{cr}} \\ &= \left\{ \begin{array}{c} \ddot{x}_B + \bar{r}_{cr}\left(\dot{\alpha}^2\cos\alpha + \ddot{\alpha}\sin\alpha\right) \\ \bar{r}_{cr}\left(\ddot{\alpha}\cos\alpha - \dot{\alpha}^2\sin\alpha\right) \\ 0 \end{array} \right\}. \end{aligned}$$

- *Moment equation - connecting rod*

$$\sum {}_{B_4}\mathbf{M_B} = {}_{B_4}\mathbf{l} \times {}_{B_4}\mathbf{f_A} = {}_{B_4}\mathbf{I_{cr}}\frac{d}{dt}\left({}_{B_4}\dot{\boldsymbol{\alpha}}\right) + {}_{B_4}\dot{\boldsymbol{\alpha}} \times \left({}_{B_4}\mathbf{I}_{cr}\ {}_{B_4}\dot{\boldsymbol{\alpha}}\right) + m_{cr} \cdot {}_{B_4}\bar{\mathbf{r}}_{\mathbf{cr}} \times {}_{B_4}\mathbf{a}_B \tag{2.17}$$

where: ${}_{B_4}\mathbf{f_A} = \mathbf{T}_\alpha \cdot {}_I\mathbf{f_A}$; ${}_{B_4}\mathbf{a_B} = \mathbf{T}_\alpha \cdot {}_I\mathbf{a_B}$; ${}_I\mathbf{a_B} = \{\ \ddot{x}_B,\quad 0,\quad 0\ \}^T$.

- *Force equation - piston*

$$\sum {}_I\mathbf{f_B} = m_p \cdot {}_I\,\mathbf{a}_B = {}_I\mathbf{f_B} + {}_I\mathbf{f_N} + {}_I\mathbf{f_p} \tag{2.18}$$

where: ${}_I\mathbf{f_p} = \{\ P_g A_p,\quad 0,\quad 0\ \}^T$.

The equations of motion can be rewritten in a matrix form as in Eq. (2.19), where the vector $\bar{\mathbf{b}}$ contains the main unknowns of the system (e.g., reaction forces, reaction moments and accelerations). This matrix system is fully described for each case in appendix A.

$$\bar{\mathbf{A}} \cdot \bar{\mathbf{b}} = \bar{\mathbf{c}} \tag{2.19}$$

where the vector $\bar{\mathbf{b}}$ for each case is given by:

$$\bar{\mathbf{b}}_{(\mathbf{I})} = \{f_{B_x},\ f_{B_y},\ f_{B_z},\ N_y,\ N_z,\ f_{A_x},\ f_{A_y},\ f_{A_z},\ f_{C_x},\ f_{C_y},\ f_{C_z},\ M_{C_x},\ M_{C_y},\ \ddot{\theta},\ \ddot{x}_B,\ \ddot{\alpha}\}^T$$
$$\bar{\mathbf{b}}_{(\mathbf{II})} = \{f_{B_x},\ f_{B_y},\ f_{B_z},\ N_y,\ N_z,\ f_{A_x},\ f_{A_y},\ f_{A_z},\ f_{C_z},\ M_{c_x},\ M_{c_y},\ \ddot{\theta},\ \ddot{x}_B,\ \ddot{\alpha},\ \ddot{x}_C,\ \ddot{y}_C\}^T$$
$$\bar{\mathbf{b}}_{(\mathbf{III})} = \{f_{B_x},\ f_{B_y},\ f_{B_z},\ N_y,\ N_z,\ f_{A_x},\ f_{A_y},\ f_{A_z},\ f_{C_z},\ \ddot{\theta},\ \ddot{x}_B,\ \ddot{\alpha},\ \ddot{x}_C,\ \ddot{y}_C,\ \ddot{\beta},\ \ddot{\Gamma}\}^T$$

2.3.4 Modelling of the rotor

In order to account for lateral displacements and tilting oscillations of the crankshaft, as defined for case (III), the crankshaft is modelled as a flexible body using a finite elements formulation where the rotor bearing system is assumed to be supported by flexible supports, and the gyroscopic and rotational inertia effects are included, as described by Nelson and McVaugh (1976). Thus, the global equation of motion for the rotor, described in the inertial reference frame I can be written as:

$$\bar{\mathbf{M}} \cdot \ddot{\mathbf{q}} = \underbrace{\bar{\mathbf{f}} - \bar{\mathbf{G}} \cdot \dot{\mathbf{q}} - \bar{\mathbf{K}} \cdot \mathbf{q}}_{\hat{\mathbf{f}}} \tag{2.20}$$

where, $\bar{\mathbf{M}}$, $\bar{\mathbf{K}}$ and $\bar{\mathbf{G}}$ are the mass, stiffness and gyroscopic matrices respectively; $\bar{\mathbf{f}}$ is the vector of loads acting on the rotor, given by: ${}_I\bar{\mathbf{f}} = {}_I\,\mathbf{f_{pl}} + {}_I\,\mathbf{f_{ub}} + {}_I\,\mathbf{f_b}$, where ${}_I\mathbf{f_{pl}}$ is the vector of static preload forces, ${}_I\mathbf{f_{ub}}$ is the vector of unbalance rotor forces, and ${}_I\mathbf{f_b}$ is the vector that contains the hydrodynamic bearing forces. In a journal bearing, the fluid film forces are strongly dependent on the dynamics of the journal. These forces will be calculated based on the theory of hydrodynamic lubrication, using analytical and numerical solutions of Reynolds equation, as detailed in the next chapter.

The flexibility of the crankshaft is coupled to the *MBD* model of the reciprocating mechanism through equations. Thus, the matrix system given by Eq. (2.19) will be coupled to the equations of the finite elements formulation of the rotor in the degrees of freedom where crank and rotor are connected, which is further explained in chapter 5.

Chapter 3

Dynamically Loaded Journal Bearings - *DLJB*s

3.1 Modelling approaches

Fluid film bearings have a strong influence on the dynamics of rotor-bearing systems, which made them the focus of numerous studies over the years. One of the earliest attempts to model fluid film bearings was reported by Stodola in 1925, who investigated the effect of oil-film stiffness on the critical speed of a shaft supported in hydrodynamic journal bearings (Sawicki et al., 1997). Likewise, the dynamic performance of reciprocating machinery can be significantly influenced by the dynamics of their bearing supports. Therefore, fluid film bearings under dynamic load conditions have been a matter of concern of numerous theoretical and experimental investigations over the last forty years (Campbell et al., 1967-1968; Martin, 1983; Xu, 1999; Goodwin et al., 2003). The mobility technique, developed by Booker (1965), was one of the earliest approaches and one of the most common methods used for the analysis of *DLB*s. The analysis of *DLJB*s, based on the assumption of a rigid bearing model, can be satisfactory in cases where only a parametric analysis is required, or in cases where the elastic deformations expected are not significant (Oh and Goenka, 1985). Nevertheless, other methods involving flexibility and thermal effects, but with higher computational complexity, have been developed during the past three decades.

In reality, bearings and housings are flexible to a certain degree, especially in the new generation of machines, which are required to work at higher speeds and under heavier load conditions, they weight less and are more flexible. Therefore, in order to account for elastic deformations, corrections are now being made by using elasto-hydrodynamic theory *EHD*, combined with *FEM* models of bearings and housing. However, in spite of the nowadays availability of highly efficient computational resources, the substantial increase in computation time required to perform an *EHD* analysis is still considered a main drawback. In practice, *EHD* calculations are presently done only in special cases (Subramanyan, 2000; Fridman et al., 2004), but are on the way to become standard in the routine bearing analysis. A summary of selected studies using *EHD* lubrication theory for the analysis of engine bearings is given in the study by Moreau et al. (2002).

In some cases of engine bearing analysis (e.g., heavily loaded main bearings and connecting rod bearings) a thermo-hydrodynamic analysis (*THD*) may be required, since the influence of thermal

effects on the hydrodynamic pressure generation and consequently on the value of journal eccentricity may be significant (Fatu et al., 2006). However, it has to be considered that *THD* analysis involves the simultaneous solution of Reynolds equation, energy and heat transfer equations, which demands high computational cost and efforts to develop.

The study of the variation of stiffness and damping coefficients in the analysis of *DLJB*, particularly crankshaft bearings, is commonly avoided due to the computational cost and lack of non-reliable close-forms of solutions, however, some studies have proposed simplified methodologies to evaluate stiffness and damping coefficients over a load cycle based on *SJB* and *LJB* approximations, as in the work of Hirani et al. (1999a).

A review of theoretical and experimental studies related to design and performance assessment of bearings in reciprocating machinery was carried out by Goodwin et al. (2003). It was found significant disagreement between theoretical and experimental results, by making a comparison between the theoretically predicted and the experimentally measured eccentricities. Such a disagreement is on one side caused by the several limitations found in the experimental methods referred in that study, and on the other side, caused by the comparison of experimental results to theoretical results obtained from well detailed and sometimes complex theoretical models for *DLJB*s. Thus, in many cases the use of simplified bearing models may be good enough to represent and understand the physics of the problem, and to obtain numerical results comparable to the experimental ones. In fact, one of the main conclusions drawn by Goodwin et al. (2003), is that in many cases, a short bearing approximation can be used with good accuracy for the purpose of modelling oil film pressure, without the need of using more sophisticated models. Some of the previous studies related to theoretical modelling and experimental methods to analyze *DLJB*, cited also by Goodwin are: Booker (1965), Campbell et al. (1967-1968), Warner (1963), Ross and Slaymaker (1969), Ritchie (1975), Martin (1983), Fantino and Frêne (1985), Goenka and Oh (1986), Pal et al. (1988), Goenka and Paranjpe (1992), Choi et al. (1992), Knoll et al. (1997), Xu (1999). A summary of relevant studies related to the analysis of *DLJB* is given in Table 3.1. It is worth noting that the list of published works related to the theoretical and experimental treatment of *DLJB*s is extensive, therefore, not all of them are mentioned in Table 3.1.

3.2 Tribology of engine bearings

In a typical *ICE*, the crankshaft is supported by journal bearings, as illustrated in Fig. 3.1a. These bearings, which are also known as main bearings, are commonly designed to operate in the hydrodynamic regime of lubrication even under the most extreme conditions of load and speed encountered in an operating engine. The analysis of engine bearings can be rather complicated since their tribological behaviour can be influenced by factors such as lubricant supply, thermal effects, dynamic loading and elasticity of the bounding solids (Tung and McMillan, 2004). The most important components that contribute to the mechanical friction losses in reciprocating engines are indicated in Fig. 3.1b. The lubricant films surrounding the main bearings support the inertial load of the crankshaft and the combustion forces transmitted from the cylinders to the crankshaft. These forces are periodic, but depending on the working load and speed conditions of the engine, they may change in magnitude from one cycle to the next, generating vibrations of the journal centre due to

the combined action of rotating inertias and reciprocating forces.

Table 3.1: *Review of literature - Studies on the modelling of dynamically loaded journal bearings (DLJBs).*

Year	Author	Overview
1965	Booker	Mobility maps, describing the journal force/velocity relationships at different eccentricities at attitude angles are investigated.
1967-1968	Campbell et al.	Mobility method is compared to approximate methods. These methods made use of a quasi-static analysis based on an 'equivalent speed' with a constant load and made use of bearing loads estimated on the basis of inertia forces only, using *SJB*, *FJB* and *LJB* solutions. Comparisons between theoretical and experimental results for the big-end journal bearing of a diesel engine running at 600rpm are presented.
1969	Ross and Slaymaker	Bearing orbits based in Ocvirk's *SJB* approximation. This paper shows that, for small length/diameter ratio bearings, the Ocvirk solution yields good prediction of bearing orbital motion.
1972	Craven and Holmes	A computational method based on *SJB* analysis, using Newton iteration and variation of the trapezium rule is developed.
1975	Ritchie	An optimized *SJB* solution is presented. First attempt to reconcile the advantages of an approximate solution with the accuracy of a full bearing solution.
1983	Martin	Review of work undertaken mainly concerned with oil film history, inertia effects, bearing non-circularity, bearing flexibility and lubricant supply port geometry.
1985	Fantino and Frêne	*EHD* analysis using *SJB* theory. Journal trajectories are published in this paper.
1985	Oh and Goenka	Results compared to data for a rigid bearing. It was conclude that a full *EHD* analysis is necessary for an accurate prediction of engine bearing performance, but that this involves a substantial increase in computation time. A rigid bearing model is satisfactory if only a parametric analysis is required.
1989	White	Analysis of orbits obtained for journal bearings (using a *FJB* solution) of a diesel engine, and a two-stage reciprocating compressor.
1992	Goenka and Paranjpe	Several methods used in General Motors for engine bearing analysis are reviewed. The implications of using the Sommerfeld and Reynolds boundary conditions were discussed. A finite volume method for identifying cavitation zones is described.
1992	Choi et al.	Theoretical analysis using the *SJB* theory and the mobility method. It was observed that crankshaft vibrations and the unbalance between the crankshaft bearings have a large influence on the minimum oil film thickness (OFT). Minimum OFT occurred during either the exhaust or compression strokes when piston and connecting rod inertia forces are dominant, and it decreased almost linearly with engine speed and did not change significantly with engine load.
1996	Vincent et al.	A numerical investigation of cavitation in *DLJB* using the mobility method was presented and a comparison of results using the cavitation formulation of Elrod was made.
1996	Paranjpe	The performance of main bearings and connecting rod bearings is studied using a full *THD* analysis, an adiabatic *THD* analysis and a simplified thermal analysis.
1997	Knoll et al.	Reynolds equation is solved for the oil film pressure profile in main bearings using the *FEM* method. This model separates the complete structure displacement into a large rigid body and small elastic deformations.

continuation of Table 3.1

1998	Hirani et al.	A semi-analytical procedure to evaluate pressure and minimum *OFT* considering a finite bearing is presented in this paper. Using the methodology proposed for two cases of engine bearings, the results obtained are compared in terms of computational time and accuracy with the short bearing approximation and finite element analysis respectively.
1999b	Hirani et al.	A 'closed-form' expression of the pressure distribution for *DLJB* is proposed. This expression is based on a combination of *SJB* and *LJB* approximations. An analytical method for evaluating the angular location of the instantaneous maximum pressure is provided. The study is validated analyzing a connecting rod big end bearing and two crankshaft main bearings.
1999	Xu	The use of *EHD* theory to the engine bearing analysis is highlighted as a significant tool for the understanding of engine bearings.
2000	Lahmar et al.	An optimised *SJB* theory was proposed and applied for nonlinear dynamic analysis of finite-width journal bearings supporting an unbalanced rigid rotor.
2002	Moreau et al.	Comparison of theoretical calculations (using *EHD* theory) and experimental measurements of *OFT* in a dynamically loaded crankshaft main bearing. A short review of previous theoretical and experimental studies is included.
2003	Goodwin et al.	A significant disagreement between published theoretical and experimental data still remains, in spite of the use of more sophisticated theoretical models. There is a general consensus that a short bearing approximation can be used with good accuracy for the purposes of modelling oil film pressure, although the modelling techniques and computing power available nowadays, also permit full bearing solutions.
2005	Alshaer et al.	A generalized model for a lubricated long journal bearing in a *MBD* model of a slider-crank mechanism is presented, where the lubricated journal bearing under study is given by the joint between connecting rod and slider. Orbits and reaction moments are obtained and analyzed.
2006	Fatu et al.	A thermo-elasto-hydrodynamic (*TEHD*) lubrication analysis of a big-end connecting rod bearing is carried out in this study. Thermal distortions and elastic deformation of the bearing surfaces are computed using *FEM* method. The change of oil viscosity with temperature is also taken into account.
2007	Bukovnik et al.	In this work several crankshaft main bearings and connecting rod big end bearings are investigated. Comparisons between results obtained by using clasical methods and complex numerical methods, such as *EHD* and *TEHD*, are presented. The simulations are performed using the comercial software *EXCITE*.
2008	Backhaus and Knoll	This paper describes a simulation software that was developed to improve calculations of oil supply to plain engine bearings, based on an *EHD* analysis.

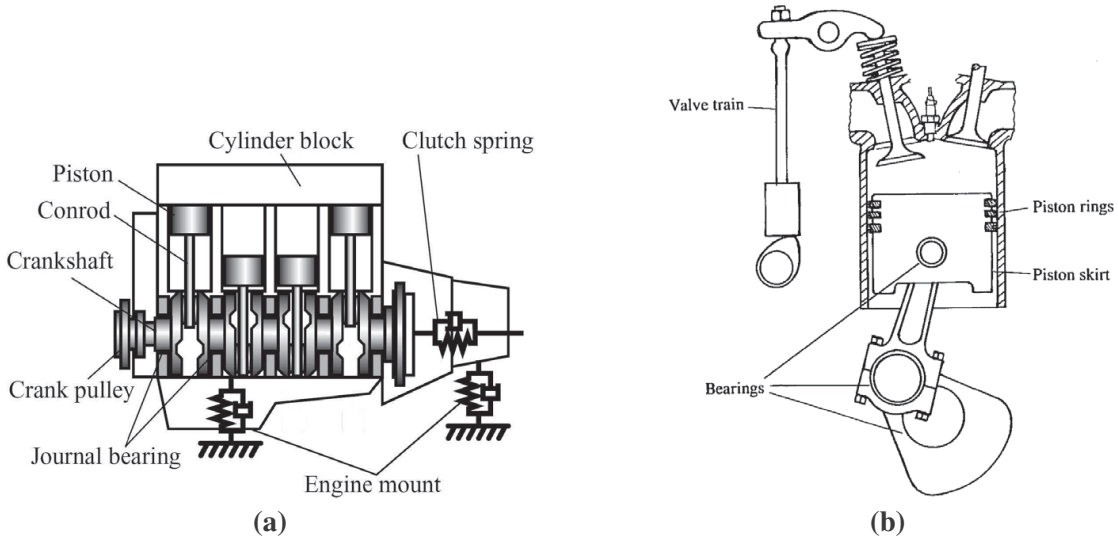

Figure 3.1: *(a) Main parts of an internal combustion engine; (b) Principal friction contributors in a reciprocating engine (Ciulli, 1992).*

Different methods for the analysis of *DLJB*s have been established. Among them, the mobility technique is the most common used, due to its robustness and simplicity (Booker, 1965). However, it is important to recall that several assumptions are implicit when this technique is used, such as, short-bearing consideration, rigid surfaces and hydrodynamic and isothermal lubrication regime, among others (Priest and Taylor, 2000). In cases where the tribological behaviour of bearings is significantly affected by elastic deformation, an elasto-hydrodynamic (*EHD*) lubrication analysis should be done. Moreover, in bearings where thermal effects are important to be considered, a thermo-hydrodynamic (*THD*) or thermo-elasto-hydrodynamic (*TEHD*) lubrication analysis, should be used (Taylor, 1998; Moreau et al., 2002). Nevertheless, these sophisticated methods introduce modelling complexity, demand of significant computational resources and high level expertise for the correct interpretation of the results. Thus, the selection of which theory should be used depends on the particular application and the type of analysis required. For instance, in cases where the crank case is made of aluminium alloy instead of cast iron, structural elastic deformations could certainly be significant, and therefore, in that case an *EHD* model should be preferred, as shown by Moreau et al. (2002). Literature review studies of relevant published work related to the analysis of engine bearings have been reported throughout the last decades by Martin (1983); Xu (1999); Goodwin et al. (2003).

In the study of engine bearings, *EHD* and *TEHD* analysis are more commonly used for connecting rod bearings than for main bearings, since the oil film pressures in the conrod bearings are usually much higher (e.g., 300-400 MPa in bearings of diesel engines), and therefore the elastic deformations and thermal effects may influence more significantly the bearing performance (Oh and Goenka, 1985; Xu, 1999; Fatu et al., 2006). Despite an important number of studies have included *EHD* and *TEHD* in the analysis of engine bearings during the last decades, these methods of analysis are not yet considered as standard tools in routine bearing design applications, mainly due to the significant increase in computational effort compared to rigid/isothermal or *THD* bearing solutions, which can be accurate enough as a benchmark and at the same time computationally more efficient

(Fridman et al., 2004). Nevertheless, *EHD* and *TEHD* analysis are increasingly being used, and are rapidly on the way to become of common use in bearing design, as it can be seen, in the studies of MAN B&W Diesel A/S (2002); Makino and Koga (2002); Bukovnik et al. (2006, 2007); AVL (2009).

The study of actively lubricated engine bearings using *EHD* or *TEHD* analysis can make the problem computationally prohibitive, considering that the hydrodynamics of the oil films has to be coupled to the dynamics of the oil injection. Additionaly, in reciprocating machines such as *ICE*s, the lubrication problem should be coupled to the dynamics of the piston-connecting rod assembly (which accounts for the acting loads coming from the combustion forces and the inertia of the mechanical components), adding complexity to the modelling. Hence, in this work, the use of *EHD* and *TEHD* analysis were not considered for the analysis of main engine bearings. It is worth to mention that the main focus of this study is on the evaluation of main bearings performance operating under controllable lubrication conditions, rather than on the estimation of elastic deformations of mechanical components. Thus, a rigid isothermal finite-bearing approach was adopted, assuming a hydrodynamic regime of lubrication and using a computationally efficient but yet accurate analysis, which is detailed in the next sections. Other investigations on tilting pad journal bearings using *EHD* analysis Haugaard and Santos (2009), theoretical and experimental *THD* analysis Santos and Nicoletti (1999, 2001), and *TEHD* analysis Heinrichson et al. (2007); Heinrichson and Santos (2008), can be found in the literature.

3.3 Mathematical modelling of dynamically loaded fluid film bearings

The governing equations of the dynamics of the thin fluid film in conventionally lubricated journal bearings operating under dynamic load conditions, are presented in this section. The main geometric relations and reference frames for a *DLJB* are shown in Fig. 3.2.

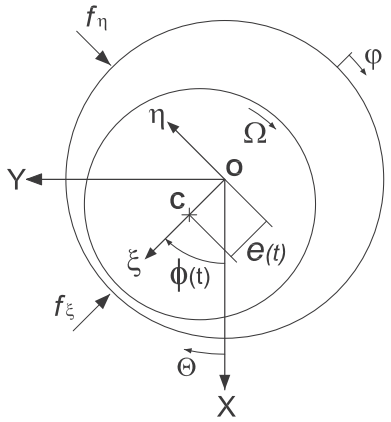

Figure 3.2: *Journal bearing geometry.*

The equation that describes the oil flow in a journal bearing in the domain $0 \leq x \leq 2\pi r_b$ and $-l_b/2 \leq z \leq l_b/2$, and which governs the pressure distribution of the oil film can be obtained from

the standard reduced form of the Reynolds equation for fluid film lubrication (Hamrock, 1991), given by:

$$\frac{\partial}{\partial x}\left(\frac{\rho h^3}{12\mu}\frac{\partial p}{\partial x}\right)+\frac{\partial}{\partial z}\left(\frac{\rho h^3}{12\mu}\frac{\partial p}{\partial z}\right)=\frac{\partial}{\partial x}\left(\frac{\rho h(U_j-U_b)}{2}\right)+\frac{\partial(\rho h)}{\partial t} \tag{3.1}$$

Equation (3.1) describes the pressure distribution $p(x,z,t)$ between rotor and sleeve, as a function of the oil properties (ρ,μ), the relative velocity between rotor and sleeve surfaces (U_j-U_b), and the gap function $h(x,z,t)$. The gap function defines the profile of the *OFT* around the bearing. Assuming that the fluid is isoviscous, Newtonian and incompressible, and considering a typical case where the journal rotates and the sleeve remains stationary (i.e., $U_j=\Omega r_b$ and $U_b=0$), the Reynolds equation for hydrodynamic lubrication can be written as

$$\frac{\partial}{\partial x}\left(h^3\frac{\partial p}{\partial x}\right)+\frac{\partial}{\partial z}\left(h^3\frac{\partial p}{\partial z}\right)=6\mu U_j\frac{\partial h}{\partial x}+12\mu\frac{\partial h}{\partial t} \tag{3.2}$$

With reference to the diagram in Fig. 3.2, the gap function can be written as

$$h=c_b(1+\varepsilon\cos\varphi) \tag{3.3}$$

where φ is the angle measured from the location of the maximum *OFT*, c_b is the radial clearance, and ε is the eccentricity ratio, given by $\varepsilon=e_b/c_b$. Using the coordinate transformation $x=r_b\varphi$, where r_b is the bearing radius, and introducing Eq. (3.3) in the right hand side of Eq. (3.2), the modified Reynolds equation for *DLJB* can be written as

$$\frac{\partial}{\partial\varphi}\left(h^3\frac{\partial p}{\partial\varphi}\right)+{r_b}^2\frac{\partial}{\partial z}\left(h^3\frac{\partial p}{\partial z}\right)=12\mu c_b{r_b}^2\left[\dot{\varepsilon}\cos\varphi+\varepsilon\sin\varphi(\dot{\phi}-\frac{\Omega}{2})\right] \tag{3.4}$$

or alternatively as:

$$3h^2\frac{\partial h}{\partial\varphi}\frac{\partial p}{\partial\varphi}+h^3\frac{\partial^2 p}{\partial\varphi^2}+{r_b}^2h^3\frac{\partial^2 p}{\partial z^2}=12\mu c_b{r_b}^2\left[\dot{\varepsilon}\cos\varphi+\varepsilon\sin\varphi(\dot{\phi}-\frac{\Omega}{2})\right] \tag{3.5}$$

where, $\dot{\varepsilon}$ corresponds to the normal squeeze velocity of the oil film, $\dot{\phi}$ is the rotational velocity of the journal centre around the bearing centre, Ω is the rotational speed of the rotor, and $\partial h/\partial\varphi=-e_b\sin\varphi$. Equation 3.5 can be used when misalignment is not considered, in other words, when *OFT* is assumed to be constant along the width direction of the bearing. Since the eccentricity and attitude angle in a *DLJB* change through the loading cycle, Eq. (3.5) can only be solved if ($\dot{\varepsilon}$, $\dot{\phi}$ and Ω) are known at any time during each cycle.

3.3.1 Analytical solutions of Reynolds equation

Acceptable analytical solutions of Eq. (3.4) can be obtained for limited cases, such as, short-width (*SJB*) and infinitely long-width (*LJB*) journal bearings (Frêne et al., 1990; Hamrock, 1991). Some attempts to develop analytical or so called 'close-form' solutions of Reynolds equation for finite-width *DLJB* were proposed by Hirani et al. (1999b,a). However, their use is not widely extended, and numerical solutions are still preferred. In the *SJB* approach, it is considered that the variation

of film pressure is more significant in the axial direction than in the circumferential direction, neglecting the first term on the left hand side of Eq. (3.4). The use of this approach is suitable for bearings with small aspect ratio ($\lambda \leq 0.5$) operating with small to moderate eccentricity ($\varepsilon \leq 0.75$). Since engine bearings are usually of short-width dimensions, this approach is commonly used for their analysis. By contrast, the *LJB* approach considers that the film pressure is constant along the axial direction, and therefore, the side-leakage term, i.e., the second term on the left hand side of Eq. (3.4) can be disregarded. The analytical solutions obtained with the *LJB* approach may be used for the analysis of long-width bearings (usually $\lambda > 2$). Since *LJB* are proned to misalignment, this approach is hardly used in common practice.

Analytical solutions for *SJB* and *LJB* approximations

Assuming that the bearing is well aligned and the viscosity of the lubricant keeps constant, and using the Gümbel boundary conditions, the reduced Reynolds equation for the *SJB* and the *LJB* approaches can be analytically integrated, obtaining the expressions given by Eqs. (3.6) and (3.7), respectively (Frêne et al., 1990). For each case, the journal bearing forces given in ξ,η coordinates (see Fig. 3.2) can be calculated integrating the pressure distribution along the bearing surface, as in Eq. (3.8), obtaining the analytical expressions listed in Table 3.2.

$$p_{SJB} = -\frac{3\mu}{h^3}\left(\frac{{l_b}^2}{4} - z^2\right)\left[(\Omega - 2\dot{\phi})\frac{\partial h}{\partial \varphi} + 2\dot{\varepsilon}c_b\cos\varphi\right] \tag{3.6}$$

$$p_{LJB} = 6\mu\left(\frac{r_b}{c_b}\right)^2\left\{(\Omega - 2\dot{\phi})\frac{\varepsilon\sin\varphi(2+\varepsilon\cos\varphi)}{(2+\varepsilon^2)(1+\varepsilon\cos\varphi)^2} + \frac{\dot{\varepsilon}}{\varepsilon}\left[\frac{1}{(1+\varepsilon\cos\varphi)^2} - \frac{1}{(1+\varepsilon)^2}\right]\right\} \tag{3.7}$$

$$\left\{\begin{array}{c} f_\xi \\ f_\eta \end{array}\right\} = \int_0^{2\pi}\int_0^{l_b} p\left\{\begin{array}{c} \cos\varphi \\ \sin\varphi \end{array}\right\} r_b dz d\varphi \tag{3.8}$$

Table 3.2: *Analytical solutions of Reynolds equation to calculate journal bearing forces (Frêne et al., 1990).*

• Short-width journal bearing (*SJB*)
$f_\xi = \frac{-r_b\mu {l_b}^3}{2{c_b}^2(1-\varepsilon^2)^2}\left[\frac{\pi\dot{\varepsilon}(1+2\varepsilon^2)}{\sqrt{(1-\varepsilon^2)}} + 2\varepsilon^2(\Omega - 2\dot{\phi})\right]$
$f_\eta = \frac{r_b\mu {l_b}^3\varepsilon}{2{c_b}^2(1-\varepsilon^2)^2}\left[4\dot{\varepsilon} + \frac{\pi}{2}(\Omega - 2\dot{\phi})\sqrt{1-\varepsilon^2}\right]$
• Long-width journal bearing (*LJB*)
$f_\xi = \frac{-12\mu {r_b}^3 l_b}{{c_b}^2}\left[\frac{\varepsilon^2(\Omega-2\dot{\phi})}{(2+\varepsilon^2)(1-\varepsilon^2)} + \frac{\dot{\varepsilon}}{(1-\varepsilon^2)^{3/2}}\left(\frac{\pi}{2} - \frac{8}{\pi(2+\varepsilon^2)}\right)\right]$
$f_\eta = \frac{12\mu {r_b}^3 l_b}{{c_b}^2}\left[\frac{\pi\varepsilon(\Omega-2\dot{\phi})}{2(2+\varepsilon^2)\sqrt{1-\varepsilon^2}} + \frac{2\varepsilon\dot{\varepsilon}}{(2+\varepsilon^2)(1-\varepsilon^2)}\right]$

Viscous friction forces

The instantaneous viscous frictional forces acting in the opposite direction of the sleeve rotation can be obtained by integrating the shear stress around the journal surface:

$$f_{vf} = \int_s \lambda^*_{xy} r_b d\varphi dz \tag{3.9}$$

where the fluid shear stress is given by $\lambda_{xy} = \mu \partial u_x / \partial y$ and u_x is obtained from Navier-Stokes equation, and it is given as a function of the pressure field by:

$$u_x = \frac{1}{2\mu}\frac{\partial p}{\partial x} y(y-h) + \frac{r_b \Omega y}{h} \tag{3.10}$$

$$\frac{\partial u_x}{\partial y} = \frac{1}{2\mu}\frac{\partial p}{\partial x}(2y-h) + \frac{r_b \Omega}{h} \tag{3.11}$$

Thus, the fluid shear stress calculated along the journal surface ($y = h$), is given by:

$$\lambda^*_{xy} = \frac{\mu r_b \Omega}{h} + \frac{h}{2r_b}\frac{dp}{d\varphi}.$$

In dimensionless form, the friction force can be written as:

$$\bar{f}_{vf} = \frac{f_{vf}}{\mu \Omega r^2}\frac{C}{l_b} \tag{3.12}$$

The friction coefficient is defined as the ratio of the friction force and the bearing load capacity. In dimensionless form (number of friction), is given by:

$$\mu_f = \frac{f_{vf}}{F_b}\frac{r_b}{C} \tag{3.13}$$

where F_b is the instantaneous bearing load capacity, calculated by: $F_b = \sqrt{{F_\xi}^2 + {F_\eta}^2}$. The instantaneous power dissipation caused by viscous frictional forces and the cyclic averaged power consumption can be written as:

$$W_{vf} = \Omega \cdot r_b \cdot f_{vf} \tag{3.14}$$

$$(W_{vf})_{avg} = \frac{1}{2\pi}\int_0^{2\pi} W_f d\theta \tag{3.15}$$

3.3.2 Numerical solution of Reynolds equation

Analytical and rapid procedures for oil film calculation, such as those based on the mobility method (Booker, 1965), cannot adequately take into account the influence of features in the bearing such as oil holes and grooves, since the solution assumes an uninterrupted oil film. Therefore, in cases where a *FJB* approach is required, the 2D Reynolds equation has to be numerically solved. Using numerical methods for bearing analysis enables additional possibilities, such as, including elastic

and thermo-elastic effects (Kim and Kim, 2001; Fatu et al., 2006), compressibility, piezoviscosity effects and non-Newtonian fluid behaviour. Typical numerical schemes used for the solution of Reynolds equation are based on the finite elements method - *FEM* (Reddi, 1969; Booker and Huebner, 1972), finite difference method - *FD* (Mitsui, 1988) and finite volumes. In this work, a *FD* scheme with the assumption of isothermal conditions (Santos and Russo, 1998), was adopted, which is described next for completeness and to establish notation.

Finite difference scheme with a uniform mesh

In this case, the Reynolds equation is discretized via finite differences using an uniform mesh of $m \times n$ nodes along φ and z directions, as shown in Fig. 3.3. Using a central difference scheme, and neglecting second and higher order terms, the first and second order derivatives can be written as:

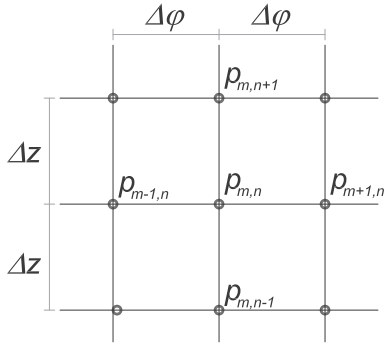

Figure 3.3: *Uniform finite difference mesh.*

$$\left.\frac{\partial p}{\partial \varphi}\right|_{m,n} = \frac{p_{m+1,n} - p_{m-1,n}}{2\Delta\varphi} \tag{3.16}$$

$$\left.\frac{\partial^2 p}{\partial \varphi^2}\right|_{m,n} = \frac{p_{m+1,n} - 2p_{m,n} + p_{m-1,n}}{\Delta\varphi^2} \tag{3.17}$$

Assuming that the bearing is well aligned (i.e., $\partial h/\partial z = 0$), and the viscosity of the fluid film keeps constant, the Reynolds equation written in finite differences is given by:

$$\begin{aligned}\Delta_{m,n}p_{m-1,n} + \Lambda_{m,n}p_{m+1,n} + \diamondsuit_{m,n}p_{m,n} + \nabla_{m,n}p_{m,n-1} + \triangle_{m,n}p_{m,n+1} \\ = 12\mu c_b {r_b}^2 \left[\dot{\varepsilon}\cos\varphi_{m,n} + \varepsilon\sin\varphi_{m,n}(\dot{\phi} - \frac{\Omega}{2})\right]\end{aligned} \tag{3.18}$$

where,

$$\Delta_{m,n} = -\frac{3h_{m,n}^2}{2\Delta\varphi}\left.\frac{\partial h}{\partial \varphi}\right|_{m,n} + \frac{h_{m,n}^3}{\Delta\varphi^2} \quad ; \quad \Lambda_{m,n} = \frac{3h_{m,n}^2}{2\Delta\varphi}\left.\frac{\partial h}{\partial \varphi}\right|_{m,n} + \frac{h_{m,n}^3}{\Delta\varphi^2}$$

$$\diamondsuit_{m,n} = -2h_{m,n}^3\left[\frac{1}{\Delta\varphi^2} + \frac{r_b^2}{\Delta z^2}\right] \quad ; \quad \nabla_{m,n} = \triangle_{m,n} = \frac{h_{m,n}^3 r_b^2}{\Delta z^2}$$

The boundary conditions that are applied for the numerical solution of Eq. (3.18) are: $p(z=0)=0$ and $p(z=l_b)=0$ (i.e., boundary pressure at the bearing edges is atmospheric); $p(\varphi=0)=0$ and $p(\varphi=2\pi)=0$, considering maximum film pressures close to the location of the minimum OFT; $p \geq = 0$, assuming the Gümbel boundary cavitation condition.

The discretized Reynolds equations is solved for each time step by using a direct system equation solver based on the well known LU factorization method (Wendt, 1992). Once the nodal pressures have been computed, the resultant forces on the sleeve are obtained by numerically integrating Eq. (3.8), for instance, using the Simpson Method.

3.3.3 Boundary conditions and cavitation approaches

The analytical solution for the oil film pressure distribution can be obtained when adequate boundary conditions (BC) are applied for the integration of Reynolds equation, when using *SJB* and *LJB* approximations. The most known boundary conditions for the analytical solutions of the Reynolds equation for *DLJB* are: Full Sommerfeld conditions, Half Sommerfeld conditions and Gümbel boundary conditions.

- **Full Sommerfeld solution** is a periodic boundary condition, which assumes that the pressures at edges of the wedge is equal to zero, i.e., $p=0$, at $\varphi=0$ and $\varphi=2\pi$. Since applying this condition large negative pressures occur in the diverging zone, it is not used in practice.
- **Half Sommerfeld solution** is a more realistic approach, which disregards negative pressures in the diverging area, i.e., $p=0$, at $\varphi=0$; $p=0$ at $\varphi=\pi/2$; $p=0$ at $\pi/2<\varphi<2\pi$. Although this boundary condition does not conserve the continuity of flow, which is physically unrealistic, it is simple to apply and can be accurate enough in many cases.
- **Gümbel cavitation condition** is another well known cavitation condition, in which the Reynolds equation is first solved subjected to the specified pressures at the bearing boundaries, and then if subambient pressures appear they are disregarded. Although the use of the Gümbel cavitation condition does not satisfy the continuity of flow at film rupture as well as reformation, it provides acceptable accuracy in the estimation of oil film pressure and bearing load capacity with low computational cost (Mourelatos, 2001b).

When numerical solutions are used, more accurate boundary cavitation conditions can be adopted, such as, the Reynolds or Swift-Stieber conditions, and the Jackobsson-Floberg and Olson (JFO) conditions, which are briefly described here.

- **Reynolds or Swift-Stieber condition** This condition ensures mass flow continuity at the rupture boundary but not at the reformation boundary. This condition assumes the pressure gradient and the pressure to be equal to zero at the cavitation boundary (φ_{cav}):

$$\begin{aligned} p(\varphi=0) &= 0 \\ p(\varphi &= \varphi_{cav})=0 \quad \text{when} \quad \frac{\partial p}{\partial \varphi}=0 \end{aligned}$$

  This condition has proved to be adequate for estimating load capacity, or alternatively, minimum *OFT* and journal orbit in *DLJB*, in cases where an isothermal oil film and oil availability are assumed (Paranjpe and Goenka, 1990; Mourelatos, 2001b).

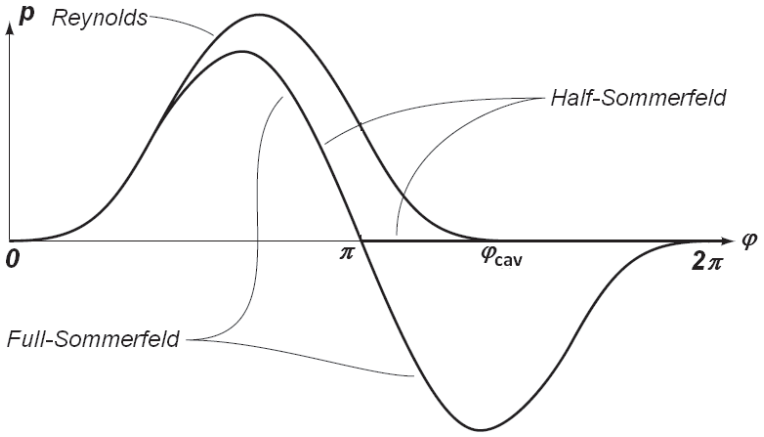

Figure 3.4: *Boundary cavitation conditions for journal bearings.*

- **Jackobsson-Floberg and Olson (*JFO*) condition** This condition conserves mass both at the rupture and the reformation boundaries but at expenses of a substantial increase in the computational time. This condition is recommended in cases where an accurate prediction of oil flow in the bearing is needed, however its implementation is not straightforward since the cavitation zone is unknown in advance. An "universal cavitation algorithm" where the *JFO* conditions are directly incorporated into the Reynolds equation by means of using a switch function was developed by Elrod (1981).

When using Reynolds or *JFO* cavitation conditions, the problem of determining the oil pressure distribution becomes nonlinear since the cavitation region is not known in advance, which can increase the computational cost substantially. It is estimated that in *DLJB* the use of Reynolds cavitation condition may increase the computational cost by at least 50% (Mourelatos, 2001b). Moreover, using the *JFO* cavitation condition could lead to only a little improvement over more crude techniques, because the calculated results depend greatly on the value of the bulk modulus used in the analysis (San Andres, 2009). Figure 3.4 illustrates the differences between some of the boundary conditions described above.

Comparison between Gümbel and Reynolds boundary cavitation conditions

When the Reynolds equation is numerically solved for different bearing aspect ratios and assuming separately Gümbel and Reynolds boundary cavitation conditions, the differences in the results in terms of eccentricity and bearing load capacity are shown in Figs. 3.5 and 3.6. It can be seen in Fig. 3.5 that the longer the bearing width, the higher differences found between the two boundary conditions. It can be observed that for any eccentricity ratio using Reynolds *BC* the bearing number obtained is always lower (i.e., higher carrying load capacity) than the one obtained using Gümbel BC, which can be better seen in Fig. 3.6a. The relative differences in the carrying load capacities using Gümbel and Reynolds boundary cavitation conditions are plot in Fig. 3.6b. It can be seen that the differences between the two solutions are more significant for bearing operating with high eccentricities (i.e., heavily loaded bearings) and for long-width bearings. Nevertheless, the differences are in any case higher than 18%. Therefore and according to what is reported in the

literature (Mourelatos, 2001b), there are several cases where Gümbel conditions can be used without significant lack of accuracy, as in *SJB* and not very heavily loaded journal bearings. In other cases, a decision has to be made based on a trade-off between the computational cost involved and the required level of accuracy of the results.

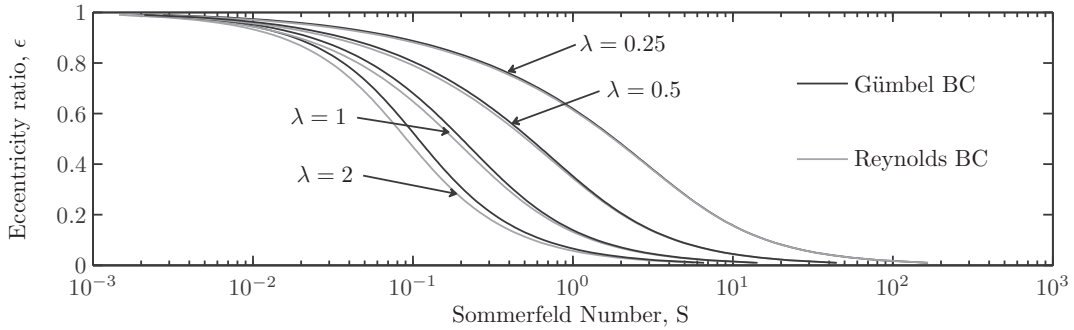

Figure 3.5: *Effect of using Gümbel and Reynolds boundary conditions - Eccentricity ratio vs Sommerfeld number.*

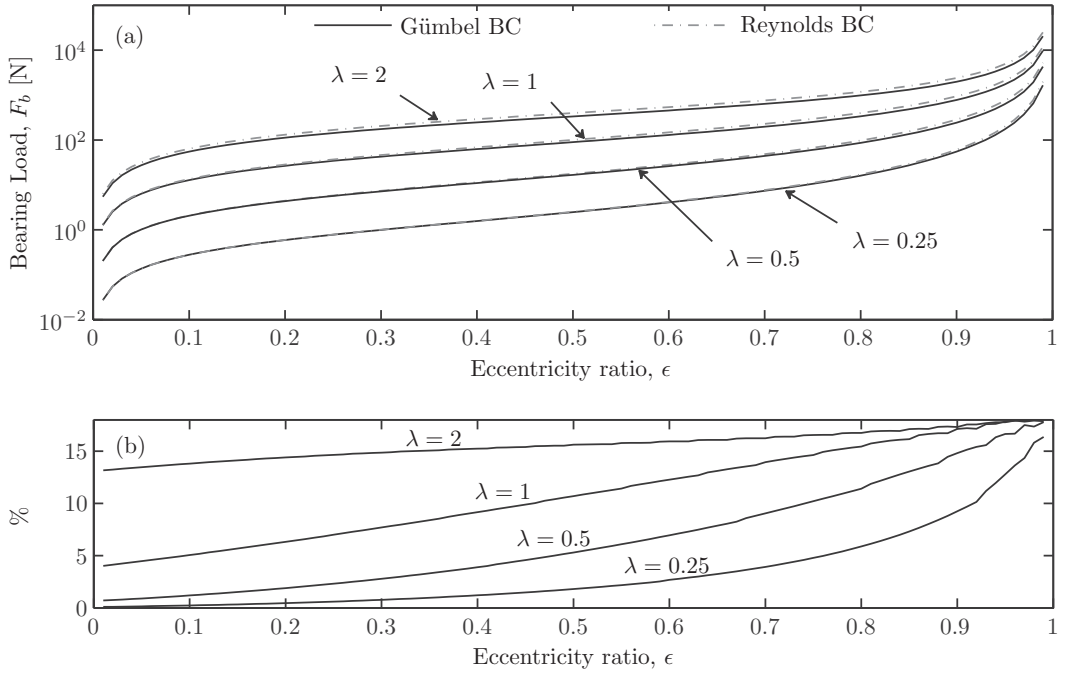

Figure 3.6: *Effect of using Gümbel and Reynolds boundary conditions - (a) Bearing load capacity vs eccentricity ratio; (b) Differences in bearing load capacity.*

Chapter 4

From Hybrid to Controllable Lubrication

4.1 Actively lubricated bearings

During the last twenty years, the combination of tribology, control techniques and informatics has enabled the development of active lubricated bearings, which are not only able to support the rotating shaf but to deal with multi-objective functions (e.g., increasing of the film thickness, reduction of friction, enlarging of stability margins, modification of stiffness and damping parameters and reduction of cross-coupling effects). A recent literature review of theoretical and experimental achievements in the development of active tribological systems is given in (Santos, 2009). Among the industrial applications using active lubrication, is the case of industrial gas compressors. In that case, lateral vibrations and rotor-bearing stability were improved by using active lubricated tilting pad journal bearings (Santos et al., 2004), and multirecess active journal bearings with active pockets (Santos and Watanabe, 2006).

The bearing considered in this study is a hole-entry type bearing with orifices disposed circumferentially along two rows, as shown in Fig. 4.1. In these type of bearings, active lubrication is achieved by injecting oil at controllable pressures $\bar{P}_{inj}(t)$, through radial orifices. From the point of view of active lubrication, and specifically considering the case of a dynamically loaded journal bearing, $\bar{P}_{inj}$ must be dynamically controlled. Although in this work several control pressure rules are proposed based on the periodic behaviour of bearing loads in reciprocating machines, the study has been more focused on the evaluation of bearing performance parameters for different hybrid bearing configurations, than in the design of the control system itself.

4.1.1 The modified Reynolds equation for active lubrication

Assuming an isoviscous, Newtonian, incompressible fluid operating in laminar regime, the governing equation for the hydrodynamic pressure distribution of an active lubricated journal bearing can be obtained from the Navier Stokes equation and the continuity equation by accommodating in the assumed boundary conditions the velocity profile of the oil injection, which is described in detail in (Santos and Russo, 1998; Santos et al., 2001). Thus, the pressure distribution for a journal bearing with radial oil injection through orifices located at (φ_i, z_i) along the bearing surface, is governed by Eq. (4.1).

$$\begin{aligned}\frac{\partial}{\partial\varphi}\left(\frac{h^3}{{r_b}^2}\frac{\partial p}{\partial\varphi}\right)+\frac{\partial}{\partial z}\left(h^3\frac{\partial p}{\partial z}\right)-\frac{3}{l_o}\sum_{i=1}^{s}F_i(\varphi,z)\cdot p \\ =12\mu c_b\left[\dot{\varepsilon}\cos\varphi+\varepsilon\sin\varphi(\dot{\phi}-\frac{\Omega}{2})\right]-\frac{3}{l_o}\sum_{i=1}^{s}F_i(\varphi,z)\cdot\bar{P}_{inj}(t)\end{aligned} \tag{4.1}$$

where: $F_i(\varphi,z)=\begin{cases}\frac{d_o^2}{4}-R^2 & \text{if} \quad R^2\le d_o^2/4\\ 0 & \text{if} \quad R^2\ge d_o^2/4\end{cases}$; and $R^2={r_b}^2(\varphi-\varphi_i)^2+(z-z_i)^2$.

The function $F_i(\varphi,z)$ is used to describe mathematically the problem and is physically related to the position of the orifices. In other words, this function will be different than zero inside the orifices region and will be zero elsewhere. On the other hand, $P_{inj}(t)$ gives the injection pressure at each orifice in function of time. It can be noted that when the radial oil injection is not operating (i.e., $\bar{P}_{inj}=0$ and $F_i(\varphi,z)=0$), Eq. (4.1) translates into the conventional Reynolds equation for hydrodynamic lubrication, given by Eq. (3.4). Equation (4.1) can be numerically solved for the pressure distribution ($p(\varphi,z)$) using finite differences, provided that the normal squeeze velocity ($\dot{\varepsilon}$) and the rotational velocities ($\dot{\phi}$ and Ω) are known from the dynamics of the mechanical system, as shown in section 4.1.2. It is worth noting that for the developing of the modified Reynolds equation for active lubrication, inertia and compressibility effects were disregarded. The fluid inertia effects were neglected considering that at not very high journal rotational speeds, the effects of viscous forces are more important than inertia effects. On the other hand, compressibility effects have not been included into the equations, considering that their influence on the fluid film pressure distribution and minimum fluid film thickness can be disregarded compared to the squeezing and wedge effects on the fluid film, when maximum film pressures are not considerably high (e.g., $p_{max}\le 12$ MPa), as shown in the cases of study included in chapter 6.

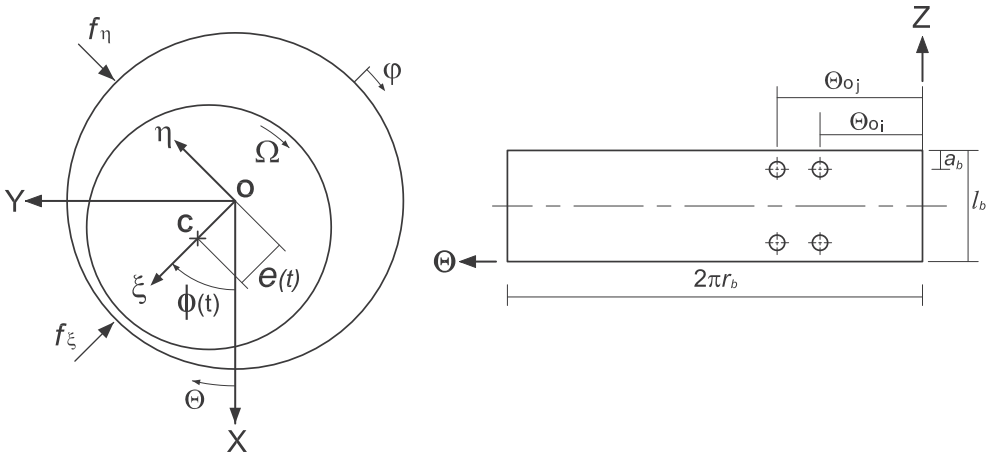

Figure 4.1: *Hole-entry type journal bearing.*

4.1.2 Numerical solution of the modified Reynolds equation for active lubrication

A FD scheme with the assumption of isothermal conditions was adopted. In order to be able to refine the mesh over the area where the orifices for oil injection are located, and consequently to obtain a better estimation of the film pressures and minimum fluid film thicknesses, a non-uniform grid has been use to discretize the bearing domain, as shown in Fig. 4.2. Similarly to the FD scheme outlined in section 3.3.2, but for a non-uniform discretization, using a central difference scheme, the first and second order derivatives can be written as:

$$\left.\frac{\partial p}{\partial \varphi}\right|_{m,n} = \frac{p_{m+1,n} - p_{m-1,n}}{\Delta\varphi_{m-1} + \Delta\varphi_m} \tag{4.2}$$

$$\left.\frac{\partial^2 p}{\partial \varphi^2}\right|_{m,n} = \frac{2}{\Delta\varphi_{m-1} + \Delta\varphi_m}\left(\frac{p_{m+1,n} - p_{m,n}}{\Delta\varphi_m} - \frac{p_{m,n} - p_{m-1,n}}{\Delta\varphi_{m-1}}\right) \tag{4.3}$$

Assuming that the bearing is well aligned (i.e., $\partial h/\partial z = 0$) and the viscosity of the fluid film keeps constant, the modified Reynolds equation in finite differences is given by equation (4.4).

$$\begin{aligned}\Delta_{m,n}p_{m-1,n} + \Lambda_{m,n}p_{m+1,n} + \diamondsuit_{m,n}p_{m,n} + \nabla_{m,n}p_{m,n-1} + \triangle_{m,n}p_{m,n+1} \\ = 12\mu c_b {r_b}^2\left[\dot{\varepsilon}\cos\varphi_{m,n} + \varepsilon\sin\varphi_{m,n}(\dot{\phi} - \frac{\Omega}{2})\right] - \frac{3r_b^2}{l_o}\sum_{i=1}^{s} F_{i_{m,n}}\bar{P}_{inj}\end{aligned} \tag{4.4}$$

where:

$$\begin{aligned}
\Delta_{m,n} &= \frac{1}{\Delta\varphi_m + \Delta\varphi_{m-1}}\left[-3h_{m,n}^2\left.\frac{\partial h}{\partial\varphi}\right|_{m,n} + \frac{2h_{m,n}^3}{\Delta\varphi_{m-1}}\right]; \\
\Lambda_{m,n} &= \frac{1}{\Delta\varphi_m + \Delta\varphi_{m-1}}\left[3h_{m,n}^2\left.\frac{\partial h}{\partial\varphi}\right|_{m,n} + \frac{2h_{m,n}^3}{\Delta\varphi_m}\right]; \\
\diamondsuit_{m,n} &= -2h_{m,n}^3\left[\frac{1}{\Delta\varphi_m + \Delta\varphi_{m-1}}\left(\frac{1}{\Delta\varphi_m} + \frac{1}{\Delta\varphi_{m-1}}\right)\right. \\
&\quad \left. + \frac{r_b^2}{\Delta z_n + \Delta z_{n-1}}\left(\frac{1}{\Delta z_n} + \frac{1}{\Delta z_{n-1}}\right)\right] - \frac{3r_b^2}{l_o}\sum_{i=1}^{s} F_{i_{m,n}} \cdot p_{m,n}; \\
\nabla_{m,n} &= \frac{2h_{m,n}^3 r_b^2}{\Delta z_{n-1}}\frac{1}{\Delta z_n + \Delta z_{n-1}} \quad ; \quad \triangle_{m,n} = \frac{2h_{m,n}^3 r_b^2}{\Delta z_n}\frac{1}{\Delta z_n + \Delta z_{n-1}}.
\end{aligned}$$

Assuming the Gümbel boundary conditions, and applying atmospheric pressures at the edges of the bearing, Eq. (4.4) can be solved by an iterative method such as the well known *SOR* (successive over relaxation) method, or by a factorization method, such as Cholesky or *LU* methods. In this work, the *LU* method was adopted. The modified Reynolds equation (4.1) can be solved for each time step if the oil injection pressures through the orifices (P_{inj}) are known as a function of the instantaneous crank angle.

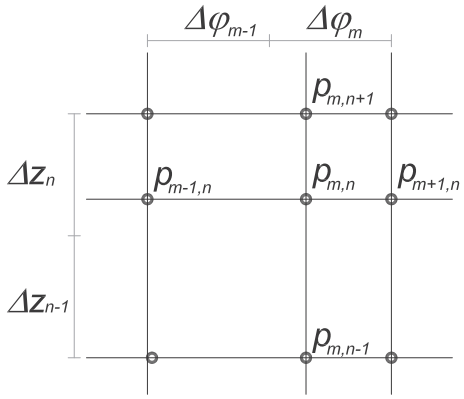

Figure 4.2: *Non-uniform finite difference mesh.*

In order to be able to control the oil injection pressures through the bearing orifices, different alternatives could be considered. Among them: mechanical cam systems, hydraulic servovalves (Santos et al., 2004; Santos and Russo, 1998) and piezoelectric nozzles (Horikawa et al., 1992; Mizumoto et al., 1996). The use of a piezo-actuated injection system and a mechanical unit injector were considered in this work. Some insights into their modelling are given in the next section.

4.1.3 Hybrid bearing configuration

Considering the geometric bearing configuration shown in Fig. 4.1, active or controllable lubrication is achieved by radially injecting oil at pressures that may be controlled in function of the instantaneous crank angular position. In order to advantageously modify the hydrodynamic bearing fluid film by applying controllable radial oil injection (i.e., hybrid lubrication), a suitable distribution of the injection orifices on the bearing surface, and appropriate control rules for the oil injection pressures have to be determined, which has been also investigated in (Estupinan and Santos, 2009c,a). Thus, important sources of information when attempting to configure and/or optimize oil injection are: the bearing acting loads, the curves of combustion forces inside the cylinders and the behaviour of bearing parameters when bearings operate under conventional lubrication conditions. In the study of Estupinan and Santos (2009c,a) appropriate locations for the injection orifices and convenient rules for changing the oil injection pressures (as a function of the instantaneous crankshaft angle), were found. However, details related to the oil injection system were not discussed.

The performance of a hybrid journal bearing depends on several geometric parameters, such as, diameter of the injection orifices, position of the orifices, bearing aspect ratio (λ), and axial land width ratio ($\bar{a}_b$). Therefore, depending on the load and speed working conditions, several types of configurations are possible (Stout and Rowe, 1974; Rowe et al., 1982). In order to optimize geometrically the design of hybrid journal bearings under different external load conditions, several studies have been carried out for specific cases, mainly related to stationary loaded conditions (Sharma et al., 1999; Jadon and Singh, 2007). Particularly, it was shown by Rowe et al. (1982), that hole-entry bearings with holes disposed circumferentially along two rows may offer advantages over other configurations.

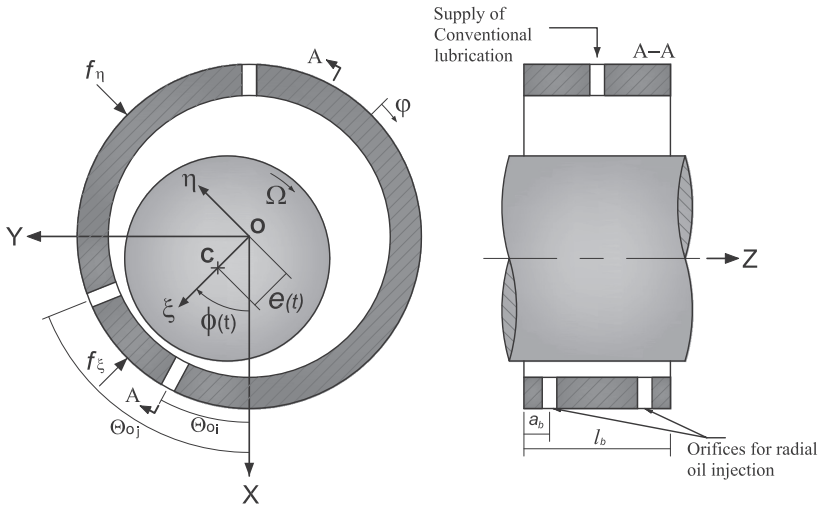

Figure 4.3: *Hybrid bearing geometry.*

4.2 Schemes for applying radial oil injection

This section presents a theoretical study that describes two different schemes for the oil injection system in actively or controllable lubricated *DLJB*s, using controllable radial oil injection to modify the conventional hydrodynamic lubrication. Figure 4.3 shows another view of the hole-entry type bearing considered in this study for applying controllable radial oil injection. The main equations that govern the dynamics of the injection for a piezo-actuated oil injector and a mechanical-actuated oil injector are presented in this section. In chapter 5 it will be shown how the dynamics of the oil injection system is coupled to the dynamics of the bearing fluid film through equations, and how the global system is numerically solved. Later in chapter 6 numerical results for the main bearing of a single-cylinder *ICE*, using a piezo-actuated injection system will be presented.

In the following, two alternatives for applying the oil injection are presented: a) a piezo-actuated injection system; and b) a mechanical unit injection system, as schematically illustrated in Figs. 4.4 and 4.8. The proposed designs for these two types of oil injectors are based on similar working principles of the injectors used in fuel injection systems in vehicles. However, notice that important differences in the fluid properties and level of injection pressures required for active lubrication, must be considered in the modelling. The main focus of the mathematical modelling of the oil injection systems was mainly put on the derivation of the equations that govern the dynamics of the injectors and their coupling to the dynamics of the fluid film bearings.

4.2.1 Piezoelectric injection system

Piezoceramic actuators has become an area of increased interest in the past fifteen years, due the several advantages they present when compared to mechanical and electro-mechanical actuators (Ulbrich, 1994). Among relevant work covering reviews of state-of-the-art actuators, and including comparison between them in terms of electrical and mechanical properties, and potential applications, are the studies of Near (1996); Prechtl and Hall (1999); Taylor and Washington (2002). In these studies was shown that piezoelectric actuators generally present a more compact design and

faster response when compared to other type of actuators.

The piezo-actuated oil injection system described in this section is schematically shown in Fig. 4.4. In this type of injector, the injection is controlled by the activation of a piezoelectric actuator. If the piezoelectric stack (*pz*) is activated by a voltage signal, the control valve (*cv*) opens, which results in a pressure drop in the control chamber (*cc*), and subsequently the opening of the injection nozzle due to the lift of the needle valve (*nv*), starting the injection. When the feeding voltage applied to the piezoelectric stack is deactivated, the control valve returns to the closed position, the servopiston and needle valve move downwards and consequently the injection ends. Several studies for the modelling of similar type of injectors, but for diesel fuel injection systems are found in the literature (Lee et al., 2002; Lino et al., 2007; Chung et al., 2008). The mathematical modelling of the piezo-actuated injector presented in this case, is based on the same methodology described by Chung et al. (2008). The main governing equations for the hydraulic, mechanical and electrical subsystems will be presented next.

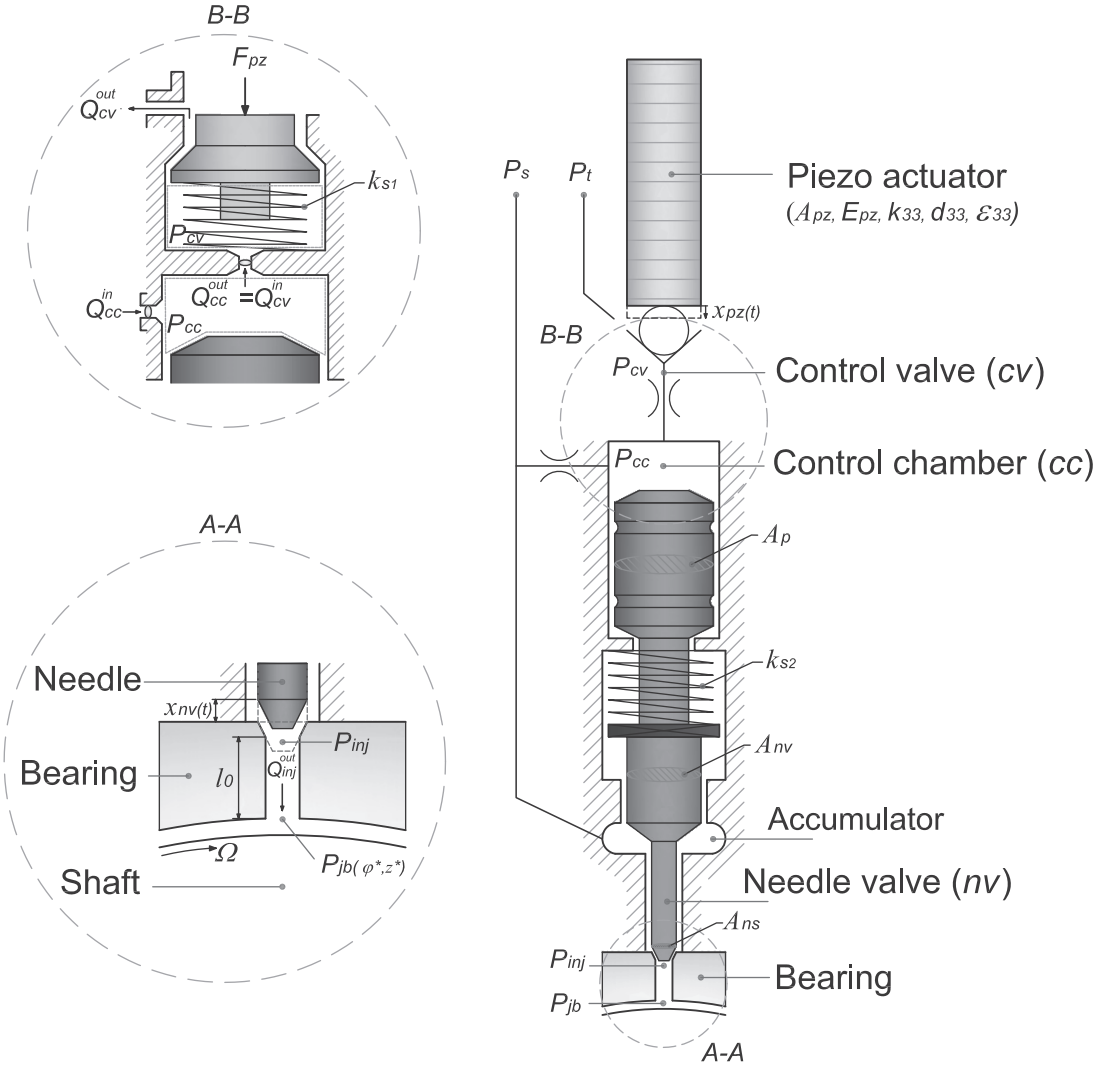

Figure 4.4: *Schematics of a piezo-actuated injector.*

For the simplicity of the modelling, the following main assumptions are made:

- oil supply pressure (P_s) is constant, i.e., the dynamics of the oil supply pump are not included.
- solid parts of injector are rigid, i.e., elastic deformations of solid parts due to pressure change are neglected.
- internal leakages are neglected.

The main equations for the modelling of the piezoelectric actuator and the hydraulic and mechanical subsystems of the injector are presented in the following section.

Modelling of the piezoelectric stack:

The material strain and the electrical displacement exhibited by a piezoelectric stack are both linearly affected by the mechanical stress and electrical field to which the ceramic is subjected, as stated by the linear constitutive equations for piezoelectric materials (ANSI/IEEE, 1987). In the case of defining the constitutive equations for piezostacks, it is typical that poling and loading directions to be defined as the 3,3 directions respectively, as shown in Fig. 4.5a. The linear constitutive equations for piezoelectric materials are defined as:

$$S_3(t) = s_{33}^E T_3(t) + d_{33} E_3(t) \tag{4.5}$$

$$D_3(t) = d_{33} T_3(t) + \varepsilon_{33}^T E_3(t) \tag{4.6}$$

where $S_3(t)$ is the strain; s_{33} is the elastic compliance $[m^2/N]$; $T_3(t)$ is the stress; d_{33} is the piezoelectric coupling coefficient (or piezo electric charge constant) $[C/N]$; $E_3(t)$ is the electric field $= v(t)/d$; $D_3(t)$ is the electric displacement $= Q_3(t)/A_{pz}$; ε_{33} is the dielectric permittivity $[F/m]$. Thus, Eq. (4.5) defines the mechanical response of the material while Eq. (4.6) defines the electrical response.

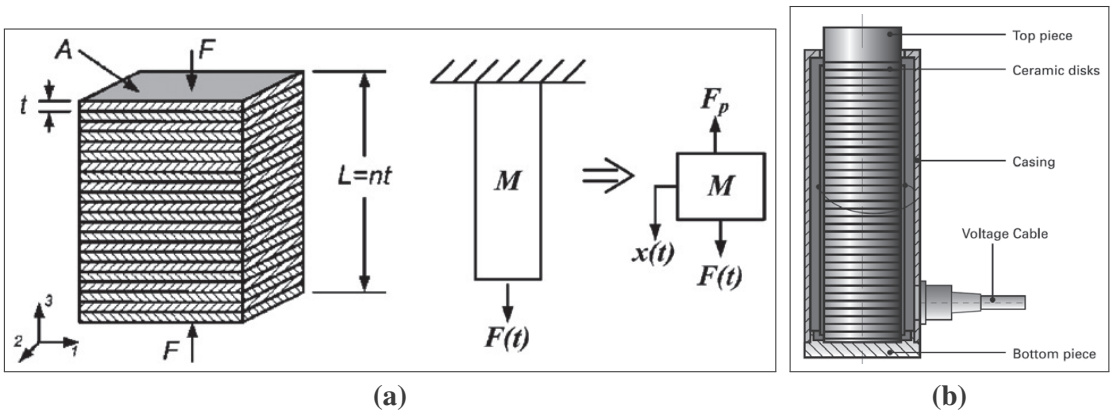

Figure 4.5: *(a) Schematic configuration of a piezostack (Feenstra et al., 2008); (b) Mechanical design of a comercial stack actuator.*

Considering that a stack actuator has several layers of piezoelectric material, the number of layers (N_{pz}), with each layer of an area of A_{pz}, and thickness d_{pz}, the resultant piezo-stack force (F_{pz}) and electric charge can be derived from the constitutive equations for piezoelectric materials:

$$F_{pz}(t) = -k_{33}x_{pz}(t) + k_{33}d_{33}N_{pz}v_{pz}(t) \tag{4.7}$$

$$Q_{pz}(t) = k_{33}d_{33}x_{pz}(t) + \varepsilon_{33}N_{pz}E_{pz}^{-1}v_{pz}(t) \tag{4.8}$$

where $x_{pz}(t)$ is the total displacement of the piezo-stack; k_{33} is the elastic stiffness of the piezo-stack; d_{33} is the piezoelectric coupling coefficient; v_{pz} is the feeding voltage; E_{pz} is the elastic modulus of the piezo-stack; and ε_{33} is the dielectric permittivity. If the hysteresis is assumed to be negligible, the free expansion of an unloaded piezoelectric stack actuator may be expressed by (Fuller et al., 1996):

$$\Delta L_{pz}(t) = d_{33}N_{pz}v_{pz}(t) \tag{4.9}$$

Modelling of hydraulic subsystems:

The hydraulic subsystems are considered as containers of unknown pressure, where the cross-sectional area is great compared with the inlet and outlet ducts of the system. Considering only elasticity of the concentrated volume but not inertia effects, an equal pressure inside the control volume can be assumed. Considering compressibility of the fluid, expressed by the bulk modulus of elasticity, the pressure change in each one of the control volumes v_i of the hydraulic subsystems (i.e., control valve (*cv*), control chamber (*cc*) and needle injector valve (*nv*)), can be solved by means of Eq. (4.10), derived from the definition of bulk modulus of elasticity (Fox et al., 2004):

$$\frac{\mathrm{d}P}{\mathrm{d}t} = -\frac{\beta}{V}\frac{\mathrm{d}V}{\mathrm{d}t} \tag{4.10}$$

where β is the bulk modulus of elasticity; V is the instantaneous volume of the fluid; $\mathrm{d}V/\mathrm{d}t$ takes into account the intake and outtake flows, Q^{in} and Q^{out}, and the volume change due to the motion of mechanical parts. The above equation yields:

$$\frac{\mathrm{d}P_{v_i}}{\mathrm{d}t} = -\frac{\beta_{v_i}}{V_{v_i}}\left(\frac{\mathrm{d}V_{v_i}}{\mathrm{d}t} - Q_{v_i}^{in} + Q_{v_i}^{out}\right) \tag{4.11}$$

where for each control volume, V_{v_i} is the instantaneous volume of the fluid; $\mathrm{d}V_{v_i}/\mathrm{d}t$ accounts for the volume change due to the motion of mechanical parts. The bulk modulus can be related to the fluid pressure by (Hountalas and Kouremenos, 1998):

$$\beta_{v_i} = 1.2\times 10^9\left[1 + 0.6\frac{P_{v_i}\times 10^{-5}}{600}\right] \tag{4.12}$$

The intake and outtake flows through each control volume Q^{in} and Q^{out}, can be calculated by applying the energy conservation law:

$$Q = sgn(\Delta P)\cdot C_d\cdot A_o\cdot\sqrt{\frac{2}{\rho}|\Delta P|} \tag{4.13}$$

where for each control volume at the inlet and outlet section, respectively: C_d is a discharge coefficient; A_o is the orifice section; ΔP is the oil pressure difference across the section A_o; and ρ is the oil density. The discharge coefficient C_d accounts for the flow losses through orifices and it is usually obtained experimentally. In the literature there is a wide spread of values for discharge coefficients, however, for short and sharp-edged orifices a value of $C_d = 0.6$ is commonly assumed for numerical simulations (Merritt, 1967). Applying Eqs. (4.11) and (4.13) to the hydraulic subsystems of the piezo-actuated injector (see Fig. 4.4), one obtains:

Control valve (cv):

$$\dot{P}_{cv} = -\frac{\beta_{cv}}{V_{cv}} \left(\dot{V}_{cv} - \underbrace{sgn(P_{cc} - P_{cv}) C_{d_{cv}}^{in} A_{o_{cv}}^{in} \sqrt{\frac{2}{\rho}|P_{cc} - P_{cv}|}}_{Q_{cv}^{in}} + \underbrace{sgn(P_{cv} - P_t) C_{d_{cv}}^{out} A_{o_{cv}}^{out} \sqrt{\frac{2}{\rho}|P_{cv} - P_t|}}_{Q_{cv}^{out}} \right) \tag{4.14}$$

Control chamber (cc):

$$\dot{P}_{cc} = -\frac{\beta_{cc}}{V_{cc}} \left(\dot{V}_{cc} - \underbrace{sgn(P_s - P_{cc}) C_{d_{cc}}^{in} A_{o_{cc}}^{in} \sqrt{\frac{2}{\rho}|P_s - P_{cc}|}}_{Q_{cc}^{in}} + \underbrace{sgn(P_{cc} - P_{cv}) C_{d_{cc}}^{out} A_{o_{cc}}^{out} \sqrt{\frac{2}{\rho}|P_{cc} - P_{cv}|}}_{Q_{cc}^{out}} \right) \tag{4.15}$$

Needle valve (nv):

$$\dot{P}_{inj} = -\frac{\beta_{nv}}{V_{nv}} \left(\dot{V}_{nv} - \underbrace{sgn(P_s - P_{inj}) C_{d_{nv}}^{in} A_{o_{nv}}^{in} \sqrt{\frac{2}{\rho}|P_s - P_{inj}|}}_{Q_{nv}^{in}} + \underbrace{sgn(P_{inj} - \bar{P}_{jb}) C_{d_{nv}}^{out} A_{o_{nv}}^{out} \sqrt{\frac{2}{\rho}|P_{inj} - \bar{P}_{jb}|}}_{Q_{nv}^{out} \Leftrightarrow \bar{Q}_{inj}} \right) \tag{4.16}$$

where P_{cv} is the pressure in the control valve; P_{cc} is the pressure in the control chamber; P_s is the supply pressure; P_t is the return pressure; and P_{inj} is the injection pressure.

Assuming incompressible flow and no pipeline deformations, the oil flow passing through the bearing orifice area $A_{o_{nv}}^{out}$ can be calculated by integrating the injection velocity profile:

$$\bar{Q}_{inj} = \int_A V_{inj} dA \tag{4.17}$$

where the injection velocity profile for each i^{th} orifice, can be written as a function of the difference between the journal pressure $\bar{P}_{jb_i}(\varphi, z, t)$ and the injection pressure $P_{inj_i}(t)$, assuming a fully developed laminar flow in an axisymmetric pipe and a linear variation of the injection pressure along the orifice (Santos and Russo, 1998):

$$V_{inj}(\varphi, z, t) = -\frac{F_i(\varphi, z)}{4\mu l_o} (P_{inj}(t) - \bar{P}_{jb}(\varphi, z, t)) \tag{4.18}$$

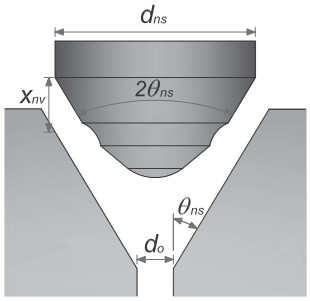

Figure 4.6: *Needle tip geometry.*

In Eq. (4.18), $\bar{P}_{jb}$ corresponds to the film pressure computed at the sleeve side of the orifice, obtained from the solution of the modified Reynolds equation (Eq. (4.1)). In other words, for each one of the i^{th} oil injection orifices, $\bar{P}_{jb_i}$ would be equal to p evaluated at the coordinates Θ_{o_i}, a_{b_i} (see Fig. 4.1). Since the value of $\bar{P}_{jb}$ depends on the dynamics of the journal bearing fluid film, its value must be updated for each time step in Eq. (4.16).

The total oil flow passing through all the s orifices can be calculated as:

$$Q_{inj}(t) = -\sum_{i=1}^{s} \int V_{inj_i}(t).dA_i \tag{4.19}$$

It is worth to notice that in Eq. (4.16) the cross section area of the inlet flow ($A^{in}_{o_{nv}}$) is not constant and it can be written as a function of the displacement of the needle of the injector (x_{nv}), as follows:

$$A^{in}_{o_{nv}} = \frac{\pi}{4}(d_{ns} + d_{in})\sqrt{(d_{ns} - d_{in})^2 + x^2_{nv}} \tag{4.20}$$

where d_{ns} is the diameter of the needle seat, and d_{in} is a variable given by: $d_{in} = d_{ns} - 2x_{nv}\cos\theta_{ns}\sin\theta_{ns}$; θ_{ns} is the angle of the tip of the needle injector, as illustrated in Fig. 4.6.

Modelling of mechanical subsystems:

In order to model the main mechanical parts of the piezoelectric injector, they are grouped in two mechanical subsystems $s1$ and $s2$, and described by *sdof* systems, as schematically seen in Fig. 4.7 The first mechanical subsystem consists of the push rod, valve piston, control valve and piezoelectric stack, and it is dynamically described by Eq. (4.21). The second subsystem includes the control piston and the needle valve, and it is described by the Eq. (4.22).

$$m_{s1}\ddot{x}_{cv} = F_{pz} - k_{s1}x_{cv} - c_{s1}\dot{x}_{cv} - A_{cv}P_{cv} \tag{4.21}$$

$$m_{s2}\ddot{x}_{nv} = -k_{s2}x_{nv} - c_{s2}\dot{x}_{nv} - A_pP_{cc} + (A_{nv} - A_{ns})P_s \tag{4.22}$$

where m_{s1} is given by the equivalent mass of the control valve cluster and the piezoelectric stack; m_{s2} is given by the total mass of the needle valve and control piston; c_{s1} is the viscous friction coefficient of the valve piston; k_{s1} is the combined stiffness of the push rod and valve springs; c_{s2} is the viscous friction coefficient of the needle injector; k_{s2} is the servo piston spring constant; A_{nv}, A_{ns}, A_p, A_{cv} are the sectional area of the needle valve, needle valve seat, servo piston and control valve respectively, as shown in Fig. 4.4.

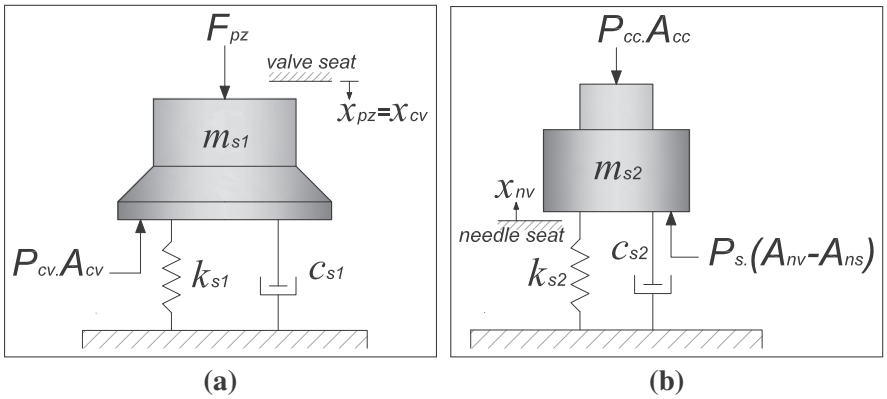

Figure 4.7: *(a) Equivalent mechanical subsystem m_{s1}: piezostack; pushrod and control valve; (b) equivalent mechanical subsystem m_{s2}: valve piston and needle valve.*

Mathematical model in state space representation

All the equations that describe the mathematical model of the piezo-actuated injector can be rewritten in state space form as

$$\dot{\boldsymbol{x}}(t) = f(t, \boldsymbol{x}(t), \boldsymbol{v}_{pz}(t))$$

where $\boldsymbol{x} = [x_{pz}\ \dot{x}_{pz}\ x_{nv}\ \dot{x}_{nv}\ P_{cv}\ P_{cc}\ P_{inj}]^T$; and the piezo-stack driving signals are the inputs: $\boldsymbol{v}_{pz}(t) = [v_{pz}(t)\ \dot{v}_{pz}(t)]^T$. As a result, the state space representation is given by:

$$\left\{\begin{array}{c} \dot{x}_{pz} \\ \ddot{x}_{pz} \\ \dot{x}_{nv} \\ \ddot{x}_{nv} \\ \dot{P}_{cv} \\ \dot{P}_{cc} \\ \dot{P}_{inj} \end{array}\right\} \Leftrightarrow \left\{\begin{array}{c} \dot{x}_1 \\ \dot{x}_2 \\ \dot{x}_3 \\ \dot{x}_4 \\ \dot{x}_5 \\ \dot{x}_6 \\ \dot{x}_7 \end{array}\right\} = \left\{\begin{array}{c} x_2 \\ \left[-k_{33}x_1 + k_{33}d_{33}N_{pz}v_{pz} - k_{s1}x_1 - c_{s1}x_2 - A_{cv}x_5\right]/m_{s1} \\ x_4 \\ \left[-k_{s2}x_3 - c_{s2}x_4 - A_p x_6 + (A_{nv} - A_{ns})P_s\right]/m_{s2} \\ -\frac{\beta_{cv}(x_5)}{V_{cv}}\left[A_{cv}x_2 - Q_{cv}^{in}(x_5, x_6) + Q_{cv}^{out}(x_5)\right] \\ -\frac{\beta_{cc}(x_6)}{V_{cc}(x_3)}\left[A_{cc}x_4 - Q_{cc}^{in}(x_6) + Q_{cc}^{out}(x_5, x_6)\right] \\ -\frac{\beta_{iv}(x_7)}{V_{iv}}\left[\dot{V}_{iv}(x_3) - Q_{iv}^{in}(x_7) + \bar{Q}_{inj}(x_7, \bar{P}_{jb})\right] \end{array}\right\} \tag{4.23}$$

A simplified model of piezo-injector

The modelling of the injector can be simplified by considering it as a control volume without considering the dynamics of the piezo-stack and the control chambers. It can be also assumed that the volume of the injector chamber remains constant and that the injection section area switches between zero and its maximum, neglecting opening and closing transients of the injector. Thus, the governing pressure for the injection can be rewritten as:

$$\dot{P}_{inj} = -\frac{\beta_{iv}}{V_{iv}}\left(-sgn(P_s - P_{inj})S_T C_{d_{inj}}^{*}\sqrt{|P_s - P_{inj}|} + \bar{Q}_{inj}\right) \tag{4.24}$$

where S_T is a square signal equal to 1 during injections and zero otherwise; and $C^*_{d_{nv}} = C^{in}_{d_{nv}} A^{max}_{o_{nv}} \sqrt{2/\rho}$.

The equations of the dynamics of the injector and the system of equations that describes the dynamics of journal bearing and reciprocating mechanism have to be simultaneously solved, since the oil injection pressures (P_{inj}) are influenced by the hydrodynamic pressure of the fluid film at the bearing side of the orifices ($\bar{P}_{jb}$), as seen in Eq. (4.16). At the same time, the updated values of P_{inj} have to be introduced into Eq. (4.1) for each time step.

4.2.2 Mechanical injection system

In the mechanical injector described here, the injection is basically controlled by an inline cam-pump system, where the design of the cam profile determines the oil injection events. An schematic diagram is shown in Fig. 4.8. The governing equations for the dynamics of the hydraulic subsystems (i.e., needle injector valve and pump) can be deducted from Eqs. (4.11) and (4.13). In this case, the dynamics of the pump has to be included in the model since the oil flows and pressures in the control volumes directly depend on the performance of the pump. To simplify the modelling of the injection, the connecting pipe between delivery valve and accumulator injector chamber is considered short, neglecting loss factors and pressure variations related to pressure waves propagation. Moreover the modelling of the delivery valve is simplified by considering it as a check valve and assuring that only flow from the pump to the accumulator chamber takes place. Previous studies related to the modelling of fuel injectors have shown that by neglecting the effects of the valve motion the introduced error is small compared to more sophisticated models (Hountalas and Kouremenos, 1998). With these simplifications, the governing equation for the pressure change in the hydraulic subsystems of the mechanical oil injection system can be written as

Cylinder pump (cp):

$$\dot{P}_{cp} = -\frac{\beta_{cp}}{V_{cp}} \left(\dot{V}_{cp} - \underbrace{sgn(P_{cp} - P_s) C^{in}_{d_{cp}} A^{in}_{o_{cp}} \sqrt{\frac{2}{\rho}|P_{cp} - P_s|}}_{Q^{in}_{cp}} + \underbrace{sgn(P_{dv} - P_{cp}) C^{out}_{d_{cp}} A^{out}_{o_{cp}} \sqrt{\frac{2}{\rho}|P_{dv} - P_{cp}|}}_{Q^{out}_{cp} \Leftrightarrow Q^{in}_{dv}} \right) \tag{4.25}$$

Delivery valve (dv):

$$\dot{P}_{dv} = -\frac{\beta_{dv}}{V_{dv}} \left(-Q^{in}_{dv} + Q^{out}_{dv} \right) \tag{4.26}$$

Accumulator chamber (ac):

$$\dot{P}_{ac} = -\frac{\beta_{ac}}{V_{ac}} \left(\underbrace{-sgn(P_{ac} - P_{dv}) C^{in}_{d_{ac}} A^{in}_{o_{ac}} \sqrt{\frac{2}{\rho}|P_{ac} - P_{dv}|}}_{Q^{in}_{ac} \Leftrightarrow Q^{out}_{dv}} + \underbrace{Q^{out}_{ac}}_{Q^{in}_{nv}} \right) \tag{4.27}$$

Needle valve (nv):

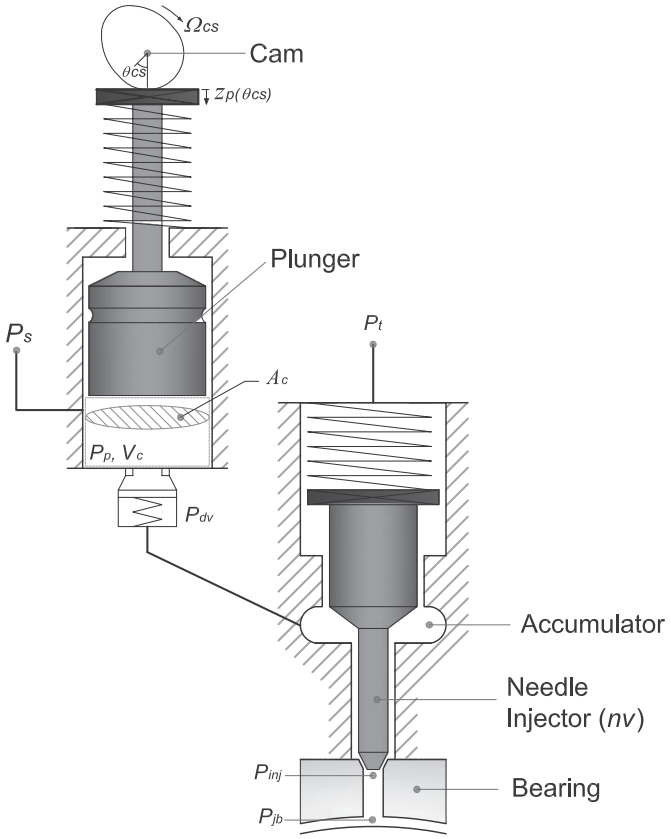

Figure 4.8: *Schematics of a mechanical unit injector.*

$$\dot{P}_{inj} = -\frac{\beta_{nv}}{V_{nv}} \left(\dot{V}_{nv} - \underbrace{sgn(P_{ac} - P_{inj}) C_{d_{nv}}^{in} A_{o_{nv}}^{in} \sqrt{\frac{2}{\rho}|P_{ac} - P_{inj}|}}_{Q_{nv}^{in}} + \underbrace{sgn(P_{inj} - \bar{P}_{jb}) C_{d_{nv}}^{out} A_{o_{nv}}^{out} \sqrt{\frac{2}{\rho}|P_{inj} - \bar{P}_{jb}|}}_{Q_{nv}^{out} \Leftrightarrow \bar{Q}_{inj}} \right) \tag{4.28}$$

where

$$\begin{aligned} Q_{dv}^{in} &= Q_{cp}^{out} \quad \text{, if} \quad P_{cp} > P_{dv} \; ; \quad \text{otherwise} \quad Q_{dv}^{in} = 0 \\ Q_{dv}^{out} &= Q_{ac}^{in} \quad \text{, if} \quad P_{dv} > P_{dv}^{op} \; ; \quad \text{otherwise} \quad Q_{dv}^{out} = 0 \end{aligned}$$

where P_{cp} is the pressure inside the cylinder of the pump; P_{dv} is the pressure in the delivery valve chamber; P_{ac} is the pressure in the accumulator chamber; P_{inj} is the injection pressure; and P_{dv}^{op} is the opening pressure of the delivery valve.

The change of volume due to piston motion can be calculated by knowing the position of the plunger with respect to the camshaft angle - $z_p(\theta_{cs})$, which can be obtained by linear interpolation of the cam profile. Hence, the instantaneous pump volume and the rate of change of pump volume

as a function of piston motion are given by:

$$V_{cp} = V_{cp}^0 - A_{cp} \cdot z_p(\theta_{cs}) \tag{4.29}$$

$$\dot{V}_{cp} = A_{cp} \cdot \dot{z}_p = A_{cp} \cdot \Omega_{cs} \cdot \frac{\mathrm{d}z_p}{\mathrm{d}\theta_{cs}} \tag{4.30}$$

where A_{cp} is the cylinder bore; z_p is the piston instantaneous axial displacement; V_{cp}^0 is the cylinder total volume; and Ω_{cs} is the camshaft speed.

Assuming a *SDOF* system, the displacement of the injector valve (needle injector) is calculated by

$$m_{s3}\ddot{x}_{nv} = -k_{s3}(x_{nv} + x_{pl}) - c_{s3}\dot{x}_{nv} + (A_{nv} - A_{ns})P_{ac} \tag{4.31}$$

where x_{pl} is the preload of the needle valve spring; k_{s3} and c_{s3} are the stiffness of the spring and damping (friction) coefficient, respectively; and m_{s3} is the equivalent mass for the injector valve.

Mathematical model in state space representation

The equations that describe the mathematical model of the mechanical unit injector can be rewritten in state space form as

$$\dot{\boldsymbol{x}}(t) = f(t, \boldsymbol{x}(t), \boldsymbol{u}_{cs}(t))$$

where $\boldsymbol{x} = [x_{nv}\ \dot{x}_{nv}\ P_{cp}\ P_{dv}\ P_{ac}\ P_{inj}]^T$; and the movement of the plunger in the pump, which depends on the camshaft profile and rotational velocity are the inputs: $\boldsymbol{u}_{cs}(t) = [z_p(t)\ \dot{z}_p(t)]^T$, where $\dot{z}_p(t) = \Omega_{cs}(\mathrm{d}z_p/\mathrm{d}\theta_{cs})$. As a result, the state space representation is given by:

$$\left\{\begin{array}{c} \dot{x}_{nv} \\ \ddot{x}_{nv} \\ \dot{P}_{cp} \\ \dot{P}_{dv} \\ \dot{P}_{ac} \\ \dot{P}_{inj} \end{array}\right\} \Leftrightarrow \left\{\begin{array}{c} \dot{x}_1 \\ \dot{x}_2 \\ \dot{x}_3 \\ \dot{x}_4 \\ \dot{x}_5 \\ \dot{x}_6 \end{array}\right\} = \left\{\begin{array}{c} x_2 \\ \left[-k_{s3}(x_1 + x_{pl}) - c_{s3}x_2 + (A_{nv} - A_{ns})x_5\right]/m_{s3} \\ -\frac{\beta_{cp}(x_3)}{V_{cp}(z_p)}\left[A_{cp}\dot{z}_p - Q_{cp}^{in}(x_3) + Q_{cp}^{out}(x_3, x_4)\right] \\ -\frac{\beta_{dv}(x_4)}{V_{dv}}\left[-Q_{dv}^{in}(x_3, x_4) + Q_{dv}^{out}(x_4, x_5)\right] \\ -\frac{\beta_{ac}(x_5)}{V_{ac}}\left[-Q_{ac}^{in}(x_4, x_5) + Q_{ac}^{out}(x_5, x_6)\right] \\ -\frac{\beta_{nv}(x_6)}{V_{nv}(x_1)}\left[\dot{V}_{nv}(x_2) - Q_{nv}^{in}(x_5, x_6) + \bar{Q}_{inj}(x_6, \bar{P}_{jb})\right] \end{array}\right\} \tag{4.32}$$

A simplified model of the mechanical unit injector

In order to simplify the modelling of the mechanical injector, and to facilitate afterwards the design of the controller, the model can be reduced by neglecting the dynamics of delivery valve and the injector, assuming that the outflow section areas switches between zero and its maximum, thus neglecting opening and closing transients. Additional assumptions consider the flow between the pump and the delivery equal to the flow between the delivery valve and the accumulator chamber; and the flow between the accumulator chamber and the injector equal to the flow between the injector and the journal bearing. With these simplifications, the governing equations become:

$$\dot{P}_{cp} = -\frac{\beta_{cp}}{V_{cp}} \left(\dot{V_{cp}} - \underbrace{sgn(P_{cp} - P_s) C_{d_{cp}}^{in} A_{o_{cp}}^{in} \sqrt{\frac{2}{\rho}|P_{cp} - P_s|}}_{Q_{cp}^{in}} + \underbrace{sgn(P_{ac} - P_{cp}) C_{d_{dv}}^{out} A_{o_{dv}}^{out} \sqrt{\frac{2}{\rho}|P_{ac} - P_{cp}|}}_{Q_{cp}^{out} \Leftrightarrow Q_{ac}^{in}} \right) \tag{4.33}$$

$$\dot{P}_{ac} = -\frac{\beta_{ac}}{V_{ac}} \left(\underbrace{-sgn(P_{ac} - P_{cp}) C_{d_{dv}}^{out} A_{o_{dv}}^{out} \sqrt{\frac{2}{\rho}|P_{ac} - P_{cp}|}}_{Q_{ac}^{in} \Leftrightarrow Q_{cp}^{out}} + \underbrace{sgn(P_{ac} - \bar{P}_{jb}) C_{d_{nv}}^{*} S_T \sqrt{|P_{ac} - \bar{P}_{jp}|}}_{Q_{ac}^{out} \Leftrightarrow \bar{Q}_{inj}} \right) \tag{4.34}$$

where S_T is a square signal equal to 1 during injections and zero otherwise; and $C_{d_{nv}}^{*} = C_{d_{nv}}^{in} A_{o_{nv}}^{max} \sqrt{2/\rho}$.

4.3 Summary

Two approaches for applying active lubrication to *DLJB*s were described in this chapter. Hydrostatic lubrication is modified by injecting oil at controllable pressures, through orifices circumferentially located around the bearing surface. The modified Reynolds equation for active lubrication and for *DLJB*s was presented and discretized in order to be solved using a *FD* scheme. The main equations that govern the dynamics of the injection for a piezo-actuated oil injector and a mechanical-actuated oil injector were presented. The next chapter describes how the injector dynamics (Eq. 4.23 for the piezoelectric injector and Eq. 4.32 for the mechanical injector) is numerically coupled to the dynamics of the bearing fluid films, and to the representative *MBD* model of a reciprocating mechanism (refer to Fig. 5.3). In chapter 6, the analysis of a main journal bearing of a reciprocating *ICE*, operating with controllable radial oil injection, and using a piezolectric injection system, will be discussed.

Chapter 5

Global Model and Numerical Implementation

The numerical coupling between the dynamics of a reciprocating mechanism, the dynamics of fluid film bearings and the dynamics of oil injection, is described in this chapter. Since the global system of equations exhibits a highly non-linear behaviour, it must be solved using numerical methods. *DLJB*s, particularly main bearings of *ICE*s support dynamic loads that change according to the dynamics of the combustion forces inside the cylinders and to the inertia forces of the reciprocating and unbalanced rotating masses. These loads notoriously vary in magnitude and direction during every cycle of the crankshaft rotation, which introduces a highly non-linear behaviour to the dynamics of the rotor-bearing system. Moreover, the modification of *CHL* through radial oil injection incorporates more complexity into the system through the modified Reynolds equation and the equations that govern the dynamics of the injectors. Thus, in order to analyze such a coupled system aiming to study the kinematic and dynamic behaviour of *DLJB*s, main mechanical components of reciprocating mechanisms, and the dynamics of oil injection systems, a simultaneous solution of the modified Reynolds equation, equations of motion of mechanical components, and governing equations of injection system, is required. Figure 5.3 schematically illustrates how the dynamics of the mechanical parts, the dynamics of fluid films, and the dynamics of the oil injection system are connected through equations.

5.1 Numerical procedure

The numerical procedure implemented for the solution of the global system, considering *CHL* and controllable lubrication, is presented in this section. A flowchart with the main steps involved in the numerical scheme of solution implemented, is shown in Fig. 5.2. In order to initialize the program, input data containing physical and geometric parameters, and initial conditions must be given. There are three main modules in the program: *MBD* module, which contains the set of motion equations of the reciprocating mechanism; *FEM* module, which gives the mass, stiffness and gyroscopic matrices of the rotor (used only when case (III) is considered, as described in section 2.3); and *FFF* module, which computes the journal bearing forces for conventionally and controllable lubricated bearings. The journal bearing forces can be computed analytically (only for *CHL*, and for *SJB* or

LJB solutions), or numerically using a *FD* scheme. The main steps involved in the numerical solution of the global system are summarized next.

5.1.1 Input data and starting values

In this part all of the geometric and physical parameters are given, i.e., geometric bearing configuration, dimensions of main mechanical parts, rotational speed of crankshaft, masses, inertias, preloads, etc. Suitable initial conditions must be given (i.e., displacements and initial velocities of components). In the cases where controllable lubrication is included, the geometric hybrid bearing configuration has to be defined, such as, distribution of orifices over the bearing surface and diameter of orifices, as well as, the rules for controlling oil injection pressures ($P_{inj}(\theta_c)$). The geometric and physical characteristic of the injectors have to be included, if the system is going to be solved considering the dynamics of the injection system.

5.1.2 Pre-processing

Based on the input data, starting values given to the program, and the case of analysis considered, the system of equations for the multibody dynamic model (*MBD* module) can be defined. It has to be mentioned that *MBD* module is required for all cases, generating a different set of equations for each case, as shown in appendix A. If the flexibility of the rotor is to be considered, as in case (III), the matrices of the *FEM* formulation of the rotor are generated using *FEM* module. During the preprocessing stage the discretization of Reynolds equation using a *FD* formulation takes place. In the cases where *CHL* is considered, the Reynolds equation is discretized using an uniform mesh over the bearing surface, as presented in section 3.3.2. For the cases where controllable radial oil injection is considered, a non-uniform mesh over the bearing surface is implemented, as the one illustrated in Fig. 5.1, and described with equations in section 4.1.2.

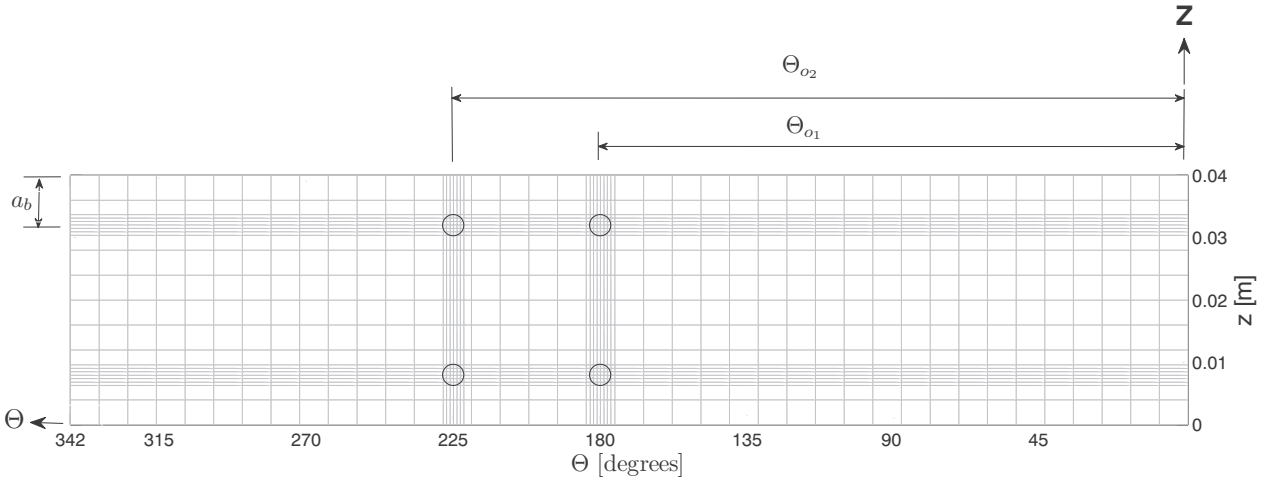

Figure 5.1: *Discretized bearing surface with a non-uniform mesh, size of $m \times n$.*

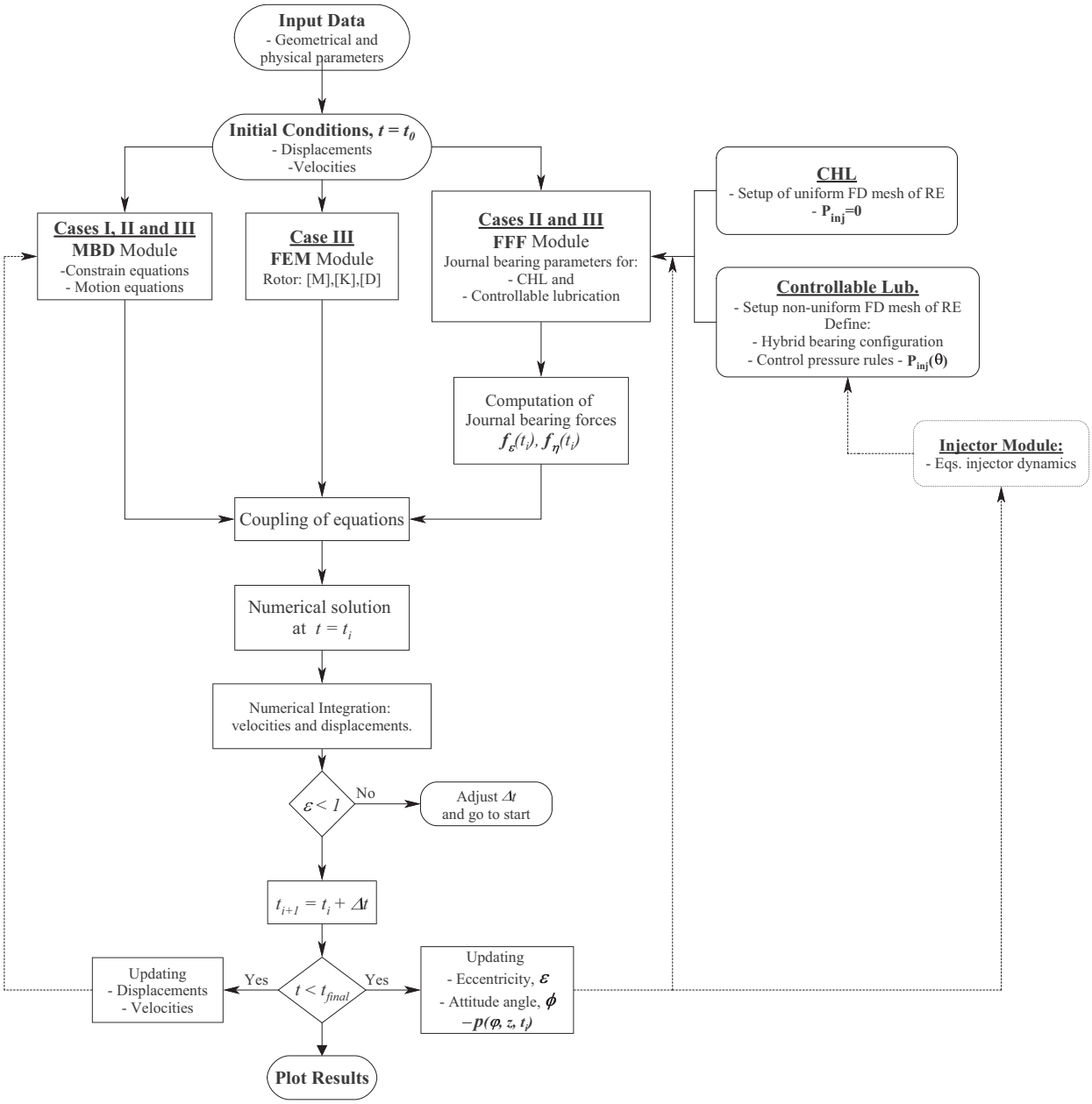

Figure 5.2: *Flowchart - overall solution scheme.*

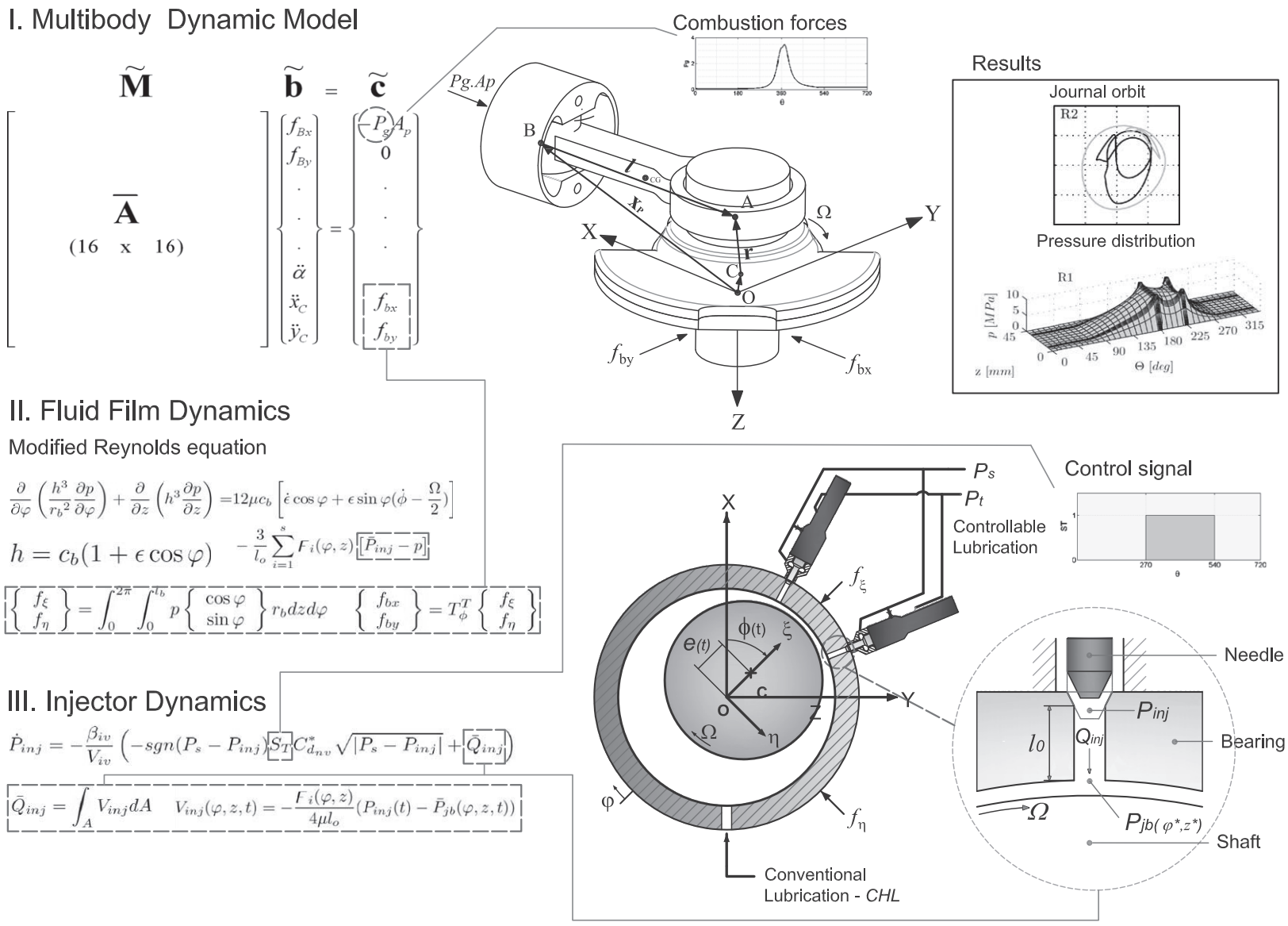

Figure 5.3: *Coupling of MBD model (case II), fluid film dynamics (with controllable lubrication), and dynamics of injector.*

5.1.3 Calculation of the fluid film bearing forces

The numerical algorithm for solving Reynolds equation is implemented inside the *FFF* module. When *CHL* is considered, the fluid film forces can be computed using either analytical, or numerical solutions of Reynolds equation for *DLJB*s. The approximated analytical solutions for *DLJB*s operating under *CHL* (given in Table 3.2) are recommended to be used only for *SJB* or *LJB* approaches. In other cases numerical methods should be used for the solution of Reynolds equation. When a *DLJB* operates with active or controllable lubrication, the modified Reynolds equation for active lubrication, presented in Eq. 4.1 has necessarily to be numerically solved. In this work the *FD* formulation described in section 4.1.2 was computationally implemented. Thus, the area over the bearing surface was discretized using an uniform mesh (for the *CHL* case), or a non-uniform mesh (for the hybrid bearing case), as illustrated in Fig. 5.1, which enables to refine the area over the oil injection orifices. The set of algebraic equations giving by the *FD* formulation of Reynolds equation is solved by using the *LU* factorization method. Considering that an important number of zero elements are usually included in the main matrix of a *FD* formulation, sparse matrix methods built in Matlab were used. The use of *LU* was prefered over an iterative method such as *SOR* or Jacobi, due to the relative simplicity for its implementation. Solving the algebraic system of equations, the pressure distribution of the bearing fluid film is obtained. Then, the bearing forces are calculated by integrating the pressure distribution along the bearing surface, as shown by Eq. (3.8). In this case, the numerical Simpson method of integration was used.

5.1.4 Numerical solution of the global system

This part of the algorithm includes the numerical coupling of equations from the three different modules. One has to remember that the complete system must be solved in time, using a time step small enough to warranty convergence in the solution. If a periodic load condition is considered, the global system of equations has to be solved for several operational cycles until a steady solution is reached. The fluid film forces must be calculated for each time step using the *FFF* module, and they must be updated in the vector $\bar{\mathbf{c}}$ of Eq. (2.19) for case II, or in the vector $\hat{\mathbf{f}}$ of Eq. (2.20) for case III. By solving the global system of equations, reaction forces and acceleration of the system are obtained for each time step. However, it has to be considered that in order to compute the fluid film forces at the time t_{i+1} the velocity and position of the journal centre (x_C,y_C,$\dot{x}_C$,$\dot{y}_C$) at t_{i+1}, must be also known, and therefore, estimated previously. In this work a scheme based on the implicit Newmark method combined with a predictor-corrector approach was used (Garcia de Jalon and Bayo, 1994). Thus, for each time step initial estimations of the position and velocity of the crank centre are obtained by using the Heun's explicit method, which lets to compute the fluid film forces based on the initial guess values and to solve the global system at the time t_{i+1}. Then, by using the implicit Newmark method new estimations of the velocity and the displacement of the journal centre can be computed and introduced into the Reynolds equation (*FFF* module). By solving Reynolds equation updated journal bearing forces are obtained and then introduced into the global system. The system is solved again, and after a few iterations the difference between two consecutive values becomes smaller than the prescribed tolerance and the computation of the global system is moved forward to a new time step. In order to warranty numerical convergence in the solution, small time steps were used ($1 \times 10^{-6} \leq \Delta t \leq 1 \times 10^{-3}$). It can be additionally mentioned that a *MBD* problem

coupled to a journal bearing may respond in a wide range of frequency. These type of problems are known as "stiff", which may require special numerical solvers or the use of small step sizes to warranty numerical stability. The numerical procedure described above was implemented in this work, and it is also documented in paper [J3]*.

Numerical scheme solution for case III

In case III, where the flexibility of the rotor is included, the structural matrices obtained from the *FEM* formulation of the rotor, given by Eq. (2.20) (*FEM* module) have to be coupled to the set of equations of the *MBD* model, given by Eq. (2.19). The coupling of these systems and the numerical method of solution are detailed in paper [J2]*, however for the completeness of this work, the main steps of the coupling and the numerical scheme of solution are given here.

If the rotor is discretized with N_E finite elements, the number of degrees of freedom ($ndof$) of the structural matrices will be equal to: $ndof = 4(N_E + 1)$, considering two lateral displacements and two angular rotations at each node, but neglecting torsion. Thus, the matrix $\bar{\mathbf{M}}$ of size $ndof \times ndof$ is coupled to the matrix $\bar{\mathbf{A}}$ of Eq. (2.19) (size 16×16), in the degrees of freedom related to the linear and angular accelerations of the crank centre, $\ddot{x}_C$, $\ddot{y}_C$, $\ddot{\beta}_C$, $\ddot{\Gamma}_C$ (e.g., $\ddot{q}_1$, $\ddot{q}_2$, $\ddot{q}_3$, $\ddot{q}_4$, assuming that the crank-rotor connection is located at one extreme of the rotor), obtaining a global mass matrix $\tilde{\mathbf{M}}$ of size $ndof + 12$. Similarly, the right hand side vector $\hat{\mathbf{f}}$ of Eq. (2.20) is coupled to the vector $\bar{\mathbf{c}}$ of Eq. (2.19). The global matrix system for case (III) can be written as: $\tilde{\mathbf{M}} \cdot \tilde{\mathbf{b}} = \tilde{\mathbf{c}}$, which is graphically illustrated in Fig. 5.4.

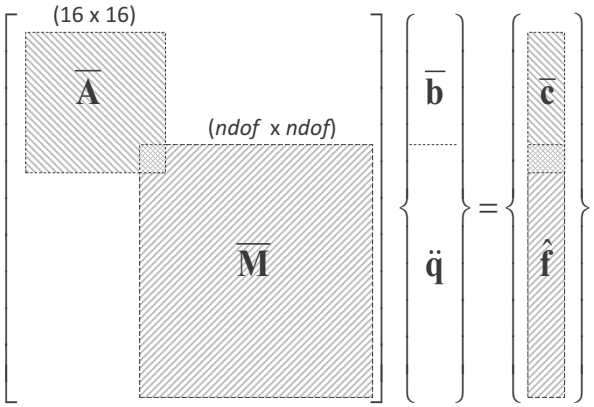

Figure 5.4: *Coupling of MBD model and FEM model - case III.*

Using the Newmark implicit method, the iterative equations for solving the global coupled system are given by:

$$\{\hat{\mathbf{b}}_{\mathbf{t_{i+1}}}, \ddot{\mathbf{q}}_{\mathbf{t_{i+1}}}\}^{\mathbf{T}} = \tilde{\mathbf{M}}^{-\mathbf{1}}_{\mathbf{t_{i+1}}} \cdot \tilde{\mathbf{c}}_{\mathbf{t_{i+1}}} \tag{5.1}$$

*Included in appendix B

$$\dot{q}_{t_{i+1}} = \dot{q}_{t_i} + \Delta t \left[(1-\hat{\gamma})\ddot{q}_{t_i} + \hat{\gamma}\ddot{q}_{t_{i+1}}\right] \tag{5.2}$$

$$q_{t_{i+1}} = q_{t_i} + \Delta t \dot{q}_{t_i} + \frac{\Delta t^2}{2}\left[(1-2\hat{\beta})\ddot{q}_{t_i} + 2\hat{\beta}\ddot{q}_{t_{i+1}}\right] \tag{5.3}$$

As mentioned before, in order to solve the system at the time t_{i+1}, the elements of vector $\tilde{\mathbf{c}}_{t_{i+1}}$ must be known in advance, which implies that the journal bearing forces at the time t_{i+1} should be also known, and consequently the displacements and velocities of the journal centre at the bearing location. In order to predict initial guesses values for $\dot{q}^0_{t_{i+1}}$ and $q^0_{t_{i+1}}$, the Heun's explicit method is used. Using these initial estimated values, journal bearing forces are computed at the time t_{i+1} (by solving Reynolds equation), and Eqs. (5.1),(5.2) and (5.2) are solved, obtaining new estimated values: $\dot{q}^1_{t_{i+1}}$ and $q^1_{t_{i+1}}$. These new predicted values are used to calculate new bearing forces and to update vector $\tilde{\mathbf{c}}_{\mathbf{t_{i+1}}}$, and by solving the system of equations new estimated values $\dot{q}^2_{t_{i+1}}$ and $q^2_{t_{i+1}}$ are obtained. This procedure is repeated until the difference between two consecutive values (e.g., displacements) becomes smaller than the prescribed tolerance given, moving forward one time step the computation of the global system, and repeating the procedure until the final time of computation is reached.

5.1.5 Coupling of the injector dynamics

The analysis of *DLJB*s operating with controllable lubrication can be made avoiding the dynamics of the injection system, assuming that the injection pressures are known as a function of time (or the instantaneous crank angle - $P_{inj}(\theta_c)$). For each particular case, initial approaches for defining the pressure injections and their rules of control can be defined based on the analysis made using *CHL* for the corresponding bearing under study, as it will be shown in next chapter. When the analysis is made considering the dynamics of the injection system, the dynamics of the fluid films are coupled to the dynamics of the injector, since the injection pressures will be determined by the operation of the injector based on the defined control pressure rules. This coupling can be visualized in Fig. 5.3. The set of equations that describes the dynamics of the injector using a piezo-actuated injector are presented in state space form in Eq. (4.23), where the last equation defines the dynamics of the injection pressures. Using piezo-actuated injectors, the injection pressures are dictated by the operation of the piezostacks (through the driving voltage signal - $v_{pz}(t)$ or $v_{pz}(\theta_c)$), which controls the opening and closing of the needle injector valve. In Fig. 5.3 the dynamics of the injector is represented by the simplified model described in section 4.2.1 by Eq. (4.24). In section 6.2.3, the analysis of a main engine bearing involving the dynamics of the injector is presented.

5.1.6 Post-processing

When the global system of equations has been solved for several operational cycles of the engine/compressor, plots of all variables can be generated in function of the time or the crank angle, as shown later in chapter 6.2. For the purposes of this work, more attention has been given to the analysis of journal orbits, minimum fluid film thicknesses, maximum film pressures and film pressure distribution.

Chapter 6

Case Studies

In this chapter, the feasibility of applying active lubrication to *DLJBs* is analyzed with the help of multibody dynamics and fluid film theory, through the study of two cases: a) upper main bearing of a hermetic reciprocating compressor; b) main crankshaft bearing of a single cylinder combustion engine. This study has been done through comparisons between the numerical results obtained for conventionally lubricated bearing performance, and for different configurations of hybridly and actively lubricated bearing performance. The results are analyzed with focus on the behaviour of parameters such as, *OFT*, maximum film pressures, journal vibrations, orbit performance, and cyclic power energy consumption. Finally, the convenience of using oil injection is evaluated by using an energetic approach. The results and conclusions presented here are complemented with the material included in the published papers listed at the beginning of this thesis, which will be referred throughout the chapter.

6.1 Application to the upper bearing of a hermetic reciprocating compressor - *HRC*

Small-scale reciprocating compressors are of common use to compress coolant gas in household refrigerators and air conditioners. These types of compressors use pistons that are driven directly through a slider-crank mechanism, converting the rotating movement of the rotor to an oscillating motion, as illustrated in Fig. 6.1. The performance of the bearings affects key functions of the compressor, such as durability, noise, and vibrations. Therefore the study and optimization of the dynamic behaviour of reciprocating compressors, taking into account the hydrodynamics of bearings, can be of significant importance for the development of new prototypes. Several studies related to the modelling of small reciprocating compressors can be found in the literature, as reported in the works of Rasmussen (1997); Rigola (2002), however, only a few of them have incorporated in their models the dynamics of the fluid films. For instance, one of the studies that has included the coupling of fluid-structure dynamics to analyse the dynamics of the piston was carried out by Cho and Moon (2005). In the work of Kim and Han (2004), the dynamics of piston and crankshaft was coupled to the dynamics of the fluid films, using a finite-width bearing approach and a short-width bearing approach. A numerical method was implemented for solving the global system of equation, giving some insights into the minimum *OFT*, cyclic averaged power consumption and oil leakage.

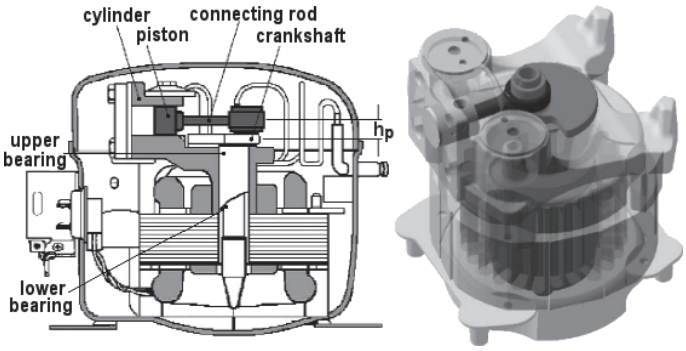

Figure 6.1: *Schematic draw and general view of a hermetic reciprocating compressor.*

Table 6.1: *Main geometrical and physical parameters - HRC.*

Radius crank-pin centre (r_c)	7.5 [mm]
Mass of crank (m_c)	0.1 [kg]
Inertia of crank (I_{c_z})	5×10^{-3} [kg.m^2]
Mass of connecting rod (m_{cr})	0.1 [kg]
Inertia of connecting rod (I_{cr_z})	1.7×10^{-5} [kg.m^2]
Diameter of piston (D_p)	23 [mm]
Mass of piston (m_p)	0.043 [kg]
Bearing aspect ratio (λ)	0.375; 0.75; 1
Land width ratio ($\bar{a}_b$)	0.1; 0.15; 0.2
Journal clearance (c_b)	15μ[m]
Fluid viscosity (μ)	0.005 [Pa.s]
Angular velocity (Ω)	312 [rad/s]
Diameter (d_o)/length orifices (l_o)	1.5 ; 20 [mm]

The study of the lubricant oil pumping system and the predictions of oil flow through the compressor components has also received recent attention, as shown by Kim and Ahn (2007). In their study, the lubrication system (including the bearings) of a hermetic compressor was modelled using an electric analogy methodology. Recently, the study of Lückmann et al. (2009) presented a model of the lubrication pumping system of a compressor using computational fluid dynamics (*CFD*), under several assumptions and neglecting the dynamics of fluid film bearings. In this framework, the case study presented in this section contributes to the analysis of the fluid film bearings of hermetic compressors. The study is based on a multibody dynamic model that describes the dynamics of the main mechanical components of a hermetic reciprocating compressor, as presented in chapter 2. Such a model is coupled to the dynamics of the fluid film bearings through equations, as presented in chapter 5. The analysis is mainly focused on the performance of the upper bearing (main radial bearing) operating with conventional (*CHL*) and hybrid (controllable) lubrication conditions.

The main geometric dimensions and physical properties of the reciprocating compressor used for the numerical simulations are given in Table 6.1. The curves of variation of the gas pressure inside the cylinder and the motor torque are shown in Figs. 6.2 and 6.3 respectively. It can be seen from Fig. 6.2 that the maximum gas pressure in the cylinder is found near the *TDC* (tod dead

centre), i.e., when $\theta_c \approx 180^o$.

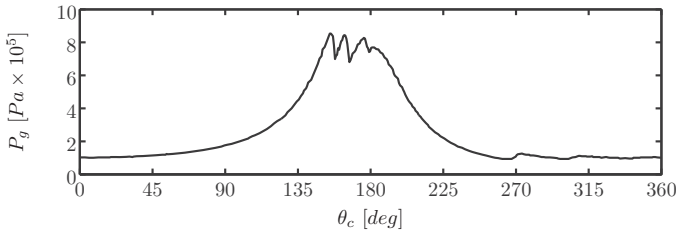

Figure 6.2: *Cylinder gas pressure - HRC (Cho and Moon, 2005).*

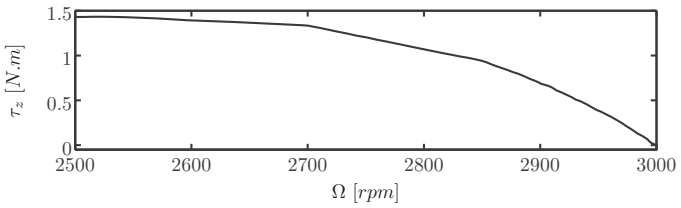

Figure 6.3: *Motor torque characteristic curve - HRC (Rigola, 2002).*

6.1.1 Results for a conventionally lubricated bearing

The numerical results presented in this section are focused on the behaviour of the upper journal bearing of the *HRC*, considering conventional hydrodynamic lubrication - *CHL*, and using the *MBD* model of case II, as described in section 2.3. Additional results using the *MBD* model of case III, including and analysis of the lower bearing performance and the influence of crank tilting oscillations on the upper bearing performance, are presented in papers [J1]*,[J2]*. Figure 6.4 shows a sketch of the compressor crankshaft illustrating the position of upper bearing, lower bearing and rotor. The numerical results were obtained by following the procedure described in chapter 5.

Using analytical solutions of Reynolds equation for *DLJB*s

For the cases when the bearing is operating under *CHL*, the most relevant results using analytical solutions of Reynolds equation are included in papers [J1]* and [J2]*. In the work presented in [J1] the behaviour of the upper bearing of the compressor is analyzed for the case when the tilting and lateral vibrations of the crankshaft are included into the model, i.e., case (III) described in section 2.3. In paper [J2], results for each one of the three approaches considered are presented. More precise estimations of the minimum *OFT* were found when using case (III), however in terms of the maximum film pressures and fluid film forces no significant differences were found compared to case (II).

*Included in appendix B

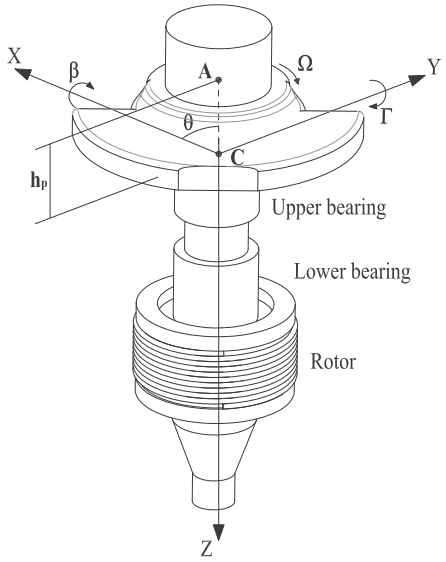

Figure 6.4: *Crankshaft of a hermetic reciprocating compressor.*

Using numerical solutions of Reynolds equation for *DLJB*s

Using the *FD* formulation of Reynolds equation for *DLJB*s, given by Eq. (3.18), and considering the case (II) for the modelling of the reciprocating mechanism, selected results are presented next. These results are complemented with results included in paper [J3]*, and in (Estupinan and Santos, 2009d). Assuming the Gümbel boundary conditions, the modified Reynolds equation is numerically solved using a *FD* scheme and the solution is computed for each time step. Thus, the fluid film pressure distribution can be obtained for each time step, and the fluid film forces in the radial and transverse directions (see ξ and η axis in Fig. 3.2) can be calculated by integrating the pressure distribution over the bearing surface as in equation (3.8).

The results obtained for the case when the upper bearing of the compressor is working with *CHL* are plotted in Figs. 6.5, 6.6 and 6.7. In Fig. 6.5a, it can be observed that the lowest minimum *OFT* obtained is approximately 3.9μm and that the lowest values occur periodically just after the *TDC* and they keep low for about 60^o of the crank rotation at each cycle. The maximum fluid film pressure and the hydrodynamic journal reaction forces are plotted in Figs. 6.5b and 6.5c respectively. It can be observed that the maximum pressure and the journal bearing forces (in the direction of the maximum loads, F_X) have a similar pattern of change, as it is expected, and the maximum values of pressure and forces are found at around the top dead centre ($\theta_c = 180^o$) at each cycle. Based on the calculation of the power losses due to the viscous frictional forces, a cyclic averaged power consumption of 1.85W was obtained as it is shown in Fig. 6.5d. Additionally, it can be seen from Fig. 6.6 that the centre of the journal goes towards the third quadrant and the orbit that is generated is reproduced periodically as long as the bearing load also changes cyclically.

The fluid film pressure distributions for three different angular positions of the crankshaft are plotted in Fig. 6.7. It can be clearly observed from this figure that the maximum oil film pressures are located in the middle plane of the bearing in the axial (width) direction, and in the range between 180^o to 225^o, in the angular direction, where the angle Θ is measured from the X-axis in clockwise direction (see Fig. 3.2).

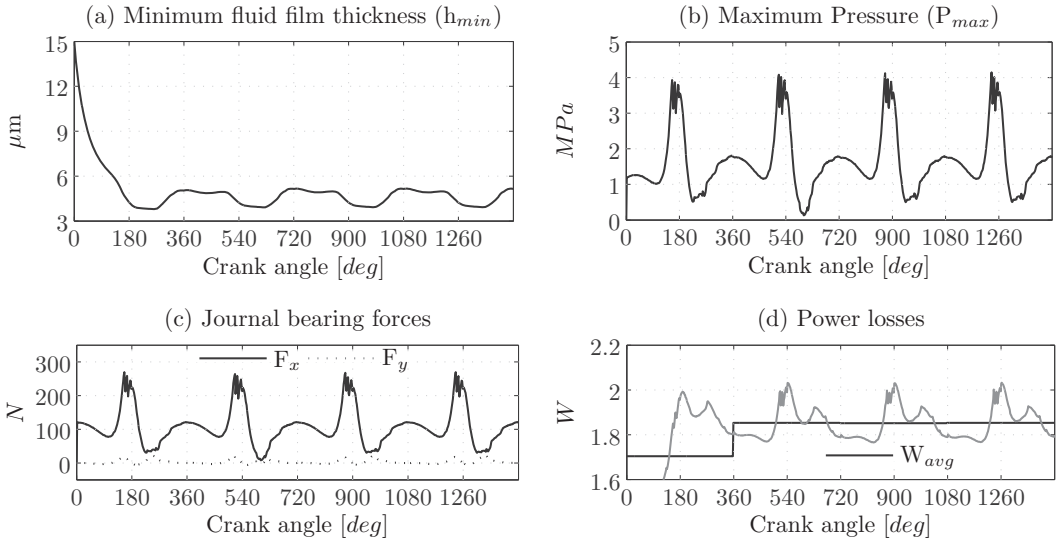

Figure 6.5: *Main upper bearing parameters - CHL.*

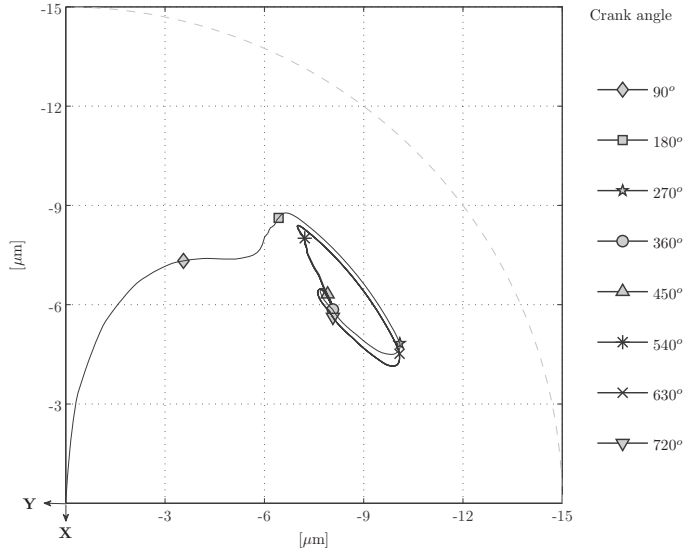

Figure 6.6: *Journal orbit - CHL.*

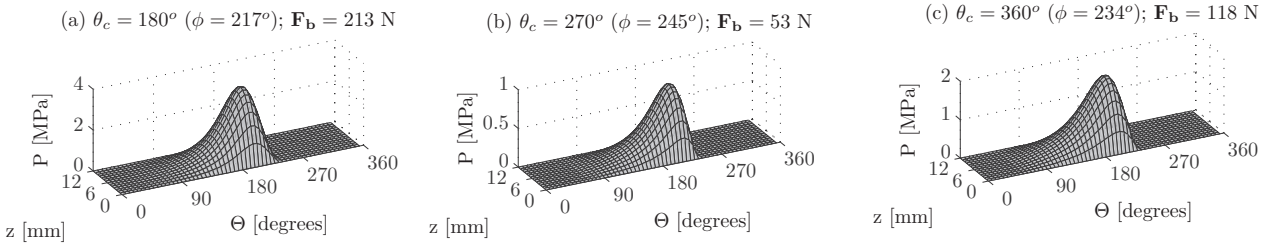

Figure 6.7: *Fluid film pressure distribution - CHL.*

6.1.2 Results for a hybridly lubricated bearing - controllable lubrication

The hybrid lubrication conditions are given by combining the *CHL* with radial oil injection. The oil is injected through orifices radially located along the bearing surface at injection pressures that may change depending on the acting bearing load, which is mainly determined by the change of gas compression forces inside the cylinder.

In order to define appropriate angular position of orifices and injection pressures for the configuration of a bearing with hybrid lubrication conditions, the results obtained for the *CHL* bearing can be used. For instance, from the plot of the orbits and the pressure distribution, it can be seen that injecting oil in the third quadrant (i.e., $180 \leq \Theta \leq 270$) may be a good choice in order to get a thicker fluid film. On the other hand, along the axial direction, the orifices should be located near the extremes of the bearing, where the injection pressures do not have to be as high as the maximum pressure taking place at the mid-plane of the bearing. In this study, the type of hybrid bearing used is a bearing with a land width ratio of 0.2, with two injection holes (symmetrically positioned in the axial direction) located at defined angular positions, as schematically illustrated in Fig. 3.2.

The variation of the angular location of the injection holes and the influence of the oil injection pressures on the hybrid bearing performance of the upper bearing of the *HRC*, was studied in paper [J3]*, and in (Estupinan and Santos, 2009d). In those studies other geometric and physical parameters were kept constant. It was found that injecting oil through orifices located at $\Theta_o = 180^o$ and $\Theta_o = 165^o$, at $P_{inj} = 2$ MPa, the minimum *OFT* could be increased up to 57% and 68% respectively, compared to the *CHL* case. These partial results show that modifying the hydrodynamic lubrication, by injecting oil pressure at specific angular positions, the *OFT* can be significantly increased. It was found that when oil is injected through orifices located in range between $165^o \leq \Theta \leq 225^o$ a significant increase of the minimum *OFT* can be obtained. On the other hand, considering that gas pressure is known and given as a function of the instantaneous crank angle, and consequently the region where the cylinder is under maximum pressure is well known, one can consider that the injection pressure may be modified actively in function of the angular position of the crankshaft. Thus, based on the obtained results for the *CHL* bearing case, the five different hybrid bearing configurations listed in Table 6.2 were proposed and evaluated when they are applied to the upper bearing compressor. Cases (a), (b) and (c) are for a bearing with oil injected through orifices located at one fixed angular position (Θ_o). Cases (d) and (e) are for a bearing with oil injected through orifices located at two fixed angular positions.

Table 6.2: *Cases of analysis - hybrid controllable lubrication.*

Case	Θ_{o_i}	**Rules of injection** (pressures in MPa)
(a)	$\Theta_o = 180^o$	$P_{inj} = 2$, for all θ_c
(b)	$\Theta_o = 180^o$	$P_{inj} = 3$, if $140^o \leq \theta_c \leq 190^o$; otherwise $P_{inj} = 1.8$
(c)	$\Theta_o = 165^o$	$P_{inj} = 3$, if $140^o \leq \theta_c \leq 190^o$; otherwise $P_{inj} = 1.8$
(d)	$\Theta_{o_1} = 150^o$	$P_{inj_1} = 2.8$, if $140^o \leq \theta_c \leq 190^o$; otherwise $P_{inj_1} = 1.0$
	$\Theta_{o_2} = 180^o$	$P_{inj_2} = 2.8$, if $140^o \leq \theta_c \leq 190^o$; otherwise $P_{inj_2} = 1.0$
(e)	$\Theta_{o_1} = 180^o$	$P_{inj_1} = 1.2$, for all θ_c
	$\Theta_{o_2} = 225^o$	$P_{inj_2} = 2.8$, if $140^o \leq \theta_c \leq 190^o$; otherwise $P_{inj_2} = 1.2$

*Included in appendix B

Figure 6.8 compares the minimum *OFT* for all the five cases considered. It can be seen that for the bearings of cases (c) and (e), the minimum *OFT* can be increased up to 90 percent, when it is compared to the minimum *OFT* of the bearing with conventional hydrodynamic lubrication. The orbits of the centre of the journal for all cases are plotted in Fig. 6.10. It can be observed that orbits of cases (c) and (e), present the best advantage compared to the conventional case. The fluid film pressure distributions for the bearing of cases (c) and (e), plotted at the crank angles $\theta_c = 180^o$ and $\theta_c = 360^o$, are shown in Figs. 6.9 and 6.11, respectively. In Fig. 6.12 can be observed that the maximum fluid film pressure found for cases (c) and (e) are lower than in the conventional lubricated bearing, and that the maximum fluid film pressures are dictated by the oil injection pressures rather than by the hydrodynamic oil film pressure. From the mechanical point of view, the fact of having lower pressures in the fluid film may be of great advantage since lower elastic deformations are expected, and therefore a smaller bearing with hybrid lubrication and a similar carrying capacity could be used instead of a conventional bearing of standard dimensions.

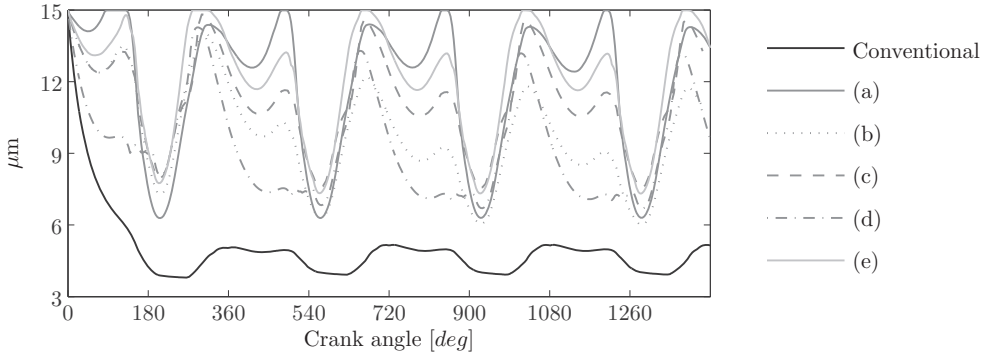

Figure 6.8: *Minimum OFT - all bearing cases.*

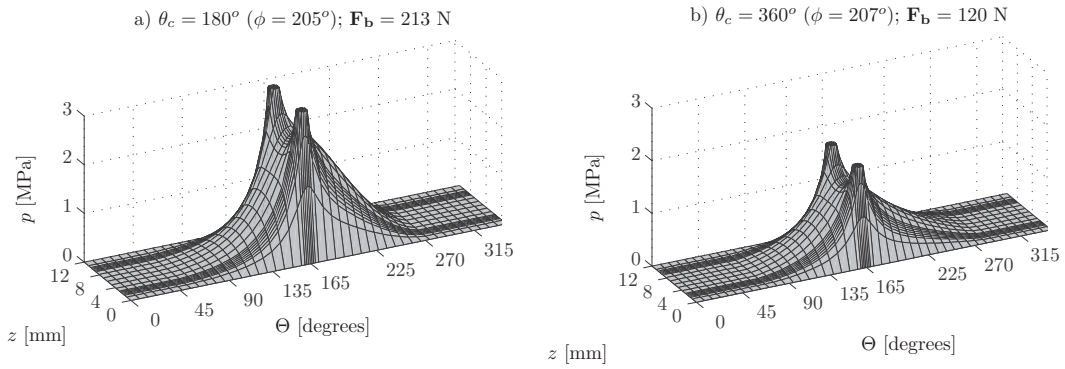

Figure 6.9: *Fluid film pressure distribution - bearing case (*c*).*

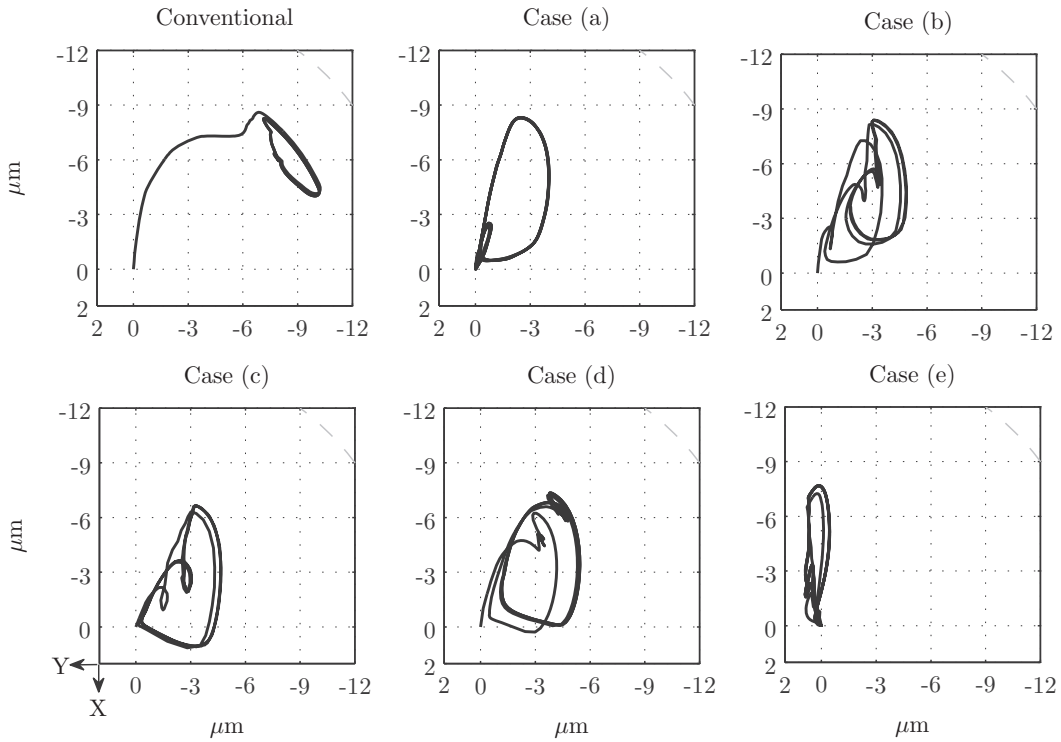

Figure 6.10: *Journal centre orbits - all bearing cases.*

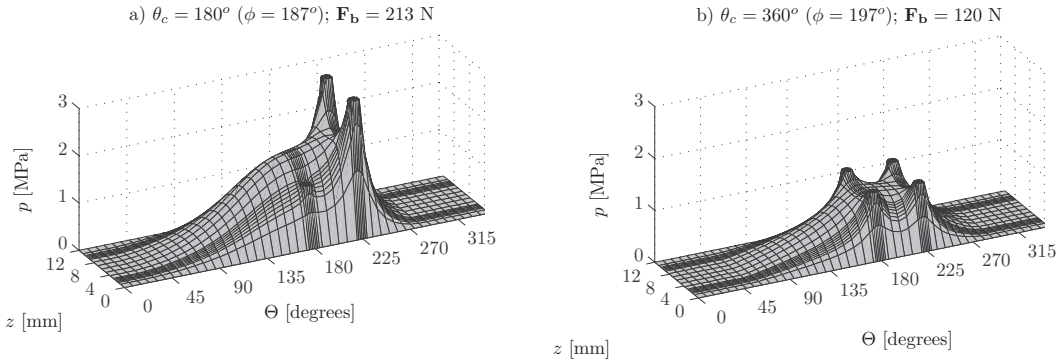

Figure 6.11: *Fluid film pressure distribution - bearing case (e).*

So far the performance of hybrid lubrication for the bearing compressor has been compared to *CHL* in terms of the minimum *OFT*, maximum fluid film pressure and size of orbits. However, in terms of the energy consumption due to viscous friction forces, it is important to evaluate the change in the friction forces and their feasibility of being reduced by using controllable radial oil injection. Thus, using Eqs. (3.14) and (3.15) the cyclic averaged power consumption was computed for each hybrid bearing case of Table 6.2, and is plotted in Fig. 6.13 together with the lowest value of the minimum *OFT* found at every crank cycle cycle. It can be seen in Fig. 6.13 that the best bearing performance is obtained for the bearing cases (c) and (e), since for those cases thicker fluid films and lower power consumptions are found, when compared to the *CHL* bearing case. Although the

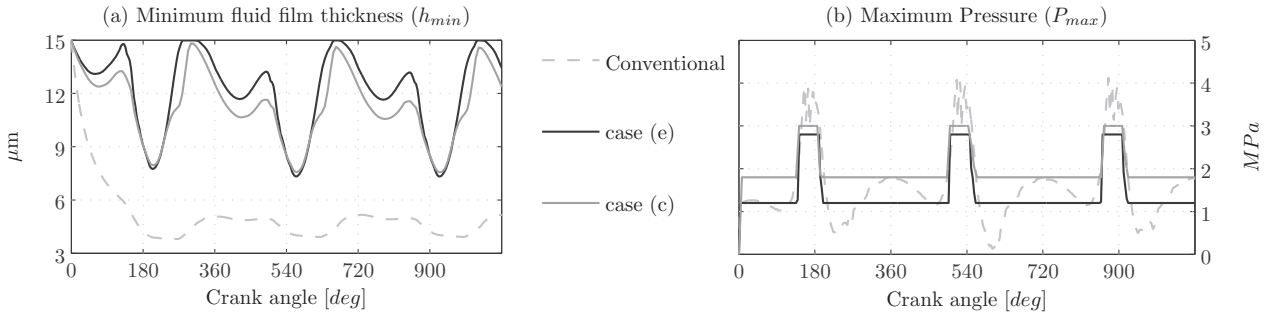

Figure 6.12: *Comparison of minimum OFT and maximum fluid film pressures.*

bearing of cases (a), (b) and (d), do not perform as good as the bearing of cases (c) and (e), they present an important advantage over the *CHL* bearing. The results obtained have shown that the minimum *OFT* in *DLJB*s can be notoriously increased (in this case up to 90% for case (c)) and at the same time the friction power losses can be reduced (in this case up to 35% for case (e)), when the conventional hydrodynamic lubrication conditions are properly modified.

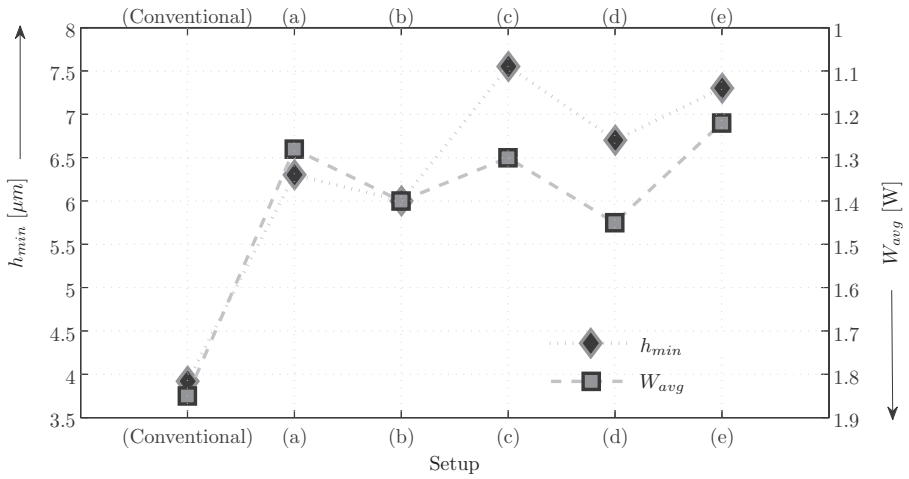

Figure 6.13: *Minimum OFT and power losses.*

6.1.3 Summary of results and conclusions

In this section the feasibility of applying controllable lubrication to the upper journal bearing of a reciprocating compressor has been demonstrated through the comparison between the results obtained for the cases with conventional hydrodynamic lubrication and hybrid lubrication. It has to be considered that the results presented are for specific hybrid journal bearing configurations, regarding to the angular position of the orifices and the injection pressures. The results have shown that the minimum *OFT* can be significantly increased when the oil injection pressures are modified as a function of the instantaneous crank angle. It was found that using for the upper bearing of a hermetic compressor a hybrid bearing with orifices located at 180^o and 225^o, the minimum *OFT*

can be increased up to 90% and the energy consumption due to the viscous forces reduced up to 35%. Thus, it was shown that by using simple oil injection pressure rules, synchronized with the instantaneous crank angle, the global performance of *DLJB* can be improved.

6.1.4 Further remarks and technological challenges

In order to define a general methodology useful to identify optimal hybrid bearing configurations for different type of bearings, more detailed studies involving the variation of other geometrical factors such as the axial land width factor, diameter and length of the orifices, bearing dimensions, etc, should be carried out. In order to be able to modify the hydrodynamics of the fluid films through radial oil injection, suitable controllable oil injection systems capable of generating the oil pressures required for the injection and with the possibility of being adapted according to the compressor operating conditions has yet to be defined. Moreover, such a system must fulfil the constraints in cost and compactness typical of these type of machines. In fact, the use of external oil pumps for the conventional lubrication system of *HRC*s is uncommon, and instead, the rotating motion of the crankshaft is used as the source for oil pumping. As previously shown, the oil injection pressures required for a controllable oil injection system in a small *HRC*s are not very high ($P_{inj} \leq$ 3MPa), therefore, the use piezoelectric hydraulic pumps for the oil injection seems to be a feasible alternative that should be considered. Although the cost of piezo-actuated systems is usually high compared to other alternatives, some attempts to develop piezohydraulic pumps of small size and low cost capable of deliver up to 4 MPa, have been made (Chapman et al., 2005). However in order to improve control pressure capabilities and operability at higher frequencies, more sophisticated piezohydraulic pumps using active valves and capable of deliver up to 8 MPa (Lee et al., 2004), may be considered, however their high cost is still an important drawback.

Although in this study a small reciprocating compressor was used to demonstrate the feasibility of applying controllable hybrid lubrication conditions to *DLJB*s, the results presented may be extended to main bearings of internal combustion engines, which will be covered in the next section.

6.2 Application to main bearings of internal combustion engines - *ICE*s

The performance of main bearings in a combustion engine affects key functions such as durability, noise and vibration. Aiming to improve engine bearing performance (i.e., to reduce friction losses and vibrations), the work presented in this section evaluates the feasibility of modifying the dynamics of the hydrodynamic fluid film in main journal bearings by using active/controllable lubrication, with oil injection pressures that can be modified depending on the operational conditions. In this study, the dynamic behaviour of the main bearing of a medium-size four-strokes *ICE* is theoretically investigated when the engine operates with controllable radial oil injection using different injection pressure control rules. Since this study is more focused on evaluating the dynamic behaviour of engine journal bearings than in the structural dynamics of the engine, and one of the main concerns is to evaluate the feasibility of applying active lubrication techniques to *DLJB*s, this theoretical investigation is based on a single-cylinder combustion engine model, where the set of motion equations of the *MBD* model are obtained following the methodology described in section 2.3. It is expected that the theoretical results obtained in this study may be extended to multiple cylinder *ICE*s, and to more complex models that could involve structural engine dynamics and combustion engine dynamics, after further experimental validations. The performance of the main engine bearing operating with controllable lubrication is compared to the performance of the bearing operating with conventional hydrodynamic lubrication, giving some insights into the minimum *OFT*, maximum fluid film pressure, viscous friction losses and maximum vibration levels. By applying controllable radial oil injection to main bearings it is expected: a) to reduce the friction losses by increasing the *OFT*; b) to reduce vibrations (i.e., result in smaller journal orbits); and c) to increase the effective carrying load area by modifying the pressure distribution profile, which can make it possible to use bearings of smaller dimensions with similar load-carrying capacity.

The results presented in this section are complemented with the material published in (Estupinan and Santos, 2008a, 2009c,a,b, 2010). The main geometric parameters of the system are given in Table 6.3 and the curves of combustion pressures inside the cylinder for three different engine speeds are shown in Fig. 6.14. Notice that in a four strokes engine every power stroke take places each two revolutions of the crankshaft.

Table 6.3: *Main geometric and physical parameters - ICE.*

Crank radius (r_c)	51.5 [mm]	Diameter of piston (D_p)	96 [mm]
Aspect ratio (λ)	0.75	Connecting rod length (l)	170 [mm] ($\bar{r}_{cr} = 120$ [mm])
Journal clearance (c_b)	30 [μm]	Masses (m_c, m_{cr}, m_p)	5, 1.5, 0.5 [kg]
Fluid viscosity at 40^oC (μ)	0.05 [Pa.s]	Angular velocity (Ω)	2400; 3000; 3600 [rpm]
Diameter of orifices (d_o)	3 [mm]	Length of orifices (l_o)	$25mm$

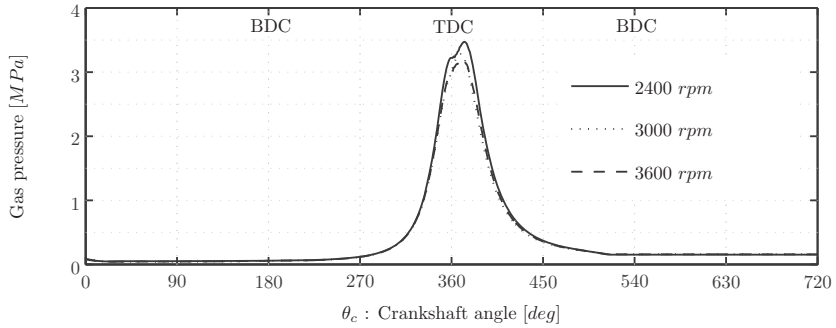

Figure 6.14: *Cylinder gas pressure - ICE.*

6.2.1 Results using conventional hydrodynamic lubrication - main engine bearing

Results obtained for the main bearing operating with conventional hydrodynamic lubrication are included in this section. The modified Reynolds equation for *DLJB*s is solved using a *FD* numerical scheme and the fluid film forces are introduced for each time step (or instantaneous crankshaft angle) into the equations of the *MBD* model of the engine, and the global system is solved as explained in chapter 5, considering case (II). The minimum *OFT*, maximum film pressures, fluid film forces and power losses, for the *CHL* bearing case, calculated for two power stroke cycles, are plotted in Fig. 6.15.

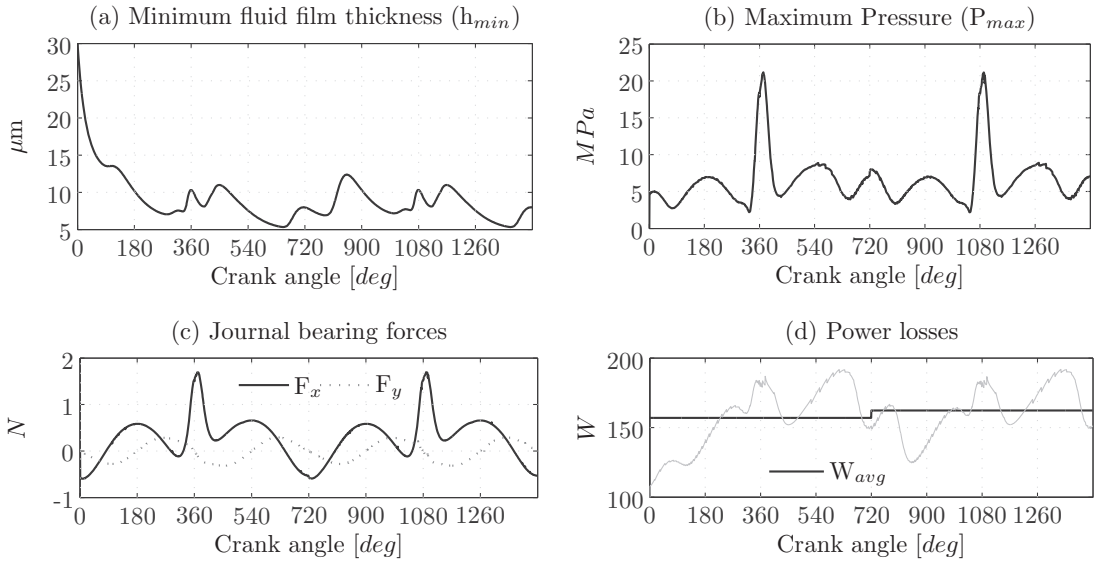

Figure 6.15: *(a) Minimum OFT; (b) Maximum film pressure - CHL ($\Omega = 3000\ rpm$).*

It can be observed in Fig. 6.15 that the lowest *OFT* is found during every cycle at around $\theta_c = 650^o$ (i.e., 70^o before *TDC* during the exhaust stroke), and it is approximately 5μm. It is clear from this figure that the behaviour of the *OFT* and the maximum fluid pressure is periodically repeated during each cycle. It is also apparent that the maximum film pressure is found at 10^o after *TDC*, during the power stroke, which coincides with the event of maximum pressure in the cylinder,

as shown in Fig. 6.14. When the power losses due to the viscous frictional force are computed, it can be observed from Fig. 6.15(d), that the instantaneous power dissipation is maximum when the minimum *OFT* is the lowest and when the maximum fluid pressure is the highest.

The fluid film pressure distributions computed at three different angular positions of the crankshaft are shown in Fig. 6.16. It should be noted that the maximum oil film pressures are located in the middle plane of the bearing in the width direction, and in the range of $180^o \leq \Theta \leq 225^o$, in the circumferential direction.

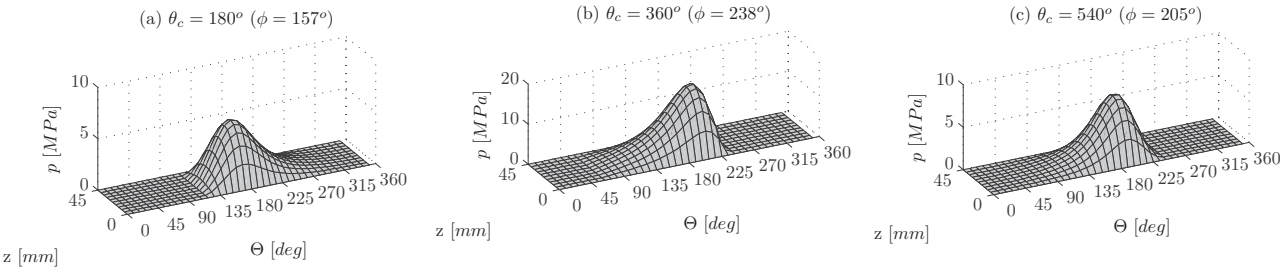

Figure 6.16: *Fluid film pressure distribution - CHL ($\Omega = 3000$ rpm).*

Fig. 6.17 shows the journal centre orbits obtained for three different crankshaft rotational speeds, whose shapes agree with typical orbits of engine journal bearings found in the literature, as illustrated in Fig. 6.18, where selected theoretical and experimental orbits are shown.

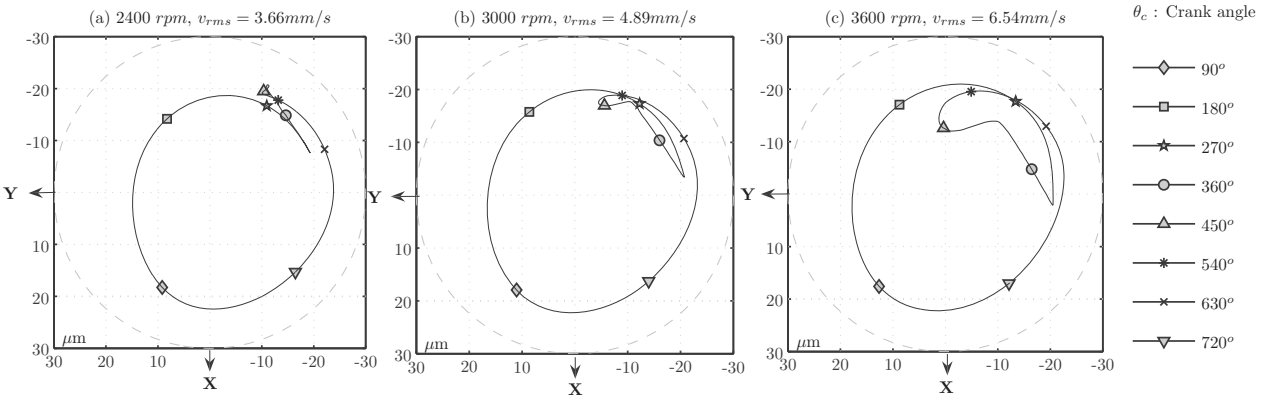

Figure 6.17: *Journal center orbits - CHL ($\Omega = 2400$; 3000; 3600 [rpm]).*

Another way of representing the movement of the journal centre throughout every combustion cycle is shown in Fig. 6.19, where eccentricity ratio and attitude angle are plotted as a function of the instantaneous crankshaft angle. Notice that eccentricity ratio and minimum *OFT* are related by: $\varepsilon = 1 - h/c_b$. Thus, the lower the minimum *OFT*, the closer the value of eccentricity ratio to 1. In Fig. 6.19, one can observe that when the highest values of ε are found the attitude angle is in the range between $180 \leq \phi \leq 270$ (i.e., third bearing quadrant), and it occurs when the crankshaft has rotated more than 360^o (i.e., during the power stroke), with the maximum value of ε found at $\theta_c = 650^o$, as confirmed from the plot of the minimum *OFT* in Fig. 6.15a.

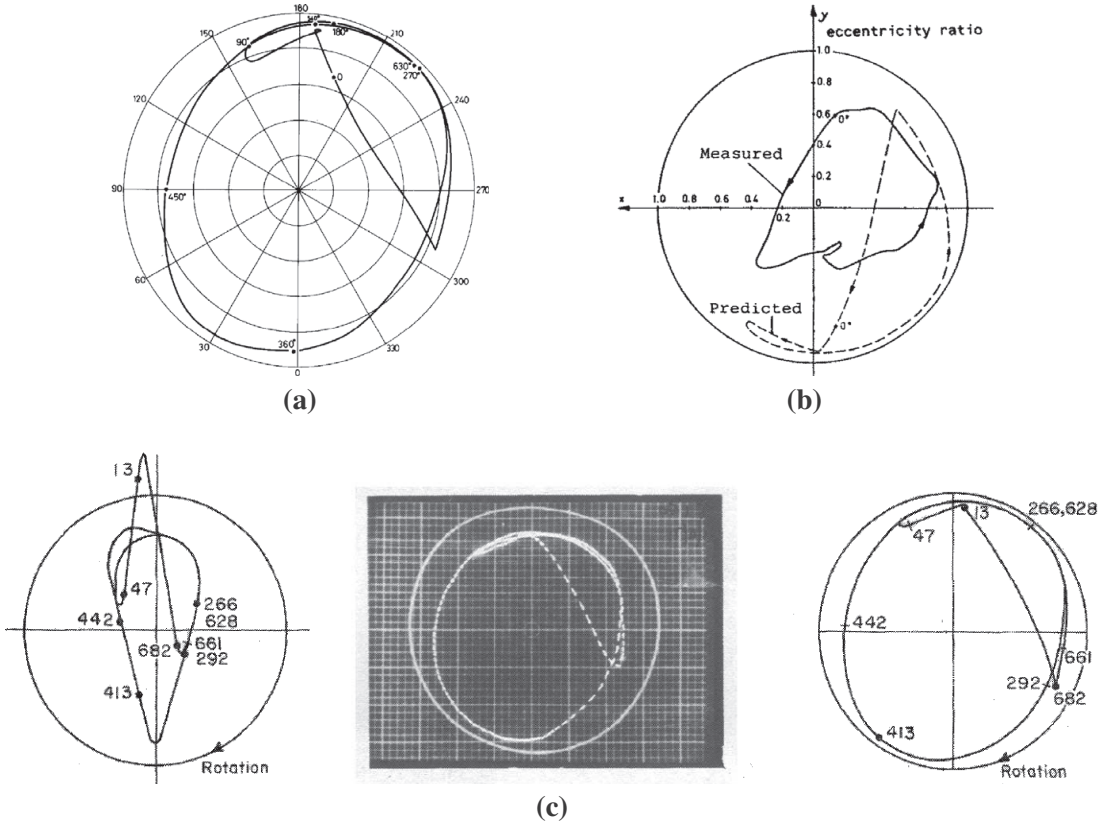

Figure 6.18: *(a) Predicted orbit for big-end connecting rod bearing of a Ruston-Hornsby 6 VEB-X engine, using a modified short bearing theory (Ritchie, 1975); (b) Predicted and measured orbit for main engine bearing of a Scania Vabis DS11 diesel engine, using a numerical FD scheme (White, 1989); (c) left: Dynamic load cycle acting on big-end bearing of a 6VEB engine; center: measured orbit; right: predicted orbit using a semi-analytical method of solution (Dede and Holmes, 1984).*

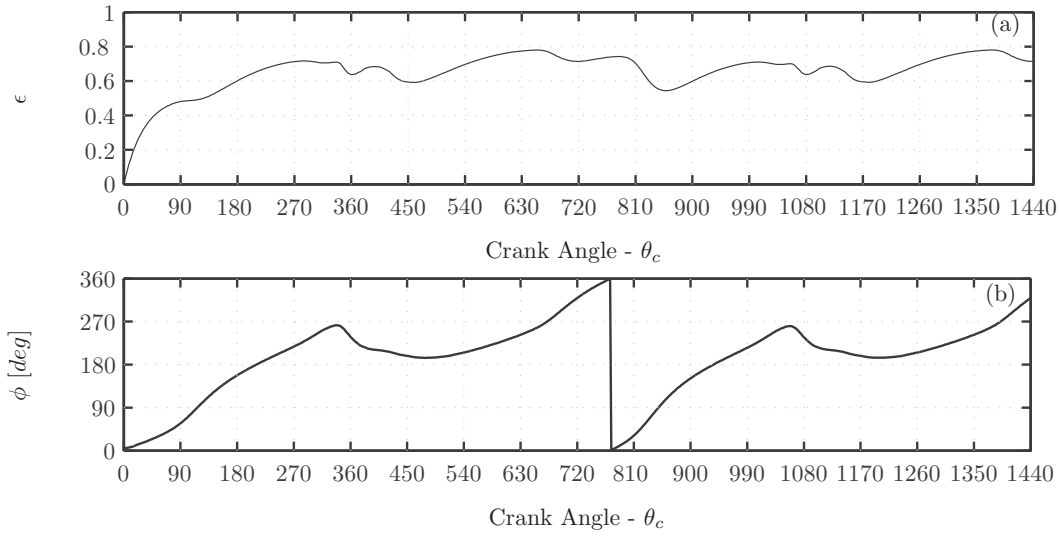

Figure 6.19: *(a) ε: Eccentricity ratio; (b) ϕ: Attitude angle - CHL ($\Omega = 3000$ rpm).*

6.2.2 Results using controllable hybrid lubrication - main engine bearing

Aiming to increase film thickness and consequently to reduce maximum film pressures and viscous friction forces, by means of using radial oil injection, adequate bearing configurations have to be defined. The results obtained previously for the conventionally lubricated main engine bearing can be initially used as a guide to identify convenient locations for the oil injection orifices as well as to define suitable values for the oil injection pressures. For instance, from the plots of journal orbits and pressure distributions obtained for the *CHL* bearing case, it can be inferred that by injecting oil at higher pressures than the *CHL* one, through orifices radially located along the third bearing quadrant (i.e., $180 \leq \Theta \leq 270$), the hydrodynamic fluid film may be advantageously modified, in other words, the minimum *OFT* may be increased. On the other hand, as in typical hybrid bearing applications, along the width of the bearing the orifices should be located near the edges of the bearing, in order to be able to inject oil at lower injection pressures than the maximum hydrodynamic film pressures (found at the middle plane of the bearing). Taking these criteria in consideration hybrid bearings with eight different geometric configurations are evaluated in this work. The main difference between them is the angular location of the orifices for the radial oil injection. These bearing configurations have been named "bearing cases", going from case *a* to case *h*, as shown in Table 6.4. In all bearing cases, a pair of orifices are located at each angular position, and they are symmetrically positioned along the axial direction, using a constant axial land ratio of $\bar{a} = 0.2$. In cases *f*, *g* and *h* oil is injected through two pairs of orifices, located at two different angular positions, as indicated in Table 6.4. Additionally, the following bearing parameters are used: bearing aspect ratio: $\lambda = 0.75$; diameter of orifices: $d_o = 3mm$; orifice length: $l_o = 25mm$.

Table 6.4: *Geometric bearing configurations - angular location of orifices.*

	Bearing cases							
	(a)	(b)	(c)	(d)	(e)	(f)	(g)	(h)
Θ_{o_1}	180^o	210^o	225^o	240^o	270^o	180^o	225	180
Θ_{o_2}						225^o	270	270

Pressure control rules

From the results obtained for the *CHL* case, it was observed that under steady operational conditions, the main bearing operational parameters (e.g., film thickness, maximum film pressures), tend to have a periodic behaviour, with the periodicity dictated by the frequency of the power strokes in the engine. Considering that the main loads acting on the bearings behave periodically, and in order to enhance bearing performance (e.g., as to increase minimum *OFT*, and to reduce maximum film pressures), several strategies for controlling the pressures of radial oil injection, given as a function of the instantaneous crank angle or the journal centre position, were numerically tested in this work. Figure 6.20, illustrates graphically the control pressure rules, from which some numerical results for the bearing configurations of Table 6.4 are presented in this section. In the following, a brief explanation of each strategy of control is given:

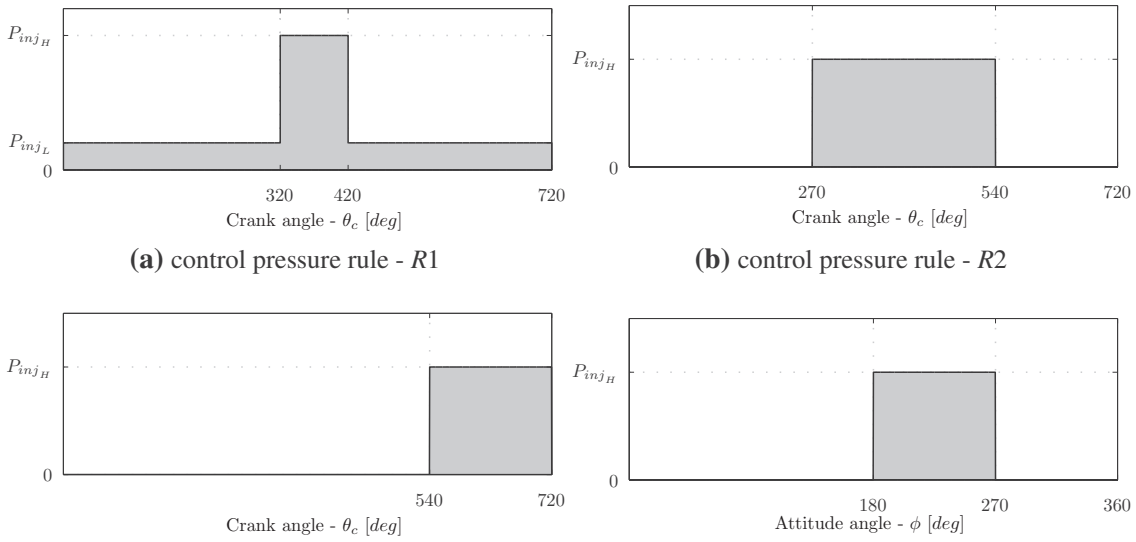

(a) control pressure rule - $R1$ **(b)** control pressure rule - $R2$

(c) control pressure rule - $R3$ **(d)** control pressure rule - $R4$

Figure 6.20: *Rules for controlling oil injection pressures.*

Pressure control rule $R1$**,** using this strategy, oil is injected through the orifices at two different pressure values depending on the crankshaft angle. A higher oil pressure P_{inj_H} is used for the injection during the crank angular interval at which the combustion forces inside the cylinder are higher (i.e., $320 \leq \theta_c \leq 420$ [deg]), as seen in Fig. 6.14. In order to keep a thicker *OFT* throughout the entire cycle, oil is injected at a lower pressure P_{inj_L} (but higher than the *CHL* one) during the rest of the crank cycle, as illustrated in Fig. 6.20a.

Pressure control rule $R2$**,** using this strategy, oil is injected at the pressure P_{inj_H} during the crank angular interval at which the maximum combustion forces are found at every crank cycle, but in contrast to $R1$ oil is injected during a wider angular interval at every cycle (i.e., $270 \leq \theta_c \leq 540$ [deg]), and there is not oil injection at a lower pressure during the rest of the crank cycle, as illustrated in Fig. 6.20b.

Pressure control rule $R3$**,** this strategy aims to increase the minimum *OFT* by injecting oil during the crank angular interval at which the lowest values of *OFT* were found for the *CHL* bearing case. Thus, using this strategy oil is injected at the pressure P_{inj_H} during the crank angular interval $540 \leq \theta_c \leq 720$ [deg], as illustrated in Fig. 6.20c.

Pressure control rule $R4$**,** in contrast to the previous pressure control strategies proposed, in this strategy oil injection is controlled as a function of the attitude angle. It was found for the *CHL* bearing case that the centre of the journal tends to be mostly positioned inside the third quadrant of the bearing ($180 \leq \phi \leq 270$) where also the lowest *OFT* during every cycle is found, as it can be noticed in the curves of eccentricity and attitude angle in Fig. 6.19, and in the orbits shown in Fig. 6.17. Thus, using control pressure rule $R4$, oil is injected at the pressure P_{inj_H} when the

instantaneous position of the journal centre is in the third quadrant of the bearing (i.e., when $180 \leq \phi \leq 270$, according to Fig. 4.3).

Evaluation of bearing configurations and pressure control rules.

In this section, the hybrid bearing performance for the bearing configurations listed in Table 6.4, using the control pressure rules $R1$ to $R4$ shown in Fig. 6.20, is analyzed through results obtained from numerical simulations. The numerical tests were carried out considering different values for the oil injection pressures. In order to facilitate the comparison between the hybrid bearing cases to the *CHL* case, the following dimensionless variables are used for the plots:

$$\bar{h}_{min} = \frac{h_{min}}{c_b}; \quad \bar{p}_{max} = \frac{p_{max}}{p_{max}^{CHL}}; \quad \bar{W}_{avg} = \frac{W_{avg}}{W_{avg}^{CHL}} \tag{6.1}$$

where $p_{max}^{CHL} = 17.7$ MPa and $W_{avg}^{CHL} = 172$ W, are the values of the highest pressure and cyclic averaged power consumption, respectively, for the conventionally hydrodynamic lubricated bearing case. For all bearing geometric configurations and control pressure rules, Figs. 6.21, 6.22 and 6.23 show the behaviour of lowest *OFT*, maximum film pressure and cyclic averaged power consumption, respectively, as a function of the oil injection pressures P_{inj_H}.

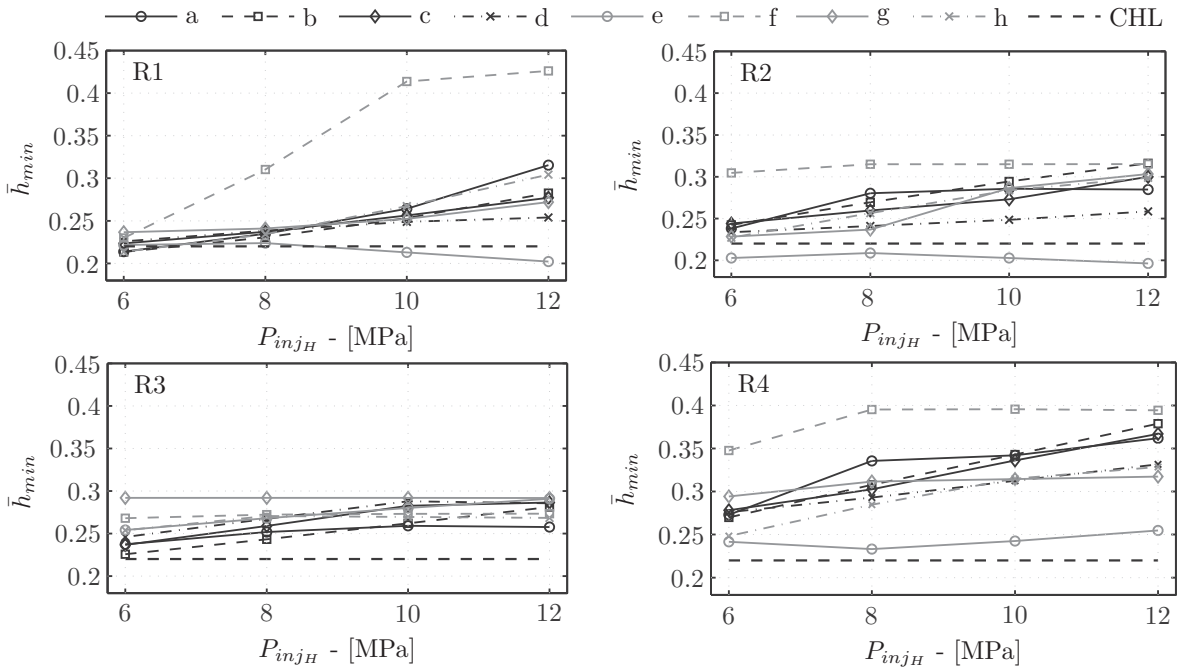

Figure 6.21: *Minimum OFT - all bearing cases.*

In terms of the minimum *OFT*, it can be observed from Fig. 6.21 that the lowest *OFT*s are found for the bearing of case *f* using the pressure control rules $R1$, $R2$ and $R4$. Although the bearing configuration of case *a* is not as good as case *f*, it also presents a good advantage compared to the *CHL* case. On the other hand, it can be seen that the bearing of case *e* is not a good configuration,

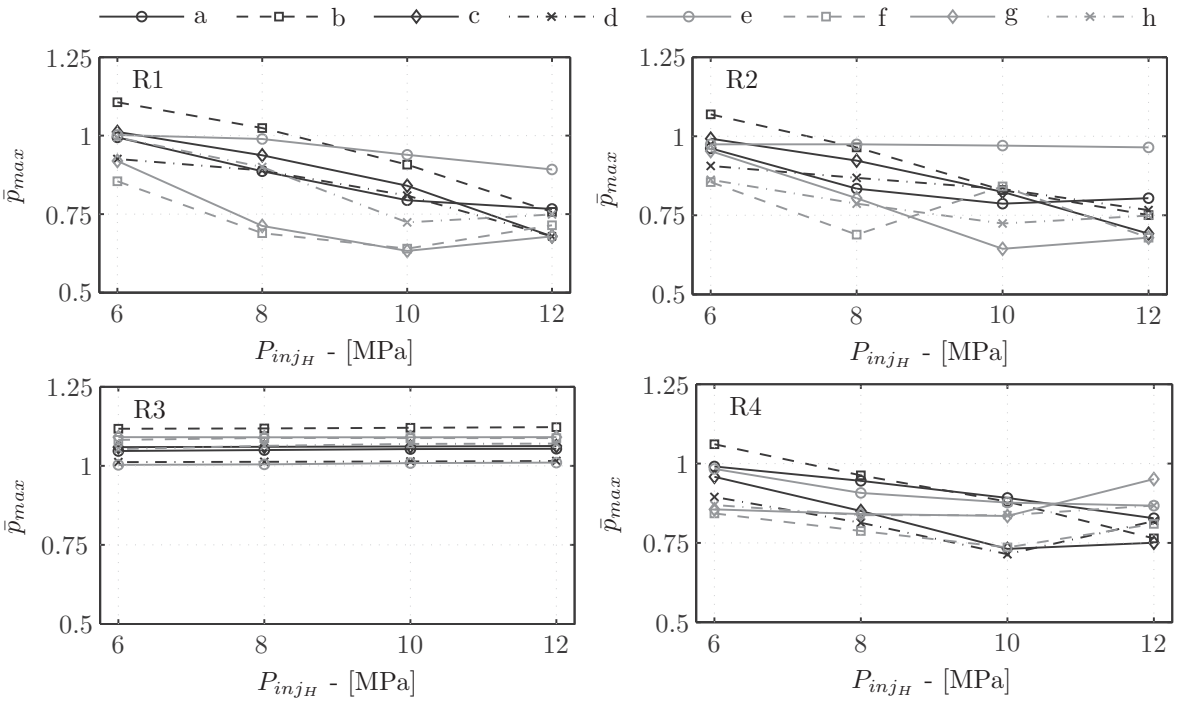

Figure 6.22: *Maximum fluid film pressure - all bearing cases.*

since the minimum *OFT* can be even reduced, as shown in the graphs for control pressure rules *R*1 and *R*2.

In terms of the maximum film pressures, it can be seen in Fig. 6.22 that in most of the hybrid bearing cases analyzed, the maximum oil film pressures found are lower than in the *CHL* case. When control pressure rule *R*3 is considered, an increase in the maximum film pressure can be noticed. In cases where *CHL* is properly combined with oil injection, the oil film pressure is built up over a wider bearing area, requiring consequently lower pressures to support the same bearing load conditions.

In terms of the energy consumption due to the viscous friction forces, it can be seen in Fig. 6.23, that a reduction up to 40% can be reached compared to the *CHL* bearing case (e.g., as in case *f* with control rule *R*1).

So far, the analysis have been made with focus on the behaviour of global values of main bearing parameters, comparing between different hybrid bearing cases based on the maximum or minimum values found. Such an analysis helps to identify which cases present advantage compared to the others. However, it is also relevant to know main bearing performance during every crankshaft cycle, in order to identify, for instance, possibilities for improvement. Figure 6.24 shows the orbits for the bearing configurations *a* and *f* using $P_{inj_H} = 8$ MPa. It can be noticed in this figure that for the hybrid bearing cases analyzed, the orbital movements of the journal centre have lower eccentricity when compared to the *CHL* bearing case (plotted in light gray colour in the figure). The orbits obtained for bearing case *f* present a more significant change in the orbital shape than the orbits of bearing case *a*, when compared to the *CHL* bearing case.

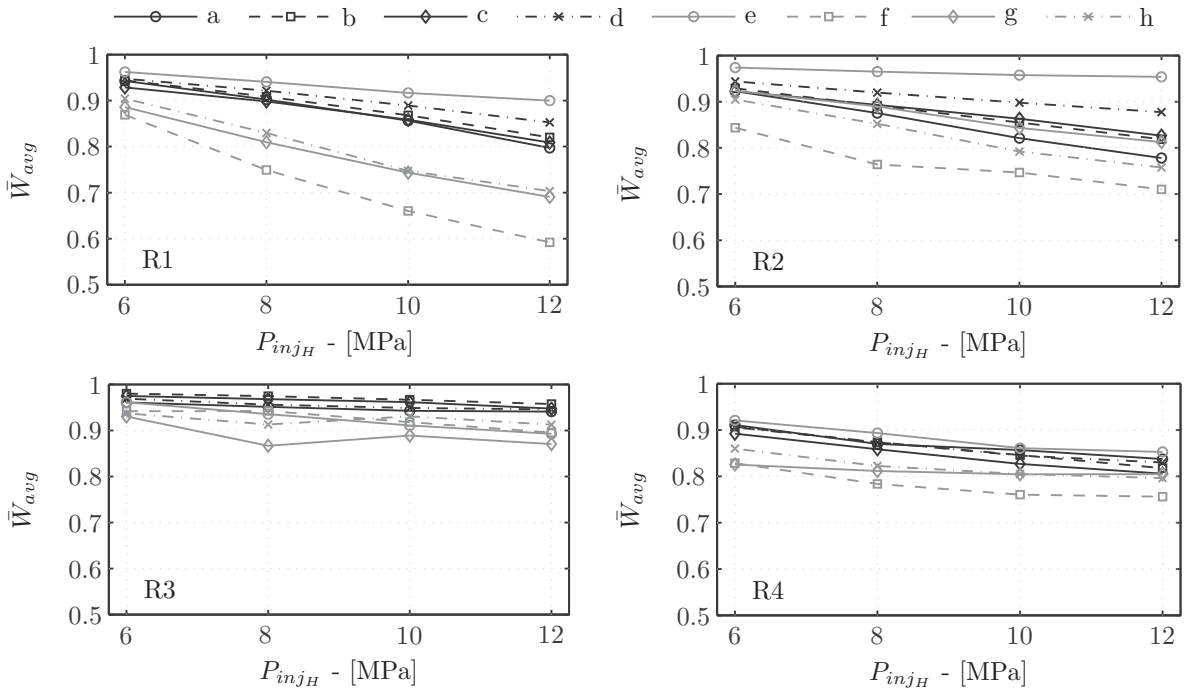

Figure 6.23: *Cyclic averaged power consumption - all cases.*

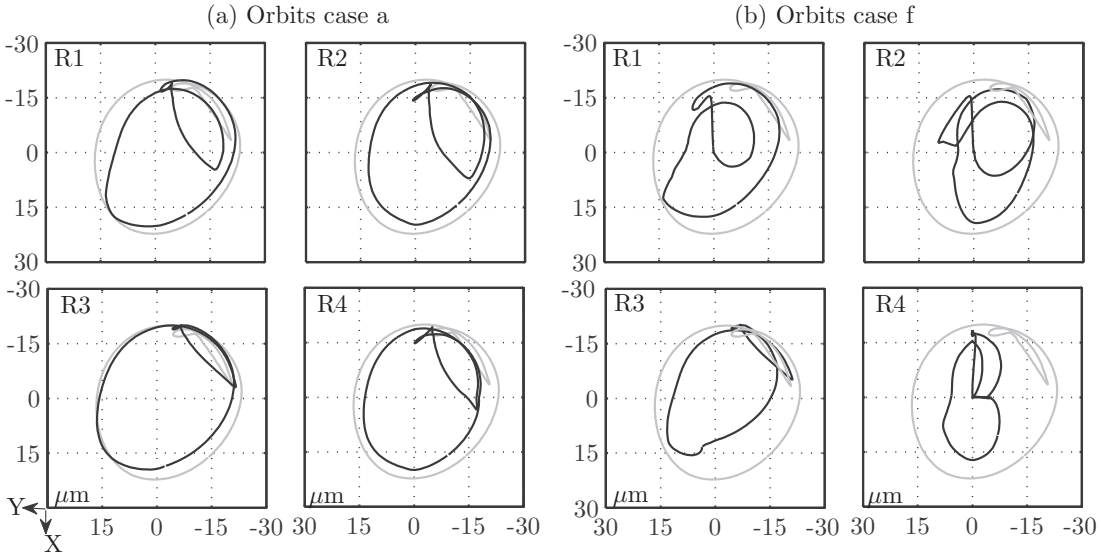

Figure 6.24: *Journal orbits - bearing cases* a *and* f*, using* $P_{inj_H} = 8$ *MPa (The light gray colour corresponds to the orbit for the CHL bearing case).*

Figure 6.25 shows minimum *OFT* and maximum film pressure as a function of the crank angle, computed during two power strokes, and considering case *f*-*R*1. It can be observed that when $P_{inj_H} = 6$ MPa, the lowest value of $\bar{h}$ is hardly modified, however, when P_{inj_H} becomes higher a significant change in the minimum *OFT* compared to the *CHL* bearing case can be obtained, and maximum film pressures are lowered.

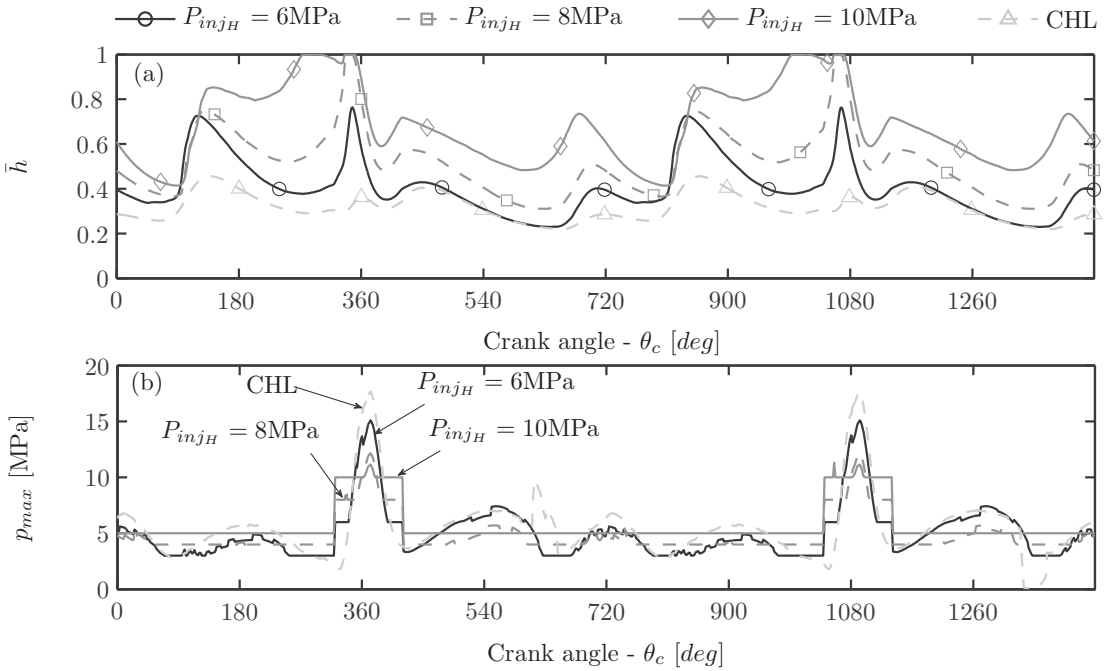

Figure 6.25: *(a) Minimum OFT; (b) Maximum film pressure - bearing case f-R*1.

In order to visualize how each pressure control rule can differently modify minimum *OFT* and maximum film pressure, Fig. 6.26 shows the results obtained for hybrid bearing case *a* using control pressure rules *R*1 to *R*4. It can be observed in Fig. 6.26 that for bearing case *a*, the less significant change in *OFT* is found when control pressure rule *R*3 is used. Likewise, it can be noticed that the most significant change in *OFT*, in the interval $540 \leq \theta_c \leq 720$ (i.e., where the lowest *OFT* was found for the *CHL* bearing case), is found when control pressure rules *R*2 and *R*4 are used. However, it can also be noticed that using control pressure rule *R*4 demands more oil injection events per cycle, and higher film pressures than the *CHL* during several crank angle intervals per cycle.

In order to visualize how the pressure distribution of the fluid film is influenced by the location of the injection orifices along the bearing surface, Fig. 6.27 shows the film pressure distribution for all cases using control pressure rule *R*2. The film pressure distributions are computed at $\theta_c = 360^o$, that is, in the region where maximum load is acting on the bearing, and therefore, high fluid film pressures to compensate such loads are expected. From Fig. 6.27 one can noticed that the pressure distributions obtained for bearing configurations of cases *d* and *e* do not have an important effect on the modification of the *CHL* pressure distribution. In fact it was shown in Fig. 6.21 that using bearing case *e*-*R*2, the minimum *OFT* is lower than in the *CHL* bearing case. From all hybrid bearing cases, it can be seen that the pressure distributions are more uniformly distributed for cases

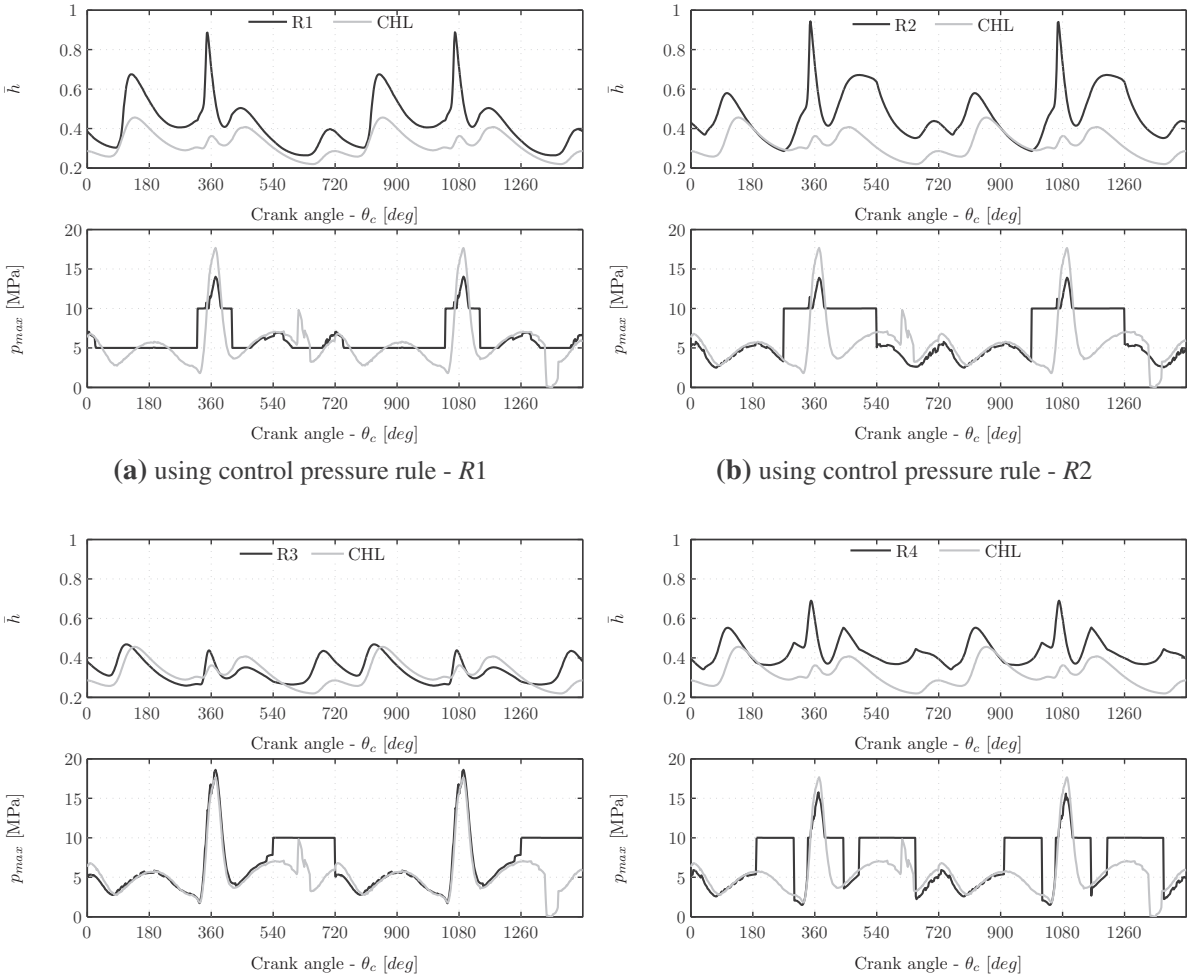

(a) using control pressure rule - *R*1

(b) using control pressure rule - *R*2

(c) using control pressure rule - *R*3

(d) using control pressure rule - *R*4

Figure 6.26: *Minimum OFT and maximum film pressures for bearing case* a*, using different control pressure rules ($P_{inj_H} = 10$ MPa; $P_{inj_L} = 5$ MPa).*

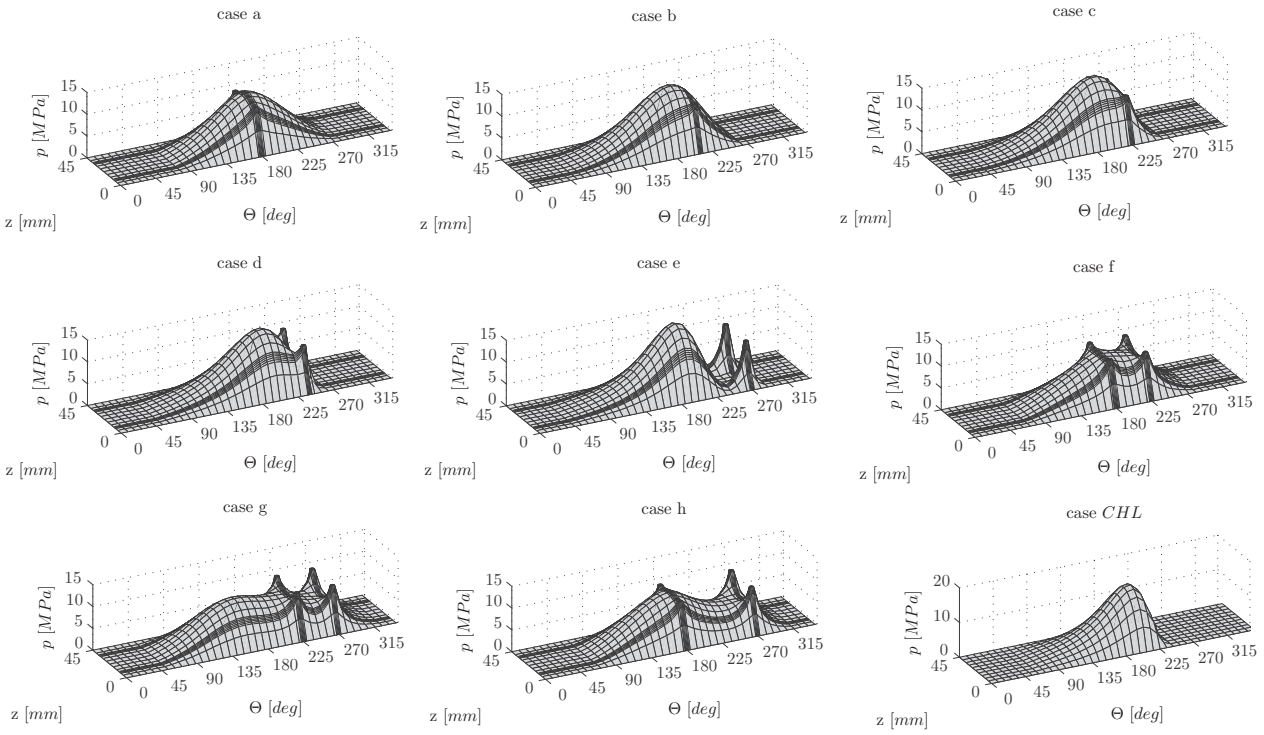

Figure 6.27: *Fluid film pressure distribution at $\theta_c = 360^o$ - all cases using control pressure rule R2 ($P_{inj_H} =$ 10 MPa).*

a, *f* and *h*. In order to illustrate how the pressure distribution of a hybrid bearing varies during each engine combustion cycle, due to the bearing load condition and to the injection pressure rules, Figs. 6.28 and 6.29 show the pressure distributions for cases *a* and *f*, calculated at three different crankshaft angles ($\theta_c = 180^o$; 360^o and 540^o), using control pressure rules *R*1 and *R*4. As expected, the higher fluid film pressures are found for $\theta_c \cong 360^o$ (i.e., near *TDC* during the power stroke at each combustion cycle). Although the pressure distributions obtained are different depending on each hybrid bearing case and on the control pressure rule selected, the fluid film forces have to equilibrate the load acting on the bearing at any time during each cycle. This can be noticed from Figs. 6.28 and 6.29, which shows the computed bearing force F_b for each case, which is calculated by integrating the pressure distribution along the bearing surface, obtaining equivalent fluid film bearing forces (F_b) for all cases.

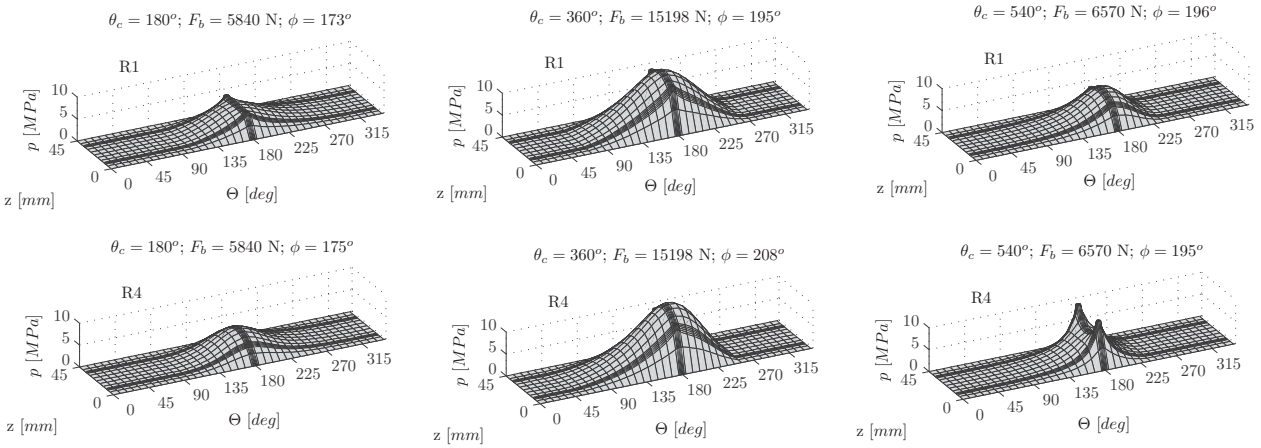

Figure 6.28: *Fluid film pressure distributions at* $\theta_c = 180^o;360^o;540^o$ *- bearing case a, using* $R1$ *and* $R4$ *(*$P_{inj_H} = 10$ *MPa;* $P_{inj_L} = 5$ *MPa).*

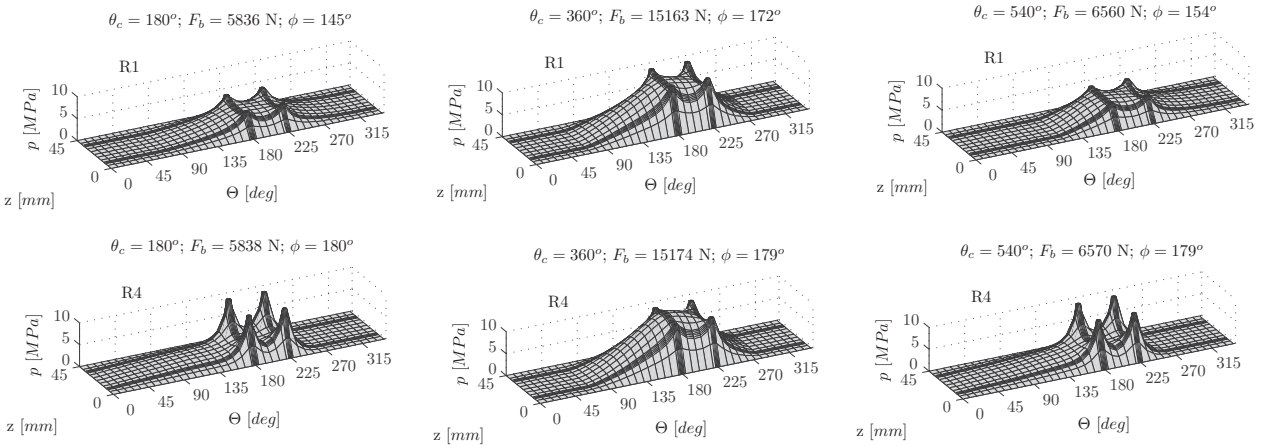

Figure 6.29: *Fluid film pressure distributions at* $\theta_c = 180^o;360^o;540^o$ *- bearing case f, using* $R1$ *and* $R4$ *(*$P_{inj_H} = 10$ *MPa;* $P_{inj_L} = 5$ *MPa).*

According to the results presented until now, the main findings can be summarized as follows:

- In terms of the minimum *OFT*, hybrid bearing of case *f* using control pressure rules $R1$ and $R4$ presents the best advantage compared to the other hybrid bearing cases considered in the analysis. Among all cases, the largest increase in the minimum *OFT* is obtained for cases f-$R1$ and f-$R4$ using $P_{inj_H} = 10$ MPa and $P_{inj_H} = 8$ MPa, respectively, as shown in Fig. 6.21.

- Hybrid bearings of cases *d* and *e* present the less convenient configuration, since an almost negligible reduction in maximum film pressures and even some increase in the minimum *OFT* compared to the *CHL* case were found.

- Although control pressure rule $R3$ was initially considered for the analysis based on the idea of injecting oil during the crank angular interval at which the lowest *OFT* for the *CHL* case was found, the results have shown that using $R3$ the lowest *OFT* can be increased, but at

expenses of reducing *OFT* at other times during each cycle, as shown in Fig. 6.26cc. It was also found that using *R*3 maximum film pressures can be even increased compared to the *CHL* bearing case.

- The energy consumption due to friction viscous forces can be lowered up to 40%, as found for hybrid bearing case *f*-*R*1. It was shown in Fig. 6.23 that the higher the injection pressures the lower the viscous friction forces. However one has to consider that using higher injection pressure demands higher energy requirements from the injection system. Thus, if $\bar{W}_a vg$ is compared for cases *f*-*R*1 and *f*-*R*2, as shown in Fig. 6.23, one can noticed that the same reduction in energy is obtained, however, using *R*2 less energy is required for the injection, since the oil is injected only during a short interval at each cycle, while using *R*1 oil is injected throughout the entire cycle, as illustrated in Fig. 6.20.

- Although control pressure rule *R*4 gives good performance in terms of increasing minimum *OFT*, particularly for cases *a* and *f*, Fig. 6.26d also shows that oil injection is required during more time throughout each crankshaft cycle.

Results using pressure control rule *R*1

Selected results using control pressure rule *R*1 and using oil injection pressures that were adjusted after several numerical simulations, are presented here. Extended results are included in (Estupinan and Santos, 2008a, 2009a). The minimum *OFT* and maximum film pressures for the *CHL* bearing case and for bearing configurations *a* and *f* are plotted as a function of the crank angle during two power strokes in Fig. 6.30. It can be seen in this figure that the predicted minimum *OFT* for bearing cases *a* and *f* are significantly thicker than those of the *CHL* bearing case. It can also be noted that the maximum values of the film pressures for bearing cases *a* and *f*, are smaller than those of the *CHL* bearing case, and that they correspond to the maximum values of oil injection pressures during each cycle. Figure 6.31 shows a plot of the film pressure distribution for bearing case *f*, plotted at three different crank angles.

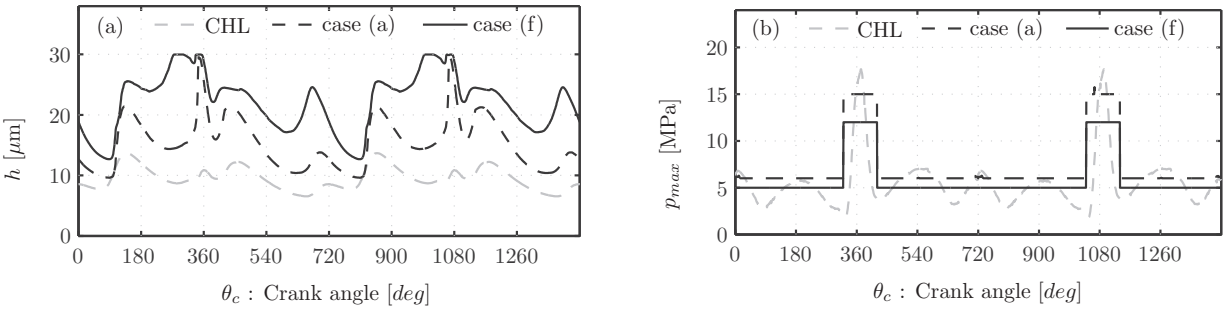

Figure 6.30: *(a) Minimum OFT; (b) Maximum pressure - controllable lubrication using R*1 *($P_{inj_{H/L}} = 15/6$ MPa for bearing case a; $P_{inj_{H/L}} = 12/5$ MPa for bearing case f).*

The predicted journal centre orbits using control pressure rule *R*1 and for two different operational speeds are shown in Fig. 6.32. In the same plots the orbits for the *CHL* case are shown in

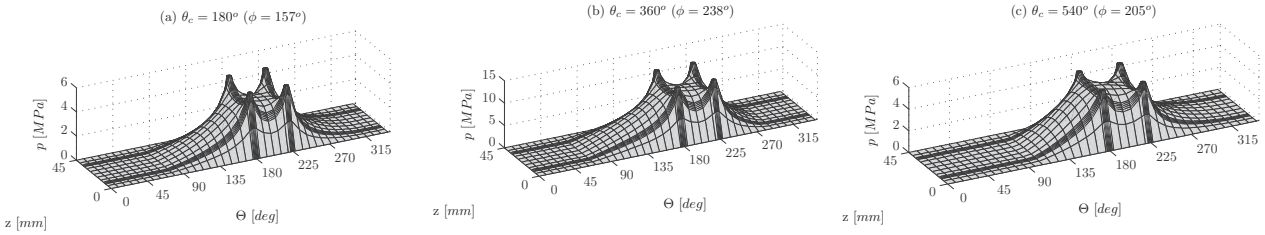

Figure 6.31: *Fluid pressure distribution - case f: controllable lubrication using R*1 *($P_{inj_{H/L}} = 12/5$ MPa).*

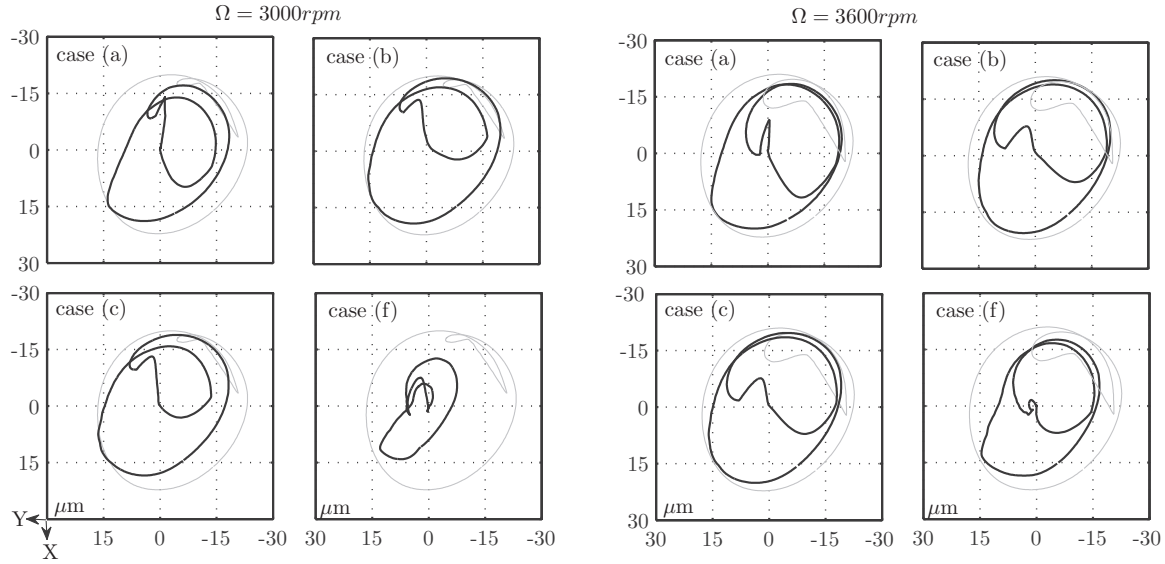

Figure 6.32: *Journal center orbits - controllable lubrication using R*1 *($P_{inj_{H/L}} = 15/6$ MPa for bearing cases a,b and c; $P_{inj_{H/L}} = 12/5$ MPa for bearing case f).*

light gray colour. It can be noticed that the size of the orbits using controllable hybrid lubrication is smaller compared to the *CHL* case, reducing the possibility of having solid contact between the journal surface and the bearing surface. It can also be observed that the orbits of bearing configurations *a* and *f* present the best advantage compared to the other two cases.

The values of the main global parameters that describe bearing performance for some of the bearing configurations tested using control rule *R*1, are plotted in Fig. 6.33. It can be seen from this figure that the bearing of case *f* exhibits the best bearing performance compared to the other cases analyzed. In this case, the cyclic power consumption considers the power dissipation due only to the viscous friction forces f_{vf} in the journal bearing, as presented in Eqs. (3.14) and (3.15).

It can be seen from the previous results that by applying controllable radial oil injection to main journal bearings: a) the *OFT* can be significantly increased (by up to 90% in case e, as shown in Fig. 6.30a); b) the maximum fluid film pressure is given by the oil injection pressures rather than by the hydrodynamic fluid film pressure, as shown in Fig. 6.30b; c) the global vibration levels can be reduced and the power consumption due to the viscous frictional forces can be reduced, as shown in Fig. 6.33. In summary, one can say that by having a thicker *OFT*, lower viscous friction losses are expected, together with a reduced possibility of solid contact between solid surfaces. Moreover, by

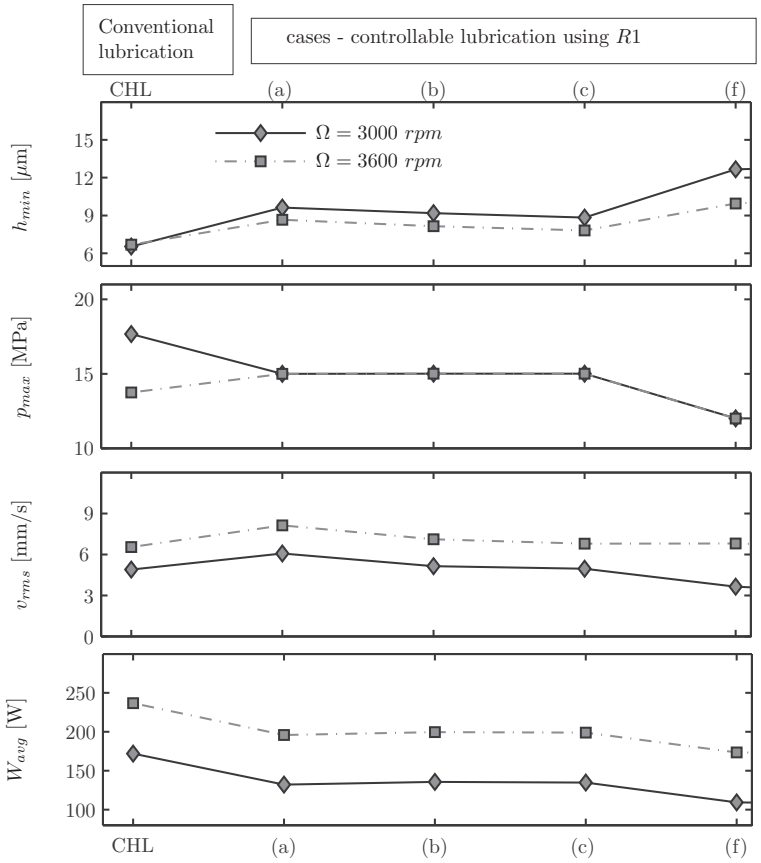

Figure 6.33: *Minimum OFT (h_{min}) - maximum pressure (p_{max}) - journal vibration (v_{rms}) - cyclic power consumption (W_{avg}), using $R1$.*

achieving a reduction in the maximum oil film pressures while keeping the same bearing carrying-load capacity, the mechanical stresses over the bearing surface may be lowered.

6.2.3 Dynamics of oil injection system coupled to the hybrid bearing problem

In the previous sections of this chapter, the numerical results presented were obtained for different pre-defined control pressure rules without including the dynamics of the oil injection system. When the dynamics of the injection system are coupled to the dynamics of the bearing, those constant predefined oil injection pressures are influenced by the dynamics of the injectors. Using a piezo-actuated injection system, as described in section 4.2.1, selected numerical results are presented in this section, including some comparisons to the results found in the previous section and to the *CHL* bearing case. The main parameters of the piezo-actuated injector used for the numerical simulations are given in Table 6.5. For the piezo-actuator, a square voltage signal was assumed to be applied to the piezostack, considering maximum voltage of $v_{pz_{max}} = 200$ V during the injections, and minimum voltage equal to zero.

Table 6.5: *Main parameters of piezo-actuated oil injector.*

Area of piezoelectric stack (A_{pz})	30 [mm^2]
Length of piezoelectric stack (L_{pz})	40 [mm]
Number of layers (N_{pz})	100
Feeding voltage (v_{pz})	200 [V]
Elastic modulus (E_{pz})	44 [GPa]
Piezoelectric coupling coefficient (d_{33})	650 [pC/N]
Dielectric permitivity (ε_{33})	6200 [pF/m]
Combined stiffness push rod and valve springs (k_{s1})	46 [kN/m]
Servo piston spring stiffness coefficient (k_{s2})	30 [kN/m]
Viscous friction coefficient of valve-piston (c_{s1})	60 [Ns/m]
Viscous friction coefficient of needle injector (c_{s2})	10 [Ns/m]
Cross section area of the control valve (A_{cv})	20 [mm^2]
Equivalent mass of control valve cluster (m_{s1})	10 [g]
Equivalent mass of needle valve and control piston (m_{s2})	11.2 [g]
Cross section of needle seat injector (A_{ns})	8 [mm^2]
Cross section of Needle valve injector (A_{nv})	25 [mm^2]
Oil density (ρ)	900 [kg/m^3]

Dynamics of piezo-actuated injector

In order to illustrate the injector behaviour in terms of the control valve displacements (determined by the displacement of the piezostack), the displacements of the needle injector, and the variation of the injection pressure as a function of crankshaft angle, Fig. 6.34 shows the results obtained for case *a* using the control pressure rules *R*1 to *R*4. It can be observed that the displacement of the piezostack, the movement of the needle injector, and the oil injection events are synchronized. When the piezoelectric stack is activated by the action of a feeding voltage, the displacement of the free end of the piezostack (x_{pz}) causes the control valve to open. Consequently a pressure drop in the control chamber occurs and causes the needle injector to move upwards (x_{iv}) and to be opened, when the pressure difference overcomes the needle spring force (see Fig. 4.4). It can be

noticed in Fig. 6.34 that when the piezoelectric actuator is activated a transient of short duration and highly damped can be observed. However, this effect does not have an important influence on the pressure injection events. It can also be observed that the instantaneous pressure injections, which are calculated after the coupled system is solved, are very close to the pressure injections defined when the system is uncoupled.

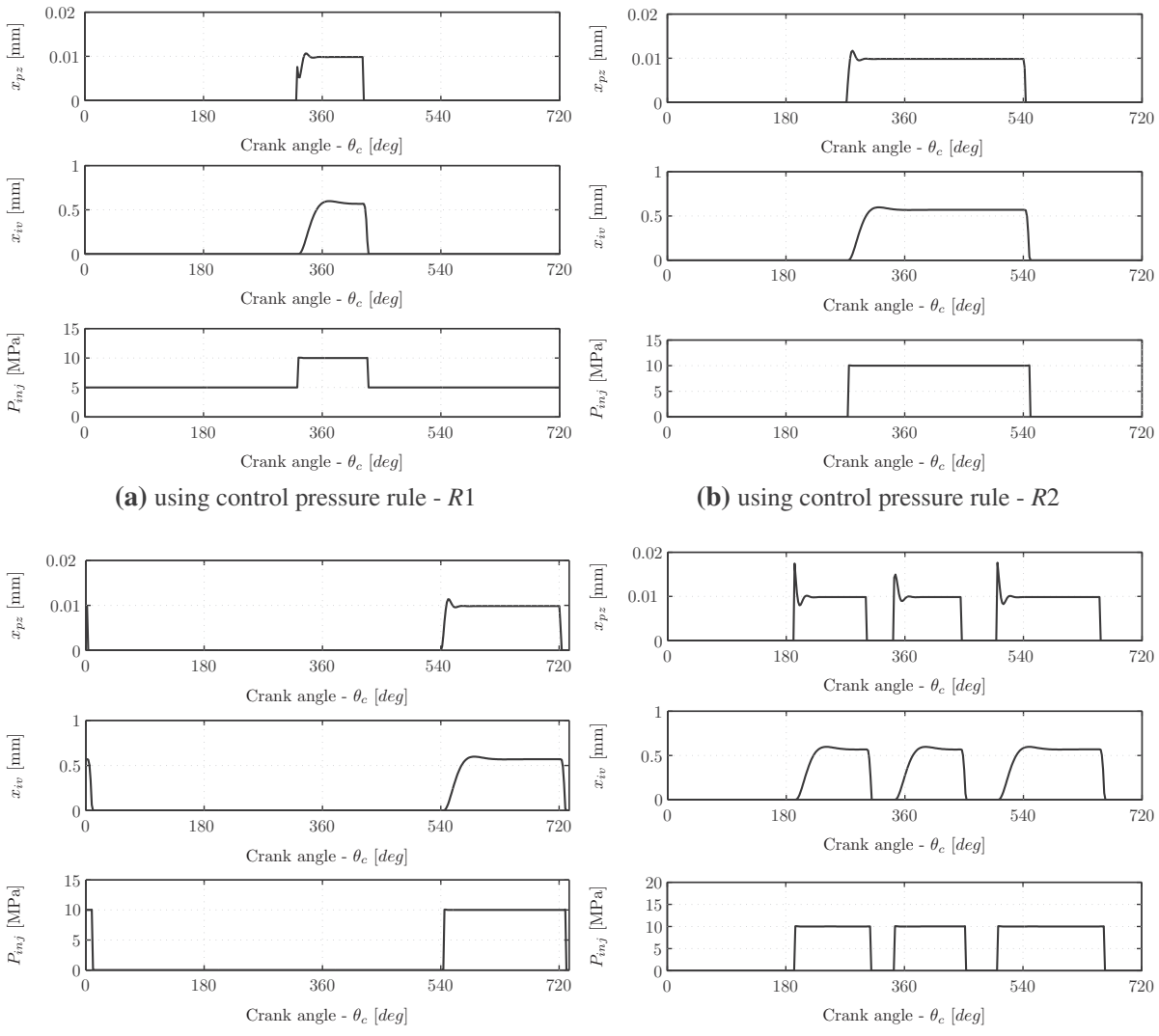

(a) using control pressure rule - $R1$ **(b)** using control pressure rule - $R2$

(c) using control pressure rule - $R3$ **(d)** using control pressure rule - $R4$

Figure 6.34: *Injection parameters - bearing case a. x_{pz}: displacement of piezostack; x_{iv}: displacement of needle injector; P_{inj}: oil injection pressure. ($P_{inj_{H/L}} = 10/5$ MPa).*

Numerical results with and without coupling the injection system to the hybrid bearing problem

The differences in terms of the minimum *OFT* and the maximum film pressures, obtained for the hybrid bearing cases *a*-*R*1 and *f*-*R*1, considering an uncoupled and a coupled solution, can be seen in Fig. 6.26. Although small differences in the minimum *OFT* can be partially found during each combustion cycle, those differences are not significant for the two cases considered, as shown in Fig. 6.35. Regarding to the behaviour of the maximum film pressure, the differences between the uncoupled and coupled system are negligible, except for a very small delay at the ends of the oil injection events, which may be mainly caused by the viscous friction of the needle injector.

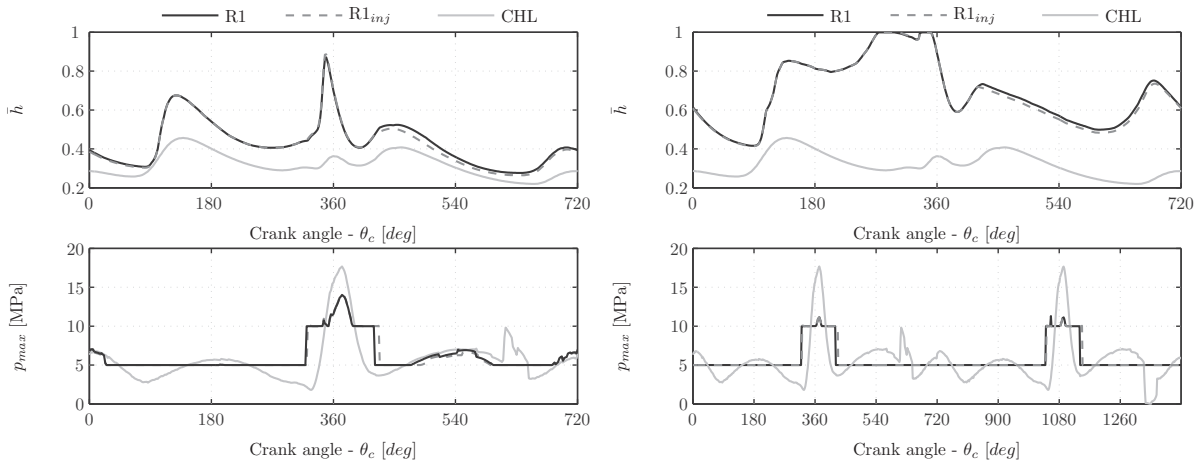

(a) case *a*, rule - *R*1 **(b)** case *f*, rule - *R*1

Figure 6.35: *Minimum OFT and maximum film pressures for bearing cases a and f, with and without including the injector dynamics ($P_{inj_{H/L}} = 10/5$ MPa).*

Evaluation of injection oil flow and power consumption

The oil flow delivered during the injections is calculated for each bearing configuration case using Eq. (4.19). The variation of oil flow delivered to the bearing through the injection holes during a complete engine combustion cycle, is plotted in Fig. 6.36, for the bearing case *a* using control pressure rules *R*1 to *R*4. It can be noticed for each case the influence of the oil injection pressure on the amount of oil delivered during the injection events. In general, one can say that the oil injection flow increases, when the injection pressure increases. When using control pressure rule *R*1, it can be noticed in Fig. 6.36a that oil flow is delivered to the bearing through the entire cycle. It can also be observed that the amount of oil injected may become higher during the crankshaft angular interval at which oil is injected at the lower pressure (P_{inj_L}). This is due to the dependency of oil flow on the pressure difference between the oil injection pressure (P_{inj}) and the hydrodynamic fluid film pressure ($\bar{P}_{jb}$).

The losses of energy caused by viscous friction forces can be reduced using controllable radial oil injection. In order to evaluate the potential savings of energy, it has been calculated in percent

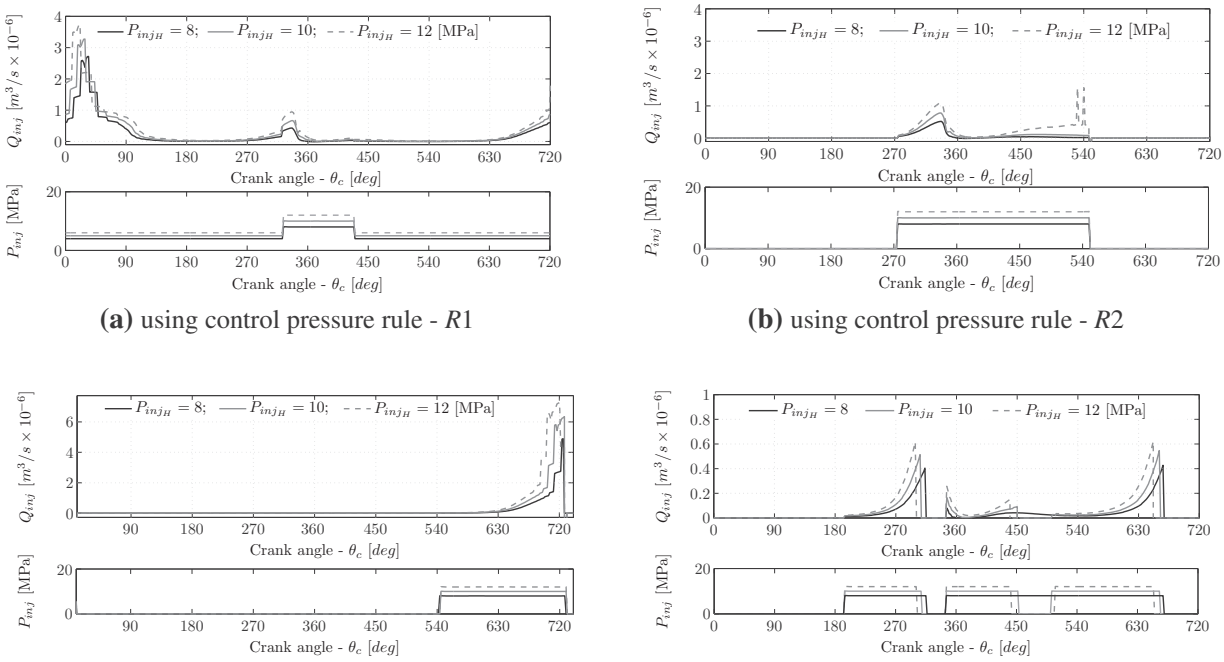

(a) using control pressure rule - $R1$

(b) using control pressure rule - $R2$

(c) using control pressure rule - $R3$

(d) using control pressure rule - $R4$

Figure 6.36: *Oil injection flow and injection pressures - bearing case a.*

the reduction in energy due to viscous friction forces for each bearing case and for each control pressure rule, calculated by:

$$\Delta \bar{W}_{vf} = \frac{W_{vf}^{CHL} - W_{vf}^{inj}}{W_{vf}^{CHL}}$$

$$\bar{W}_{inj} = \frac{W_{inj}}{W_{vf}^{CHL}}$$

$$\bar{W}_{diff} = \Delta \bar{W}_{vf} - \bar{W}_{inj}$$

where W_{vf}^{CHL} and W_{vf}^{inj} are the power dissipation caused by viscous friction forces for the conventionally lubricated bearing and for the controllable hybrid bearing cases, respectively; $\bar{W}_{inj}$ is the energy required for the oil flow through the orifices, which is calculated based on the demands of oil flow and pressure injections: $W_{inj} = Q_{inj} \cdot \bar{P}_{inj}$. Thus, $\bar{W}_{diff}$ gives an estimation of the savings in energy due to the reduction in the viscous friction forces. For each bearing case and control pressure rule, and considering three different injection pressures, $\bar{W}_{diff}$ was computed and the values obtained are shown in Fig. 6.37. It can be noticed in Fig. 6.37 that the bearing of case *f* using control pressure rule $R1$ presents the best advantage compared to the other cases analyzed. It can also be observed that the earnings of energy using $R3$ are much lower compared to the other cases.

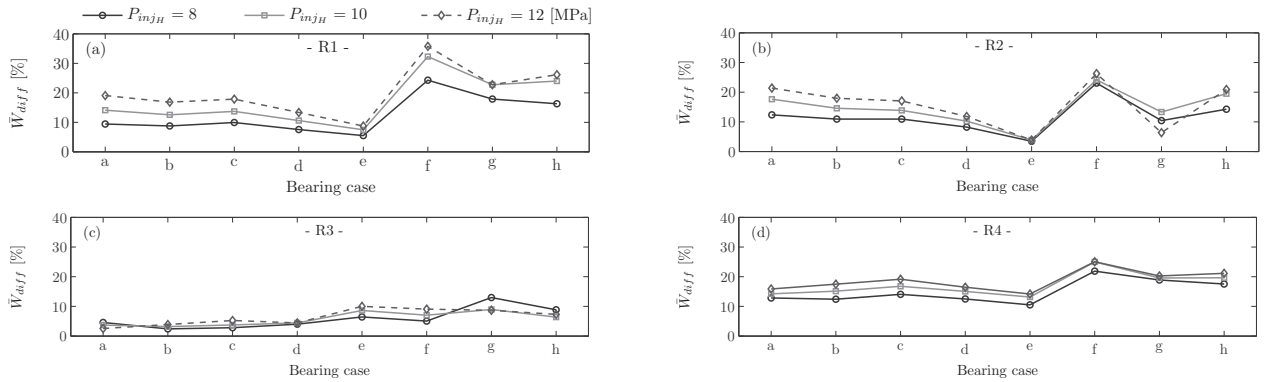

Figure 6.37: *Savings in cyclic power consumption.*

6.2.4 Summary of results

The results presented in this section for a main engine bearing operating with controllable lubrication have shown that the lubrication performance of main engine bearings can be significantly enhanced by combining conventional hydrodynamic lubrication with controllable radial oil injection. It was shown from the results that the fluid film thickness can be increased up to 90% and at the same time the friction losses and vibrations can be reduced up to 40%. The bearing cases that present the best hybrid bearing performance in terms of the minimum OFT were for cases *a* and *f*, operating with control pressure rules $R1$ and $R2$. However, when the savings of energy were analyzed, the hybrid bearing of case *f* operating with control pressure rule $R1$ presented the best advantage compared to the other bearing cases.

6.2.5 Further remarks and technological challenges

The use of piezoelectric actuation for the oil injection system presents several advantages in terms of compactness and fast response when it is compared to mechanical unit injectors and servohydraulic oil injection systems. This type of oil injection system may be also a good substitute of active oil injection systems operating with servohydraulic valves, which have been successfully used in other bearing applications, such as, actively-lubricated tilting pad journal bearings (Santos and Russo, 1998; Santos et al., 2004).

Further studies should be carried out in order to experimentally validate hybrid bearing performance operating with the control pressure rules proposed in this section. Although the numerical simulations were carried out considering the main bearing of a single-cylinder *ICE*, similar oil injection strategies may be applied to main bearings of multiple cylinder combustion engines and in general to other type of reciprocating machines using fluid film bearings, in order to enhance their tribological performance.

Chapter 7

Conclusions and Future Aspects

The feasibility of applying controllable lubrication to dynamically loaded journal bearings (*DLJB*s) was studied in this project by analyzing the behaviour of minimum oil film thickness (*OFT*), maximum pressure, orifices distribution over the bearing surface, oil injection pressures, friction forces, and feasible oil injection systems. It was shown that adequate hybrid bearing configurations and oil injection control rules may be defined based on the bearing performance under conventional lubrication conditions (*CHL*). Several advantages of using controllable lubrication over conventional lubrication in *DLJB*s were presented, mainly in terms of increasing the minimum fluid film thickness, increasing the effective carrying load area and lowering the viscous friction forces. In order to control the oil injection, several strategies were evaluated, where the oil injection pressures are given as a function of the rotational crank angle. Two different cases were considered during this study: a) main bearing of a hermetic reciprocating compressor (*HRC*); b) crankshaft main bearing of a single-cylinder four-strokes internal combustion engine (*ICE*). From the mathematical models developed, their computational implementation, and the analysis of numerical results obtained for these two particular cases of study, the main technical conclusions can be summarized as follows:

Hermetic reciprocating compressor - *HRC*

- From the modelling of a *HRC* using three different approaches, and considering *CHL* for the upper and lower bearings, no significant differences were found between the three cases regarding to the estimation of the hydrodynamic journal bearing forces and the fluid film pressures. It was found that under *CHL* conditions, the maximum values of fluid film pressures and bearing forces are found close to $\theta_c = 180^o$. The lowest minimum *OFT* is found at every crank cycle at $\theta_c = 260^o$, with the orbit of the journal centre oscillating in the third bearing quadrant, as also shown in [J1],[J2], and in (Santos and Estupinan, 2007).

- The results obtained using hybrid controllable lubrication showed that the minimum *OFT* can be significantly increased through radial oil injection, with controllable injection pressures rules given as a function of the crank angle. It was found that injecting oil through orifices located at $\Theta_o = 180^o$ and $\Theta_o = 225^o$, and with oil injection pressures varying between 2MPa to 3MPa, the minimum *OFT* can be increased more than 90% compared to the *CHL* bearing case. These results are also shown in [J3], and in (Estupinan and Santos, 2008b, 2009d). When the cyclic averaged power consumption was computed for the controllable lubricated

bearing cases, it was found a reduction in the cyclic power consumption due to the viscous friction forces up to 35% compared to the *CHL* bearing case.

Internal combustion engine - *ICE*

- Based on the analysis made for the main engine bearing of an *ICE*, operating with *CHL*, eight geometric hybrid bearing configurations (cases *a* to *h*) and four rules for controlling oil injection pressures ($R1$ to $R4$) were proposed in this work. It was found for the *CHL* bearing case that the lowest *OFT* is found at $\theta_c = 650^o$, that is, 70^o before the *TDC* during the exhaust stroke (Estupinan and Santos, 2008a). Good correlation was found between the bearing orbits obtained in this work for the *CHL* engine bearing case, and the engine bearing orbits published in the literature.

- In general, it was found that the changes in the hydrodynamic oil film pressure, obtained by means of applying controllable radial oil injection, lead to significant increase of minimum *OFT* and reduction of viscous friction losses, however the hybrid bearing performance must be evaluated for each case individually, since the results are very dependent on the geometric bearing configurations, the control pressure rules and the oil injection pressures. Additionally, it was found that vibrations of crankshaft can be also reduced, which is reflected by the fact of having smaller journal centre orbits when controllable lubrication is applied (Estupinan and Santos, 2009a).

- It was found that for the hybrid bearing of case *f* with oil injected through orifices located at $\Theta_o = 180^o$ and $\Theta_o = 225^o$, using control pressure rule $R1$ (with $P_{inj_{H/L}} = 12/5$ MPa), the minimum *OFT* can be increased up to 90% compared to the *CHL* bearing case. This is also shown in (Estupinan and Santos, 2008a, 2009a).

- In terms of the minimum *OFT*, hybrid bearing of case *f* using control pressure rules $R1$ and $R4$ presents the best advantage compared to the other hybrid bearing cases considered in the analysis. Among all cases, the largest increase in the minimum *OFT* was obtained for cases *f*-$R1$ and *f*-$R4$ using $P_{inj_H} = 10$MPa and $P_{inj_H} = 8$MPa, respectively. Inadequate hybrid bearing configurations were found for the bearing cases *d* and *e* (i.e., orifices located at $\Theta_o = 240^o$ and $\Theta_o = 270^o$, respectively), since almost a negligible increase in the minimum *OFT* compared to the *CHL* bearing case was found. In cases *e*-$R1$ and *e*-$R2$ the minimum *OFT* calculated was lower than in the *CHL* bearing case.

- From the four pressure control strategies analyzed, the results showed that the lowest *OFT* can be increased using $R3$, but at the expense of reducing *OFT* at other times during each cycle. It was also found that using $R3$ maximum film pressures were higher than to the *CHL* bearing case.

- In terms of the savings of power consumption due to the reduction of the viscous friction forces, the best performance was obtained for bearing case *f* using control pressure rule $R1$. It was found that the energy consumption due to friction viscous forces can be reduced up to 40%.

- Although using control pressure rule $R4$ gives good bearing performance in terms of increasing minimum OFT, particularly for cases a and f, oil injection is required during a longer time throughout each crankshaft cycle.

- In this work two oil injection systems were described. The results obtained by coupling the dynamics of a piezo-actuated injection system to the dynamics of the main journal bearings showed that not significant differences were found in the behaviour of the global bearing parameters. Nevertheless, it is worth to point out that the coupling of the injector dynamics to the hybrid bearing dynamics, will help in further studies to evaluate hybrid bearing performance using more sophisticated oil injection control rules.

As shown, through theoretical analysis and numerical simulations of *CHL* bearing performance and controllable hybrid bearing performance of *DLJB*s, significant improvements can be obtained applying controllable radial oil injection. Nevertheless, further studies should be carried out in order to experimentally evaluate the oil injection systems presented in this work. Moreover, the need for introducing thermal effects in the modelling of main engine bearings operating with active/controllable lubrication systems, could be confirmed by comparing numerical results to experimental data. Additionally, bearing parametric studies should be carried out in order to be able to define optimal geometric hybrid bearing configurations.

The feasibility study carried out in this work was based on numerical results obtained from the solution of a mathematical model which included the dynamics of the main components of typical reciprocating machines, the dynamics of the bearing fluid films, and the dynamics of the oil injection. The main results were presented for the upper bearing of a *HRC*, and for the main crankshaft bearing of a single-cylinder *ICE*, operating with *CHL* and active/controllable lubrication conditions. The strategies for controlling radial oil injection, and the oil injection systems presented in this work, can be considered to be used in main bearings of multiple cylinder *ICE*s and in general in other type of reciprocating machines using fluid film bearings, such as, industrial compressors and large diesel engines. In this last case the effects of introducing radial oil injection can become quite important in terms of reducing energy losses, since there is a high potential for reduction in friction forces.

"It is just a matter of time before active bearings will be regularly employed in machine tools, gas turbines, terrestrial turbines, engine suspensions, valve control, and various other mechanisms" (Ulbrich, 1994).

Bibliography

Alshaer, B., Nagarajan, H., Beheshti, H., Lankarani, H., Shivaswamy, S., 2005. Dynamics of a multibody mechanical system with lubricated long journal bearings. Transactions of the ASME. Journal of Mechanical Design 127 (3), 493–498.

ANSI/IEEE, 1987. IEEE standard on piezoelectricity. Tech. Rep. Std 176-1987, IEEE Ultrasonics, Ferroelectrics, and Frequency Control Society, New York.

Arnold, M., Burgermeister, B., Eichberger, A., 2007. Linearly implicit time integration methods in real-time applications: Daes and stiff odes. Multibody System Dynamics 17 (2-3), 99–117.

Arnold, M., Carrarini, A., Heckmann, A., Hippmann, G., 2004. Simulation techniques for multidisciplinary problems in vehicle system dynamics. Vehicle System Dynamics 40, 17–35.

AVL, 2009. AVL Excite Power Unit: Elastohydrodynamic contact models. Advanced Simulation Technologies - Data sheet. Available at: http://www.avl.com/excite.

Backhaus, K., Knoll, G., October 2008. Oil flow interaction of engine bearings. In: Proceedings of the STLE/ASME International Joint Tribology Conference. No. IJTC2008-71036. Miami, FL, USA.

Booker, J., 1965. Dynamically loaded journal bearings – mobility method of solution. American Society of Mechanical Engineers – Transactions – Journal of Basic Engineering 87 (3), 537–546.

Booker, J., Huebner, K., 1972. Application of finite element methods to lubrication: An engineering approach. J Lubr Technol Trans ASME 94 Ser F (4), 313–323.

Boysal, A., Rahnejat, H., 1997. Torsional vibration analysis of a multi-body single cylinder internal combustion engine model. Applied Mathematical Modelling 21 (8), 481–493.

Bremer, H., 1988. Dynamik und regelung mechanischer systeme. B.G. Teubner Verlag, Stuttgart, Germany.

Bremer, H., 1999. On the dynamics of elastic multibody systems. Applied Mechanics Reviews - Including Supplement 52 (9), 275.

Bukovnik, S., Dorr, N., Caika, V., Bartz, W., Loibnegger, B., 2006. Analysis of diverse simulation models for combustion engine journal bearings and the influence of oil condition. Tribology International 39 (8), 820–826.

Bukovnik, S., Offner, G., Caika, V., Priebsch, H., Bartz, W., 2007. Thermo-elasto-hydrodynamic lubrication model for journal bearing including shear rate-dependent viscosity. Lubrication Science 19 (4), 231–245.

Campbell, J., Love, P., Martin, F., Rafique, S., 1967-1968. Bearings for reciprocating machinery – review of present state of theoretical, experimental and service knowledge. Institution on Mechnical Engineers – Proceedings 182 (Part 3A), 51–74.

Chapman, E., Herdic, S., Keller, C. A., Lynch, C., 2005. Development of miniaturized piezo-hydraulic pumps. Proceedings of SPIE - The International Society for Optical Engineering 5762, 299–310.

Cho, J., Moon, S., 2005. A numerical analysis of the interaction between the piston oil film and the component deformation in a reciprocating compressor. Tribology International 38 (5), 459–468.

Choi, J., Lee, J., Han, D., 1992. Oil film thickness in engine main bearings: comparison between calculation and experiment by total capacitance method. SAE Special Publications (936), 147–160.

Chung, N.-H., Oh, B.-G., Sunwoo, M.-H., 2008. Modelling and injection rate estimation of common-rail injectors for direct-injection diesel engines. Proceedings of the Institution of Mechanical Engineers - D 222 (6), 1089.

Ciulli, E., 1992. Review of internal combustion engine losses part 1: specific studies on the motion of pistons, valves and bearings. Proceedings of the Institution of Mechanical Engineers, Part D: Journal of Automobile Engineering 206 (4), 223–236.

Craven, A., Holmes, R., 1972. The vibration of engine crankshafts-a fast numerical solution. International Journal for Numerical Methods in Engineering 5 (1), 17–24.

Dede, M., Holmes, R., 1984. On prediction and experimental assessment of engine-bearing performance. Tribology International 17 (5), 251–258.

Drab, C., Engl, H., Haslinger, J., Offner, G., Pfau, R., Zulehner, W., 2009. Dynamic simulation of crankshaft multibody systems. Multibody System Dynamics 22 (2), 133–144.

Eberhard, P., Schiehlen, W., 2006. Computational dynamics of multibody systems: history, formalisms, and applications. Transactions of ASME. Journal of Computational and Nonlinear Dynamics 1 (1), 3–12.

Elrod, H., 1981. A cavitation algorithm. Transactions of the ASME. Journal of Lubrication Technology 103 (3), 350–354.

Estupinan, E., Santos, I., September 2008a. Feasibility of applying controllable lubrication to the main bearings of reciprocating engines. In: Proceedings of 23rd International Conference on Noise and Vibration Engineering - ISMA 2008. Leuven, Belgium, pp. 2015–27, ISBN 978-90-7380-286-5.

Estupinan, E., Santos, I., October 2008b. Linking rigid and flexible multibody systems via thin fluid films actively controlled. In: Proceedings of STLE/ASME International Joint Tribology Conference - IJTC 2008. Miami (FL), USA., ISBN 978-0-7918-3837-2.

Estupinan, E., Santos, I., June 2008c. Linking rigid multibody systems via controllable thin fluid films. In: Proceedings of NORDTRIB 2008, 13th Nordic Symposium on Tribology. No. NT2008-42-30. Tampere, Finland, ISBN 978-952-15-1959-8.

Estupinan, E., Santos, I., July 5-9 2009a. Active lubrication applied to internal combustion engines - evaluation of control strategies. In: Proceedings of the 16th International Congress on Sound and Vibration. Krakow, Poland, ISBN: 978-83-60716-71-7.

Estupinan, E., Santos, I., September 2009b. Active lubrication strategies applied to dynamically loaded fluid film bearings. In: Proceedings of World Tribology Conference 2009 - WTC IV. Kyoto, Japan, ISBN: 978-4-9900139-9-8.

Estupinan, E., Santos, I., May 2009c. Feasibility of applying active lubrication to dynamically loaded fluid film bearings. In: STLE 2009 Annual Meeting. Orlando - FL, USA.

Estupinan, E., Santos, I., March 2009d. Feasibility of applying controllable lubrication to dynamically loaded journal bearings. In: Proceedings of XIII International Symposium on Dynamic Problems of Mechanics - DINAME 2009. Angra dos Reis, RJ, Brazil.

Estupinan, E., Santos, I., January 2010. Schemes for applying active lubrication to main engine bearings. In: Proceedings of 11th Pan-American Congress of Applied Mechanics - PACAM XI. Foz do Iguaçu, Brazil.

Fantino, B., Frêne, J., 1985. Comparison of dynamic behavior of elastic connecting-rod bearing in both petrol and diesel engines. Journal of Tribology, Transactions of the ASME 107 (1), 87–91.

Fatu, A., Hajjam, M., Bonneau, D., 2006. A new model of thermoelastohydrodynamic lubrication in dynamically loaded journal bearings. Transactions of the ASME. Journal of Tribology 128 (1), 85–95.

Feenstra, J., Granstrom, J., Sodano, H., 2008. Energy harvesting through a backpack employing a mechanically amplified piezoelectric stack. Mechanical Systems and Signal Processing 22 (3), 721–734.

Fox, R., McDonald, A., Pritchard, P., 2004. Introduction to Fluid Mechanics. John Wiley & Sons, Inc., USA.

Frêne, J., Nicolas, D., Degueurce, B., Berthe, D., Godet, M., 1990. Lubrification Hydrodynamique. Editions Eyrolles, Paris.

Fridman, V., Piraner, I., Musolff, C., 2004. Some applications of the hydrodynamic and elasto-hydrodynamic analysis to the diesel engine bearings. Proceedings of the ASME/STLE International Joint Tribology Conference, IJTC 2004 (PART A), 807–829.

Fuller, C., Elliot, S., Nelson, P., 1996. Active Control of Vibration. Academic Press, Inc.

Garcia de Jalon, J., Bayo, E., 1994. Kinematic and Dynamic Simulation of Multibody Systems. The Real-Time Challenge. Springer-Verlag, New-York.

Goenka, P., Oh, K., 1986. Optimum short bearing theory for the elastohydrodynamic solution of journal bearings. Journal of Tribology, Transactions of the ASME 108 (2), 294–299.

Goenka, P. K., Paranjpe, R. S., 1992. Review of engine bearing analysis methods at general motors. Engine Tribology and SAE Special Publications (919), 67–75.

Goodwin, M. J., Nikolajsen, J. L., Ogrodnik, P. J., 2003. Reciprocating machinery bearing analysis: Theory and practice. Proceedings of the Institution of Mechanical Engineers, Part J: Journal of Engineering Tribology 217 (6), 409–426.

Hamrock, B. J., 1991. Fundamental of Fluid Film Lubrication. NASA Reference Publication, USA.

Han, H. S., 2004. Web-based dynamic simulation system for multi-body systems. Advances in Engineering Software 35 (2), 75–84.

Haugaard, A. M., Santos, L. F., 2009. Modeling of flexible tilting pad journal bearings with radial oil injection. 2008 Proceedings of the STLE/ASME International Joint Tribology Conference, IJTC 2008, 335–337.

Heinrichson, N., Santos, I. F., 2008. Reducing friction in tilting-pad bearings by the use of enclosed recesses. Journal of Tribology 130 (1).

Heinrichson, N., Santos, I. F., Fuerst, A., 2007. The influence of injection pockets on the performance of tilting-pad thrust bearings - part i: Theory. Journal of Tribology 129 (4), 895–903.

Hirani, H., Athre, K., Biswas, S., 1998. Rapid and globally convergent method for dynamically loaded journal bearing design. Proceedings of the Institution of Mechanical Engineers -J- Journal of Engineering Tribology 212 (3), 207.

Hirani, H., Athre, K., Biswas, S., 1999a. Dynamic analysis of engine bearings. International Journal of Rotating Machinery 5, 283–293.

Hirani, H., Athre, K., Biswas, S., 1999b. Dynamically loaded finite length journal bearings: Analytical method of solution. Journal of Tribology, Transactions of the ASME 121 (4), 844–852.

Horikawa, O., Sato, K., Shimokohbe, A., 1992. An active air journal bearing. Nanotechnology 3 (2), 84–90.

Hountalas, D. T., Kouremenos, A. D., 1998. Development of a fast and simple simulation model for the fuel injection system of diesel engines. Advances in Engineering Software 29 (1), 13–28.

Isermann, R., 2006. Automotive mechatronic systems - general developments and examples. Automatisierungstechnik 54 (9), 419–429.

Jadon, V., Singh, M., 2007. Study of supply cut-off and bearing geometric parameters on design of hybrid journal bearing. Industrial Lubrication and Tribology 59 (2), 92–102.

Katano, H., Iwamoto, A., Saitoh, T., 1991. Dynamic behaviour of internal combustion engine crankshaft under operating conditions. In: Proceedings of IMech E Conference. paper C430/049/91. pp. 205–209.

Kawamoto, A., Inagaki, M., Aoyama, T., Mori, N., Ikeura, O., Uno, T., Yamamoto, K., 2000. Prediction of structural and kinematic coupled vibration on internal combustion engine. Proceedings of the 25th International Conference on Noise and Vibration Engineering - ISMA 25, 1323–1330.

Kim, B.-J., Kim, K.-W., 2001. Thermo-elastohydrodynamic analysis of connecting rod bearing in internal combustion engine. Journal of Tribology 123 (3), 444–454.

Kim, H. J., Ahn, J. M., 2007. Numerical simulation of oil supply system of a reciprocating compressor for household refrigerators. HVAC and R Research 13 (5), 833–847.

Kim, T. J., Han, J. S., 2004. Comparison of the dynamic behavior and lubrication characteristics of a reciprocating compressor crankshaft in both finite and short bearing models. Tribology Transactions 47 (1), 61–69.

Knoll, G., Schoenen, R., Wilhelm, K., 1997. Full dynamic analysis of crankshaft and engine block with special respect to elastohydrodynamic bearing coupling. American Society of Mechanical Engineers, Internal Combustion Engine Division (Publication) ICE 3, 1–8.

Knoll, G. D., Peeken, H. J., 1982. Hydrodynamic lubrication of piston skirts. Trans. ASME J. Lubrication Technology 104 (4), 504–509.

Kortüm, W., Vaculín, O., 2004. Is multibody simulation software suitable for mechatronic systems? Vehicle System Dynamics 40, 1–16.

Kushwaha, M., Gupta, S., Kelly, P., Rahnejat, H., 2002. Elasto-multi-body dynamics of a multicylinder internal combustion engine. Proceedings of the Institution of Mechanical Engineers - K 216 (4), 281–294.

Lacy, D. J., 1987. Computers in analysis techniques for reciprocating engine design. In: Proceedings of IMech E Conference. paper C14/87. pp. 55–68.

Lahmar, M., Haddad, A., Nicolas, D., 2000. An optimised short bearing theory for nonlinear dynamic analysis of turbulent journal bearings. European Journal of Mechanics - A/Solids 19 (1), 151–177.

Lückmann, A. J., Alves, M. V. C., Barbosa, Jader R., J., 2009. Analysis of oil pumping in a reciprocating compressor. Applied Thermal Engineering 29 (14-15), 3118–3123.

Lee, D. G., Or, S. W., Carman, G. P., 2004. Design of a piezoelectric-hydraulic pump with active valves. Journal of Intelligent Material Systems and Structures 15 (2), 107–115.

Lee, H.-K., Russell, M., Bae, C., 2002. Mathematical model of diesel fuel injection equipment incorporating non-linear fuel injection. Proceedings of the Institution of Mechanical Engineers, Part D: Journal of Automobile Engineering 216 (3), 191–204.

Lino, P., Maione, B., Rizzo, A., 2007. Nonlinear modelling and control of a common rail injection system for diesel engines. Applied Mathematical Modelling 31 (9), 1770–1784.

Lugner, P., Plochl, M., 2004. Modelling in vehicle dynamics of automobiles. Zeitschrift fur Angewandte Mathematik und Mechanik 84 (4), 219–236.

Ma, Z. D., Perkins, N. C., 2003. An efficient multibody dynamics model for internal combustion engine systems. Multibody System Dynamics 10 (4), 363–91.

Makino, T., Koga, T., 2002. Crank bearing design based on 3-d elasto-hydrodynamic lubrication theory. Technical Review - Mitsubishi Heavy Industries 39 (1), 16–20.

MAN B&W Diesel A/S, September 2002. Elasto-hydro-dynamic evaluation of main bearing performance. Technical report, available at: http://www.mandiesel.com/files/news/filesof2580/p396-0209.pdf.

Martin, F. A., 1983. Developments in engine bearing design. Tribology International 16 (3), 147–164.

Merritt, H. E., 1967. Hydraulic Control Systems. John Wiley & Sons, Inc., New York.

Mitsui, J., 1988. Journal Bearing Databook. Springer Verlag, Berlin Heidelberg, Ch. Method of Calculation for Bearing Characteristics, pp. 231–240.

Mizumoto, H., Arii, S., Kami, Y., Goto, K., Yamamoto, T., Kawamoto, M., 1996. Active inherent restrictor for air-bearing spindles. Precision Engineering 19 (2-3), 141–147.

Moreau, H., Maspeyrot, P., Chomat-Delalex, A., Bonneau, D., Frêne, J., 2002. Dynamic behaviour of elastic engine main bearings: Theory and measurements. Proceedings of the Institution of Mechanical Engineers, Part J: Journal of Engineering Tribology 216 (4), 179–193.

Morita, T., Okamura, H., 1995. Simple modeling and analysis for crankshaft three-dimensional vibrations, part 2: application to an operating engine crankshaft. Journal of Vibration and Acoustics, Transactions of the ASME 117 (1), 80–86.

Mourelatos, Z., 2001a. An efficient journal bearing lubrication analysis for engine crankshafts. Tribology Transactions 44 (3), 351–358.

Mourelatos, Z. P., 2001b. A crankshaft system model for structural dynamic analysis of internal combustion engines. Computers and Structures 79 (20-21), 2009–2027.

Near, C., 1996. Piezoelectric actuator technology. Proceedings of the SPIE - The International Society for Optical Engineering 2717, 246–258.

Nelson, H. D., McVaugh, J. M., May 1976. The dynamics of rotor-bearing systems using finite elements. Journal of Engineering for Industry, 593–600.

Offner, G., Krasser, J., Laback, O., Priebsch, H., 2001. Simulation of multi-body dynamics and elastohydrodynamic excitation in engines especially considering piston-liner contact. Proceedings of the Institution of Mechanical Engineers - K 215 (2), 93–102.

Oh, K. P., Goenka, P. K., 1985. Elastohydrodynamic solution of journal bearings under dynamic loading. Journal of Tribology, Transactions of the ASME 107 (3), 389–395.

Okamura, H., Shinno, A., Yamanaka, T., Suzuki, A., Sogabe, K., 1995. Simple modeling and analysis for crankshaft three-dimensional vibrations, part 1: background and application to free vibrations. Journal of Vibration and Acoustics, Transactions of the ASME 117 (1), 70–79.

Orlandea, N., Chace, M. A., Calahan, D. A., 1977. Sparsity-oriented approach to the dynamic analysis and design of mechanical systems em dash parts 1 and 2. J Eng Ind Trans ASME 99 Ser B (3), 773–784.

Pal, R., Sinhasan, R., Singh, D., 1988. Analysis of a big-end bearing - a finite element approach. Wear 121 (1), 117–120.

Paranjpe, R. S., 1996. A study of dynamically loaded engine bearings using a transient thermohydrodynamic analysis. Tribology Transactions 39 (3), 636–644.

Paranjpe, R. S., Goenka, P. K., 1990. Analysis of crankshaft bearings using a mass conserving algorithm. Tribology Transactions 33 (3), 333–344.

Perera, M., Theodossiades, S., Rahnejat, H., 2007. A multi-physics multi-scale approach in engine design analysis. Proceedings of the Institution of Mechanical Engineers, Part K: Journal of Multi-body Dynamics 221 (3), 335–348.

Prechtl, E. F., Hall, S. R., 1999. Design of a high efficiency, large stroke, electromechanical actuator. Smart Materials and Structures 8 (1), 13–30.

Priest, M., Taylor, C., 2000. Automobile engine tribology - approaching the surface. Wear 241 (2), 193–203.

Rahnejat, H., 1998. Multi-Body Dynamics, Vehicles, machines, and mechanisms. Professional Engineering Publishing, London.

Rahnejat, H., 2000. Multi-body dynamics: Historical evolution and application. Proceedings of the Institution of Mechanical Engineers -C- Journal of Mechanical Engineering Science 214 (1), 149–174, special Millennium Issue.

Rakopoulos, C., Giakoumis, E., 2007. Prediction of friction development during transient diesel engine operation using a detailed model. International Journal of Vehicle Design 44 (1-2), 143–166.

Rasmussen, B. D., 1997. Variable speed hermetic reciprocating compressors for domestic refrigerators. Ph.D. thesis, Technical University of Denmark, Denmark.

Reddi, M., 1969. Finite element solution of the incompressible lubrication problem jolt, 91, ser. f, (3) (1969) 524-533; 14 figs. 1 table, 16 refs. J. Lubric. Technol. Trans. ASME 91 (3), 524 – 533.

Rezeka, S., Henein, N., February 1984. A new approach to evaluate instantaneous friction and its components in internal combustion engines. SAE Paper 840179.

Richardson, D., 2000. Review of power cylinder friction for diesel engines. Journal of Engineering for Gas Turbines and Power 122 (4), 506.

Rigola, J., 2002. Numerical simulation and experimental validation of hermetic reciprocating compressors. Ph.D. thesis, Universidad Politécnica de Cataluña, Spain.

Ritchie, G. S., 1975. The prediction of journal loci in dynamically loaded internal combustion engine bearings. Wear 35 (2), 291–297.

Roberson, R. E., Schwertassek, R., 1988. Dynamics of multibody systems. Springer-Verlag, Germany.

Ross, J. M., Slaymaker, R. R., 1969. Journal center orbits in piston engine bearings. SAE Papers.

Rowe, W., Xu, S., Chong, F., Weston, W., 1982. Hybrid journal bearings with particular reference to hole-entry configurations. Tribology International 15 (6), 339–348.

San Andres, L., 2009. Cavitation in liquids film bearings. Lecture notes no.6, University of Texas A&M, available at: http://phn.tamu.edu/me626.

Santos, I., 1994. Design and evaluation of two types of active tilting pad journal bearings. In: Burrows, C., Keogh, P. (Eds.), Active Control of Vibration. Mechanical Engineering Publications Limited, London, England, pp. 79–87, iSBN: 0-85298-916-4.

Santos, I., 2001. Dinâmica de Sistemas Mecanicos. Makron Books, Sao Paulo.

Santos, I., 2009. Trends in active lubricated bearings. In: Verlag, S. (Ed.), IUTAM Conference on Future Trends in Rotordynamics. (In press).

Santos, I., Estupinan, E., November 2007. Combining multibody dynamics, finite elements method and fluid film lubrication to describe hermetic compressor dynamics. In: Proceedings of the 6th WSEAS International Conference on System Science and Simulation in Engineering (ICOSSSE'07). Venice, Italy, pp. 237–42, ISBN: 978-960-6766-14-5.

Santos, I., Nicoletti, R., 1999. Thd analysis in tilting-pad journal bearings using multiple orifice hybrid lubrication. Journal of Tribology 121 (4), 842–900.

Santos, I., Nicoletti, R., 2001. Influence of orifice distribution on the thermal and static properties of hybridly lubricated bearings. International Journal of Solids and Structures 38 (10-13), 2069–2081.

Santos, I., Nicoletti, R., Scalabrin, A., 2004. Feasibility of applying active lubrication to reduce vibration in industrial compressors. Transactions of the ASME. Journal of Engineering for Gas Turbines and Power 126 (4), 848–54.

Santos, I., Russo, F. H., 1998. Tilting-pad journal bearings with electronic radial oil injection. Transactions of the ASME - F - Journal of Tribology 120 (3), 583.

Santos, I., Scalabrin, A., Nicoletti, R., 2001. Ein beitrag zur aktiven schmierungstheorie. In: edited by H. Irretier, Nordmann, R., Springer, H. (Eds.), Schwingungen in rotierenden Maschinen. Vol. 5. Vieweg Verlag, Braunshweig, Germany, pp. 21–30, [in German].

Santos, I., Watanabe, F., 2006. Lateral dynamics and stability analysis of a gas compressor supported by hybrid and active lubricated multirecess journal bearing. Journal of the Brazilian Society of Mechanical Sciences and Engineering 28 (4), 485–495.

Sawicki, J. T., Capaldi, R. J., Adams, M. L., 1997. Experimental and theoretical rotordynamic characteristics of a hybrid journal bearing (96-trib-2). Transactions of the ASME - F - Journal of Tribology 119 (1), 132.

Schiehlen, W., 2007. Research trends in multibody system dynamics. Multibody System Dynamics 18 (1), 3–13.

Schöner, H.-P., 2004. Automotive mechatronics. Control Engineering Practice 12 (11), 1343–1351.

Schulte, H., Wirth, M., November 2004. Internal combustion engines for the future. In: Proceedings of the International Conference on Automotive Technologies - ICAT 2004. Istanbul, available at: http://www.icatconf.org/icat2000-2006/tr/2004%20listpapers.html.

Sharma, S., Kumar, V., Jain, S., Sinhasan, R., Subramanian, M., 1999. A study of slot-entry hydrostatic/hybrid journal bearing using the finite element method. Tribology International 32 (4), 185–196.

Spearot, J. A., May 2000. Friction, wear, health, and environmental impacts tribology in the new millennium. A keynote lecture at the STLE Annual Meeting. Nashville, Tennessee.

Stout, K., Rowe, W., 1974. Externally pressurized bearings - design for manufacture part 1 - journal bearing selection. Tribology 7 (3), 98–106.

Subramanyan, P. K., 2000. The Engineering Handbook. Boca Raton: CRC Press LLC, Ch. Crankshaft Journal Bearings.

Taraza, D., Henein, N., W., B., 2000. Friction losses in multi-cylinder diesel engines. SAE Transactions 109 (3), 874–84.

Taylor, C., 1998. Automobile engine tribology-design considerations for efficiency and durability. Wear 221 (1), 1–8.

Taylor, C. J., Washington, G. N., 2002. A comprehensive piezoceramic actuator review. Proceedings of SPIE - The International Society for Optical Engineering 4701, 443–454.

Tung, S. C., McMillan, M. L., 2004. Automotive tribology overview of current advances and challenges for the future. Tribology International 37 (7), 517–536.

Ulbrich, H., 1994. Comparison of different actuator concepts for applications in rotating machinery. International Journal of Rotating Machinery 1 (1), 61–71.

Ulbrich, H., 1996. Maschinendynamik. B.G. Teubner Verlag, Stuttgart, Germany.

Vaculín, O., Krüger, W. R., Valášek, M., 2004. Overview of coupling of multibody and control engineering tools. Vehicle System Dynamics 41 (5), 415–29.

Vincent, B., Maspeyrot, P., Frene, J., 1996. Cavitation in dynamically loaded journal bearings using mobility method. Wear 193 (2), 155–162.

Warner, P. C., 1963. Static and dynamic properties of partial journal bearings. American Society of Mechanical Engineers – Transactions – Journal of Basic Engineering 85 (2), 247–257.

Wendt, J. F., 1992. Computational Fluid Dynamics. Springer-Verlag.

White, M. F., 1989. Dynamic loading and response of bearings in reciprocating machinery. Wear 130 (1), 81–92.

Xu, H., 1999. Recent advances in engine bearing design analysis. Proceedings of the Institution of Mechanical Engineers -J- Journ of Engineering Tribology 213 (4), 239.

Zeischka, J., Mayor, L. S., Schersen, M., Maessen, F., 1994. Multi-body dynamics with deformable bodies applied to the flexible rotating crankshaft and the engine block. In: ASME 94 Fall Technical Conference.

Appendix A

Equations of motion in matrix form

A.1 Case I

$$\bar{\mathbf{A}}_{(\mathbf{I})} \cdot \bar{\mathbf{b}}_{(\mathbf{I})} = \bar{\mathbf{c}}_{(\mathbf{I})}$$

$$\begin{Bmatrix}
1 & 0 & 0 & 0 & 0 & 0 & 0 & 0 & 0 & 0 & 0 & 0 & 0 & m_p & 0 \\
0 & -1 & 0 & 1 & 0 & 0 & 0 & 0 & 0 & 0 & 0 & 0 & 0 & 0 & 0 \\
0 & 0 & 1 & 0 & -1 & 0 & 0 & 0 & 0 & 0 & 0 & 0 & 0 & 0 & 0 \\
1 & 0 & 0 & 0 & 0 & -1 & 0 & 0 & 0 & 0 & 0 & 0 & 0 & -m_{cr} & -m_{cr}\bar{r}_{cr}s\alpha \\
0 & 1 & 0 & 0 & 0 & 0 & -1 & 0 & 0 & 0 & 0 & 0 & 0 & 0 & -m_{cr}\bar{r}_{cr}c\alpha \\
0 & 0 & 1 & 0 & 0 & 0 & 0 & 1 & 0 & 0 & 0 & 0 & 0 & 0 & 0 \\
0 & 0 & 0 & 0 & 0 & 1 & 0 & 0 & -1 & 0 & 0 & 0 & 0 & 0 & 0 \\
0 & 0 & 0 & 0 & 0 & 0 & 1 & 0 & 0 & -1 & 0 & 0 & 0 & 0 & 0 \\
0 & 0 & 0 & 0 & 0 & 0 & 0 & 1 & 0 & 0 & 1 & 0 & 0 & 0 & 0 \\
0 & 0 & 0 & 0 & 0 & 0 & 0 & l & 0 & 0 & 0 & 0 & 0 & 0 & 0 \\
0 & 0 & 0 & 0 & 0 & ls\alpha & lc\alpha & 0 & 0 & 0 & 0 & 0 & 0 & m_{cr}\bar{r}_{cr}s\alpha & I_{cr_z} \\
0 & 0 & 0 & 0 & 0 & 0 & 0 & 0 & 0 & 0 & 0 & c\theta & s\theta & 0 & 0 \\
0 & 0 & 0 & 0 & 0 & 0 & 0 & r_c & 0 & 0 & 0 & -s\theta & c\theta & 0 & 0 \\
0 & 0 & 0 & 0 & 0 & r_c s\theta & -r_c c\theta & 0 & 0 & 0 & 0 & 0 & 0 & I_{c_z} & 0 \\
0 & 0 & 0 & 0 & 0 & 0 & 0 & 0 & 0 & 0 & 0 & 0 & 0 & r_c s\theta & 1 \\
0 & 0 & 0 & 0 & 0 & 0 & 0 & 0 & 0 & 0 & 0 & 0 & 0 & -r_c c\theta & 0
\end{Bmatrix}
\begin{Bmatrix}
f_{B_x} \\ f_{B_y} \\ f_{B_z} \\ N_y \\ N_z \\ f_{A_x} \\ f_{A_y} \\ f_{A_z} \\ f_{C_x} \\ f_{C_y} \\ f_{C_z} \\ M_{C_x} \\ M_{C_y} \\ \ddot{\theta} \\ \ddot{x}_B \\ \ddot{\alpha}
\end{Bmatrix} =
\begin{Bmatrix}
-P.A_p \\ 0 \\ -m_p g \\ m_{cr}\dot{\alpha}^2\bar{r}_{cr}c\alpha \\ -m_{cr}\dot{\alpha}^2\bar{r}_{cr}s\alpha \\ m_{cr}g \\ 0 \\ 0 \\ m_c g \\ \bar{r}_{cr}m_{cr}g \\ 0 \\ 0 \\ 0 \\ T_m \\ -r_c\dot{\theta}^2c\theta - l\dot{\alpha}^2c\alpha \\ -r_c\dot{\theta}^2s\theta + l\dot{\alpha}^2s\alpha
\end{Bmatrix}$$

A.2 Case II

$$\bar{\mathbf{A}}_{(\mathbf{II})} \cdot \bar{\mathbf{b}}_{(\mathbf{II})} = \bar{\mathbf{c}}_{(\mathbf{II})}$$

$$\begin{Bmatrix}
1 & 0 & 0 & 0 & 0 & 0 & 0 & 0 & 0 & 0 & 0 & 0 & m_p & 0 & 0 & 0 \\
0 & -1 & 0 & 1 & 0 & 0 & 0 & 0 & 0 & 0 & 0 & 0 & 0 & 0 & 0 & 0 \\
0 & 0 & 1 & 0 & -1 & 0 & 0 & 0 & 0 & 0 & 0 & 0 & 0 & 0 & 0 & 0 \\
1 & 0 & 0 & 0 & 0 & -1 & 0 & 0 & 0 & 0 & 0 & -m_{cr} & 0 & 0 & -m_{cr}\bar{r}_{cr}s\alpha & 0 \\
0 & 1 & 0 & 0 & 0 & 0 & -1 & 0 & 0 & 0 & 0 & 0 & 0 & 0 & -m_{cr}\bar{r}_{cr}c\alpha & 0 \\
0 & 0 & 1 & 0 & 0 & 0 & 0 & 1 & 0 & 0 & 0 & 0 & 0 & 0 & 0 & 0 \\
0 & 0 & 0 & 0 & 0 & 0 & 0 & 1 & 1 & 0 & 0 & 0 & 0 & 0 & 0 & 0 \\
0 & 0 & 0 & 0 & 0 & 0 & 0 & l & 0 & 0 & 0 & 0 & 0 & 0 & 0 & 0 \\
0 & 0 & 0 & 0 & 0 & ls\alpha & lc\alpha & 0 & 0 & 0 & 0 & 0 & m_{cr}\bar{r}_{cr}s\alpha & I_{cr_z} & 0 & 0 \\
0 & 0 & 0 & 0 & 0 & 0 & 0 & 0 & 0 & c\theta & s\theta & 0 & 0 & 0 & 0 & 0 \\
0 & 0 & 0 & 0 & 0 & 0 & 0 & r_c & 0 & -s\theta & c\theta & 0 & 0 & 0 & 0 & 0 \\
0 & 0 & 0 & 0 & 0 & r_c s\theta & -r_c c\theta & 0 & 0 & 0 & 0 & I_{c_z} & 0 & 0 & 0 & 0 \\
0 & 0 & 0 & 0 & 0 & 0 & 0 & 0 & 0 & 0 & 0 & r_c s\theta & 1 & ls\alpha & -1 & 0 \\
0 & 0 & 0 & 0 & 0 & 0 & 0 & 0 & 0 & 0 & 0 & -r_c c\theta & 0 & lc\alpha & 0 & -1 \\
0 & 0 & 0 & 0 & 0 & -1 & 0 & 0 & 0 & 0 & 0 & 0 & 0 & 0 & m_c & 0 \\
0 & 0 & 0 & 0 & 0 & 0 & -1 & 0 & 0 & 0 & 0 & 0 & 0 & 0 & 0 & m_c
\end{Bmatrix}
\begin{Bmatrix}
f_{B_x} \\ f_{B_y} \\ f_{B_z} \\ N_y \\ N_z \\ f_{A_x} \\ f_{A_y} \\ f_{A_z} \\ f_{C_x} \\ f_{C_y} \\ f_{C_z} \\ M_{C_x} \\ M_{C_y} \\ \ddot{\theta} \\ \ddot{x}_B \\ \ddot{\alpha} \\ \ddot{x}_C \\ \ddot{y}_C
\end{Bmatrix} =
\begin{Bmatrix}
-P.A_p \\ 0 \\ -m_p g \\ m_{cr}\dot{\alpha}^2\bar{r}_{cr}c\alpha \\ -m_{cr}\dot{\alpha}^2\bar{r}_{cr}s\alpha \\ m_{cr}g \\ m_c g \\ \bar{r}_{cr}m_{cr}g \\ 0 \\ 0 \\ 0 \\ T_m \\ -r_c\dot{\theta}^2c\theta - l\dot{\alpha}^2c\alpha \\ -r_c\dot{\theta}^2s\theta + l\dot{\alpha}^2s\alpha \\ f_{c_x} \\ f_{c_y}
\end{Bmatrix}$$

A.3 Case III

$$\bar{\mathbf{A}}_{(\mathbf{III})} \cdot \bar{\mathbf{b}}_{(\mathbf{III})} = \bar{\mathbf{c}}_{(\mathbf{III})}$$

$$\begin{Bmatrix}
1 & 0 & 0 & 0 & 0 & 0 & 0 & 0 & 0 & 0 & m_p & 0 & 0 & 0 & 0 & 0 \\
0 & 1 & 0 & -1 & 0 & 0 & 0 & 0 & 0 & 0 & 0 & 0 & 0 & 0 & 0 & 0 \\
0 & 0 & 1 & 0 & -1 & 0 & 0 & 0 & 0 & 0 & 0 & 0 & 0 & 0 & 0 & 0 \\
-1 & 0 & 0 & 0 & 0 & 1 & 0 & 0 & 0 & 0 & m_{cr} & m_{cr}\bar{r}_{cr}s\alpha & 0 & 0 & 0 & 0 \\
0 & -1 & 0 & 0 & 0 & 0 & 1 & 0 & 0 & 0 & 0 & m_{cr}\bar{r}_{cr}c\alpha & 0 & 0 & 0 & 0 \\
0 & 0 & 1 & 0 & 0 & 0 & 0 & 1 & 0 & 0 & 0 & 0 & 0 & 0 & 0 & 0 \\
0 & 0 & 0 & 0 & 0 & 0 & 0 & l & 0 & 0 & 0 & 0 & 0 & 0 & 0 & 0 \\
0 & 0 & 0 & 0 & 0 & ls\alpha & lc\alpha & 0 & 0 & 0 & m_{cr}\bar{r}_{cr}s\alpha & I_{cr_z} & 0 & 0 & 0 & 0 \\
0 & 0 & 0 & 0 & 0 & 0 & 0 & -1 & 1 & 0 & 0 & 0 & 0 & 0 & 0 & 0 \\
0 & 0 & 0 & 0 & 0 & C_1 & C_2 & C_3 & 0 & -I_{c_z} - I_{m_z} & 0 & 0 & -m_c e_c s\Gamma & -m_c e_c s\beta c\Gamma & -I_{c_z} s\Gamma & 0 \\
0 & 0 & 0 & 0 & 0 & 0 & 0 & 0 & 0 & r_c c\Gamma s\theta & 1 & ls\alpha & -1 & 0 & 0 & C_4 \\
0 & 0 & 0 & 0 & 0 & 0 & 0 & 0 & 0 & C_5 & 0 & lc\alpha & 0 & -1 & C_6 & C_7 \\
0 & 0 & 0 & 0 & 0 & -1 & 0 & 0 & 0 & 0 & 0 & 0 & m_c & 0 & 0 & 0 \\
0 & 0 & 0 & 0 & 0 & 0 & -1 & 0 & 0 & 0 & 0 & 0 & 0 & m_c & 0 & 0 \\
0 & 0 & 0 & 0 & 0 & -h_p C_1 r_c^{-1} & -h_p C_2 r_c^{-1} & -h_p C_3 r_c^{-1} & 0 & 0 & 0 & 0 & 0 & 0 & I_{c_x} c\Gamma c\theta & I_{c_x} s\theta \\
0 & 0 & 0 & 0 & 0 & C_8 & C_9 & C_{10} & 0 & 0 & 0 & 0 & C_{11} & C_{12} & -I_{c_y} c\Gamma s\theta & I_{c_y} c\theta
\end{Bmatrix}
\begin{Bmatrix}
f_{B_x} \\ f_{B_y} \\ f_{B_z} \\ N_y \\ N_z \\ f_{A_x} \\ f_{A_y} \\ f_{A_z} \\ f_{C_z} \\ \ddot{\theta} \\ \ddot{x}_B \\ \ddot{\alpha} \\ \ddot{x}_C \\ \ddot{y}_C \\ \ddot{\beta} \\ \ddot{\Gamma}
\end{Bmatrix} =$$

$$\begin{Bmatrix}
-P.A_p \\
0 \\
-m_p g \\
-m_{cr}\dot{\alpha}^2 \bar{r}_{cr} c\alpha \\
m_{cr}\dot{\alpha}^2 \bar{r}_{cr} s\alpha \\
m_{cr} g \\
\bar{r}_{cr} m_{cr} g \\
0 \\
m_c g \\
\dot{\beta}\dot{\Gamma} I_{c_z} c\Gamma - T_m \\
C_{13} \\
C_{14} \\
0 \\
0 \\
I_{c_x}(\dot{\beta}\dot{\Gamma} s\Gamma c\theta + \dot{\beta}\dot{\theta} c\Gamma s\theta - \dot{\Gamma}\dot{\theta} c\theta) + (\dot{\beta} s\Gamma + \dot{\theta})(\dot{\Gamma} c\theta - \dot{\beta} c\Gamma s\theta)(I_{c_y} - I_{c_z}) \\
I_{c_y}(\dot{\beta}\dot{\theta} c\Gamma c\theta + \dot{\Gamma}\dot{\theta} s\theta - \dot{\beta}\dot{\Gamma} s\Gamma s\theta) + (\dot{\beta} s\Gamma + \dot{\theta})(\dot{\Gamma} s\theta + \dot{\beta} c\Gamma c\theta)(I_{c_z} - I_{c_x})
\end{Bmatrix} \tag{A.1}$$

where:

$$\begin{aligned}
C_1 &= -r_c c\Gamma s\theta \\
C_2 &= r_c(c\beta c\theta - s\beta s\Gamma s\theta) \\
C_3 &= r_c(c\beta s\Gamma s\theta - s\beta c\theta) \\
C_4 &= r_c s\Gamma c\theta + h_p c\Gamma \\
C_5 &= r_c(s\beta s\Gamma s\theta - c\beta c\theta) \\
C_6 &= r_c(s\beta s\theta - c\beta s\Gamma c\theta) - h_p c\beta c\Gamma \\
C_7 &= -r_c s\beta c\Gamma c\theta + h_p s\beta s\Gamma \\
C_8 &= r_c s\Gamma + h_p c\Gamma c\theta \\
C_9 &= -r_c s\beta c\Gamma + h_p(s\beta s\Gamma c\theta + c\beta s\theta) \\
C_{10} &= r_c c\beta c\Gamma + h_p(s\beta s\theta - c\beta s\Gamma c\theta) \\
C_{11} &= -m_{cr} e_c c\Gamma s\theta \\
C_{12} &= m_{cr} e_c(c\beta c\theta - s\beta s\Gamma s\theta) \\
C_{13} &= \dot{\Gamma}^2(h_p s\Gamma - r_c c\Gamma c\theta) + r_c\dot{\theta}(2\dot{\Gamma} s\Gamma s\theta - \dot{\theta} c\Gamma c\theta) - l\dot{\alpha}^2 c\alpha \\
C_{14} &= l\dot{\alpha}^2 s\alpha - r_c\dot{\theta}^2(c\beta s\theta + s\beta s\Gamma c\theta) - \dot{\beta}^2(r_c c\beta s\theta + r_c s\theta s\Gamma c\theta + h_p s\beta c\Gamma) - \dot{\Gamma}^2(r_c s\beta s\Gamma c\theta + h_p s\beta c\Gamma) \\
&\quad -2r_c\dot{\theta}\dot{\beta}(s\beta c\theta + c\beta s\Gamma s\theta) + 2\dot{\beta}\dot{\Gamma}(r_c c\beta c\Gamma c\theta - h_p c\beta s\Gamma) - 2r_c\dot{\theta}\dot{\Gamma} s\beta c\Gamma s\theta
\end{aligned}$$

In these equations: $s\theta = \sin\theta$; $c\theta = \cos\theta$; $s\alpha = \sin\alpha$; $c\alpha = \cos\alpha$; $s\beta = \sin\beta$; $c\beta = \cos\beta$; $s\Gamma = \sin\Gamma$; $c\Gamma = \cos\Gamma$.

Appendix B

Journal papers

B.1 [J1] - *International Journal of Mechanics*, Vol.1 (4), 2007, pp. 36-43.

INTERNATIONAL JOURNAL OF MECHANICS

Dynamic Modeling of Hermetic Reciprocating Compressors, Combining Multibody Dynamics, Finite Elements Method and Fluid Film Lubrication

Edgar A. Estupiñan and Ilmar F. Santos

***Abstract*—**A multibody dynamic model of the main mechanical components of a hermetic reciprocating compressor is presented in this work. The dynamics of the mechanical components are described with help of Dynamics of Multibody Systems (rigid components) and Finite Element Method (flexible components). Some of the mechanical elements are supported by fluid film bearings where the hydrodynamics interaction forces are described by the modified Reynolds equation. The system of nonlinear equations is numerically solved, taking into account the lateral and tilting vibration of the center of the crank. Particularly, in this study the main focus is on the lubrication behavior of the upper and lower bearings of the crankshaft, considering hydrodynamic lubrication conditions. The behavior of the orbits and the pressure distribution in the journal bearings is presented giving some insights into design parameters, such as, maximal fluid film pressure, minimum fluid film thickness and maximum vibration levels.

***Keywords*—** Multibody dynamics, hydrodynamic lubrication, journal bearings, hermetic compressor.

I. Introduction

Small-scale hermetic reciprocating compressors are widely used to compress coolant gas in household refrigerators and air-conditioners. Almost since the 60's these small machines became a necessary appliance in every household in the industrialized countries. Since then, a lot of research has been done to optimize the design and to improve the thermal and mechanical efficiency. Hermetic reciprocating compressors use pistons that are driven directly through a slider-crank mechanism, converting the rotating movement of the rotor to an oscillating motion. In this type of compressors, motor and compressor are directly coupled on the same shaft and the assembly is installed inside a welded steel shell. A schematic view of a hermetic reciprocating compressor used in household refrigerators is shown in Fig. 1.

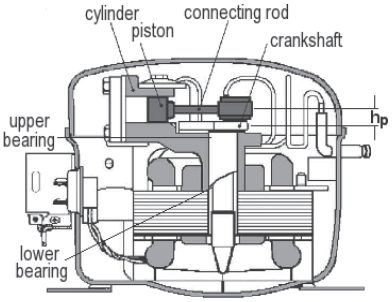

Fig. 1. Hermetic reciprocating compressor

The study and optimization of the dynamic behavior of reciprocating compressors, taking in account the hydrodynamics of bearings is of significant importance for the development of new prototypes. The performance of the bearings affects key functions such as durability, noise and vibration of the compressor. Optimization of the behavior of journal bearings by means of numerical simulation may reduce development costs for prototype testing work significantly.

Several computational models for the analysis of small reciprocating compressors can be found in the literature. They range from simple simulations including steady-state energy balance until more complex models of unsteady analysis of the heat and work transfer and thermal and fluid dynamic analysis. A complete literature review of previous studies with focus on compressor simulation models is included in [1]. Some of these studies require numerical simulations of the refrigerant flow through the valves and inside the cylinder during the compression cycle [2], whereas other studies focus mainly on the dynamics of motion in steady and transient conditions [3]. For instance, a study that included the coupling of fluid-structure dynamics to analyze the dynamics of piston is presented in [4]. Reference [5] shows an analytical model of the coupled dynamic behavior of the piston and crankshaft, with comparisons between a finite bearing model and a short

Manuscript received April 29, 2007: Revised version received Octob. 3, 2007. The authors gratefully acknowledge the support given by the Programme Alβan, the European Union Programme of High Level Scholarships for Latin America, scholarship No. E06D101992CO.

Edgar A. Estupiñan (corresponding author) is with the Mechanical Engineering Department, Technical University of Denmark, Kgs. Lyngby, DK 2800 Denmark. (phone: +45- 4525-5678; fax: +45-4593-1475; e-mail: eep@mek.dtu.dk).

Ilmar F. Santos, is Associate Professor of the Mechanical Engineering Department, Technical University of Denmark, Kgs. Lyngby, DK 2800 Denmark. (e-mail: ifs@mek.dtu.dk).

bearing approach. In the same study, a numerical procedure combining Newton-Raphson method and the successive over relaxation scheme to solve the equations was presented. In the study carried out by Cho and Moon [4], a time-incremental numerical algorithm to solve a finite differences model for the estimation of the oil film pressure is coupled with a finite element model for the computation of the structural deformation of the piston.

Although most of the work done related to modeling of compressors is related to the thermal and fluid dynamic behavior, in this work the main focus and contribution are on the developing of a multibody dynamic model that represents the dynamics of the main mechanical components of hermetic compressors. This model is coupled with a finite element model of the rotor, where the hydrodynamic interaction forces are computed using analytical solutions of Reynolds equation. The elastohydrodynamic theory, which takes into account the bearing and housing flexibility, is not considered in this paper, since it is presented only in very special cases.

II. Mathematical Modeling

In this section the formulation of representative equations describing the mathematical simulation model for a hermetic compressor is developed. The motion of the piston has been modeled as particle, the motion of the connecting rod and crank as rigid bodies and the shaft is modeled as a flexible body via finite elements. The motion equations for the piston connecting-rod crank system are formulated using the Newton-Euler's method. Fig. 2 shows a sketch indicating the inertial referential frame system XYZ and the main angles of rotation for the moving reference frames.

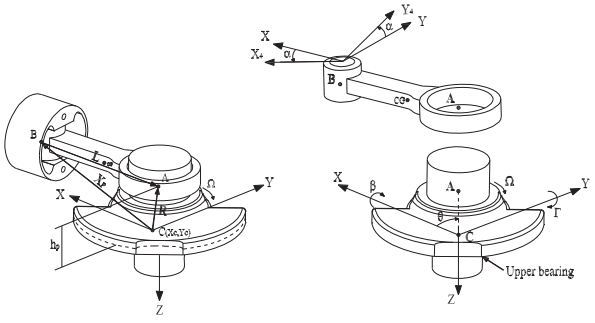

Fig. 2. Piston – connecting rod – crank system. Geometry and reference frames

A. Reference Frames

One inertial reference frame (I_{XYZ}) and four moving reference frames (B_1, B_2, B_3 and B_4) have been defined. The reference frames B_1, B_2 and B_3 are attached to the crank to describe the tilting and rotational movement of the crank and the reference frame B_4 is attached to the connecting rod. B_1 ($X_1Y_1Z_1$) is obtained by rotating I the angle β around X axis; B_2 ($X_2Y_2Z_2$), is obtained by rotating B_1 the angle Γ around Y_1 axis; B_3 ($X_3Y_3Z_3$), is obtained by rotating B_2 the angle θ around Z_2 axis and B_4 ($X_4Y_4Z_4$), is obtained by rotating I the angle α around Z axis.

B. Constraint Equations

A constraint equation that takes into account lateral displacements and tilting oscillations of the center of the crank is given in (1). A simplified sketch illustrating how the basic elements of the system are connected is shown in Figure 2b.

$$ {}_I\mathbf{X}_p + {}_I\mathbf{L} = {}_I\mathbf{R} + {}_I\mathbf{C} \tag{1}$$

where: ${}_I\mathbf{R} = \mathbf{T}_\beta^T \cdot \mathbf{T}_\Gamma^T \cdot \mathbf{T}_\theta^T \cdot {}_{B_3}\mathbf{R}$; ${}_{B_3}\mathbf{R} = \left\{ \begin{array}{ccc} r_c & 0 & -h_p \end{array} \right\}^{\mathrm{T}}$

C. Kinematics

The absolute angular velocity ($\boldsymbol{\omega}$) written with help of B_3, is given by:

$$ {}_{B_3}\boldsymbol{\omega} = {}_{B_3}\dot{\boldsymbol{\beta}} + {}_{B_3}\dot{\boldsymbol{\Gamma}} + {}_{B_3}\dot{\boldsymbol{\theta}} \tag{2}$$

where: ${}_{B_3}\dot{\boldsymbol{\beta}} = \mathbf{T}_\theta \cdot \mathbf{T}_\Gamma \cdot \mathbf{T}_\beta \cdot {}_I\dot{\boldsymbol{\beta}}$; ${}_{B_3}\dot{\boldsymbol{\Gamma}} = \mathbf{T}_\theta \cdot \mathbf{T}_\Gamma \cdot {}_{B_1}\dot{\boldsymbol{\Gamma}}$; ${}_{B_3}\dot{\boldsymbol{\theta}} = \mathbf{T}_\theta \cdot {}_{B_2}\dot{\boldsymbol{\theta}}$

The velocities and accelerations of the piston ($\dot{x}_B, \ddot{x}_B$) and the connecting rod ($\dot{\alpha}, \ddot{\alpha}$), are obtaining when the constraint equation (1) is differentiated once and twice respectively, obtaining:

$$ \begin{bmatrix} 1 & l\sin\alpha \\ 0 & l\cos\alpha \end{bmatrix} \begin{Bmatrix} \dot{x}_B \\ \dot{\alpha} \end{Bmatrix} = \begin{Bmatrix} v_1 \\ v_2 \end{Bmatrix} \tag{3}$$

$$ \begin{bmatrix} 1 & l\sin\alpha \\ 0 & l\cos\alpha \end{bmatrix} \begin{Bmatrix} \ddot{x}_B \\ \ddot{\alpha} \end{Bmatrix} = \begin{Bmatrix} a_1 \\ a_2 \end{Bmatrix} \tag{4}$$

where, the variables v_1, v_2, a_1, a_2 are giving in appendix (A).

D. Equations of Motion

The equations of motion are formulated using Newton-Euler's method [6]. The equations of motion for each body are given in Table I.

The equations of motion for the multibody dynamic model may be written in a matrix form as in (10), where vector $\bar{\mathbf{f}}$ contains the unknown variables such as: reaction forces, reaction moments and accelerations of the system. This matrix system will be coupled to the equations from the finite element formulation of the crankshaft, which is explained later in section IV.

$$ \overline{\mathbf{A}} \cdot \bar{\mathbf{f}} = \bar{\mathbf{c}} \tag{10}$$

TABLE I
EQUATIONS OF MOTION

Body	*Force Equation*	*Moment Equation*
Crank	$\sum {}_I\mathbf{F} = m_c \cdot {}_I\bar{\mathbf{a}}_c = {}_I\mathbf{F}_A = m_c\{\ddot{x}_C, \ddot{y}_C\}^{\mathrm{T}}$ (5)	$\sum {}_{B_3}\mathbf{M}_O = {}_{B_3}\mathbf{r}\times{}_{B_3}\mathbf{F}_A + {}_{B_3}\mathbf{T}_m$ (6) $= {}_{B_3}\mathbf{I}_O \frac{d}{dt}\left({}_{B_3}\boldsymbol{\omega}\right) + {}_{B_3}\boldsymbol{\omega}\times\left({}_{B_3}\mathbf{I}_O\times{}_{B_3}\boldsymbol{\omega}\right) + m_c\cdot{}_{B_3}\bar{\mathbf{r}}_{C-cm}\times{}_{B_3}\mathbf{a}_O$ where: ${}_{B_3}\mathbf{F}_A = \mathbf{T}_\theta\cdot\mathbf{T}_\Gamma\cdot\mathbf{T}_\beta\cdot{}_I\mathbf{F}_A$; ${}_{B_3}\mathbf{T}_m = \{0, 0, T_z\}^{\mathrm{T}}$; ${}_{B_3}\bar{\mathbf{r}}_{C-cm} = \{e_c, 0, 0\}^{\mathrm{T}}$
Connecting rod	$\sum {}_I\mathbf{F} = m_{cr}\cdot{}_I\bar{\mathbf{a}}_{cr} = {}_I\mathbf{F}_A + {}_I\mathbf{F}_B$ (7) where: ${}_I\bar{\mathbf{a}}_{cr} = {}_I\mathbf{a}_B + {}_I\dot{\boldsymbol{\alpha}}\times{}_I\bar{\mathbf{r}}_{cr} + {}_I\boldsymbol{\alpha}\times({}_I\boldsymbol{\alpha}\times{}_I\bar{\mathbf{r}}_{cr}) + {}_I\ddot{\boldsymbol{\alpha}}\times{}_I\bar{\mathbf{r}}_{cr}$ $= \begin{Bmatrix} \ddot{x}_B + \bar{r}_{cr}\left(\dot{\alpha}^2\cos\alpha + \ddot{\alpha}\sin\alpha\right) \\ \bar{r}_{cr}\left(\ddot{\alpha}\cos\alpha - \dot{\alpha}^2\sin\alpha\right) \\ 0 \end{Bmatrix}$	$\sum {}_{B_4}\mathbf{M}_B = {}_{B_4}\mathbf{l}\times{}_{B_4}\mathbf{F}_A$ (8) $= {}_{B_4}\mathbf{I}_{cr}\times\frac{d}{dt}\left({}_{B_4}\dot{\boldsymbol{\alpha}}\right) + {}_{B_4}\dot{\boldsymbol{\alpha}}\times\left({}_{B_4}\mathbf{I}_{cr}\times{}_{B_4}\dot{\boldsymbol{\alpha}}\right) + m_{cr}\cdot{}_{B_4}\bar{\mathbf{r}}_{cr}\times{}_{B_4}\mathbf{a}_B$ where: ${}_{B_4}\mathbf{F}_A = \mathbf{T}_\alpha\,{}_I\mathbf{F}_A$; ${}_{B_4}\mathbf{a}_B = \mathbf{T}_\alpha\,{}_I\mathbf{a}_B$; ${}_I\mathbf{a}_B = \{\ddot{x}_B, 0, 0\}^{\mathrm{T}}$
Piston	$\sum {}_I\mathbf{F}_B = m_p\cdot{}_I\mathbf{a}_B = {}_I\mathbf{F}_B + {}_I\mathbf{N} + {}_I\mathbf{F}_p$ (9) where: ${}_I\mathbf{F}_p = \{P_g\cdot A_p, 0, 0\}^{\mathrm{T}}$	

where:

$\bar{\mathbf{f}} = \left\{f_{B_x}, f_{B_y}, f_{B_z}, N_y, N_z, f_{A_x}, f_{A_y}, f_{A_z}, f_{C_z}, \ddot{\theta}, \ddot{x}_B, \ddot{\alpha}, \ddot{q}_1, \ddot{q}_2, \ddot{q}_3, \ddot{q}_4\right\}^{\mathrm{T}}$

and $\ddot{q}_1, \ddot{q}_2, \ddot{q}_3, \ddot{q}_4$, correspond to the angular accelerations of the crank center.

A. Modeling of the Rotor

The main rotor-shaft of the compressor, which drives the crank-connecting rod-piston system, is modeled as a flexible body via finite elements method [7]. The global equation of motion described in the inertial reference frame is given by:

$$\overline{\overline{\mathbf{M}}}.\ddot{\mathbf{q}} = \underbrace{\overline{\overline{\mathbf{F}}} - \overline{\overline{\mathbf{D}}}.\dot{\mathbf{q}} - \overline{\overline{\mathbf{K}}}.\mathbf{q}}_{\overline{\overline{\mathbf{f}}}} \tag{11}$$

where $\overline{\overline{\mathbf{F}}}$, is the vector that includes the external forces on the rotor such as: preload forces, rotor unbalance forces and the fluid film bearing forces.

III. FLUID FILM FORCES

The main geometrical relations of a journal bearing are shown in Fig. 3. The governing equation for the pressure distribution of the oil film in dynamically loaded journal bearings may be obtained from the general formulation of Reynolds' equation [8]. The modified Reynolds equation for dynamically loaded journal bearings is given by (12), where, $\dot{\phi}$ is the rotational speed of the journal center about the bearing center and ε is the relative eccentricity. The fluid film thickness may be calculated using: $h_b = c_b(1+\varepsilon\cos\varphi)$, where φ is the angle measured from the location of the maximum film thickness.

$$\frac{\partial}{\partial\varphi}\left(\frac{h_b^3}{\mu}\frac{\partial p}{\partial\varphi}\right) + r_b^2\frac{\partial}{\partial z}\left(\frac{h_b^3}{\mu}\frac{\partial p}{\partial z}\right) = 12c_b r_b^2\left[\frac{\partial\varepsilon}{\partial t}\cos\varphi + \varepsilon\sin\varphi\left(\frac{\partial\phi}{\partial t} - \frac{\Omega}{2}\right)\right] \tag{12}$$

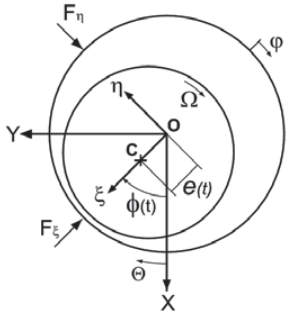

Fig. 3. Journal bearing geometry

With dynamically loaded bearings the eccentricity and attitude angle will vary through the loading cycle. The pressure generated when a journal bearing is dynamically loaded can be determined if the normal squeeze velocity ($\dot{\varepsilon}$) and the rotational velocities ($\dot{\phi}, \Omega$) are known at any eccentricity ratio. Complete solutions of (12) may be obtained

numerically, and solutions for limited cases may be also obtained analytically. In this work analytical solutions for the short-width bearing and infinitely-long-width bearing theories have been used. The short-journal-bearing theory assumes that the variation of pressure is more significant in the axial direction than in the circumferential direction and therefore the first term in (12) can be neglected. In contrast, for an infinitely long-width-journal-bearing, the pressure in the axial direction is assumed to be constant, therefore, in this case, the side-leakage term, i.e., the second term in (12), can be neglected. For each one of these two particular cases, the fluid film pressure distribution can be easily computed, analytically integrating the Reynolds equation and similarly, the journal bearing forces in ξ, η coordinates can be calculated, integrating the pressure distribution analytically obtained. If the pressure is integrated over all the fluid film around the bearing (i.e, $0 \le \varphi \le 2\pi$), this solution is known as a full Sommerfeld solution. However, if the analysis is limited to the convergent film (i.e., $0 \le \varphi \le \pi$), this is known as a half Sommerfeld solution. The analytical expressions used in this paper for the computation of the radial and transversal fluid film forces (F_ξ, F_η), for a long and a short journal bearing, are giving in [9].

IV. Numerical Solution

The equation of motions for each connected body of the multibody system together with the *FEM* model of the shaft and the analytical expressions for the fluid film forces yield to a system of high complexity and non-linearity. The numerical algorithm implemented is shown in Fig. 4. Considering that the system has a "stiff" behavior because of the combination of a rigid body model with a finite element model, a Newmark implicit method combined with a predictor-corrector approach [10], is used in this work. The simulation procedure is summarized in the following main steps:

Input data and starting values. In this part the geometrical and physical parameters must be given, such as, physical dimensions, rotational speed, masses, inertias, preloads, initial displacements and initial velocities.

Pre-processing. This part includes the generation of structural matrices for the multibody model (**MBD** module) and the matrices of the flexible rotor (**FEM** module). Based on the initial conditions, initial fluid film forces are computed using the **FFF** module.

Numerical computation. This part includes the coupling of matrices, the computation of the journal bearing forces at each time step and the numerical solution of the global system. At each time step, new fluid film forces are computed and included in the global matrix system (13) where the equilibrium has to be achieved. In (13), the matrix $\hat{\mathbf{M}}$ is formed by the matrix $\overline{\overline{\mathbf{M}}}$ of size $ndof \times ndof$, coupled to the matrix $\overline{\mathbf{A}}$ of size 16×16 in the degrees of freedom related to the linear and angular accelerations of the crank center node ($\ddot{q}_1, \ddot{q}_2, \ddot{q}_3, \ddot{q}_4$). Thus, the final size of the global mass matrix ($\hat{\mathbf{M}}$) is $ndof + 12$. Similarly, in (13) the global right hand side vector, $\hat{\mathbf{Q}}$, is formed by coupling the resultant right hand side vector, $\overline{\overline{\mathbf{f}}}$, in (11), to the vector $\overline{\mathbf{c}}$, in (10). The iterative equations to solve the global system (13), by using the Newmark implicit method, are given by (14)-(16).

$$\hat{\mathbf{M}} \cdot \left\{\hat{\mathbf{f}}, \ddot{\mathbf{q}}\right\}^{\mathrm{T}} = \hat{\mathbf{Q}} \tag{13}$$

where:
$\hat{\mathbf{f}} = \left\{f_{B_x}, f_{B_y}, f_{B_z}, N_y, N_z, f_{A_x}, f_{A_y}, f_{A_z}, f_{C_z}, \ddot{\theta}, \ddot{x}_B, \ddot{\alpha}\right\}^{\mathrm{T}}$ and
$\ddot{\mathbf{q}} = \left\{\ddot{q}_1, \ddot{q}_2, ..., \ddot{q}_{ndof}\right\}^{\mathrm{T}}$.

$$\left\{\hat{\mathbf{f}}_{t_{i+1}}, \ddot{\mathbf{q}}_{t_{i+1}}\right\}^{\mathrm{T}} = \hat{\mathbf{M}}^{-1}_{t_{i+1}} \cdot \hat{\mathbf{Q}}_{t_{i+1}} \tag{14}$$

$$\dot{q}_{t_{i+1}} = \dot{q}_{t_i} + h\left[\ (1-\hat{\gamma})\ddot{q}_{t_i} + \hat{\gamma}\ddot{q}_{t_{i+1}}\ \right] \tag{15}$$

$$q_{t_{i+1}} = q_{t_i} + h\dot{q}_{t_i} + \frac{h^2}{2}\left[\ (1-2\hat{\beta})\ddot{q}_{t_i} + 2\hat{\beta}\ddot{q}_{t_{i+1}}\ \right] \tag{16}$$

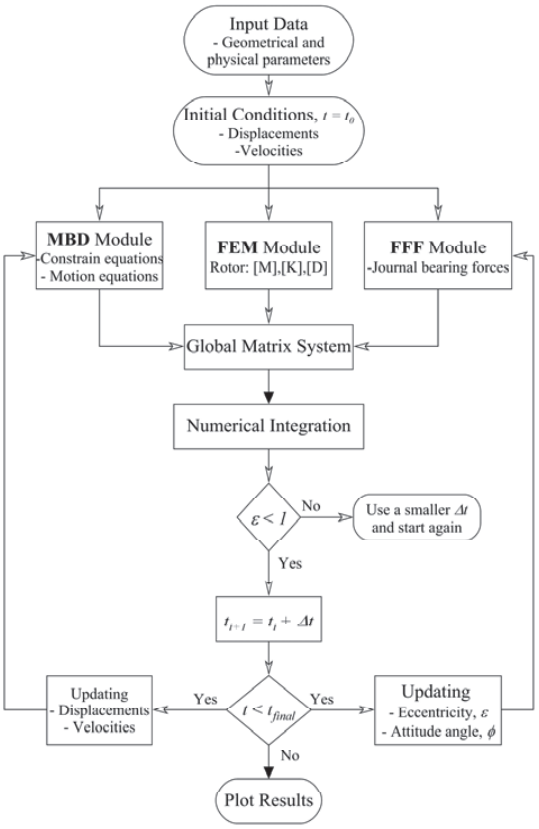

Fig. 4. Flowchart of the numerical computer code

To compute $\ddot{q}_{t_{i+1}}$, the load vector $\hat{\mathbf{Q}}_{t_{i+1}}$ must be estimated previously, which implies to calculate the vector of journal bearing forces ${}_b\mathbf{Q}_{t_{i+1}}$, which depends on the positions and velocities at the time t_{i+1}. Therefore, initial values for $\dot{q}^0_{t_{i+1}}$ and $q^0_{t_{i+1}}$ are predicted by using the Heun's explicit method. Then, $\ddot{q}^1_{t_{i+1}}$ can be initially estimated by using (14) and then, $\dot{q}^1_{t_{i+1}}$ and $q^1_{t_{i+1}}$ can be calculated using (15) and (16) respectively. With these new estimated values, the journal bearing forces are updated and using again (14) a new estimation of $\ddot{q}^2_{t_{i+1}}$ can be obtained, and so on until the difference of two consecutive values is smaller than the prescribed tolerance given. Additionally, by using the explicit Euler method, the crank angle θ_{t_i} and the instantaneous angular velocity $\dot{\theta}_{t_i}$ are estimated at each time step.

Post-processing. This part includes the generation of plots of journal bearing orbits, journal bearing forces, maximum oil film pressure, minimum fluid film thickness and reaction forces as a function of the instantaneous crank angle.

V. Numerical Results

The main geometrical dimensions and physical properties of the reciprocating compressor used for the numerical simulations are given in Table II. The curve of gas pressure (Pg) as function of the crank angle, used for the simulations in this work, is giving in [4] and is shown in Fig. 5. An experimental curve of motor torque for a typical motor of a hermetic compressor is taken from [1] and shown in Fig. 6.

The following results were obtained, using a computer code implemented according to the flow chart of Fig. 4 and using a time step of $\Delta t = 1e-6$ s to warranty the convergence of the solution.

TABLE II.
MAIN GEOMETRICAL AND PHYSICAL PARAMETERS

Radius crank-pin center	$r_c = 7.5$ *mm*
Radius of bearings	$r_b = 8$ *mm*
Width of bearings	$l_b = 6$ *mm*
Journal clearance	$c_b = 15$ μm
Length of crank pin	$h_p = 10$ *mm*
Distance between bearings	$L = 80$ *mm*
Moments of inertia of motor-rotor	I_x, $I_y = 0.4\text{x}10^{-3}$ *kg.m*^{2}, $I_z = 0.1\text{x}10^{-2}$ *kg.m*^{2}
Diameter of piston	$D_p = 23$ *mm* ($A_p = 415.5$ *mm*^{2})
Mass of the piston	$m_p = 0.043$ *kg*
Lubricant viscosity	$\mu = 0.005$ *Pa.s*
Angular velocity	$\Omega = 312$ *rad/s* (2980 *rpm)*
Crank unbalance	$m_{ub} = 0.05$ *kg*, $r_{ub} = 5$ *mm*

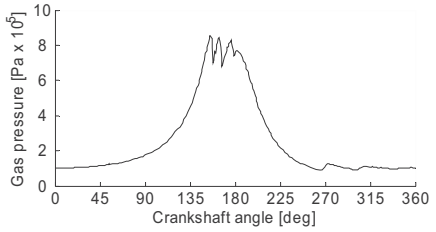

Figure 5. Curve of the gas pressure (P_g) as a function of the crankshaft angle

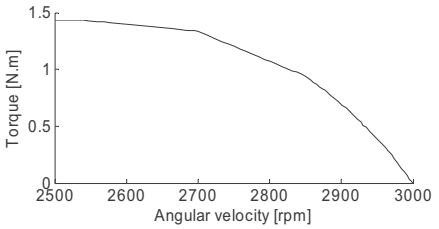

Fig. 6. Curve of the motor torque (T_m) as a function of the angular velocity.

Fig. 7 shows the journal bearing forces for the upper and

lower bearing. It can be observed from this figure that the maximum forces are found when the piston is close to the top dead center (i.e., when the pressure inside the cylinder is maximal). It can be also noticed a transient oscillation, damped a few cycles, and which is more evident for the lower bearing due to the lower values of the bearing forces.

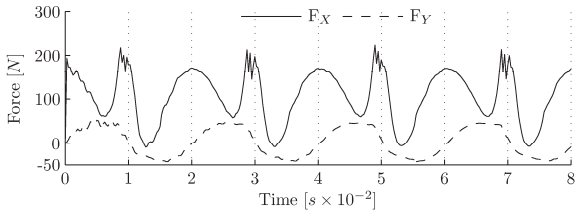

(a) Upper bearing

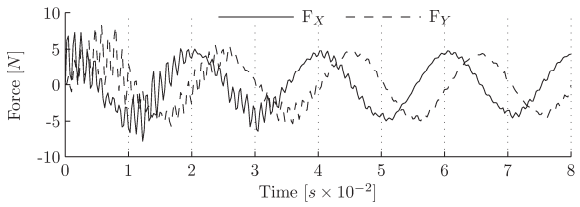

(b) Lower bearing

Fig. 7. Journal bearing forces

The minimum fluid film thickness is plotted in Fig. 8, which shows that the lowest values of oil film thickness are found during the compression cycle, approximately 65º before the piston reaches the top dead center (i.e., when $\theta \approx 115^o, \theta \approx 475^o, \theta \approx 835^o, \ldots$).

The maximum pressure is shown in Fig. 9, where it can be seen that the highest pressure values are found in the intervals between the times when the minimum fluid film thickness is reached at each cycle and the top dead centre position ($\theta \approx 180^o, \theta \approx 540^o, \theta \approx 900^o, \ldots$). This plot, shows the maximum pressure computed for two different lengths ($h_p = 0$ and $h_p = 10$mm) and it is observed a transient oscillation when the length of the crank pin is used, which comes from higher vibration modes of the flexible rotor influenced by the tilting oscillations of the crank.

Fig. 10 compares the minimum film thickness using a length of the crank pin of $h_p = 10$mm and $h_p = 0$. It can be observed in this figure that the difference between the lowest values of minimum film thickness could be as high as 18% (e.g., at $\theta \approx 1180^o$). Therefore, the length of the crank pin is a parameter that should be included in the calculations, particularly when the tilting oscillations are considered in the model.

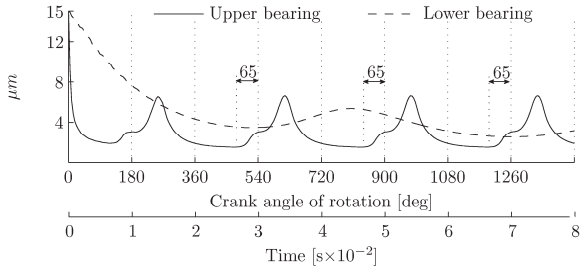

Fig. 8. Minimum fluid film thickness for the upper and lower bearing

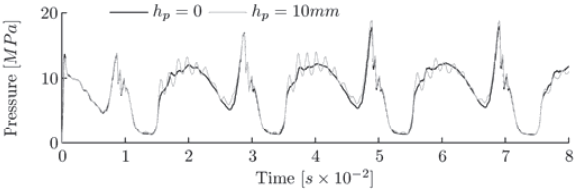

Fig. 9. Maximum fluid film pressure in upper journal bearing

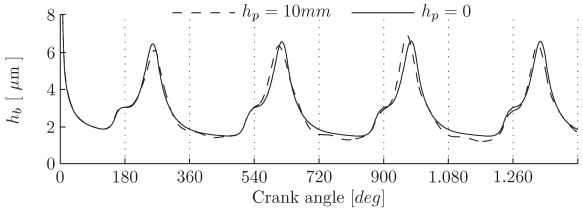

Fig. 10. Influence of the crank pin length (h_p) in the computation of the minimum fluid film thickness

Fig. 11 shows orbits of the upper bearing obtained for cases with different amount of unbalance of the crank. It can be seen in this figure that the orbit of the journal tends to be bigger when the amount of unbalance increases, but the stationary position around which the orbit is generated does not change, which is expected because no additional static forces have been added. The orbits obtained has a similar shape compared to orbits predicted theoretically in several studies related to the analysis of main journal bearings of internal combustion engines [11], [12].

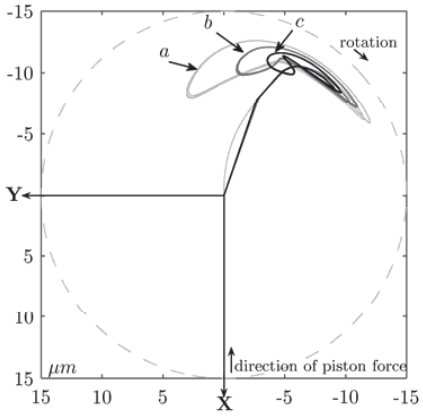

Fig. 11. Orbits of upper journal bearing, varying the amount of crank unbalance (m_{ub}). (a) m_{ub}= 0.05kg, (b) m_{ub}= 0.05kg, (c) m_{ub}= 0kg.

VI. Conclusion

In the model of the compressor developed, the lateral and tilting vibration of the crank have been included. Therefore and considering that the oil film thickness is only a few micrometers thick, more precise estimations of the journal bearing forces and minimum film thickness are obtained. The simulations were carried out for a short bearing, with a width to radius ratio equal to 0.75, therefore the use of the short bearing approach was preferred for this study. The maximum forces and the minimum fluid film thickness are obtained when the piston is close to the top dead centre.

The influence of the amount of unbalance was studied and it was found that, although it influences the orbit of motion of the journal, the journal forces and the minimum film thickness do not change significantly. The consideration that the reaction forces coming from the crank pin are out of the plane of the centre of mass of the crank, was taking into account including in the equations the crank pin length. The results showed differences up to 20% for the minimum film thickness and 5% for the maximum pressure when the length of the crank was included in the equations, due mainly to the increase in the tilting oscillations of the crank.

Appendix

(A). KINEMATIC VARIABLES

$$v_1 = -r_c(\dot{\Gamma} s\Gamma c\theta + \dot{\theta} c\Gamma s\theta) - h_p \dot{\Gamma} c\Gamma + \dot{x}_C$$

$$v_2 = r_c\dot{\beta}(c\beta s\Gamma c\theta - s\beta s\theta) + r_c\dot{\theta}(c\beta c\theta - s\beta s\Gamma s\theta) + \dot{\Gamma}(r_c s\beta c\Gamma c\theta - h_p s\beta s\Gamma) + \dot{\beta} h_p c\beta c\Gamma + \dot{y}_C$$

$$a_1 = -r_c\ddot{\Gamma} s\Gamma c\theta + \dot{\Gamma}^2(h_p s\Gamma - r_c c\Gamma c\theta) + 2r_c\dot{\theta}\dot{\Gamma} s\Gamma s\theta - r_c\dot{\theta}_2 c\Gamma c\theta - h_p\ddot{\Gamma} c\Gamma - r_c\ddot{\theta} c\Gamma s\theta - l\dot{\alpha}^2 c\alpha + \ddot{x}_C$$

$$a_2 = -r_c\dot{\theta}^2(c\beta s\theta + s\beta s\Gamma c\theta) - \dot{\beta}^2(r_c c\beta s\theta + r_c s\beta s\Gamma c\theta + h_p s\beta c\Gamma) - \dot{\Gamma}^2(r_c s\beta s\Gamma c\theta + h_p s\beta c\Gamma) + \ddot{\beta}(h_p c\beta c\Gamma - r_c s\beta s\theta + r_c c\beta s\Gamma c\theta) + \ddot{\Gamma}(r_c s\beta c\Gamma c\theta - h_p s\beta s\Gamma) - 2r_c\dot{\theta}\dot{\beta}(s\beta c\theta + c\beta s\Gamma s\theta) + 2\dot{\beta}\dot{\Gamma}(r_c c\beta c\Gamma c\theta - h_p c\beta s\Gamma) - 2r_c\dot{\theta}\dot{\Gamma} s\beta c\Gamma s\theta + r_c\ddot{\theta}(c\beta c\theta - s\beta s\Gamma s\theta) + l\dot{\alpha}^2 s\alpha + \ddot{y}_C$$

where: $s\theta = \sin\theta$; $c\theta = \cos\theta$; $s\alpha = \sin\alpha$; $c\alpha = \cos\alpha$; $s\beta = \sin\beta$; $c\beta = \cos\beta$; $s\Gamma = \sin\Gamma$; $c\Gamma = \cos\Gamma$.

(B). NOMENCLATURE

Symbol	Quantity	Units
A_p	transversal area of the piston	m^2
c_b	radial clearance of bearing	m
F_ξ, F_η	radial and transversal fluid film forces	
h_b	oil film thickness	m
h_p	length of crank pin	m
l	length of the connecting rod	m
l_b	width of bearing	m
m	mass	kg
ndof	number of degrees of freedom	
P_g	pressure of gas inside the cylinder	*Pa*
rpm	revolutions per minute	
r_b	radio of bearing	m
r_c	radius crank-pin center	m
$\mathbf{T}_i$	transformation matrix in the *i-th* coordinate	
T_z	motor shaft torque	N.m
Greek symbols		
Ω	rotational speed of the rotor and	*Rpm*
$\dot{\theta}$	rotational speed of the rotor	rad/s
θ	rotation angle of the crank	rad
α	rotation angle of the connecting rod	rad
β	rotation angle around X-X axis	rad
Γ	rotation angle around Y-Y axis	rad
μ	viscosity oil film	Pa.s
ε	eccentricity ratio	
ϕ	attitude angle	rad
ξ, η	radial and transversal directions	
Subscripts		
b	bearing	
B_i	*i-th* mobile reference frame	
c	crank	
cr	connecting rod	
p	Piston	
ub	Unbalance	

REFERENCES

[1] J. Rigola, "Numerical simulation and experimental validation of hermetic reciprocating compressors", PhD dissertation, Universidad Politécnica de Cataluña, Barcelona, Spain, 2002.
[2] G. Longo and A. Gasparella, "Unsteady state analysis of the compression cycle of a hermetic reciprocating compressor", *International Journal of Refrigeration,* vol. 26, no. 6, pp. 681-689, 2003.
[3] R. Dufour, J. Der Hagopian and M. Lalanne, "Transient and steady state dynamic behaviour of single cylinder compressors: Prediction and experiments", *Journal of Sound and Vibration,* vol. 181**,** no. 1, pp. 23-41, 1995.
[4] J. R. Cho and S. J. Moon, "A numerical analysis of the interaction between the piston oil film and the component deformation in a reciprocating compressor", *Tribology International,* vol. 38 no. 5, pp. 459-468, 2005.
[5] T. J. Kim and J. S. Han, "Comparison of the dynamic behavior and lubrication characteristics of a reciprocating compressor crankshaft in both finite and short bearing models", *Tribology Transactions,* vol. 47, no. 1, pp. 61-69, 2004.
[6] I. F. Santos, *Dinâmica de Sistemas Mecanicos*, (in Portuguese). Makron Books, Sao Paulo, Brazil, 2001.
[7] H. D. Nelson, , "A finite rotating shaft element using Timoshenko beam theory", *Journal of Mechanical Design, Transactions of the ASME*, vol. 102, no. 4, pp. 793-803, 1980.
[8] B. J. Hamrock, *Fundamental of Fluid Film Lubrication*, NASA Reference Publication, USA, 1991.
[9] J. Frêne, D. Nicolas, B. Degueurce, D. Berthe and M. Godet, *Lubrification Hydrodynamique*, Editions Eyrolles, Paris, 1990.
[10] J. Garcia de Jalon and E. Bayo, *Kinematic and Dynamic Simulation of Multibody Systems. The Real-Time Challenge*, Springer-Verlag, New-York, 1994.
[11] R. Pal, R. Sinhasan and D. Singh, "Analysis of a big-end bearing - a finite element approach", *Wear*, vol. 121, no. 1, pp. 117-120, 1988.
[12] G. S. Ritchie, "The prediction of journal loci in dynamically loaded internal combustion engine bearings", *Wear,* vol. 35, no. 2, pp. 291-297, 1975.

B.2 [J2] - *Journal of the Brazilian Society of Mechanical Sciences and Engineering*, Vol.31 (1), 2009, pp. 35-46.

B.2 [J2] - *Journal of the Brazilian Society of Mechanical Sciences and Engineering*, Vol.31 (1), 2009, pp. 35-46. **113**

Edgar A. Estupiñan
eep@mek.dtu.dk

Ilmar F. Santos
Senior Member, ABCM
ifs@mek.dtu.dk
Technical University of Denmark
Department of Mechanical Engineering
Nils Koppels Allé, Building 404, DK-2800
Kgs. Lyngby, Denmark

Modelling Hermetic Compressors Using Different Constraint Equations to Accommodate Multibody Dynamics and Hydrodynamic Lubrication

In this work, the steps involved for the modelling of a reciprocating linear compressor are described in detail. The dynamics of the mechanical components are described with the help of multibody dynamics (rigid components) and finite elements method (flexible components). Some of the mechanical elements are supported by fluid film bearings, where the hydrodynamic interaction forces are described by the Reynolds equation. The system of nonlinear equations is numerically solved for three different restrictive conditions of the motion of the crank, where the third case takes into account lateral and tilting oscillations of the extremity of the crankshaft. The numerical results of the behaviour of the journal bearings for each case are presented giving some insights into design parameters such as, maximum oil film pressure, minimum oil film thickness, maximum vibration levels and dynamic reaction forces among machine components, looking for the optimization and application of active lubrication towards vibration reduction.
***Keywords**: hermetic compressor, multibody dynamics, journal bearing, Reynolds equation, hydrodynamic lubrication.*

Introduction

One of the most common types of compressors used in the refrigeration field is the piston compressor, also known as reciprocating compressor. Small-scale hermetic reciprocating compressors are widely used to compress coolant gas in household refrigerators and air-conditioners. It was at the beginning of the Sixties when these small machines became a household appliance of common use in the industrialized countries. Since then, numerous research studies have been carried out in order to optimize the design and to improve the thermal and mechanical efficiency of refrigeration compressors. Positive displacement compressors mechanically drive the refrigerant gas from the evaporator at low-pressure side to the condenser at high-pressure side, reducing the compressor chamber volume. Reciprocating compressors use pistons that are driven directly through a slider-crank mechanism, converting the rotating movement of the rotor to an oscillating motion. A hermetic reciprocating compressor is a particular case where motor and compressor are directly coupled on the same shaft and contained within the same housing (welded steel shell) and in contact with the refrigerant and oil (Rigola, 2002). A picture and a schematic draw of a hermetic reciprocating compressor used in household refrigerators are shown in Fig.1.

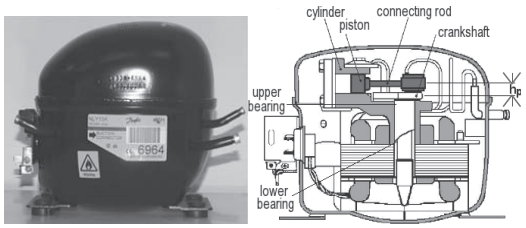

Figure 1. Picture and schematic draw of a hermetic reciprocating compressor.

The study and optimization of the dynamic behaviour of reciprocating compressors, taking in account the hydrodynamics of bearings, are of significant importance for the development of new prototypes. The performance of the bearings affects key functions such as durability and noise and vibration behaviour of the compressor. Optimization studies of the performance of journal bearings by means of numerical simulation may reduce development costs for prototype testing work significantly. Several studies that involve numerical studies and computational models for the analysis of small reciprocating compressors are found in the literature, as it can be seen in the works carried out by Rasmussen (1997) and Rigola (2002). In some studies, numerical simulations of the refrigerant flow through the valves and inside the cylinder during the compression cycle have been included (Longo and Gasparella, 2003), whereas in others the focus has been on the dynamics of motion in steady and transient conditions (Dufour, *et al*., 1995). Some researchers have included the coupling of fluid-structure dynamics in order to particularly analyse the dynamics of the piston (Gommed and Etsion, 1993; Cho and Moon, 2005). In a study carried out by Kim and Han (2004), an analytical model of the coupled dynamic behaviour of the piston and crankshaft was developed and comparisons between a finite bearing model and a short bearing approach were included. In the same study, a numerical procedure that combines Newton-Raphson method and the successive over relaxation scheme was also presented. In the study carried out by Cho and Moon (2005), a time-incremental numerical algorithm to solve a finite differences model for the estimation of the oil film pressure was coupled with a finite element model for the computation of the structural deformation of the piston. As it is described here, many of the research studies related to compressor modelling are mainly focused on the study of the thermal and fluid dynamic behaviour. In contrast, the main focus of the present work is on the developing of a multibody dynamic model of a hermetic compressor, where the dynamics of the fluid film bearings and the flexibility of the crankshaft are included. The multibody dynamic model, which includes the main mechanical components of the hermetic compressor, is coupled with a finite elements model of the rotor and the hydrodynamic interaction forces, which are computed using analytical solutions of the Reynolds equation. The influence of the crankshaft tilting oscillations on design parameters, such as the minimum film

Paper accepted December, 2008. Technical Editor: Domingos A. Rade.

thickness and maximum pressures are carefully investigated, since the finite element model allows capturing of such movements. The elasto-hydrodynamic theory, which takes in account the bearing and housing flexibility, is not considered in this work, since it is presented only in very special cases.

Nomenclature

A_p =transversal area of the piston, m^2
c_b =radial clearance of the bearing, m
D_p =piston diameter, m
e_c =mass eccentricity of the crank, m
$\mathbf{f}$ =vector of forces, N
$\mathbf{f}_b$ =vector of journal bearing forces, N
h_b =oil film thickness, m
h_p =length of crank pin, m
$\mathbf{I}$ =moment of inertia tensor
l =length of the connecting rod, m
l_b =width of the bearing, m
m =mass, kg
$ndof$ =number of degrees of freedom
P_g =gas pressure inside the cylinder, Pa
p =fluid film pressure, Pa
rpm =revolutions per minute
r =radius, m
S =Sommerfeld number
T_i =transformation matrix in the coordinate i
x_B =piston position along the X direction, m

Greek Symbols

Ω =rotational speed of the crankshaft, rad/s
θ =rotation angle of the crank around Z-Z axis, rad
α =rotation angle of the connecting rod, rad
β =rotation angle around X-X axis, rad
Γ =rotation angle around Y1-Y1 axis, rad
μ =viscosity oil film, Pa.s
ε =eccentricity ratio
ϕ =attitude angle, rad
τ_z =motor shaft torque, Nm

Subscripts

A,B,C =relative to the points A, B or C, respectively
b =relative to the bearing
B_i =relative to the i-th mobile reference frame
c =relative to the crank
cr =relative to the connecting rod
p =relative to the piston
I =relative to the inertial reference frame
N =relative to normal reaction forces cylinder-piston
LJB =relative to infinitely long-width journal bearing
SJB =relative to short-width journal bearing
X,Y =relative to the X and Y directions
ξ, η =relative to the radial and transversal directions

Mathematical Modelling

In this section the formulation of representative motion equations to describe the mathematical model of a hermetic reciprocating compressor is developed. The main components of the reciprocating mechanism (i.e., connecting rod and crank) are modelled as rigid bodies, the piston motion is modelled as a particle and the main shaft is modelled as a flexible body via finite elements. Three different approaches which differ in the definition of the restrictive conditions of motion of the centre of the crank have been comparatively studied. These three cases are:

- **Case (I).** Neglecting lateral displacements and tilting oscillations of the crank (no hydrodynamic bearings).
- **Case (II).** Considering lateral displacements but not tilting oscillations of the crank (rigid crankshaft).
- **Case (III).** Considering lateral displacements and tilting oscillations of the crank (flexible crankshaft).

Although the two first approaches make the problem simpler and reduce the computational time, by including the tilting crank effect in the model (case III), a more precise estimation of the journal bearing forces and the journal orbits may be obtained, considering that the oil film thickness is usually only a few micrometers thick. In order to include the tilting oscillations of the crank, the crankshaft is modelled via finite elements and coupled to the motion equations of the piston-slider-crank mechanism through the degrees of freedom where the shaft is connected to the crank. Furthermore, the fluid film forces in the upper and lower bearings are calculated by using analytical solutions of the Reynolds equation, and introduced into the equations of the rotor at each time. Therefore, depending on the case of study, the dynamics of the compressor is described by a different global system of equations.

Developing of the Multibody Dynamics Model

The motion equations of the piston-connecting rod-crank system have been formulated using the Newton-Euler's method, following the methodology suggested by Santos (2001). Figure 2 shows a sketch indicating the inertial referential frame I_{XYZ} and the main angles of rotation for the four moving reference frames.

(a) Definition of the Inertial and Moving Reference Systems.

One inertial reference frame I_{XYZ} and four moving reference frames have been defined. The inertial reference frame is attached to the centre of the bearing (point **O**), whereas, the moving reference frames B_1, B_2 and B_3 are attached to the crank, and the moving reference frame B_4 is attached to the connecting rod. B_1 ($X_1Y_1Z_1$) is obtained by rotating I, the angle β, around the X axis; B_2 ($X_2Y_2Z_2$) is obtained by rotating B_1, the angle Γ, around the Y_1 axis; B_3 ($X_3Y_3Z_3$) is obtained by rotating B_2, the angle θ, around the Z_2 axis, and B_4 ($X_4Y_4Z_4$) is obtained by rotating I, the angle α, around the Z axis. The transformation matrices are given by:

$\mathbf{T}_\beta$: transformation from the inertial frame I to the moving frame B_1.

$$\mathbf{T}_\beta = \begin{bmatrix} 1 & 0 & 0 \\ 0 & \cos\beta & \sin\beta \\ 0 & -\sin\beta & \cos\beta \end{bmatrix}$$

$\mathbf{T}_\Gamma$: transformation from the inertial frame B_1 to the moving frame B_2.

$$\mathbf{T}_\Gamma = \begin{bmatrix} \cos\Gamma & 0 & -\sin\Gamma \\ 0 & 1 & 0 \\ \sin\Gamma & 0 & \cos\Gamma \end{bmatrix}$$

$\mathbf{T}_\theta$: transformation from the inertial frame B_2 to the moving frame B_3.

$$\mathbf{T}_\theta = \begin{bmatrix} \cos\theta & \sin\theta & 0 \\ -\sin\theta & \cos\theta & 0 \\ 0 & 0 & 1 \end{bmatrix}$$

$\mathbf{T}_\alpha$: transformation from the inertial frame I to the moving frame B_4.

$$\mathbf{T}_\alpha = \begin{bmatrix} \cos\alpha & -\sin\alpha & 0 \\ \sin\alpha & \cos\alpha & 0 \\ 0 & 0 & 1 \end{bmatrix}$$

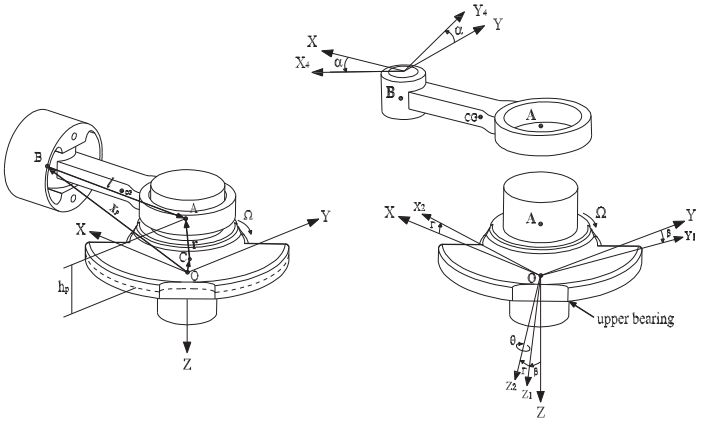

Figure 2. Geometry and reference systems.

(b) Position Vectors and Constraint Equations.

A different constraint equation is established for each one of the three cases studied. A simplified sketch illustrating how the main parts of the system are connected is shown in Fig. 2. The constraint equations for each case are given by Eq. (1-3).

Case (I):

$$ {}_I\mathbf{x}_p + {}_I\mathbf{l} = {}_I\mathbf{r} \tag{1}$$

where,

$$ {}_I\mathbf{r} = \mathbf{T}_\theta^T \cdot {}_{B_3}\mathbf{r} \;;\; {}_{B_3}\mathbf{r} = \{\, r_c \quad 0 \quad -h_p \,\}^{\mathrm{T}} \;;$$
$$ {}_I\mathbf{l} = \{\, -l\cos\alpha \quad l\sin\alpha \quad 0 \,\}^{\mathrm{T}} \;;\; {}_I\mathbf{x}_p = \{\, x_B \quad 0 \quad -h_p \,\}^{\mathrm{T}}$$

Case (II):

$$ {}_I\mathbf{x}_p + {}_I\mathbf{l} = {}_I\mathbf{r} + {}_I\mathbf{c} \tag{2}$$

where, the position vector of the centre of the crank is given by:

$$ {}_I\mathbf{c} = \{\, x_c \quad y_c \quad 0 \,\}^T$$

Case (III):

$$ {}_I\mathbf{x}_p + {}_I\mathbf{l} = {}_I\mathbf{r} + {}_I\mathbf{c} \tag{3}$$

In this case rotations in β and Γ are considered, therefore the vector ${}_I\mathbf{r}$ is given by:

$$ {}_I\mathbf{r} = \mathbf{T}_\beta^T \cdot \mathbf{T}_\Gamma^T \cdot \mathbf{T}_\theta^T \cdot {}_{B_3}\mathbf{r}$$

(c) Kinematic Relations.

The angular velocities for each one of the moving reference frames may be written as in Eq. (4).

$$ {}_I\dot{\boldsymbol{\beta}} = \{\, \dot\beta \quad 0 \quad 0 \,\}^{\mathrm{T}} \;;\; {}_{B_1}\dot{\boldsymbol{\Gamma}} = \{\, 0 \quad \dot\Gamma \quad 0 \,\}^{\mathrm{T}} \;;$$
$$ {}_{B_2}\dot{\boldsymbol{\theta}} = \{\, 0 \quad 0 \quad \dot\theta \,\}^{\mathrm{T}} \;;\; {}_I\dot{\boldsymbol{\alpha}} = \{\, 0 \quad 0 \quad -\dot\alpha \,\}^{\mathrm{T}} \tag{4}$$

For the cases (I) and (II), the absolute angular velocity of the crank is given by $\omega = \dot\theta$, since $\dot\beta$ and $\dot\Gamma$ are equal to zero. Thus, in these cases the moving reference frame B_3 will be simply obtained by rotating I, the angle θ, around the Z axis. For the case (III) the absolute angular velocity written with help of the moving reference frame B_3, is given by:

$$ {}_{B_3}\boldsymbol{\omega} = {}_{B_3}\dot{\boldsymbol{\beta}} + {}_{B_3}\dot{\boldsymbol{\Gamma}} + {}_{B_3}\dot{\boldsymbol{\theta}} \tag{5}$$

where:

$$ {}_{B_3}\dot{\boldsymbol{\beta}} = \mathbf{T}_\theta \cdot \mathbf{T}_\Gamma \cdot \mathbf{T}_\beta \cdot {}_I\dot{\boldsymbol{\beta}} \;;$$
$$ {}_{B_3}\dot{\boldsymbol{\Gamma}} = \mathbf{T}_\theta \cdot \mathbf{T}_\Gamma \cdot {}_{B_1}\dot{\boldsymbol{\Gamma}} \;;\; {}_{B_3}\dot{\boldsymbol{\theta}} = \mathbf{T}_\theta \cdot {}_{B_2}\dot{\boldsymbol{\theta}}$$

The expressions to calculate the velocities and accelerations of the piston ($\dot x_B$, $\ddot x_B$) and the connecting rod ($\dot\alpha$, $\ddot\alpha$) are obtained by differentiating the constraint equation for each case respectively, Eq. (6-11).

Case (I):

- Velocities:

$$ \begin{bmatrix} 1 & l\sin\alpha \\ 0 & l\cos\alpha \end{bmatrix} \begin{Bmatrix} \dot x_B \\ \dot\alpha \end{Bmatrix} = \begin{Bmatrix} -r_c\dot\theta\sin\theta \\ r_c\dot\theta\cos\theta \end{Bmatrix} \tag{6}$$

- Accelerations:

$$ \begin{bmatrix} 1 & l\sin\alpha \\ 0 & l\cos\alpha \end{bmatrix} \begin{Bmatrix} \ddot x_B \\ \ddot\alpha \end{Bmatrix} = \begin{Bmatrix} -r_c(\ddot\theta\sin\theta - \dot\theta^2\cos\theta) - l\dot\alpha^2\cos\alpha \\ r_c(\ddot\theta\cos\theta - \dot\theta^2\sin\theta) + l\dot\alpha^2\sin\alpha \end{Bmatrix} \tag{7}$$

Case (II):

- Velocities:

$$\begin{bmatrix} 1 & l\sin\alpha \\ 0 & l\cos\alpha \end{bmatrix} \begin{Bmatrix} \dot{x}_B \\ \dot{\alpha} \end{Bmatrix} = \begin{Bmatrix} -r_c\dot{\theta}\sin\theta + \dot{x}_C \\ r_c\dot{\theta}\cos\theta + \dot{y}_C \end{Bmatrix} \tag{8}$$

- Accelerations:

$$\begin{bmatrix} 1 & l\sin\alpha \\ 0 & l\cos\alpha \end{bmatrix} \begin{Bmatrix} \ddot{x}_B \\ \ddot{\alpha} \end{Bmatrix} = \begin{Bmatrix} -r_c(\ddot{\theta}\sin\theta - \dot{\theta}^2\cos\theta) - l\dot{\alpha}^2\cos\alpha + \ddot{x}_C \\ r_c(\ddot{\theta}\cos\theta - \dot{\theta}^2\sin\theta) + l\dot{\alpha}^2\sin\alpha + \ddot{y}_C \end{Bmatrix} \tag{9}$$

Case (III):

- Velocities

$$\begin{bmatrix} 1 & l\sin\alpha \\ 0 & l\cos\alpha \end{bmatrix} \begin{Bmatrix} \dot{x}_B \\ \dot{\alpha} \end{Bmatrix} = \begin{Bmatrix} w_1 \\ w_2 \end{Bmatrix} \tag{10}$$

- Accelerations:

$$\begin{bmatrix} 1 & l\sin\alpha \\ 0 & l\cos\alpha \end{bmatrix} \begin{Bmatrix} \ddot{x}_B \\ \ddot{\alpha} \end{Bmatrix} = \begin{Bmatrix} w_3 \\ w_4 \end{Bmatrix} \tag{11}$$

where:

$$w_1 = -r_c(\dot{\Gamma}s\Gamma c\theta + \dot{\theta}c\Gamma s\theta) - h_p\dot{\Gamma}c\Gamma + \dot{x}_C \tag{12}$$

$$w_2 = r_c\dot{\beta}(c\beta s\Gamma c\theta - s\beta s\theta) + r_c\dot{\theta}(c\beta c\theta - s\beta s\Gamma s\theta) + \dot{\Gamma}(r_c s\beta c\Gamma c\theta - h_p s\beta s\Gamma) + \dot{\beta}h_p c\beta c\Gamma + \dot{y}_C \tag{13}$$

$$w_3 = -r_c\ddot{\Gamma}s\Gamma c\theta + \dot{\Gamma}^2(h_p s\Gamma - r_c c\Gamma c\theta) + 2r_c\dot{\theta}\dot{\Gamma}s\Gamma s\theta - r_c\ddot{\theta}_2 c\Gamma c\theta - h_p\ddot{\Gamma}c\Gamma - r_c\ddot{\theta}c\Gamma s\theta - l\dot{\alpha}^2 c\alpha + \ddot{x}_C \tag{14}$$

$$w_4 = -r_c\dot{\theta}^2(c\beta s\theta + s\beta s\Gamma c\theta) - \dot{\beta}^2(r_c c\beta s\theta + r_c s\beta s\Gamma c\theta + h_p s\beta c\Gamma) - \dot{\Gamma}^2(r_c s\beta s\Gamma c\theta + h_p s\beta c\Gamma) + \ddot{\beta}(h_p c\beta c\Gamma - r_c s\beta s\theta + r_c c\beta s\Gamma c\theta) + \ddot{\Gamma}(r_c s\beta c\Gamma c\theta - h_p s\beta s\Gamma) - 2r_c\dot{\theta}\dot{\beta}(s\beta c\theta + c\beta s\Gamma s\theta) + 2\dot{\beta}\dot{\Gamma}(r_c c\beta c\Gamma c\theta - h_p c\beta s\Gamma) - 2r_c\dot{\theta}\dot{\Gamma}s\beta c\Gamma s\theta + r_c\ddot{\theta}(c\beta c\theta - s\beta s\Gamma s\theta) + l\dot{\alpha}^2 s\alpha + \ddot{y}_C \tag{15}$$

In Eq.(12-15):

$$s\theta = \sin\theta;\quad c\theta = \cos\theta;\quad s\alpha = \sin\alpha;\quad c\alpha = \cos\alpha;$$
$$s\beta = \sin\beta;\quad c\beta = \cos\beta;\quad s\Gamma = \sin\Gamma;\quad c\Gamma = \cos\Gamma.$$

(d) Equations of Motion.

The equations of motion for each body and for the case (III) are given by Eq. (16-20). Since the piston is not the focus of the present analysis, it should be noticed that in the modelling of the piston the friction forces are not included.

Crank

$$\sum {}_I\mathbf{f} = m_c \cdot {}_I\bar{\mathbf{a}}_c \;\Rightarrow\; {}_I\mathbf{f}_A = m_c\{\ddot{x}_c\ ,\ddot{y}_c\}^{\mathrm{T}} \tag{16}$$

$$\sum {}_{B_3}\mathbf{M}_C = {}_{B_3}\mathbf{r}\times{}_{B_3}\mathbf{f}_A + {}_{B_3}\boldsymbol{\tau} = {}_{B_3}\mathbf{I}_c\cdot\frac{d}{dt}\left({}_{B_3}\boldsymbol{\omega}\right) + {}_{B_3}\boldsymbol{\omega}\times\left({}_{B_3}\mathbf{I}_c\cdot{}_{B_3}\boldsymbol{\omega}\right) + m_c\cdot{}_{B_3}\bar{\mathbf{r}}_{C-cm}\times{}_{B_3}\mathbf{a}_C \tag{17}$$

where,

$${}_{B_3}\mathbf{f}_A = \mathbf{T}_\theta\cdot\mathbf{T}_\Gamma\cdot\mathbf{T}_\beta\cdot{}_I\mathbf{f}_A;\quad {}_{B_3}\boldsymbol{\tau} = \{0\,,0\,,\tau_z\}^{\mathrm{T}};\quad {}_{B_3}\bar{\mathbf{r}}_{C-cm} = \{e_c\,,0\,,0\}^{\mathrm{T}}$$

Connecting Rod

$$\sum {}_I\mathbf{f} = m_{cr}\cdot{}_I\bar{\mathbf{a}}_{cr} = {}_I\mathbf{f}_A + {}_I\mathbf{f}_B \tag{18}$$

$$\sum {}_{B_4}\mathbf{M}_B = {}_{B_4}\mathbf{l}\times{}_{B_4}\mathbf{f}_A = {}_{B_4}\mathbf{I}_{cr}\cdot\frac{d}{dt}\left({}_{B_4}\dot{\boldsymbol{\alpha}}\right) + {}_{B_4}\dot{\boldsymbol{\alpha}}\times\left({}_{B_4}\mathbf{I}_{cr}\cdot{}_{B_4}\dot{\boldsymbol{\alpha}}\right) + m_{cr}\cdot{}_{B_4}\bar{\mathbf{r}}_{cr}\times{}_{B_4}\mathbf{a}_B \tag{19}$$

where,

$${}_I\bar{\mathbf{a}}_{cr} = {}_I\mathbf{a}_B + {}_I\dot{\boldsymbol{\alpha}}\times{}_I\bar{\mathbf{r}}_{cr} + {}_I\dot{\boldsymbol{\alpha}}\times{}_I\bar{\mathbf{r}}_{cr} + {}_I\ddot{\boldsymbol{\alpha}}\times{}_I\bar{\mathbf{r}}_{cr} = \begin{Bmatrix} \ddot{x}_B + \bar{r}_{cr}\left(\dot{\alpha}^2\cos\alpha + \ddot{\alpha}\sin\alpha\right) \\ \bar{r}_{cr}\left(\ddot{\alpha}\cos\alpha - \dot{\alpha}^2\sin\alpha\right) \\ 0 \end{Bmatrix};$$

$${}_{B_4}\mathbf{f}_A = \mathbf{T}_\alpha\cdot{}_I\mathbf{f}_A;\quad {}_{B_4}\mathbf{a}_B = \mathbf{T}_\alpha\cdot{}_I\mathbf{a}_B;\quad {}_I\mathbf{a}_B = \{\ddot{x}_B\,,0\,,0\}^{\mathrm{T}}$$

Piston

$$\sum {}_I\mathbf{f}_B = m_p\cdot{}_I\mathbf{a}_B = {}_I\mathbf{f}_B + {}_I\mathbf{f}_N + {}_I\mathbf{f}_p \tag{20}$$

where,

$${}_I\mathbf{f}_p = \left\{P_g\cdot A_p\ ,0\ ,0\right\}^{\mathrm{T}}$$

For each case the equations of motion may be written in a matrix form as in Eq. (21), where the vector $\bar{\mathbf{b}}$ contains the main unknowns (i.e., reaction forces, reaction moments and accelerations). This matrix system is fully described for each case in the appendices A, B and C respectively. For the case (III), where the flexibility of the shaft is included, the matrix system of Eq. (21) has to be coupled to the motion equations of the rotor obtained via a finite elements formulation, which is presented in the next sections.

$$\bar{\mathbf{A}}\cdot\bar{\mathbf{b}} = \bar{\mathbf{c}} \tag{21}$$

Modelling of the Rotor

For the case (III), the main shaft of the compressor is considered as a simply rotating beam, supported by the upper and lower bearings, as illustrated in Fig. 1. The shaft is modelled as a flexible body using a finite elements formulation for a rotor bearing system, which includes gyroscopic and rotatory inertia effects (Nelson and McVaugh, 1976). Considering that the main focus of this study is on the lower mode shapes, the use of this formulation is appropriated to this case and only few finite elements have been used to model the rotor. The global equation of motion can be written as in Eq. (22), where, $\bar{\mathbf{M}}$, $\bar{\mathbf{K}}$, $\bar{\mathbf{G}}$ are the mass, stiffness and gyroscopic matrices respectively, and $\bar{\mathbf{f}}$ is the vector of loads on the rotor, which includes: static preload forces ($_I\mathbf{f}_{pl}$), unbalance rotor forces ($_I\mathbf{f}_{ub}$) and the hydrodynamic bearing forces ($_I\mathbf{f}_b$). Based on the fluid film theory, the bearing forces are calculated by using analytical solutions of the Reynolds equation. These forces depend on the linear displacements and velocities of the nodes that in the finite element model represent the journal bearings centre.

$$\overline{\mathbf{M}} \cdot \ddot{\mathbf{q}} = \underbrace{\overline{\mathbf{f}} - \overline{\mathbf{G}} \cdot \dot{\mathbf{q}} - \overline{\mathbf{K}} \cdot \mathbf{q}}_{\overline{\mathbf{f}}} \tag{22}$$

Fluid Film Forces

The governing equation for the pressure distribution of the oil film in dynamically loaded journal bearings is given by Eq. (23). This equation is obtained from the general formulation of the Reynolds equation (Hamrock, 1991). In this equation, $\dot{\phi}$ is the rotational speed of the journal centre about the bearing centre and ε is the relative eccentricity.

$$\frac{\partial}{\partial\varphi}\left(\frac{h_b^3}{\mu}\frac{\partial p}{\partial\varphi}\right) + r_b^2\frac{\partial}{\partial z}\left(\frac{h_b^3}{\mu}\frac{\partial p}{\partial z}\right) = 12c_b r_b^2\left[\frac{\partial\varepsilon}{\partial t}\cos\varphi + \varepsilon\sin\varphi\left(\frac{\partial\phi}{\partial t} - \frac{\Omega}{2}\right)\right] \tag{23}$$

The main geometric parameters and reference frames used to describe a journal bearing are shown in Fig. 3. The fluid film thickness around the bearing circumference can be calculated by using the expression: $h_b = c_b(1+\varepsilon\cos\varphi)$, where φ is the angle measured from the location of the maximum film thickness. In dynamically loaded bearings, the eccentricity and attitude angle will vary through the loading cycle. Therefore, the fluid film pressure distribution at any eccentricity ratio may be determined only if the normal squeeze velocity ($\dot{\varepsilon}$) and the rotational velocities ($\dot{\phi}, \Omega$) are known for the same eccentricity ratio. Complete solutions of Eq. (23) may be obtained numerically, and solutions for limited cases may be also obtained analytically.

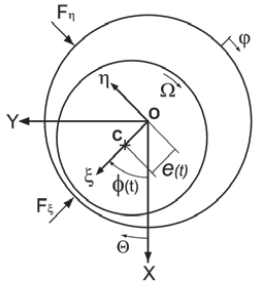

Figure 3. Journal bearing geometry.

In this work, analytical solutions for the short-width bearing (*SJB*) and infinitely-long-width bearing (*LJB*) theories have been used. The short-journal-bearing theory assumes that the variation of pressure is more significant in the axial direction than in the circumferential direction, and therefore the first term on the left side of Eq. (23) can be neglected. In contrast, for an infinitely long-width-journal-bearing, the pressure in the axial direction is assumed to be constant, and therefore the side-leakage term, i.e., the second term on the left side of Eq. (23) can be neglected. Thus, the modified Reynolds equation for each case can be integrated twice and analytical expressions for the pressure distribution can be found. Assuming that the bearing is well aligned and the viscosity of the lubricant keeps constant, the pressure distribution for a *SJB* and a *LJB* is given by Eq. (24-25).

$$p_{SJB} = -\frac{3\mu}{h_b^3}\left(\frac{l_b^2}{4} - z^2\right)\left[\left(\Omega - 2\frac{\partial\phi}{\partial t}\right)\frac{\partial h_b}{\partial\varphi} + 2c_b\cos\varphi\frac{\partial\varepsilon}{\partial t}\right] \tag{24}$$

$$p_{LJB} = 6\mu\left(\frac{r_b}{c_b}\right)^2\left\{\left(\Omega - 2\frac{\partial\phi}{\partial t}\right)\frac{\varepsilon\sin\varphi(2+\varepsilon\cos\varphi)}{(2+\varepsilon^2)(1+\varepsilon\cos\varphi)^2} + \frac{1}{\varepsilon}\frac{\partial\varepsilon}{\partial t}\left[\frac{1}{(1+\varepsilon\cos\varphi)^2} - \frac{1}{(1+\varepsilon)^2}\right]\right\} \tag{25}$$

The journal bearing forces are calculated by integrating the pressure distribution. If the pressure is integrated over all the fluid film around the bearing (i.e, $0 \le \varphi \le 2\pi$), the analytical solution is known as a *full Sommerfeld solution*. However, if the analysis is limited to the convergent film (i.e., $0 \le \varphi \le \pi$), the analytical solution is known as a *half Sommerfeld solution*. Because in real bearings pressures lower than the ambient's are rarely found, and using the last approach more realistic predictions may be obtained (Hamrock, 1991). Thus, the analytical expressions to calculate the bearing forces in ξ, η coordinates, using the half Sommerfeld conditions for the *SJB* and *LJB* approaches respectively, are given by Eq. (26-29). A detailed procedure to obtain these expressions is included in the reference (Frêne, 1990).

- ***Hydrodynamic fluid film forces: Short-journal-bearing***

$$F_\xi = \frac{-r_b\mu l_b^3}{2c_b^2(1-\varepsilon^2)^2}\left[\frac{\pi(1+2\varepsilon^2)}{(1-\varepsilon^2)^{1/2}}\frac{\partial\varepsilon}{\partial t} + 2\varepsilon^2\left(\Omega - 2\frac{\partial\phi}{\partial t}\right)\right] \tag{26}$$

$$F_\eta = \frac{r_b\mu l_b^3\varepsilon}{2c_b^2(1-\varepsilon^2)^2}\left[4\frac{\partial\varepsilon}{\partial t} + \frac{\pi(1-\varepsilon^2)^{1/2}}{2}\left(\Omega - 2\frac{\partial\phi}{\partial t}\right)\right] \tag{27}$$

- ***Hydrodynamic fluid film forces: Infinitely-long-journal-bearing***

$$F_\xi = \frac{-12\,r_b^3\mu l_b}{c_b^2}\left[\frac{\varepsilon^2}{(2+\varepsilon^2)(1-\varepsilon^2)}\left(\Omega - 2\frac{\partial\phi}{\partial t}\right) + \left(\frac{1}{(1-\varepsilon^2)^{3/2}}\right)\left(\frac{\pi}{2} - \frac{8}{\pi(2+\varepsilon^2)}\right)\frac{\partial\varepsilon}{\partial t}\right] \tag{28}$$

$$F_\eta = \frac{12\,r_b^3\mu l_b}{c_b^2}\left[\frac{\pi\varepsilon}{2(2+\varepsilon^2)(1-\varepsilon^2)^{1/2}}\left(\Omega - 2\frac{\partial\phi}{\partial t}\right) + \left(\frac{2\varepsilon}{(2+\varepsilon^2)(1-\varepsilon^2)}\right)\frac{\partial\varepsilon}{\partial t}\right] \tag{29}$$

In order to describe the fluid film forces in the inertial reference frame, the transformation given by Eq. (30) is used, where the attitude angle $\phi(t)$ is the angle measured between the X-axis and the location of the minimum oil film thickness. For the case (II), the bearing forces F_X and F_Y are coupled directly to the vector $\overline{\mathbf{c}}$ of Eq. (21), whereas, for the case (III), they correspond to the components of the vector ${}_I\mathbf{f}_b$ of Eq. (22).

$$\begin{Bmatrix} F_X \\ F_Y \end{Bmatrix} = \begin{bmatrix} \cos\phi(t) & -\sin\phi(t) \\ \sin\phi(t) & \cos\phi(t) \end{bmatrix}\begin{Bmatrix} F_\xi \\ F_\eta \end{Bmatrix} \tag{30}$$

Numerical Implementation

The equations of motion that describe the dynamics of the system together with the *FEM* model of the shaft and the analytical expressions for the fluid film forces yield to a system of high complexity and non-linearity. A flowchart, with the main steps

involved in the numerical algorithm implemented to solve the system of equations, is shown in Fig. 4. In this case, a Newmark implicit method combined with a predictor-corrector approach has been used (Garcia, 1994). The simulation procedure is summarized in the following four main steps:

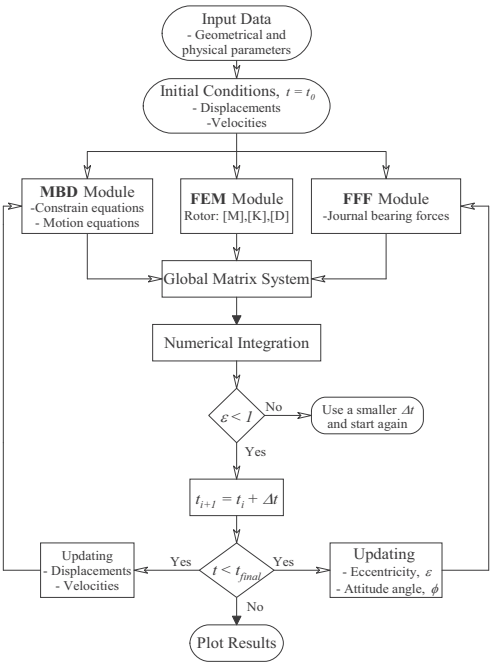

Figure 4. Flow chart of the computer code.

a) *Input data and starting values*. In this part, the geometrical and physical parameters must be given, i.e., dimensions, rotational speed, mass, inertia, preloads, etc. Starting values, such as initial displacements and velocities of the journal bearings centre, should be also given.

b) *Pre-processing*. This part includes the generation of structural matrices of the multibody model (MBD module) and the matrices of the flexible rotor (FEM module). Initial fluid film forces can be computed within the FFF module, based on the given initial conditions.

c) *Numerical computation*. This is the main core of the code, which includes the coupling of matrices, the computation of the journal bearing forces at each time step and the numerical solution of the global system. For the cases (I) and (II), the global systems of equations to be numerically solved are included in appendixes A and B respectively. However, for the case (III), the system of equations shown in appendix C must be coupled to the equations of the rotor. In order to couple the MBD matrix system given by Eq. (21) to the equations of the flexible rotor given by Eq. (22), the matrix $\overline{\mathbf{M}}$ (size $ndof \times ndof$) is coupled to the matrix $\overline{\mathbf{A}}$ (size 16×16) in the degrees of freedom related to the linear and angular accelerations of the crank centre ($\ddot{q}_1, \ddot{q}_2, \ddot{q}_3, \ddot{q}_4$), obtaining the global mass matrix $\widetilde{\mathbf{M}}$ (size $ndof+12$). Similarly, the vector $\hat{\mathbf{f}}$, which is the resultant right hand side vector of Eq. (22), is coupled to the vector $\overline{\mathbf{c}}$ of Eq. (21). Thus, the global matrix system for case (III) can be written as in Eq. (31).

$$\widetilde{\mathbf{M}} \cdot \widetilde{\mathbf{b}} = \widetilde{\mathbf{c}} \tag{31}$$

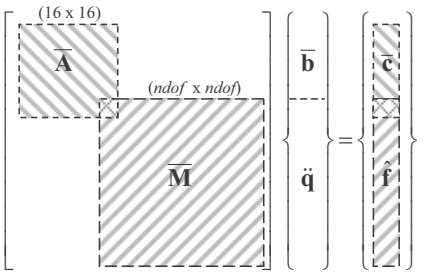

where,

$$\overline{\mathbf{b}} = \left\{ f_{B_x}, f_{B_y}, f_{B_z}, N_y, N_z, f_{A_x}, f_{A_y}, f_{A_z}, f_{C_z}, \ddot{\theta}, \ddot{x}_B, \ddot{\alpha} \right\}^{\mathrm{T}};$$
$$\ddot{\mathbf{q}} = \left\{ \ddot{q}_1, \ddot{q}_2, ..., \ddot{q}_{ndof} \right\}^{\mathrm{T}}$$

When the system of Eq. (31) is initially solved, the initial forces and accelerations ($\widetilde{\mathbf{b}}_0$) are calculated from the initial conditions, computing: $\widetilde{\mathbf{M}}_{t_0}^{-1} \cdot \widetilde{\mathbf{c}}_{t_0}$. Using the Newmark implicit method, the iterative equations are given by Eq. (32-34).

$$\left\{ \overline{\mathbf{b}}_{t_{i+1}}, \ddot{\mathbf{q}}_{t_{i+1}} \right\}^{\mathrm{T}} = \widetilde{\mathbf{M}}_{t_{i+1}}^{-1} \cdot \widetilde{\mathbf{c}}_{t_{i+1}} \tag{32}$$

$$\dot{q}_{t_{i+1}} = \dot{q}_{t_i} + \Delta t \left[\left(1-\hat{\gamma}\right) \ddot{q}_{t_i} + \hat{\gamma}\, \ddot{q}_{t_{i+1}} \right] \tag{33}$$

$$q_{t_{i+1}} = q_{t_i} + \Delta t\, \dot{q}_{t_i} + \frac{\Delta t^2}{2} \left[\left(1-2\hat{\beta}\right) \ddot{q}_{t_i} + 2\hat{\beta}\, \ddot{q}_{t_{i+1}} \right] \tag{34}$$

To compute $\ddot{q}_{t_{i+1}}$, the elements of the vector $\widetilde{\mathbf{c}}_{t_{i+1}}$ must be estimated in advance, which implies to calculate first the journal bearing forces $\mathbf{f}_b$ at the time t_{i+1}. Since the bearing forces depend on the instantaneous position and velocities of the journal centre, the Heun's explicit method is used to predict initial guesses for $\dot{q}_{t_{i+1}}^0$ and $q_{t_{i+1}}^0$. Then, using Eq. (32-34) $\ddot{q}_{t_{i+1}}^1$ can be calculated, as well as new estimated values for $\dot{q}_{t_{i+1}}^1$ and $q_{t_{i+1}}^1$ respectively. These new estimated values are used to update the journal bearing forces and then, using again Eq. (32) a new estimate for $\ddot{q}_{t_{i+1}}^2$ can be obtained, and so on until the difference of two consecutive values becomes smaller than the prescribed tolerance given. Additionally, the explicit Euler method of first order is used to estimate the crank angle θ_{t_i} and the instantaneous angular velocity.

d) *Post-processing*. This part includes the generation of plots of journal bearing orbits, journal bearing forces, maximum oil film pressure, minimum fluid film thickness, reaction forces and reaction moments as a function of the time and the rotational crank angle during each cycle.

Results and Discussion

The system of equations described in the previous sections has been numerically solved for each one of the three approaches presented. Particularly, the numerical results have been analysed with focus on the behaviour of the main bearing of the crankshaft (upper journal bearing shown in Fig. 1. The main geometrical dimensions and physical properties of the reciprocating compressor used in this study are given in table 1. The gas pressure as a function of the crank angle is taken from Cho and Moon (2005) and it is shown in Fig. 5a. The variation of torque in function of the angular velocity for a hermetic compressor with similar characteristics to the one used in this work is taken from Rigola (2002) and it is shown in Fig. 5b.

Table 1. Main geometrical and physical parameters.

Radius crank-pin centre	r_c	7.5 *mm*
Radius of bearings	r_b	8 *mm*
Width of bearings	l_b	6 *mm*
Journal clearance	c_b	15 μm
Length crank pin	h_p	10 *mm*
Distance between bearings	L	80 *mm*
Inertia of motor-rotor		I_x, I_y = 0.4x10^{-3} ; I_z = 0.1x10^{-2} *kg.m*^{2}
Diameter of piston	D_p	23 *mm* (A_p = 415.5 *mm*^{2})
Length of the piston	l_p	22 *mm*
Mass of the piston	m_p	0.043 *kg*
Lubricant viscosity	μ	0.005 *Pa.s*
Angular velocity	Ω	312 *rad/s* (2980 *rpm)*
Mass eccentricity of crank	e_c	5 *mm*

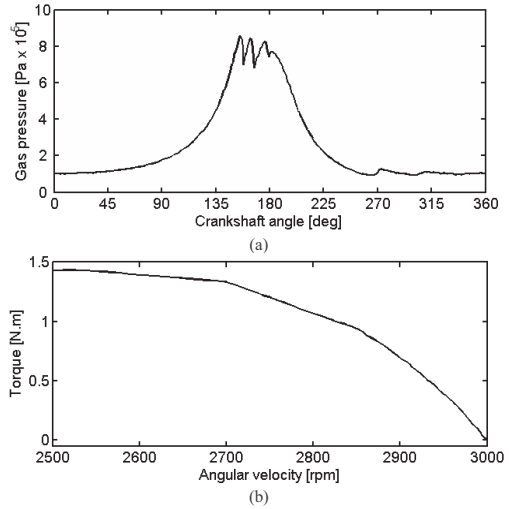

Figure 5. (a) Curve of the gas pressure (Pg) as a function of the crankshaft angle. (b) Curve of the motor torque (τ_z) as a function of the angular velocity.

Results - Case (I)

In this case, lateral displacements and tilting oscillations of the crank are neglected. Therefore, the hydrodynamic bearing forces are not calculated, but instead the reaction forces and the reaction moments at the centre of the crank are calculated. The reaction forces in the joint crank pin-connecting rod ($\mathbf{f}_A$) and in the joint piston-connecting rod ($\mathbf{f}_B$) are shown in Fig. 6. The plot of the reaction moments is shown in Fig. 7. The maximum forces are found close to the top dead centre and it can be seen clearly that the reaction forces in *X*-direction are dominated by the compression force coming from the piston and the inertial effects.

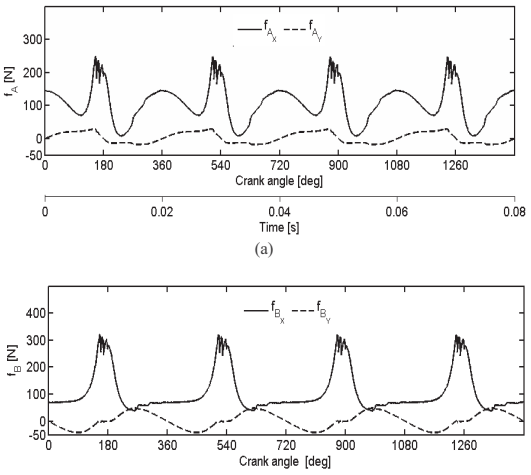

Figure 6. Reaction forces. (a) Joint piston-connecting rod. (b) Joint crank-connecting rod – case(I).

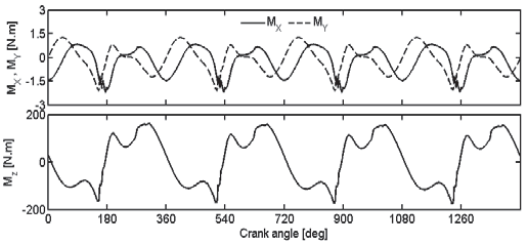

Figure 7. Crank reaction moments – case (I).

Results - Case (II)

In this case, tilting oscillations of the crank are neglected and lateral displacements are allowed. The hydrodynamic journal forces for the upper bearing are computed using Eq. (26-27) and they are shown in Fig. 8. It can be seen from this figure that the upper bearing forces are similar to the reaction forces obtained for case (I), which is expected, due to the fact that the equilibrium conditions have to be always accomplished, even if the crank centre is allowed to have lateral oscillations.

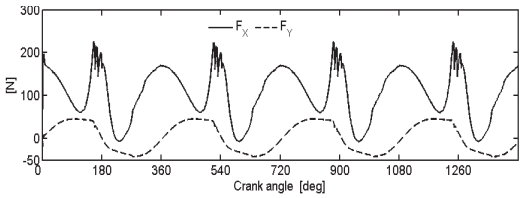

Figure 8. Journal bearing forces – case (II).

The orbit of the journal centre for the upper bearing using the *SJB* approach is shown in Fig. 9. The orbit obtained has a similar shape compared to predicted orbits of main bearings of internal combustion engines (Ritchie, 1975; Pal, 1988). The maximum fluid film pressure is computed for each crank angle during four cycles, as shown in Fig. 10. It can be observed that the highest values of hydrodynamic pressure in the bearings are found at each cycle around the top dead centre position of the piston, i.e., when the pressure in the cylinder is maximum.

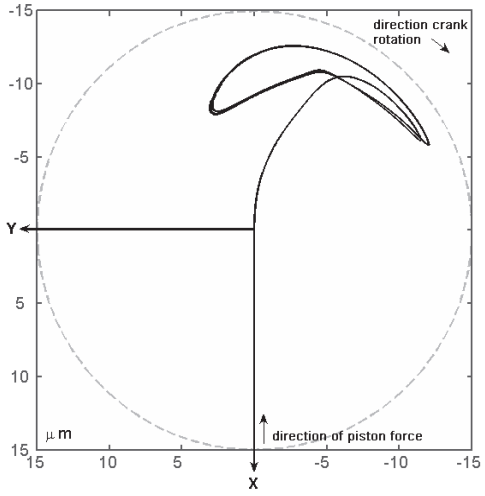

Figure 9. Orbit journal centre – case (II).

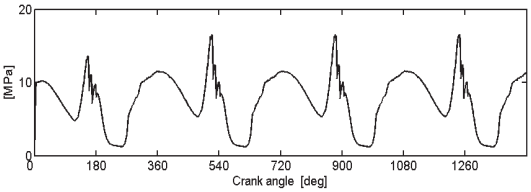

Figure 10. Maximum fluid film pressure – case (II).

Results - Case (III)

In this case, lateral displacements and tilting oscillations of the crank are allowed. Therefore, the matrix system of equations of the multibody model is coupled to the equations of the finite elements formulation of the crankshaft. Considering that this study is more focused on the hydrodynamic behaviour of the journal bearings than in the dynamics of the crankshaft, only four finite elements were used for the calculations, which are enough to include the flexible supports (journal bearings), crank and rotor unbalance, and to describe the tilting oscillations of the crank. Moreover, the main interest is to cover frequency range from 0 to 5000 Hz. Using a linearized model for the journal bearings the first and second bending eigenfrequencies of the shaft are around 1050 Hz and 6810 Hz respectively. Following the flow chart of Fig. 4, the global system of equations was solved by using a time step of Δt=*1e-6s*, in order to ensure convergence of the solution.

The fluid film forces computed for the upper and lower bearings are shown in Fig. 11. It can be seen from this figure that the upper bearing forces are similar to the ones obtained for case (II), however, in this case, small transient oscillations occur during the first cycles of the crank rotation. The transient oscillations are more evident in the plot of the lower bearing forces, since the fluid film forces for this bearing are much lower compared to the upper bearing forces. During the numerical simulations, it was noticed that these oscillations are of numerical origin, caused by the initial conditions adopted. The transient response disappears after the first cycles and the system operates under steady-state conditions.

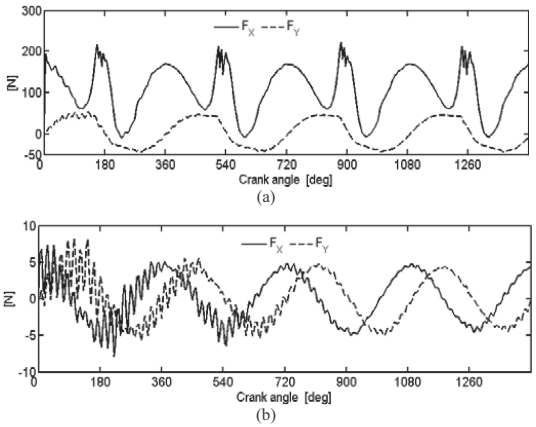

Figure 11. Journal bearing forces. (a) Upper bearing, (b) Lower bearing – case (III).

The minimum fluid film thickness for the upper bearing is plotted in Fig. 12a. It is observed in this figure that the lowest values of oil film thickness are found during the gas compression cycle, at approximately 65*deg* before the piston reaches the top dead centre (i.e., when $\theta \approx 115deg$, $\theta \approx 475deg$, $\theta \approx 835deg$,…). When the plot of minimum fluid film thickness is compared with the plot of maximum pressure, shown in Fig. 12b, it can be seen that the highest pressures values occur at approximately 30*deg* after the lowest fluid film thickness is reached during each cycle.

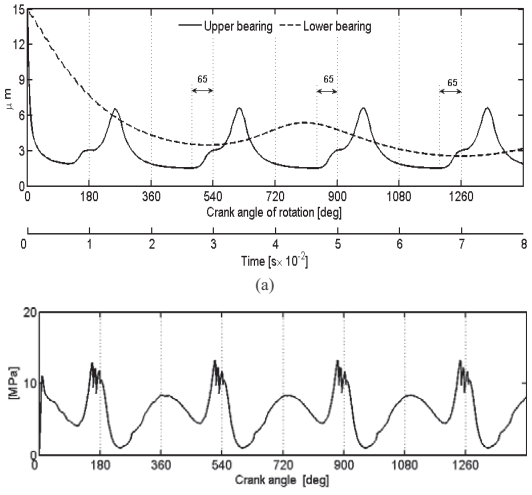

Figure 12. (a) Minimum fluid film thickness. (b) Maximum pressure – upper journal bearing – case(III).

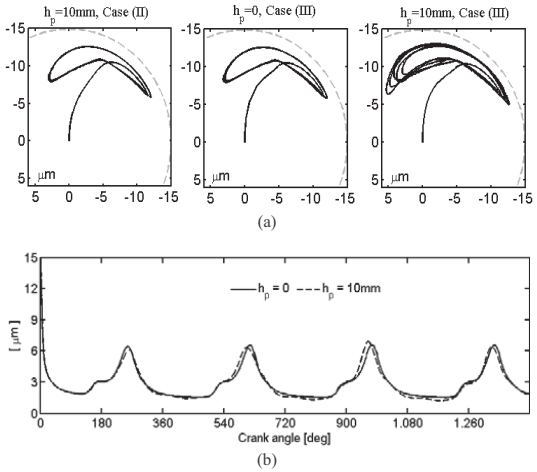

Figure 13. Effect of the crank pin length (hp). (a) Orbits. (b) Minimum fluid film thickness.

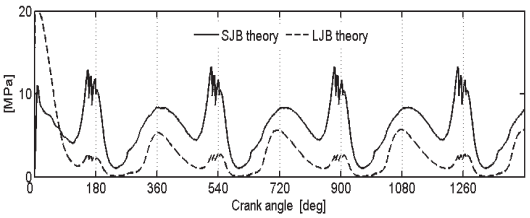

Figure 14. Maximum fluid film pressure using the SJB and LJB approaches.

The effect of including the length of the crank pin (h_p) on the behaviour of the upper bearing has been studied through the comparison of orbits and curves of the minimum fluid film thickness, obtained for two different values of h_p. Figure 13a shows the journal orbits obtained for cases (II) and (III) using $h_p = 10mm$ and $h_p = 0$. It is shown in the figure that the influence of the parameter h_p in the orbits is more significant for case (III) than for case (II). This is explained by the fact that in the cases (I) and (II), tilting oscillations of the crank are not allowed, therefore, transversal moments over the crank due to the reaction force $\mathbf{f}_A$ are equilibrated by the reaction moments M_X and M_Y, as shown in Fig. 7. The influence of the parameter h_p on the variation of the minimum fluid film thickness for case (III) can be observed in Fig. 13b. Despite the fact that the difference between the two plots does not seem to be significant, it is found that at some crank positions (e.g., when $\theta = 1180deg$) the difference between the two film thicknesses may be as high as 18%. Therefore, in order to estimate more accurately the effect of the tilting oscillations of the crank on the behaviour of the bearings, it is relevant to include the parameter h_p in the multibody model of the compressor.

The difference between the maximum hydrodynamic pressures computed by using the *SJB* and *LJB* approaches respectively can be significant, as it can be seen in Fig. 14. Thus, in order to ensure a better estimation of the load carrying capacity, and taking into consideration that the bearings of the compressor used for this study are short ($l_b \backslash r_b = 0.75$), all the results presented in this section were obtained by using the *SJB* approach.

Conclusions and Further Aspects

Three different approaches for the modelling of a hermetic reciprocating compressor have been analysed in this work. It was found that when the lateral and tilting vibration of the crank are included in the model, more precise estimations of the minimum film thickness are obtained. However, no significant differences were found in the estimation of the hydrodynamic journal bearing forces and the fluid film pressures between the different cases studied. The maximum forces and the minimum film thickness are obtained when the piston is close to the top dead centre. Furthermore, a delay of approximately 30*deg* between the lowest value of the minimum oil film thickness and the maximum fluid film pressure at each cycle was found. The results showed that the nonlinear behaviour of the orbits increases due to the tilting oscillations of the crank, influenced by the length of the crank pin. The increase of the minimum fluid film thickness and the reduction of the bearing vibrations seem to be feasible by modifying the hydrodynamic lubrication conditions through the implementation of a controllable lubrication system based on the periodic behaviour of the bearing performance. In order to develop such a system, further work will be carried out.

Acknowledgments

The authors gratefully acknowledge the support given by the Programme Alβan, the European Union Programme of High Level Scholarships for Latin America, scholarship No. E06D101992CO.

References

Cho, J. R. and Moon, S.J., 2005, "A Numerical Analysis of the Interaction between the Piston Oil Film and the Component Deformation in a Reciprocating Compressor", *Tribology International*, Vol.38, pp. 459-468.

Dufour, R., Der Hagopian, J. and Lalanne, M., 1995, "Transient and Steady State Dynamic Behaviour of Single Cylinder Compressors: Prediction and Experiments", *Journal of Sound and Vibration*, Vol.181, pp. 23-41.

Frêne, J., Nicolas, D., Degueurce, B., Berthe, D. and Godet, M., 1990, "Lubrification Hydrodynamique", Ed. Eyrolles, Paris, 488 p.

Garcia de Jalon, J. and Bayo, E., 1994, "Kinematic and Dynamic Simulation of Multibody Systems", Ed. Springer-Verlag, New-York, 440 p.

Gommed, K. and Etsion, I., 1993, "Dynamic Analysis of Gas Lubricated Reciprocating Ringless Pistons - Basic Modelling", *Journal of Tribology*, Vol.115, pp. 207-213.

Hamrock, B. J., 1991, "Fundamental of Fluid Film Lubrication", NASA Reference Publication, USA, 635 p.

Kim, T. J. and Han, J. S., 2004, "Comparison of the Dynamic Behavior and Lubrication Characteristics of a Reciprocating Compressor Crankshaft in Both Finite and Short Bearing Models", *Tribology Transactions*, Vol.47, No.1, pp. 61-69.

Longo, G. and Gasparella, A. 2003, "Unsteady State Analysis of the Compression Cycle of a Hermetic Reciprocating Compressor", *International Journal of Refrigeration*, Vol.26, pp. 681-689.

Nelson, H. D. and McVaugh, J. M., 1976, "The dynamics of Rotor-Bearing Systems Using Finite Elements", *Journal of Engineering for Industry*, Vol.98, pp. 593-600.

Pal, R., Sinhasan, R. and Singh, D.V, 1988, "Analysis of a Big-End Bearing - a Finite Element Approach", *Wear*, Vol.121, No.1, pp. 117-120.

Rasmussen, B.D., 1997, "Variable Speed Hermetic Reciprocating Compressors for Domestic Refrigerators", Ph.D. Thesis, Technical University of Denmark, Lyngby, Denmark, Vol.1, 158 p.

Rigola, S. J., 2002, "Numerical Simulation and Experimental Validation of Hermetic Reciprocating Compressors", Ph.D. Thesis, Universidad Politécnica de Cataluña, Barcelona, Spain, 109 p.

Ritchie, G.S., 1975, "The Prediction of Journal Loci in Dynamically Loaded Internal Combustion Engine Bearings", *Wear*, Vol.35, No.2, pp. 291-297.

Santos, I. F., 2001, "Dinâmica de Sistemas Mecanicos", Ed. Makron Books, Sao Paulo, Brasil, 272 p.

Appendix A.

Full Matrix of the Multibody Dynamic Model – **Case (I):** $[\bar{\mathbf{A}}]_{\mathbf{I}} \cdot \{\bar{\mathbf{b}}\}_{\mathbf{I}} = \{\bar{\mathbf{c}}\}_{I}$

$$\begin{bmatrix}
1 & 0 & 0 & 0 & 0 & 0 & 0 & 0 & 0 & 0 & 0 & 0 & 0 & 0 & m_p & 0 \\
0 & -1 & 0 & 1 & 0 & 0 & 0 & 0 & 0 & 0 & 0 & 0 & 0 & 0 & 0 & 0 \\
0 & 0 & 1 & 0 & -1 & 0 & 0 & 0 & 0 & 0 & 0 & 0 & 0 & 0 & 0 & 0 \\
1 & 0 & 0 & 0 & 0 & -1 & 0 & 0 & 0 & 0 & 0 & 0 & 0 & 0 & -m_{cr} & -m_{cr}\bar{r}_{cr}s\alpha \\
0 & 1 & 0 & 0 & 0 & 0 & -1 & 0 & 0 & 0 & 0 & 0 & 0 & 0 & 0 & -m_{cr}\bar{r}_{cr}c\alpha \\
0 & 0 & 1 & 0 & 0 & 0 & 0 & 1 & 0 & 0 & 0 & 0 & 0 & 0 & 0 & 0 \\
0 & 0 & 0 & 0 & 0 & 1 & 0 & 0 & -1 & 0 & 0 & 0 & 0 & 0 & 0 & 0 \\
0 & 0 & 0 & 0 & 0 & 0 & 1 & 0 & 0 & -1 & 0 & 0 & 0 & 0 & 0 & \\
0 & 0 & 0 & 0 & 0 & 0 & 0 & 1 & 0 & 0 & 1 & 0 & 0 & 0 & 0 & \\
0 & 0 & 0 & 0 & 0 & 0 & 0 & l & 0 & 0 & 0 & 0 & 0 & 0 & 0 & \\
0 & 0 & 0 & 0 & 0 & ls\alpha & lc\alpha & 0 & 0 & 0 & 0 & 0 & 0 & 0 & m_{cr}\bar{r}_{cr}s\alpha & I_{cr_z} \\
0 & 0 & 0 & 0 & 0 & 0 & 0 & 0 & 0 & 0 & 0 & c\theta & s\theta & 0 & 0 & 0 \\
0 & 0 & 0 & 0 & 0 & 0 & 0 & r_C & 0 & 0 & 0 & -s\theta & c\theta & 0 & 0 & 0 \\
0 & 0 & 0 & 0 & 0 & r_C s\theta & -r_C c\theta & 0 & 0 & 0 & 0 & 0 & 0 & I_{cz} & 0 & 0 \\
0 & 0 & 0 & 0 & 0 & 0 & 0 & 0 & 0 & 0 & 0 & 0 & 0 & r_C s\theta & 1 & ls\alpha \\
0 & 0 & 0 & 0 & 0 & 0 & 0 & 0 & 0 & 0 & 0 & 0 & 0 & -r_C c\theta & 0 & lc\alpha
\end{bmatrix}
\begin{Bmatrix}
f_{B_x} \\ f_{B_y} \\ f_{B_z} \\ N_y \\ N_z \\ f_{A_x} \\ f_{A_y} \\ f_{A_z} \\ f_{C_x} \\ f_{C_y} \\ f_{C_z} \\ M_{C_x} \\ M_{C_y} \\ \ddot{\theta} \\ \ddot{x}_B \\ \ddot{\alpha}
\end{Bmatrix} =
\begin{Bmatrix}
-P_g A_p \\ 0 \\ -m_p g \\ m_{cr}\dot{\alpha}^2\bar{r}_{cr}c\alpha \\ -m_{cr}\dot{\alpha}^2\bar{r}_{cr}s\alpha \\ m_{cr}g \\ 0 \\ 0 \\ m_c g \\ \bar{r}_{cr}m_{cr}g \\ 0 \\ 0 \\ 0 \\ 0 \\ \tau_z \\ -r_C\dot{\theta}^2c\theta - l\dot{\alpha}^2c\alpha \\ -r_C\dot{\theta}^2s\theta - l\dot{\alpha}^2s\alpha
\end{Bmatrix}$$

Appendix B

Full Matrix of the Multibody Dynamic Model – **Case (II):** $[\overline{A}]_{II} \cdot \{\overline{b}\}_{II} = \{\overline{c}\}_{II}$

$$\begin{bmatrix}
1 & 0 & 0 & 0 & 0 & 0 & 0 & 0 & 0 & 0 & 0 & m_p & 0 & 0 & 0 \\
0 & -1 & 0 & 1 & 0 & 0 & 0 & 0 & 0 & 0 & 0 & 0 & 0 & 0 & 0 \\
0 & 0 & 1 & 0 & -1 & 0 & 0 & 0 & 0 & 0 & 0 & 0 & 0 & 0 & 0 \\
1 & 0 & 0 & 0 & 0 & -1 & 0 & 0 & 0 & 0 & -m_{cr} & 0 & 0 & -m_{cr}\bar{r}_{cr}s\alpha & 0 \\
0 & 1 & 0 & 0 & 0 & 0 & -1 & 0 & 0 & 0 & 0 & 0 & 0 & -m_{cr}\bar{r}_{cr}c\alpha & 0 \\
0 & 0 & 1 & 0 & 0 & 0 & 0 & 1 & 0 & 0 & 0 & 0 & 0 & 0 & 0 \\
0 & 0 & 0 & 0 & 0 & 0 & 0 & 1 & 1 & 0 & 0 & 0 & 0 & 0 & 0 \\
0 & 0 & 0 & 0 & 0 & 0 & 0 & l & 0 & 0 & 0 & 0 & 0 & 0 & 0 \\
0 & 0 & 0 & 0 & 0 & ls\alpha & lc\alpha & 0 & 0 & 0 & 0 & m_{cr}\bar{r}_{cr}s\alpha & I_{cr_Z} & 0 & 0 \\
0 & 0 & 0 & 0 & 0 & 0 & 0 & 0 & 0 & c\theta & s\theta & 0 & 0 & 0 & 0 \\
0 & 0 & 0 & 0 & 0 & 0 & 0 & r_C & 0 & -s\theta & c\theta & 0 & 0 & 0 & 0 \\
0 & 0 & 0 & 0 & 0 & -r_C s\theta & -r_C c\theta & 0 & 0 & 0 & 0 & I_{c_Z} & 0 & 0 & 0 \\
0 & 0 & 0 & 0 & 0 & 0 & 0 & 0 & 0 & 0 & -r_c s\alpha & 1 & ls\alpha & -1 & 0 \\
0 & 0 & 0 & 0 & 0 & 0 & 0 & 0 & 0 & 0 & -r_c c\alpha & 0 & lc\alpha & 0 & -1 \\
0 & 0 & 0 & 0 & 0 & -1 & 0 & 0 & 0 & 0 & 0 & 0 & 0 & m_C & 0 \\
0 & 0 & 0 & 0 & 0 & 0 & -1 & 0 & 0 & 0 & 0 & 0 & 0 & 0 & m_C
\end{bmatrix}
\begin{Bmatrix}
f_{B_X} \\ f_{B_Y} \\ f_{B_Z} \\ N_Y \\ N_Z \\ f_{A_X} \\ f_{A_Y} \\ f_{A_Z} \\ f_{C_Z} \\ M_{C_X} \\ M_{C_Y} \\ \ddot{\theta} \\ \ddot{x}_B \\ \ddot{\alpha} \\ \ddot{x}_C \\ \ddot{y}_C
\end{Bmatrix} =
\begin{Bmatrix}
-P_g A_p \\ 0 \\ -m_p g \\ m_{cr}\dot{\alpha}^2\bar{r}_{cr}c\alpha \\ -m_{cr}\dot{\alpha}^2\bar{r}_{cr}s\alpha \\ m_{cr}g \\ m_c g \\ \bar{r}_{cr}m_{cr}g \\ 0 \\ 0 \\ 0 \\ \tau_z \\ -r_c\dot{\theta}^2 c\theta - l\dot{\alpha}^2 c\alpha \\ -r_c\dot{\theta}^2 s\theta - l\dot{\alpha}^2 s\alpha \\ F_X \\ F_Y
\end{Bmatrix}$$

Appendix C

Full Matrix of the Multibody Dynamic Model – **Case (III):** $[\overline{A}]_{III} \cdot \{\overline{b}\}_{III} = \{\overline{c}\}_{III}$

$$\begin{bmatrix}
1 & 0 & 0 & 0 & 0 & 0 & 0 & 0 & 0 & 0 & m_p & 0 & 0 & 0 & 0 & 0 \\
0 & 1 & 0 & -1 & 0 & 0 & 0 & 0 & 0 & 0 & 0 & 0 & 0 & 0 & 0 & 0 \\
0 & 0 & 1 & 0 & -1 & 0 & 0 & 0 & 0 & 0 & 0 & 0 & 0 & 0 & 0 & 0 \\
-1 & 0 & 0 & 0 & 0 & 1 & 0 & 0 & 0 & 0 & m_{cr} & m_{cr}\bar{r}_{cr}s\alpha & 0 & 0 & 0 & 0 \\
0 & -1 & 0 & 0 & 0 & 0 & 1 & 0 & 0 & 0 & 0 & m_{cr}\bar{r}_{cr}c\alpha & 0 & 0 & 0 & 0 \\
0 & 0 & 1 & 0 & 0 & 0 & 0 & 1 & 0 & 0 & 0 & 0 & 0 & 0 & 0 & 0 \\
0 & 0 & 0 & 0 & 0 & 0 & 0 & l & 0 & 0 & 0 & 0 & 0 & 0 & 0 & 0 \\
0 & 0 & 0 & 0 & 0 & ls\alpha & lc\alpha & 0 & 0 & 0 & m_{cr}\bar{r}_{cr}s\alpha & I_{cr_Z} & 0 & 0 & 0 & 0 \\
0 & 0 & 0 & 0 & 0 & 0 & 0 & -1 & 1 & 0 & 0 & 0 & 0 & 0 & 0 & 0 \\
0 & 0 & 0 & 0 & 0 & C_1 & C_2 & C_3 & 0 & -I_{c_Z} - I_{m_Z} & 0 & 0 & -m_c e_c s\Gamma & -m_c e_c s\beta c\Gamma & -I_{c_Z} s\Gamma & 0 \\
0 & 0 & 0 & 0 & 0 & 0 & 0 & 0 & 0 & r_c c\Gamma s\theta & 1 & ls\alpha & -1 & 0 & 0 & C_4 \\
0 & 0 & 0 & 0 & 0 & 0 & 0 & 0 & 0 & C_5 & 0 & lc\alpha & 0 & -1 & C_6 & C_7 \\
0 & 0 & 0 & 0 & 0 & -1 & 0 & 0 & 0 & 0 & 0 & 0 & m_c & 0 & 0 & 0 \\
0 & 0 & 0 & 0 & 0 & 0 & -1 & 0 & 0 & 0 & 0 & 0 & 0 & m_c & 0 & 0 \\
0 & 0 & 0 & 0 & 0 & -h_p C_1 r_c^{-1} & -h_p C_2 r_c^{-1} & -h_p C_3 r_c^{-1} & 0 & 0 & 0 & 0 & 0 & 0 & I_{c_X} c\Gamma c\theta & I_{c_X} s\theta \\
0 & 0 & 0 & 0 & 0 & C_8 & C_9 & C_{10} & 0 & 0 & 0 & 0 & C_{11} & C_{12} & -I_{c_Y} c\Gamma s\theta & I_{c_Y} c\theta
\end{bmatrix}
\begin{Bmatrix}
f_{B_X} \\ f_{B_Y} \\ f_{B_Z} \\ N_Y \\ N_Z \\ f_{A_X} \\ f_{A_Y} \\ f_{A_Z} \\ f_{C_Z} \\ \ddot{\theta} \\ \ddot{x}_B \\ \ddot{\alpha} \\ \ddot{x}_C \\ \ddot{y}_C \\ \ddot{\beta} \\ \ddot{\Gamma}
\end{Bmatrix} =
\begin{Bmatrix}
-P_g A_p \\ 0 \\ -m_p g \\ -m_{cr}\dot{\alpha}^2\bar{r}_{cr}c\alpha \\ -m_{cr}\dot{\alpha}^2\bar{r}_{cr}s\alpha \\ m_{cr}g \\ \bar{r}_{cr}m_{cr}g \\ 0 \\ m_c g \\ \beta\ddot{\Gamma}I_{c_Z}c\Gamma - \tau_z \\ C_{13} \\ C_{14} \\ 0 \\ 0 \\ C_{15} \\ C_{16}
\end{Bmatrix}$$

where:

$$
\begin{aligned}
C_1 &= -r_c c\Gamma s\theta \\
C_2 &= r_c(c\beta c\theta - s\beta s\Gamma s\theta) \\
C_3 &= r_c(c\beta s\Gamma s\theta - s\beta c\Gamma) \\
C_4 &= r_c s\Gamma c\theta + h_p c\Gamma \\
C_5 &= r_c(s\beta s\Gamma s\theta - c\beta c\theta) \\
C_6 &= r_c(s\beta s\theta - c\beta s\Gamma c\theta) - h_p c\beta c\Gamma \\
C_7 &= -r_c s\beta c\Gamma c\theta + h_p s\beta s\Gamma \\
C_8 &= r_c s\Gamma + h_p c\Gamma c\theta \\
C_9 &= -r_c s\beta c\Gamma + h_p(s\beta s\Gamma c\theta + c\beta s\theta)
\end{aligned}
$$

$$
\begin{aligned}
C_{10} &= r_c c\beta c\Gamma + h_p(s\beta s\theta - c\beta s\Gamma c\theta) \\
C_{11} &= -m_{cr} e_c c\Gamma s\theta \\
C_{12} &= m_{cr} e_c(c\beta c\theta - s\beta s\Gamma s\theta) \\
C_{13} &= \dot{\Gamma}^2(h_p s\Gamma - r_c c\Gamma c\theta) + r_c\dot{\theta}(2\dot{\Gamma}s\Gamma s\theta - \dot{\theta}c\Gamma c\theta) - l\dot{\alpha}^2 c\alpha \\
C_{14} &= l\dot{\alpha}^2 s\alpha - r_c\dot{\theta}^2(c\beta s\theta + s\beta s\Gamma c\theta) - \dot{\beta}^2(r_c c\beta s\theta + r_c s\theta s\Gamma c\theta + h_p s\beta c\Gamma) - \dot{\Gamma}^2(r_c s\beta s\Gamma c\theta + h_p s\beta c\Gamma) \\
&= -2r_c\dot{\theta}\dot{\beta}(s\beta c\theta + c\beta s\Gamma s\theta) + 2\beta\dot{\Gamma}(r_c c\beta c\Gamma c\theta - h_p c\beta s\Gamma) - 2r_c\theta\dot{\Gamma}s\beta c\Gamma s\theta \\
C_{15} &= I_{c_X}(\beta\dot{\Gamma}s\Gamma c\theta + \beta\dot{\theta}c\Gamma s\theta - \dot{\Gamma}\dot{\theta}c\theta) + (\beta s\Gamma + \dot{\theta})(\dot{\Gamma}c\theta - \dot{\beta}c\Gamma s\theta)(I_{c_Y} - I_{c_Z}) \\
C_{16} &= I_{c_Y}(\beta\dot{\theta}c\Gamma c\theta + \dot{\Gamma}\dot{\theta}s\theta - \beta\dot{\Gamma}s\Gamma s\theta) + (\dot{\beta}s\Gamma + \dot{\theta})(\dot{\Gamma}s\theta + \dot{\beta}c\Gamma c\theta)(I_{c_{Z0}} - I_{c_X})
\end{aligned}
$$

B.3 [J3] - *Tribology International*, Vol. 42 (10), 2009, pp. 1478-86.

Tribology International 42 (2009) 1478–1486

Contents lists available at ScienceDirect

Tribology International

journal homepage: www.elsevier.com/locate/triboint

Linking rigid multibody systems via controllable thin fluid films

E.A. Estupiñan, I.F. Santos *

Technical University of Denmark, Department of Mechanical Engineering, Nils Koppels Alle, 404, Kgs. Lyngby DK-2800, Denmark

ARTICLE INFO

Article history:
Received 8 July 2008
Received in revised form
22 January 2009
Accepted 7 May 2009
Available online 15 May 2009

Keywords:
Controllable thin fluid film
Hybrid lubrication
Fluid film journal bearing
Reciprocating compressor

ABSTRACT

This work deals with the mathematical modelling of multibody systems interconnected via thin fluid films. The dynamics of the fluid films can be actively controlled by means of different types of actuators, allowing significant vibration reduction of the system components. In this framework, this paper gives a theoretical contribution to the combined fields of fluid–structure interaction and vibration control. The methodology is applied to a reciprocating linear compressor, where the dynamics of the mechanical components are described with help of multibody dynamics. The crank is linked to the rotor via a thin fluid film, where the hydrodynamic pressure is described by the Reynolds equation, which is modified to accommodate the controllable lubrication conditions. The fluid film forces are coupled to the set of nonlinear equations that describes the dynamics of the reciprocating linear compressor. The system of equations is numerically solved for the case when the system operates with conventional hydrodynamic lubrication and for several cases of the bearing operating under controlled hybrid lubrication conditions. The analysis of the results is carried out with focus on the behaviour of the journal orbits, maximum fluid film pressure and minimum fluid film thickness.

1. Introduction

The feasibility of applying active lubrication to the main bearings of a hermetic reciprocating compressor is studied in this work, with the help of multibody dynamics and fluid film theory. Small-scale reciprocating compressors are of common use to compress coolant gas in household refrigerators and air conditioners. This type of compressors have pistons that are driven directly through a slider-crank mechanism, converting the rotating movement of the rotor to an oscillating motion, as illustrated in Fig. 1. The performance of the bearings affects key functions of the compressor, such as durability, noise, and vibrations. Therefore the study and optimization of the dynamic behaviour of reciprocating compressors, taking into account the hydrodynamics of bearings, can be of significant importance for the development of new prototypes. Several studies related to the modelling of small reciprocating compressors can be found in the literature [3,4], however, only a few of them have incorporated in their models the dynamics of the fluid films. For instance, a study that includes the coupling of fluid–structure dynamics to analyse the dynamics of the piston is described in Ref. [5]. In the work of Ref. [6], a model of the coupled dynamic behaviour of the piston and crankshaft is developed and some comparisons between a finite-width bearing model and a short-width bearing approach are included in the study. In contrast to previous studies, in this work a multibody dynamic model that represents the dynamics of the main mechanical components of a reciprocating compressor is coupled to the dynamics of the fluid film bearings, and the analysis is focused on the performance of the upper bearing working under hydrodynamic and hybrid (controllable) lubrication conditions. In a reciprocating machine, the lubricant films surrounding the main bearings commonly have to support inertial loads, crankshaft unbalance forces and the reciprocating forces coming from the gas pressure dynamics. The behaviour of these forces is quasi-periodic, since some changes in magnitude and frequency can occur from one cycle to the next, depending on the operating conditions. It causes that the centre of the journal bearing does not conserve a steady position, generating unwanted vibrations of the journal. The most common approach used for the analysis of dynamically loaded bearings is the mobility technique, which was developed more than 40 years ago [1]. Other methods involving bearing flexibility and thermal effects have been developed in the last two decades [2], however they are characterized by a higher computational complexity. In this study, the fluid film theory based on hydrodynamic lubrication conditions has been used to describe the governing equation of the fluid pressure distribution along the bearing surface, since the analysis is more focused on studying the feasibility of actively modifying the hydrodynamic fluid films through radial oil injection (controllable hybrid lubrication), than in the estimation of the elastic deformations of the system. One refers to hybrid lubrication when the hydrostatic and the hydrodynamic lubrication are simultaneously combined in a journal bearing. When part of the hydrostatic pressure is dynamically modified, one refers to active lubrication [7]. Besides the operational conditions, the performance of a hybrid

* Corresponding author. Tel.: +45 45256269; fax: +45 45931475.
E-mail address: ifs@mek.dtu.dk (I.F. Santos).

0301-679X/$ - see front matter © 2009 Elsevier Ltd. All rights reserved.
doi:10.1016/j.triboint.2009.05.009

Nomenclature

a_b	axial land (m)
$\bar{a}_b$	axial land width ratio, $\bar{a}_b = a_b/l_b$
A_p	transversal area of the piston (m^2)
c_b	clearance of bearing (m)
d_o	diameter of orifices (m)
e_c	mass eccentricity of the crank (m)
FB	finite-width journal bearing
f	vector of reaction forces (N)
$\mathbf{f_b}$	vector of journal bearing forces (N)
$h(\varphi, t)$	oil film thickness (m)
l	length (m)
l_b	width of bearing (m)
LJB	long-width journal bearing
m_c	mass of the crank (kg)
m_{cr}	mass of the connecting rod (kg)
m_p	mass of the piston (kg)
P_g	gas pressure inside the cylinder (Pa)
$p(\varphi, z, t)$	fluid film pressure distribution (Pa)
P_{inj}	injection pressure (Pa)
r	radius (m)
SJB	short-width journal bearing
$\mathbf{T_i}$	transformation matrix in the angle i
U	tangential velocity (m/s)
α	rotation angle of the connecting rod (rad)
ε	eccentricity ratio
λ	bearing aspect ratio, $\lambda = l_b/2r_b$
μ	oil film viscosity (Pa s)
ϕ	attitude angle (rad)
Ω	angular velocity of the rotor (rad/s)
ρ	fluid density (kg/m^3)
τ_z	motor shaft torque (N m)
θ	rotational angle of the crank (rad)
Θ	angle measured from X axis (rad)

Subscripts

A, B, C	relative to the points A, B or C, respectively
B_i	relative to the i-th moving reference frame
b	relative to the bearings
c	relative to the crank
cr	relative to the connecting rod
I	relative to the inertial reference frame
j	relative to the journal
o	relative to the orifices

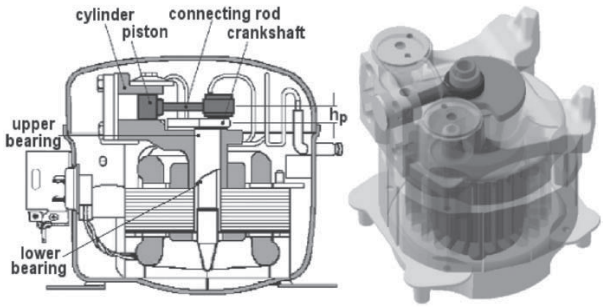

Fig. 1. Schematic draw and general view of a hermetic reciprocating compressor.

journal bearing depends on several geometric parameters, such as position and diameter of the orifices, bearing aspect ratio and axial land width ratio [8,9]. Several studies have been carried out to geometrically optimize the design of hybrid journal bearings for specific configurations and for different external load conditions [10,11]. Depending on the load and speed working conditions, several types of configurations are possible for hybrid journal bearings. Particularly, it has been shown by Rowe [9], that for hybrid performance and easy manufacture, hole-entry type bearings with holes disposed circumferentially along two rows may offer advantages over other configurations.

The present work compares the tribological performance of the upper journal bearing of a compressor working with conventional

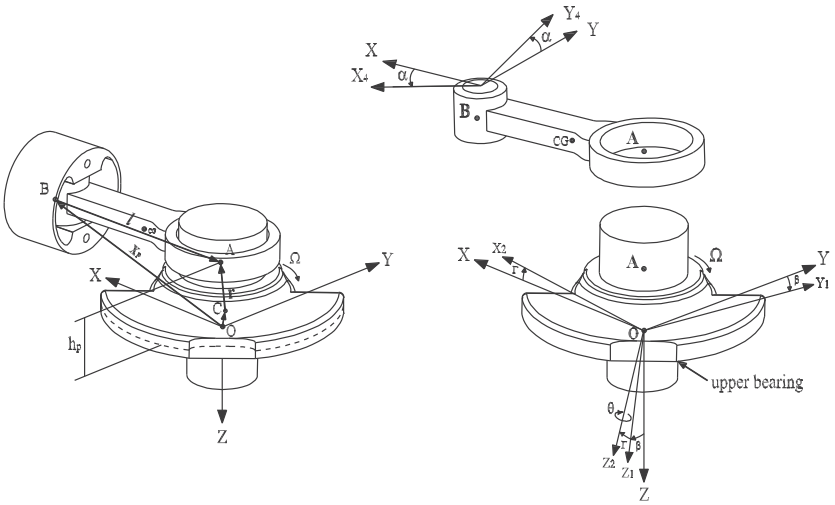

Fig. 2. Geometry and reference systems. Left: illustration of the main constraint equation; right: reference frames and rotation angles.

hydrodynamic lubrication and with four different configurations of hybrid lubrication, proposing some rules for the variation of the injection pressure in function of the crank angle. The equations of motion for the reciprocating mechanism are developed using multibody dynamics. The crank and rotor are interconnected via a thin fluid film where the hydrodynamic pressure distribution is described by the Reynolds equation, which is modified in order to include the dynamics of the active lubrication and numerically solved by means of the finite-difference method. The analysis of the results is focused on the behaviour of the journal orbits, maximum fluid film pressure and minimum fluid film thickness.

2. Mathematical modelling

In this section the formulation of representative equations describing the mathematical model for a hermetic compressor is developed. The motion equations for the piston-connecting rod–crank system are formulated with the help of multibody dynamics theory, using Newton–Euler's method and using a frame notation of common use in multibody dynamics [12–14]. Fig. 2 shows a sketch indicating the reference frames and the main angles of rotation (β, Γ, θ and α). In order to be able to describe all the representative vectors, one inertial reference frame (I_{XYZ}) and four moving reference frames (B_i) have been defined. The inertial reference frame is attached to the centre of the bearing (point **O**), the moving reference frames $B_1(X_1Y_1Z_1)$, $B_2(X_2Y_2Z_2)$ and $B_3(X_3Y_3Z_3)$ are attached to the crank and the moving reference frame $B_4(X_4Y_4Z_4)$ is attached to the connecting rod. With the help of the geometrical transformation matrices $\mathbf{T}_\beta$, $\mathbf{T}_\Gamma$, $\mathbf{T}_\theta$ and $\mathbf{T}_\alpha$ any vector can be easily transformed from one reference frame to another. According to Fig. 2, the main constraint equation of the system is given by

$$ {}_I\mathbf{x_p}+{}_I\mathbf{l}={}_I\mathbf{r}+{}_I\mathbf{c} \tag{1}$$

where ${}_I\mathbf{x_p}=\{x_B,0,-h_p\}^T$; ${}_I\mathbf{l}=\{-l_{cr}\cos\alpha,\ l_{cr}\sin\alpha,0\}^T$; ${}_I\mathbf{r}=\mathbf{T}_\beta^{\mathbf{T}}\cdot\mathbf{T}_\Gamma^{\mathbf{T}}\cdot\mathbf{T}_\theta^{\mathbf{T}}\cdot{}_{B_3}\mathbf{r}$; ${}_{B_3}\mathbf{r}=\{r_c,0,-h_p\}^T$; and ${}_I\mathbf{c}=\{x_c,y_c,0\}^T$.

The equations of motion for each body are given by Eqs. (2)–(6). The force equations are described in the inertial reference frame and the moment equations of the crank and the connecting rod are described in the moving reference frames B_3 and B_4, respectively.

- *Force equation—crank*:

$$\sum {}_I\mathbf{f}=m_c\cdot{}_I\bar{\mathbf{a}}_c\Rightarrow {}_I\mathbf{f_A}+{}_I\mathbf{f_{ub}}+{}_I\mathbf{f_b}=m_c\{\ddot{x}_c,\ddot{y}_c,0\}^T \tag{2}$$

where ${}_I\mathbf{f_{ub}}$ is the vector of the crank unbalance force and ${}_I\mathbf{f_b}$ is the vector of the dynamic journal bearing forces.

- *Moment equation—crank*:

$$\sum {}_{B_3}\mathbf{M_C}={}_{B_3}\mathbf{r}\times{}_{B_3}\mathbf{f_A}+{}_{B-3}\boldsymbol{\tau}={}_{B_3}\mathbf{I_c}\frac{d}{dt}({}_{B_3}\boldsymbol{\omega})+{}_{B_3}\boldsymbol{\omega}\times({}_{B_3}\mathbf{I}_C\cdot{}_{B_3}\boldsymbol{\omega})+m_c\cdot{}_{B_3}\bar{\mathbf{r}}_{C-cm}\times{}_{B_3}\mathbf{a_C} \tag{3}$$

where ${}_{B_3}\mathbf{f_A}=\mathbf{T}_\theta\cdot\mathbf{T}_\Gamma\cdot\mathbf{T}_\beta\cdot{}_I\mathbf{f_A}$; ${}_{B_3}\boldsymbol{\tau}=\{0,0,\tau_z\}^T$; and ${}_{B_3}\bar{\mathbf{r}}_{C-cm}=\{e_c,0,0\}^T$.

- *Force equation—connecting rod*:

$$\sum {}_I\mathbf{f}=m_{cr}\cdot{}_I\bar{\mathbf{a}}_{cr}={}_I\mathbf{f_A}+{}_I\mathbf{f_B} \tag{4}$$

where

$${}_I\bar{\mathbf{a}}_{cr}={}_I\mathbf{a}_B+{}_I\dot{\boldsymbol{\alpha}}\times{}_I\bar{\mathbf{r}}_{\mathbf{cr}}+{}_I\boldsymbol{\alpha}\times{}_I\boldsymbol{\alpha}\times{}_I\bar{\mathbf{r}}_{\mathbf{cr}}=\begin{Bmatrix}\ddot{x}_B+\bar{r}_{cr}(\dot{\alpha}^2\cos\alpha+\ddot{\alpha}\sin\alpha)\\ \bar{r}_{cr}(\ddot{\alpha}\cos\alpha-\dot{\alpha}^2\sin\alpha)\\ 0\end{Bmatrix}.$$

- *Moment equation—connecting rod*

$$\sum {}_{B_4}\mathbf{M_B}={}_{B_4}\mathbf{I}\times{}_{B_4}\mathbf{f_A}={}_{B_4}\mathbf{I}_{cr}\frac{d}{dt}({}_{B_4}\dot{\boldsymbol{\alpha}})+{}_{B_4}\dot{\boldsymbol{\alpha}}\times({}_{B_4}\mathbf{I}_{crB_4}\dot{\boldsymbol{\alpha}})+m_{cr}\cdot{}_{B_4}\bar{\mathbf{r}}_{cr}\times{}_{B_4}\mathbf{a}_B \tag{5}$$

where ${}_{B_4}\mathbf{f_A}=\mathbf{T}_{\alpha\cdot I}\mathbf{f_A}$; ${}_{B_4}\mathbf{a_B}=\mathbf{T}_{\alpha\cdot I}\mathbf{a_B}$; ${}_I\mathbf{a_B}=\{\ddot{x}_B,0,0\}^T$.

- *Force equation—piston*

$$\sum {}_I\mathbf{f_B}=m_{p\cdot I}\mathbf{a}_B={}_I\mathbf{f_B}+{}_I\mathbf{f_N}+{}_I\mathbf{f_p} \tag{6}$$

where ${}_I\mathbf{f_p}=\{P_gA_p,0,0\}^T$.

The equations of motion may be written in a matrix form as in (7), where the vector $\bar{\mathbf{b}}$ includes the unknown reaction forces, reaction moments and accelerations of the system:

$$\bar{\mathbf{A}}\cdot\bar{\mathbf{b}}=\bar{\mathbf{c}} \tag{7}$$

where

$$\bar{\mathbf{b}}=\{f_{B_x},f_{B_y},f_{B_z},N_y,N_z,f_{A_x},f_{A_y},f_{A_z},f_{C_z},\ddot{\theta},\ddot{x}_B,\ddot{\alpha},\ddot{x}_c,\ddot{y}_c\}^T$$

3. Fluid film forces

The equations that govern the dynamics of the fluid films in a dynamically loaded journal bearing, for the conventional hydrodynamic lubrication case and for the active lubrication case, are presented. The main geometrical relations of a fluid film journal bearing are shown in Fig. 3. The governing equation for the pressure distribution of the oil film in journal bearings can be obtained from the standard reduced form of the Reynolds equation for elastohydrodynamic lubrication [15], given by

$$\frac{\partial}{\partial x}\left(\frac{\rho h^3}{12\mu}\frac{\partial p}{\partial x}\right)+\frac{\partial}{\partial z}\left(\frac{\rho h^3}{12\mu}\frac{\partial p}{\partial z}\right)=\frac{\partial}{\partial x}\left(\frac{\rho h(U_j-U_b)}{2}\right)+\frac{\partial(\rho h)}{\partial t} \tag{8}$$

Eq. (8) describes the flow in the journal bearing in the domain $0\le x\le 2\pi r_b$ and $-l_b/2\le z\le l_b/2$. For the upper bearing of the compressor: $U_j=\Omega r_b$ and $U_b=0$. The fluid film thickness measured from $\varphi=0$ can be calculated using: $h=c_b(1+\varepsilon\cos\varphi)$, where φ is the angle measured from the location of the maximum fluid film thickness, as shown in Fig. 3. Thus, using the coordinate transformation $x=r_b\varphi$ in Eq. (8) and assuming that the fluid is isoviscous, Newtonian and incompressible, the Reynolds equation can be rewritten as

$$\frac{\partial}{\partial\varphi}\left(\frac{h^3}{\mu}\frac{\partial p}{\partial\varphi}\right)+r_b^2\frac{\partial}{\partial z}\left(\frac{h^3}{\mu}\frac{\partial p}{\partial z}\right)=12c_br_b^2\left[\dot{\varepsilon}\cos\varphi+\varepsilon\sin\varphi\left(\dot{\phi}-\frac{\Omega}{2}\right)\right] \tag{9}$$

In dynamically loaded bearings the eccentricity and attitude angle varies through the loading cycle. Therefore, as seen in Eq. (9), the pressure distribution may be only determined if the normal squeeze velocity ($\dot{\varepsilon}$) and the rotational velocities ($\dot{\phi}$ and Ω)

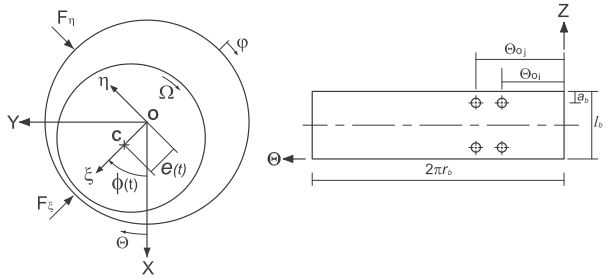

Fig. 3. Journal bearing geometry. Left: front view; right: side view—unwrapped bearing.

are known at any time during each cycle. The journal bearing forces can be calculated by integrating the pressure distribution over the bearing surface as

$$\begin{Bmatrix} F_\xi \\ F_\eta \end{Bmatrix} = \int_0^{2\pi} \int_{-l_b/2}^{l_b/2} p \begin{Bmatrix} \cos\varphi \\ \sin\varphi \end{Bmatrix} r_b \, dz \, d\varphi \tag{10}$$

When the computation of the fluid film forces is limited to the convergent film the solution is known as the half Sommerfeld solution. Another well known cavitation condition is the Gümbel condition in which the Reynolds equation is first solved subjected to the specified pressures at the bearing boundaries and then if subambient pressures appear they are neglected. Although the use of the Gümbel cavitation condition does not satisfy the continuity of flow at film rupture as well as reformation, it provides acceptable accuracy in the estimation of oil film pressure and bearing load capacity with low computational cost [17]. However, in cases where an acceptable estimation of oil flow is required, a more accurate cavitation condition should be used, such as the Jakobsson–Floberg and Olsson cavitation condition [18], which conserves mass both at the rupture and the reformation boundaries but substantially increases the computational cost.

Analytical solutions of Eq. (9) may be obtained only for limited cases: a short-width journal bearing (*SJB*) and an infinitive long-width journal bearing (*LJB*). The short journal bearing approach assumes that the variation of pressure is more significant in the axial direction than in the circumferential direction and therefore the first term on the left side of Eq. (9) can be neglected. For an infinitely long-journal-bearing solution the pressure in the axial direction is assumed to be constant, therefore, the side-leakage term, i.e., the second term on the left side in (9), can be neglected. Thus, using the Gümbel cavitation condition, the analytical expressions to calculate journal forces in ξ, η coordinates using a short-journal-bearing approach and an infinitely long journal approach are given by the equations listed in Table 1.

3.1. The modified Reynolds equation for active lubrication

The governing equation for the hydrodynamic pressure distribution of an active lubricated journal bearing can be obtained from the Navier Stokes equation and the continuity equation by accommodating in the assumed boundary conditions the velocity profile of the oil injection, which is described in detail in Refs. [19,20]. Thus, the pressure distribution for a journal bearing with radial oil injection through orifices located at (φ_i, z_i) along the bearing surface is governed by

$$\frac{\partial}{\partial\varphi}\left(\frac{h^3}{r_b^2\mu}\frac{\partial p}{\partial\varphi}\right) + \frac{\partial}{\partial z}\left(\frac{h^3}{\mu}\frac{\partial p}{\partial z}\right) - \frac{3}{\mu l_o}\sum_{i=1}^{s}\mathsf{F}_i(\varphi,z)\cdot p = 12c_b\left[\dot{\varepsilon}\cos\varphi + \varepsilon\sin\varphi\left(\dot{\phi} - \frac{\Omega}{2}\right)\right] - \frac{3}{\mu l_o}\sum_{i=1}^{s}\mathsf{F}_i(\varphi,z)\cdot P_{inj}(t) \tag{11}$$

Table 1
Analytical equations to calculate journal bearing forces, Ref. [16].

Short-width journal bearing (*SJB*)

$$F_\xi = \frac{-r_b\mu l_b^3}{2c_b^2(1-\varepsilon^2)^2}\left[\frac{\pi\dot{\varepsilon}(1+2\varepsilon^2)}{\sqrt{[]}(1-\varepsilon^2)} + 2\varepsilon^2(\Omega - 2\dot{\phi})\right]$$

$$F_\eta = \frac{r_b\mu l_b^3\varepsilon}{2c_b^2(1-\varepsilon^2)^2}\left[4\dot{\varepsilon} + \frac{\pi}{2}(\Omega - 2\dot{\phi})\sqrt{[]}1-\varepsilon^2\right]$$

Long-width journal bearing (*LJB*)

$$F_\xi = -\frac{12\mu r_b^3 l_b}{c_b^2}\left[\frac{\varepsilon^2(\Omega-2\dot{\phi})}{(2+\varepsilon^2)(1-\varepsilon^2)} + \frac{\dot{\varepsilon}}{(1-\varepsilon^2)^{3/2}}\left(\frac{\pi}{2} - \frac{8}{\pi(2+\varepsilon^2)}\right)\right]$$

$$F_\eta = \frac{12\mu r_b^3 l_b}{c_b^2}\left[\frac{\pi\varepsilon(\Omega-2\dot{\phi})}{2(2+\varepsilon^2)\sqrt{[]}1-\varepsilon^2} + \frac{2\varepsilon\dot{\varepsilon}}{(2+\varepsilon^2)(1-\varepsilon^2)}\right]$$

where

$$\mathsf{F}_i(\varphi,z) = \begin{cases} \dfrac{d_o^2}{4} - R^2 & \text{if} \quad R^2 \le d_o^2/4 \\ 0 & \text{if} \quad R^2 \ge d_o^2/4 \end{cases}$$

and $R^2 = r_b^2(\varphi-\varphi_i)^2 + (z-z_i)^2$.

In this equation, the function $\mathsf{F}_i(\varphi,z)$ is used to describe mathematically the problem and is physically related to the position of the orifices. In other words, this function will be different than zero inside the orifices region and will be zero elsewhere. On the other hand, $P_{inj}(t)$ gives the injection pressure at each orifice in function of time. It can be observed that when the bearing is operating only under conventional hydrodynamic lubrication, the function $\mathsf{F}_i(\varphi,z) = 0$ and Eq. (11) changes into the traditional Reynolds equation given by (9).

From the point of view of active lubrication and specifically considering the case of a dynamically loaded journal bearing, P_{inj} must be dynamically controlled. However, and taking into account the periodic behaviour of the load acting on the upper bearing, this work is more focused on the evaluation of the tribological performance of the bearing operating with different configurations of radial oil injection, than in the design of the control system. Thus, the modified Reynolds equation (11) is solved at each time step assuming that the oil injection pressures for each one of the orifices are known and are given in function of the instantaneous crank angle. In order to control the bearing oil injection pressures, different alternatives may be considered, such as mechanical cam systems, hydraulic servovalves [7,19] and piezoelectric nozzles [21,22].

4. Numerical procedure

The steps to obtain the fluid film forces, reaction forces and rotor equilibrium position in function of time, are summarized in the following main steps:

- *Pre-processing*: Based on the geometric and physical parameters of the system (i.e., dimensions, rotational speed, inertias, etc.) and on the kinematic initial conditions, the initial system of equations for the multibody dynamic model can be defined.
- *Solution of the Reynolds equation*: The Reynolds equation for conventional hydrodynamic lubrication (9) can be solved analytically (for the *SJB* and *LJB* approaches) by using the expressions of Table 1. However, when a solution for a finite-width bearing (*FB*) is required or when the Reynolds equation includes the terms that account for the active lubrication, as in Eq. (11), numerical methods have to be used. In this work, the modified Reynolds equation is discretized via finite differences and solved for each time step by using a direct system equation solver based on the well known LU factorization method [23]. To compute the fluid film forces, the pressure distribution is numerically integrated over the journal surface, as in Eq. (10), using the Simpson Method. To represent the fluid film forces in the inertial reference frame, a standard transformation in the angle ϕ is used, i.e., ${}_I\mathbf{f_b} = \mathbf{T}_\phi\{F_\xi, F_\eta\}^\mathbf{T}$. In order to discretize the modified Reynolds equation for active lubrication, a non-uniform grid is used to be able to refine the mesh over the area where the orifices for oil injection are located and to obtain more accurate results for the film pressures and the minimum fluid film thicknesses. If the bearing surface is discretized in φ and z directions with a non-uniform grid of $m \times n$ nodes, respectively, and assuming that the bearing is well aligned (i.e., $\partial h/\partial z = 0$) and the viscosity of the fluid film keeps constant,

the Reynolds equation in finite differences is given by

$$\Delta_{m,n}p_{m-1,n} + \Lambda_{m,n}p_{m+1,n} + \diamond_{m,n}p_{m,n} + \nabla_{m,n}p_{m,n-1} + \Delta_{m,n}p_{m,n+1} = 12c_b r_b^2\left[\dot{\varepsilon}\cos\varphi_{m,n} + \varepsilon\sin\varphi_{m,n}\left(\dot{\phi} - \frac{\Omega}{2}\right)\right] - \frac{3r_b^2}{\mu l_o}\sum_{i=1}^{s}\mathrm{F}_{i_{m,n}}\bar{P}_{inj} \quad (12)$$

where

$$\Delta_{m,n} = \frac{1}{\Delta\varphi_m + \Delta\varphi_{m-1}}\left[-\frac{3h_{m,n}^2}{\mu}\frac{\partial h}{\partial\varphi}\Big|_{m,n} + \frac{2h_{m,n}^3}{\mu\Delta\varphi_m}\right]$$

$$\Lambda_{m,n} = \frac{1}{\Delta\varphi_m + \Delta\varphi_{m-1}}\left[\frac{3h_{m,n}^2}{\mu}\frac{\partial h}{\partial\varphi}\Big|_{m,n} + \frac{2h_{m,n}^3}{\mu\Delta\varphi_m}\right]$$

$$\diamond_{m,n} = -\frac{2h_{m,n}^3}{\mu}\left[\frac{1}{\Delta\varphi_m + \Delta\varphi_{m-1}}\left(\frac{1}{\Delta\varphi_m} + \frac{1}{\Delta\varphi_{m-1}}\right) + \frac{r_b^2}{\Delta z_n + \Delta z_{n-1}}\left(\frac{1}{\Delta z_n} + \frac{1}{\Delta z_{n-1}}\right)\right] - \frac{3r_b^2}{\mu l_o}\sum_{i=1}^{s}\mathrm{F}_{i_{m,n}}\cdot p_{m,n}$$

$$\nabla_{m,n} = \frac{2h_{m,n}^3 r_b^2}{\mu\Delta z_{n-1}}\frac{1}{\Delta z_n + \Delta z_{n-1}}, \quad \Delta_{m,n} = \frac{2h_{m,n}^3 r_b^2}{\mu\Delta z_n}\frac{1}{\Delta z_n + \Delta z_{n-1}}$$

In order to solve Eq. (12), suitable boundary conditions must be defined. Since the boundary pressure at the bearing edges is atmospheric, it may be taken as zero: $p = 0$; for $z = 0$ and l_b. Along the φ direction, the Reynolds equation is solved considering that $p = 0$ at $\varphi = 0$ and 2π, and if subambient pressures appear they are replaced by zero, assuming the Gümbel boundary conditions.

- *Numerical solution of the global system*: In order to solve the global system given by Eq. (7) and to obtain the reaction forces and accelerations of the system, the fluid film forces must be calculated and updated at each time step in the vector $\bar{\mathbf{c}}$. However, the calculation of the fluid film forces at the time t_{i+1} depends on the velocity and position of the crank centre at t_{i+1}, which must be estimated previously. Therefore, in this work a scheme based on the implicit Newmark method combined with a predictor–corrector approach has been used [24]. Thus, for each time step initial estimations of the position and velocity of the crank centre are obtained by using the Heun's explicit method, which allows to compute the fluid film forces based on the initial guess values and to solve the global system at the time t_{i+1}. Then, by using the implicit Newmark method new estimations of the velocity and displacement of the crank centre can be calculated and used to update the journal bearing forces in the global system, which is solved again, and after a few iterations the difference between two consecutive values becomes smaller than the prescribed tolerance and the computation of the global system is moved forward to new time step.
- *Post-processing*: After the global system is solved for several cycles of the compressor, plots of all the variables can be generated in function of the time or the crank angle. For the purpose of this work, the main plots of interest are the plots of the journal orbits, the minimum fluid film thickness, the maximum film pressure and the film pressure distribution.

5. Numerical results

The main geometrical dimensions and physical properties of the reciprocating compressor used for the numerical simulations are given in Table 2. The curves of variation of the gas pressure inside the cylinder and the motor torque are shown in Figs. 4 and 5, respectively. The numerical results presented in this section are obtained from the solution of the global system of equations and the analysis is centred on the upper journal bearing of the compressor.

5.1. Comparison between analytical and numerical solutions of the Reynolds equation

The results obtained for the upper journal bearing, operating under conventional hydrodynamic lubrication and by using analytical and numerical solutions of the Reynolds equation are presented in this section. The journal bearing forces are analytically computed by using the equations of Table 1, and numerically calculated by using finite differences. The orbits obtained using the analytical *SJB* approach and using the numerical solution for a finite-width bearing are shown in Fig. 6. It can be observed that the shape of the orbits is similar in both cases, however, higher eccentricities are found by using the finite-width bearing approach, which can be explained by the assumption of neglecting the variation of pressure in the circumferential direction with the *SJB* approach. A plot that compares the maximum fluid film pressures by using analytical and numerical solutions of the Reynolds equation is presented in Fig. 7. It can be observed that the maximum film pressures obtained with the *LJB* approach are much lower than the pressures obtained with the other approaches. Since these results are for a

Table 2
Main geometrical and physical parameters of the compressor.

Radius crank-pin centre (r_c)	7.5 (mm)
Mass of crank (m_c)	0.1 (kg)
Inertia of crank (I_{c_z})	5×10^{-3} (kg m^2)
Mass of connecting rod (m_{cr})	0.1 (kg)
Inertia of connecting rod (I_{cr_z})	1.7×10^{-5} (kg m^2)
Diameter of piston (D_p)	23 (mm)
Mass of piston (m_p)	0.043 (kg)
Bearing aspect ratio (λ)	0.375; 0.75; 1
Land width ratio ($\bar{a}_b$)	0.1; 0.15; 0.2
Journal clearance (c_b)	15 μ (m)
Fluid viscosity (μ)	0.005 (Pa s)
Angular velocity (Ω)	312 (rad/s)
Diameter (d_o)/length orifices (l_o)	1.5; 20 (mm)

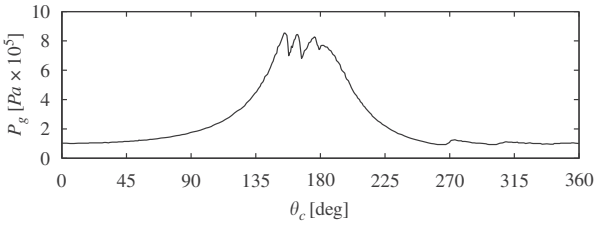

Fig. 4. Cylinder gas pressure [5].

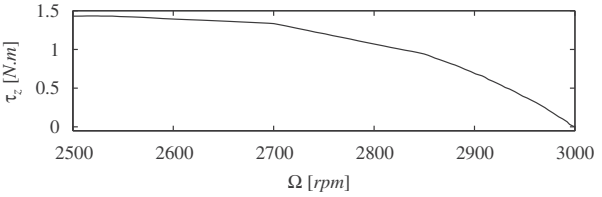

Fig. 5. Motor torque characteristic curve [4].

bearing of short dimensions ($\lambda \leq 0.5$), the more realistic estimations of the maximum film pressure are obtained with the analytical *SJB* approach and the numerical solutions for a finite-width bearing. To make sure of the correctness of the numerical solutions obtained, a convergence analysis was carried out. It was found that using a grid with $n_\varphi = 90$ and $n_z = 21$ nodes for the solution of the Reynolds equation, and using a time step of $\Delta t = 2 \times 10^{-6}$ s for the solution of the global system, good approximations for the minimum fluid film thickness and the pressure distribution can be obtained.

5.2. Influence of the bearing geometric parameters, λ and $\bar{a}_b$

In this section, the influence of the bearing aspect ratio and the axial land ratio on the bearing performance is analysed for conventional hydrodynamic lubrication and hybrid lubrication conditions. Fig. 8 illustrates the influence of the parameter λ on the orbit of the bearing, the minimum fluid film thickness and the maximum fluid film pressure. It can be observed that with a larger aspect ratio the minimum fluid film thickness becomes larger and the maximum pressure lower, which means that the journal orbit is generated closer to the centre of the bearing, which is expected due to the increase of the bearing area supporting the external load. The fluid film pressure distributions at four different crank angles during one cycle, for a bearing of $\lambda = 0.75$, are shown in Fig. 9. It can be observed from this figure that the maximum oil film pressures are located at the middle of the bearing along the width direction, and in the range of $180^\circ \leq \Theta \leq 225^\circ$, along the circumferential direction. For the case when lubricant is injected through orifices located at $\Theta_o = 180^\circ$ with $\bar{a}_b = 0.2$ and $P_{inj} = 2$ MPa, the effect of the parameter λ on the fluid film thickness is shown in Fig. 10. If Figs. 10 and 8(b) are compared, it can be observed that for the cases with $\lambda = 0.5$ and 0.375, the influence of the injection pressure on the minimum fluid film thickness is minimum, due to the fact that the fluid film pressure generated hydrodynamically is higher than the oil injection pressure. When the bearing aspect ratio is higher ($\lambda = 0.75$), the hydrodynamic film pressure becomes lower, and therefore, the influence of the radial oil injection $P_{inj} = 2$ MPa becomes more significant, as seen in Fig. 10. The influence of the axial land width ratio ($\bar{a}_b$) on the minimum fluid film thickness for the same hybrid lubrication conditions is shown in Fig. 11. It can be seen that the minimum fluid film thickness is not significantly affected by the change of $\bar{a}_b$, specially during the times where the lowest film thicknesses are found. Some studies related to the geometrical optimization of hybrid journal bearings have shown that typical values for the bearing aspect ratio of hybrid bearings are: $0.75 \leq \lambda \leq 1$, and for the axial land width ratio: $0.1 \leq \bar{a}_b \leq 0.4$ [9,11]. It has been shown in Ref. [11] that a hybrid bearing with $\lambda = 1$ and $\bar{a}_b = 0.2$ is a good configuration for a bearing with high load carrying capacity.

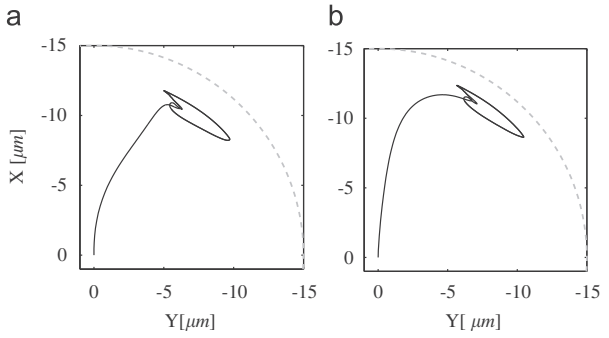

Fig. 6. Journal bearing orbits—conventional hydrodynamic lubrication. (a) Analytical solution—*SJB* approach; (b) numerical solution—*FB*, $\lambda = 0.375$.

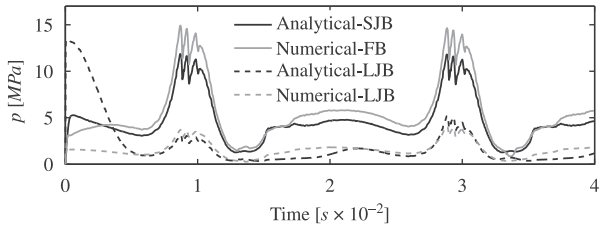

Fig. 7. Maximum film pressure using analytical and numerical solutions—conventional hydrodynamic lubrication ($\lambda = 0.375$).

5.3. Hybrid journal bearing

The results obtained for the compressor upper bearing operating with hybrid lubrication conditions are included in this section. In order to define appropriate angular position of orifices and injection pressures for the upper bearing working with hybrid lubrication conditions, the results obtained previously for the conventional hydrodynamic bearing can be used. For instance, it can be seen from the plots of orbits and pressure distributions,

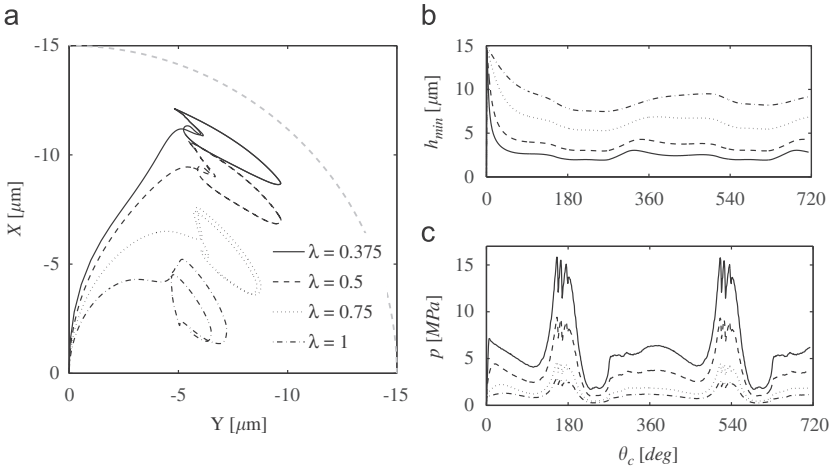

Fig. 8. Influence of the bearing aspect ratio λ—conventional hydrodynamic lubrication; (a) journal orbits; (b) minimum film thickness; (c) maximum film pressure.

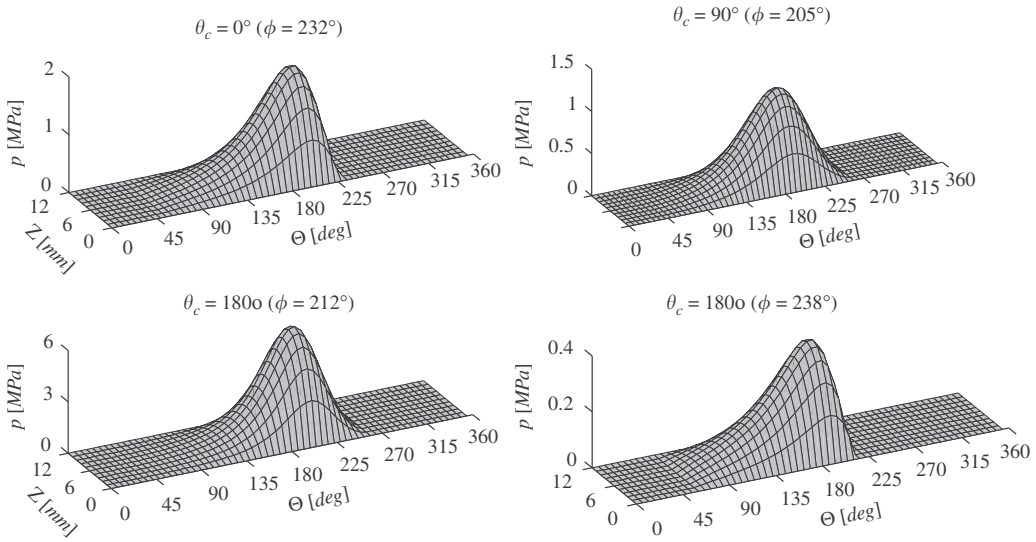

Fig. 9. Fluid film pressure distribution—conventional hydrodynamic lubrication ($\lambda = 0.75$).

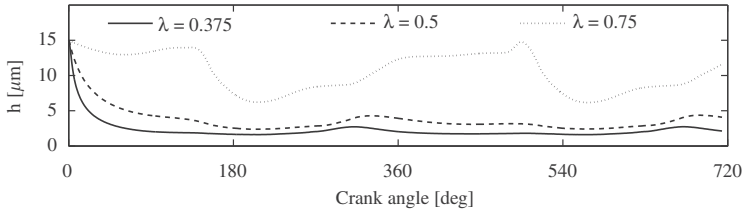

Fig. 10. Influence of λ on the minimum fluid film thickness—hybrid lubrication ($P_{inj} = 2$ MPa, $\Theta_o = 180^\circ$, $\bar{a}_b = 0.2$).

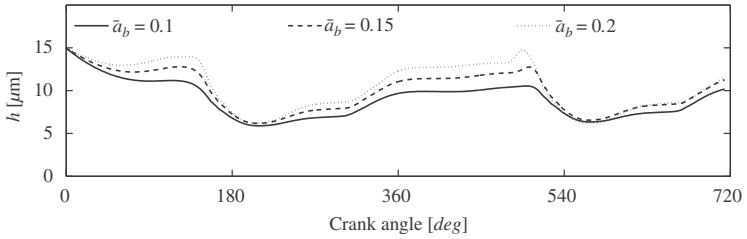

Fig. 11. Influence of $\bar{a}_b$ on the minimum fluid film thickness—hybrid lubrication ($P_{inj} = 2$ MPa, $\Theta_o = 180^\circ$, $\lambda = 0.75$).

shown in Figs. 8 and 9 that modifying the hydrodynamic lubrication by injecting oil through orifices located along the third quadrant of the bearing (i.e., $180 \leq \Theta \leq 270$), the maximum hydrodynamic pressure may be reduced and the minimum film thickness increased. The effects of changing the angular location of the injection holes and the oil injection pressures on the minimum film thickness, when others geometrical and physical parameters are kept constant, are analysed in order to find optimal hybrid lubrication configurations. Fig. 12 shows the minimum fluid film thickness computed for different angular positions of the orifices, assuming a constant injection pressure during the entire cycle. It can be seen from the cases analysed that, when the orifices are located at $\Theta_o = 180^\circ$ and 210° and oil is injected at $P_{inj} = 2$ MPa, the lowest fluid film thickness may be increased up to 56% and 25%, respectively, compared to

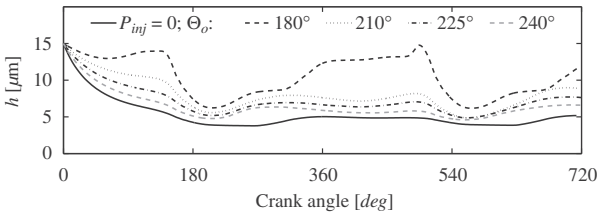

Fig. 12. Influence of the angular positions of the orifices on the minimum fluid film thickness—hybrid lubrication ($P_{inj} = 2$ MPa, $\lambda = 0.75$, $\bar{a}_b = 0.2$).

conventional hydrodynamic lubrication. On the other hand, the effect of using different oil injection pressures (with a constant value through each operating cycle of the compressor) on the

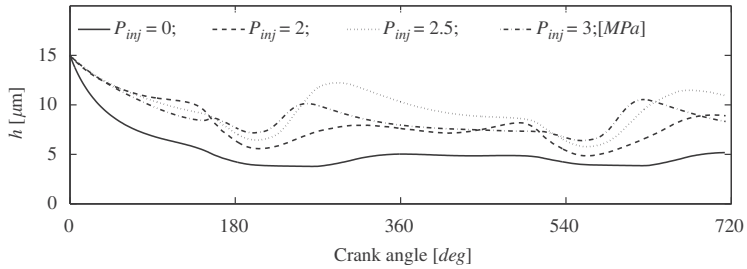

Fig. 13. Influence of P_{inj} on the minimum fluid film thickness—hybrid lubrication ($\Theta_o = 210^\circ$, $\lambda = 0.75$, $\bar{a}_b = 0.2$).

Table 3
Cases of analysis—hybrid controllable lubrication.

Case	Θ_{o_i}	Rules of injection (pressures in MPa)
(a)		Conventional hydrodynamic lubrication
(b)	$\Theta_o = 225^\circ$	$P_{inj} = 2$, for all $\theta(t)$
(c)	$\Theta_o = 180^\circ$	$P_{inj} = 2$, for all $\theta(t)$
(d)	$\Theta_o = 180^\circ$	$P_{inj} = 3$, if $140^\circ \le \theta(t) \le 190^\circ$ Otherwise $P_{inj} = 2$
(e)	$\Theta_{o_1} = 180^\circ$ $\Theta_{o_2} = 225^\circ$	$P_{inj_1} = 2$, for all $\theta(t)$ $P_{inj_2} = 3$, if $140^\circ \le \theta(t) \le 190^\circ$ Otherwise $P_{inj_2} = 2$

minimum fluid film for a bearing with orifices located at $\Theta = 210^\circ$ is shown in Fig. 13. It can be seen from this figure that for the cases where $P_{inj} = 3$ and 2.5 MPa, the lowest fluid film thickness may be increased up to 85% and 46%, respectively, compared to conventional hydrodynamic lubrication. These results show that modifying the hydrodynamic lubrication, by radially injecting oil at specific angular positions, the fluid film thickness can be significantly increased.

Taking into account that the gas pressure is periodic and the region where the cylinder is under maximum pressure is well known (Fig. 4), one can consider that the injection pressure may be actively modified in function of the angular position of the crankshaft. From the previous results, it has been also found that when oil is injected through orifices located between $180^\circ \le \Theta \le 225^\circ$ a significant increase of the minimum fluid film thickness can be obtained, as shown in Figs. 12 and 13. Based on this analysis and on the results previously obtained for the bearing working with hybrid lubrication and with conventional hydrodynamic lubrication, four different configurations of hybrid lubrication are proposed for the upper bearing of the compressor, which are listed in Table 3. Cases (b)–(d) are for a bearing with oil injected through orifices located at only one angular position (Θ_o), and case (e) is for a bearing with oil injected through orifices located at two angular positions. As seen in Table 3, in cases (d) and (e) the injection pressure changes depending on the angular position of the crank. A plot that compares the minimum fluid film thickness obtained for all the cases is shown in Fig. 14. It can be seen from this figure that for the bearings of cases (d) and (e), the minimum fluid film thickness can be increased up to 140%, when it is compared to the minimum fluid film thickness of the bearing with conventional hydrodynamic lubrication.

In order to illustrate how the fluid film pressure distribution is modified by the oil injection, Fig. 15 shows the fluid film pressure distribution for the hybrid bearing of case (c), plotted for every 90° of the crank rotation, during one full cycle. It can be observed from Fig. 15 that the maximum oil film pressure (at $\theta_c = 180^\circ$) is lower than the maximum oil film pressure computed for the case when the bearing is operating with conventional hydrodynamic lubrication (see Fig. 9). From the mechanical point of view, the fact of having lower pressures in the fluid film may be of great advantage since lower elastic deformations are expected, and therefore, a bearing with a more compact design operating with hybrid lubrication and a similar carrying capacity could be used.

6. Conclusions and future aspects

This work has been concentrated on the dynamic behaviour of a hermetic reciprocating compressor and the feasibility of applying controllable lubrication to the upper journal bearing. The global matrix system that describes the multibody dynamic model for a reciprocating compressor has been coupled to the numerical solution of the modified Reynolds equation, obtained by finite differences. The global system has been numerically solved obtaining the reaction forces, kinematical variables, minimum fluid thickness and equilibrium position for the journal at each time step.

The feasibility of controlling the lubrication for the upper journal bearing of a reciprocating compressor has been demonstrated through the comparison between the results obtained for the cases with conventional hydrodynamic lubrication and hybrid lubrication. The results presented in this paper are for specific configurations of the journal bearing, regarding to the angular position of the orifices and the injection pressures. The results obtained have shown that the minimum fluid film thickness can be significantly increased when the injection pressure is actively modified. It was found that for the bearing with orifices located at 180° and 225° the minimum fluid film thickness may be increased more than 100%. Nevertheless, more studies considering the influence of other bearing geometric factors such as the axial land width factor, diameter and length of the orifices, should be carried out in order to be able to define optimal hybrid bearing configurations for different cases.

Although in this study a small reciprocating compressor has been used to demonstrate the feasibility of applying controllable hybrid lubrication to dynamically loaded journal bearings, the results presented in this paper may be extended to the main bearings of large machines such as internal combustion engines and industrial reciprocating compressors, where wear and vibrations can be significantly reduced by actively modifying the conventional hydrodynamic lubrication. Depending on the type of machine and the flow and injection pressures required, an adequate strategy of control has to be defined, therefore further studies will be carried out to evaluate between different control systems (e.g., using piezoelectric nozzles, cams systems, hydraulic servovalves) which one could be more efficiently implemented.

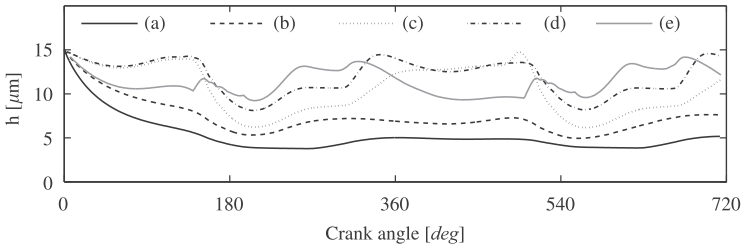

Fig. 14. Minimum fluid film thickness for different bearing configurations—hybrid lubrication ($\lambda = 0.75$ and $\bar{a}_b = 0.2$).

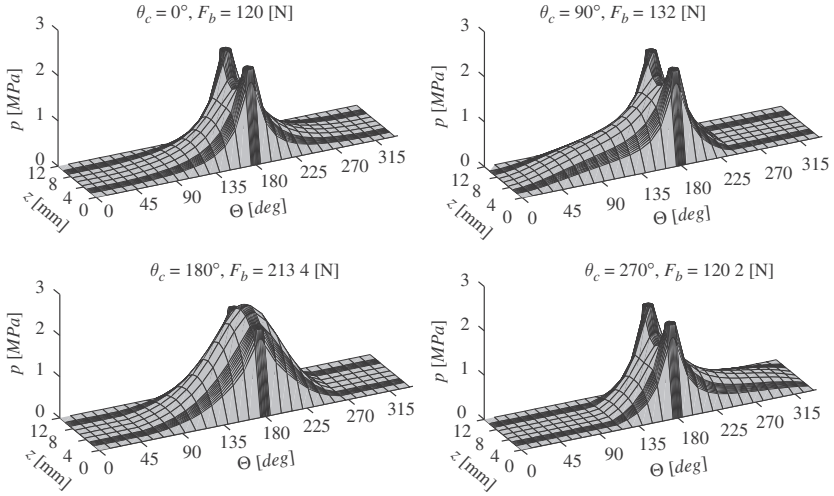

Fig. 15. Pressure distribution, bearing with orifices located at $\Theta_o = 180^\circ$ ($P_{inj} = 2$ MPa, $\lambda = 0.75$, $\bar{a}_b = 0.2$).

Acknowledgements

Supported by the Programme Alβan, the European Union Programme of High Level Scholarships for Latin America, scholarship No. E06D101992CO.

References

[1] Booker JF. Dynamically loaded journal bearings—mobility method of solution. J Basic Eng 1965;87(3):537–46.
[2] Goodwin MJ, Nikolajsen JL, Ogrodnik PJ. Reciprocating machinery bearing analysis: theory and practice. Proc Inst Mech Eng Part J—J Eng Tribol 2003;217(6):409–26.
[3] Rasmussen BD. Variable speed hermetic reciprocating compressors for domestic refrigerators. PhD thesis, Technical University of Denmark, Denmark; 1997.
[4] Rigola J. Numerical simulation and experimental validation of hermetic reciprocating compressors. PhD thesis, Universidad Politécnica de Cataluña, Spain; 2002.
[5] Cho JR, Moon SJ. A numerical analysis of the interaction between the piston oil film and the component deformation in a reciprocating compressor. Tribol Int 2005;38(5):459–68.
[6] Kim TJ, Han JS. Comparison of the dynamic behavior and lubrication characteristics of a reciprocating compressor crankshaft in both finite and short bearing models. Tribol Trans 2004;47(1):61–9.
[7] Santos IF, Nicoletti R, Scalabrin A. Feasibility of applying active lubrication to reduce vibration in industrial compressors. J Eng Gas Turbines Power 2004;126(4):848–54.
[8] Stout K, Rowe W. Externally pressurized bearings—design for manufacture Part 1—journal bearing selection. Tribology 1974;7(3):98–106.
[9] Rowe W, Xu SX, Chong FS, Weston W. Hybrid journal bearings with particular reference to hole-entry configurations. Tribol Int 1982;15(6):339–48.
[10] Sharma S, Kumar V, Jain S, Sinhasan R, Subramanian M. A study of slot-entry hydrostatic/hybrid journal bearing using the finite element method. Tribol Int 1999;32(4):185–96.
[11] Jadon V, Singh M. Study of supply cut-off and bearing geometric parameters on design of hybrid journal bearing. Ind Lubr Tribol 2007;59(2):92–102.
[12] Bremer H. Dynamik und regelung mechanischer systeme. Stuttgart Germany: B.G. Teubner; 1988 [in German].
[13] Ulbrich H. Maschinendynamik. Stuttgart, Germany: B.G. Teubner; 1996 [in German].
[14] Santos IF. Dinâmica de sistemas mecanicos. Sao Paulo: Makron Books; 2001 [in Portuguese].
[15] Hamrock BJ. Fundamentals of fluid film lubrication. New York: McGraw-Hill; 1991.
[16] Frêne J, Nicolas D, Degueurce B, Berthe D, Godet M. Lubrification hydrodynamique. Paris: Editions Eyrolles; 1990.
[17] Mourelatos ZP. An efficient journal bearing lubrication analysis for engine crankshafts. Tribol Trans 2001;44(3):351–8.
[18] Elrod HG. A cavitation algorithm. J Lubr Technol 1981;103(3):350–4.
[19] Santos IF, Russo FH. Tilting-pad journal bearings with electronic radial oil injection. J Tribol 1998;120(3):583–94.
[20] Santos IF, Scalabrin A, Nicoletti R. Beitrag zur aktiven schmierungstheorie. In: Schwingungen in Rotierenden Maschinen, vol. 5. Braunshweig, Germany: Vieweg Verlag; 2001. p. 21–30 [in German].
[21] Horikawa O, Sato K, Shimokohbe A. An active air journal bearing. Nanotechnology 1992;3(2):84–90.
[22] Mizumoto H, Arii S, Kami Y, Goto K, Yamamoto T, Kawamoto M. Active inherent restrictor for air-bearing spindles. Precis Eng 1996;19(2–3):141–7.
[23] Wendt JF. Computational fluid dynamics. Berlin: Springer; 1992.
[24] Garcia de Jalon J, Bayo E. Kinematic and dynamic simulation of multibody systems. The real-time challenge. New York: Springer; 1994.

DTU Mechanical Engineering
Section of Solid Mechanics
Technical University of Denmark

Nils Koppels Allé, Bld. 404
DK- 2800 Kgs. Lyngby
Denmark
Phone (+45) 45 25 42 50
Fax (+45) 45 93 14 75
www.mek.dtu.dk
ISBN: 978-87-89502-95-3

DCAMM
Danish Center for Applied Mathematics and Mechanics

Nils Koppels Allé, Bld. 404
DK-2800 Kgs. Lyngby
Denmark
Phone (+45) 4525 4250
Fax (+45) 4593 1475
www.dcamm.dk
ISSN: 0903-1685